IN SITU X-RAY STUDY OF ORTHORHOMBIC LITHIUM MANGANESE OXIDE

by

Immo Kötschau

B.Sc.(Honours), Trent University Peterborough Ont.,1994

THESIS SUBMITTED IN PARTIAL FULFILLMENT

OF THE REQUIREMENTS FOR THE DEGREE OF

MASTER OF SCIENCE

in the Department

of

Physics

SIMON FRASER UNIVERSITY

July 1997

APPROVAL

Name: Immo Kötschau

Degree: Master of Science

Title of thesis: *IN SITU* X-RAY Study of
Orthorhombic
Lithium Manganese Oxide

Examining Committee: Dr. Colombo Bolognesi, Assistant Professor
(Chair)

Dr. Jeffery R. Dahn, Professor of Physics
and Chemistry
Dalhousie University
Senior Supervisor

Dr. Mike Plischke, Professor

Dr. Robert F. Frindt, Professor

Dr. Albert E. Curzon, Professor
Department of Physics
Internal Examiner

Date Approved: 25 July 1997

Abstract

The electrochemical behaviour of Li/$LiPF_6$(1M EC–DEC)/$LiMnO_2$ cells has been investigated. Large capacity-fade on initial charge and discharge, as well as for the subsequent cycles, has been confirmed. A new design for the study of powder cathodes has been developed and tested for *in situ* experiments.

Extensive *in situ* X-ray studies have been carried out in order to map out the evolution of the crystal structure upon subsequent charge and discharge of the cathode material. It has been confirmed that $LiMnO_2$ converts irreversibly to a different structure (cubic) $LiMn_2O_4$ after the initial charge (=delithiation) of the cathode. The difficulties of cycling this new phase reversibly without capacity loss are reported. A model is proposed to explain the poor capacity retention of this promising Li-ion intercalation compound.

Dedication

To my Parents, Ulrike my sister, Kai, Carl and Anne

Acknowledgments

The author is grateful for the continuing support of his committee and in particular his supervisor, Dr. Jeff Dahn. His direct and precise comments were always useful to further the progress of this thesis project.

I would like to thank my former lab members, who are now in Halifax, for their support and collaboration. In particular Ian Courtney, Mark Obrovac, Edward Buiel, Dr. Oliver Schilling and Monique Richard. Special thanks go to Dr. Alf Wilson who helped me in desperate situations of getting my PC hardware fixed. Throughout the last year I became friends with many new graduate students who were given office space in the empty lab where I used to work all by myself after Jeff Dahn's group moved to Halifax. I would like to thank them for their great support and for many useful discussions. Special thanks to Andrew DeBenedictis, Eldon Emberly and James Gupta for their advice in matters of style and formulation. Thanks to Dan Vernon for his support using special software and for solving many related problems. Thanks to Anuj Aneja for many interesting discussions and for reminding me of deadlines. Thanks to Karn Kallio, Ted Monchesky and Richard Arès for reducing my load as a teaching assistant, particularly towards the end of this thesis project. Thanks to Wolfgang Mück who wrote the LaTeX style file and for answering many related questions. Special thanks to Scott Wilson, who helped many times when I had problems with the X-ray setup and to Sharon Beever our graduate secretary for her love and support.

Finally, I would like to thank my parents and my sister with her family, to whom the thesis is dedicated, for their love and continuous support.

Contents

List of Tables

List of Figures

Chapter 1

Introduction

Understanding processes in nature which involve the conversion of one form of energy into another has always been of interest to mankind. About 300 years ago mankind succeeded in kindling the fire of coal and wood and converting thermal into mechanical energy by the invention of the steam engine. One hundred years later Allesandro Volta discovered that a different kind of energy could also be stored in matter: the advent of electricity. Another 40 years later the lead acid battery system was reported in the Journal of the Electrochemical Society and a machine capable of converting electrical energy into mechanical energy was invented 40 years later by Nicola Tesla. Mankind felt empowered by all these inventions and their subsequent development of technologies was only a matter of decades. An interesting side observation for the battery researcher is, that by the turn of the century there were more electric vehicles (EV's) on the road than automobiles powered by internal combustion engines. Politics and corporate interests, the determinants of available research funding, decided to promote internal combustion engines since combustion fuels were more abundant and the potential in making profits seemed to be infinite at the time. The demand for finding denser and lighter storage media for electrical energy was gone. Except for the development of batteries used in military applications, 'beasts' like the sodium sulfur system (operated at 300°C), no apparent progress was made up to the eighties. As the century of inexpensive oil draws to a close, politicians and corporations ring the bell at the electro-chemist's door, an effective battery for EV's is needed now. The history of these very recent developments is excellently reviewed by Alf Wilson [1].

From a scientific point of view, dramatic changes have occured since the origin of the atomic spectra could be explained at the beginning of this century. Since

then we have learned that the energetic changes which govern processes in nature as well as in our daily lives are related to the differences in the binding of *electrons* to the nuclei found in atoms and molecules. In chemistry we learn today in high school that burning of firewood is an oxidation process in which hydrocarbons are transformed into a number of products including carbon dioxide. The difference in molecular binding energy between the reactants and the products is released in the form of heat[1]. The fudamental rearrangement of the binding and structuring in matter allows for the release of enormous amounts of energy in the form of heat. Just over 60 years ago mankind found that the atomic hypothesis can be exploited, by accessing the energetic differences in the binding of the nucleus itself, which are a factor of a million larger than molecular binding energies. The atomic bomb and the development of fission reactors are well known applications.

Burning of fuels and the fission of nuclei are very intense processes and the fuels are subject to fundamental structural changes. Processes found in nature, in particular those found in living organisms are more subtle processes which also require energy. The energetics behind these processes can be understood by the same principle: differences in electronic binding. However, the overall energy scale and the energy densities involved are smaller. In a battery we imitate related processes in a very controlled manner and on a large scale in order to store electricity.

1.1 $LiMnO_2$ – Lithium Manganese Oxide as an Energy Reservoir.

In contrast to conventional lead acid batteries, lithium-ion batteries do not simply rely on the principle of 'dissolving' solid matter (lead) in an electrolyte and subsequent electroplating of Pb^{2+} ions[2] out of the electrolyte onto the metallic surface of the electrode. Although this is also an option for lithium, and realized in primary lithium metal batteries, lithium metal performs poorly as a plating electrode employed in secondary batteries [1], (see also chapter 3). Researchers found it safer to employ the reactive lithium confined in chemical compounds where it is more 'diluted' over three-dimensional space.

[1] besides other energy forms like em radiation.

[2] Anode reaction: $PbSO_4$ (s) + $2e^-$ $\longrightarrow$ Pb(s) + $SO_4{}^{2-}$. [2]

Compounds in which lithium occupies regular interstitial sites in a crystal lattice are called *host materials*. If the host material allows for reversible insertion and extraction of lithium-ions such that the underlying crystal framework is maintained, we refer to such a compound as an *intercalation compound*. Since solid matter is held together by attractive and repulsive forces mediated by the Coulomb interaction, we seek hosts which can accommodate the extraction of (positive) lithium ions, but yet maintain their electrostatic balance. This poses strong constraints on the choice of compounds.

Lithium transition metal oxides are known to possess these properties. Whereas lithium gives up only one electron very easily to form Li^+, transition metals ions usually exist in a number of oxidation states. This, in particular, is a common feature of the 3d transition metals such as Ti, V, Cr, Mn, Fe, Co and Nickel. A change of oxidation state is even possible if embedded in a regular lattice formed by a transition metal and oxygen.

$LiMn_2O_4$ for example, is an excellent intercalation compound, and is already employed in many commercial applications. Many related lithium cathode compounds were studied in the recent past; $LiCoO_2$, $LiNiO_2$, Li_xTiO_2, Li_xMoO_2 and $LiNiVO_4$ are the more important ones. $LiMnO_2$ became interesting after Ohzuku reported in 1992 the synthesis of this compound at low temperatures [3] and demonstrated high amounts of Li^+ can be removed.

One year later, Reimers *et al.* [4] found that the crystal structure of $LiMnO_2$ is unstable upon removal of lithium on initial charge. They also succeeded in synthesizing $LiMnO_2$ at low temperatures and did, under the direction of my senior supervisor, the first *in situ* X-ray study on this cathode compound. The structural transformation upon initial charge was confirmed by Gummow *et al.* [5], Laurence Crogennec *et al.* [6] and most recently by Weiping Tang *et al.* [7] who studied the extraction of Li^+ from $LiMnO_2$ by plain *chemical* rather than electrochemical means.

Historically $LiMnO_2$ was first reported by Johnston and Heikes, who studied the magnetic properties of Li-Mn-O compounds in 1956 [8]. Most recently Tabuchi *et al.* [9] published results particularly about $LiMnO_2$. An accurate analysis of the crystal structure of $LiMnO_2$ was performed by Hoppe, Brachtel and Jansen in 1975 [10].

$LiMnO_2$, is the highest capacity oxide known which is directly suitable for Li-ion cells. It also promises to be cheap to manufacture and can be regarded as environmentally friendly. Lithium-Ion battery technology carries the potential to provide an

answer to problems of energy storage for any portable application where electrical energy is needed. In particular in electric vehicle (=EV) applications, batteries which carry high energy densities at little weight, are highly in demand. Manganese is still an abundant ore, and hence $LiMnO_2$ meets all the criteria for becoming a cathode material in EV applications.

However, the question remains, as to whether $LiMnO_2$ will perform as an intercalation host which allows reversible insertion and extraction of Li^+ over hundreds of discharge and charge cycles ? This is the point where I entered the field of research when I joined the Simon Fraser graduate program in physics under Jeff Dahn's supervision in fall 1994. A Belgium company, Sedema, supplied samples of $LiMnO_2$, which seemed to perform even better than those synthesized previously in our lab by Monique Richard and Reimers *et al.* . My first project in Jeff's lab was to do a study of their many cycle behavior. Indirectly we confirmed [11], that structural changes occur in the cathode. However we did not understand the mechanisms which resulted in the sometimes good many cycle performance and in strong capacity fade in other experiments.

The next natural step was therefore to capture and understand the structural changes in the cathode compound. The best method at hand which was conveniently accessible and manageable for a masters student was to take powder X-ray diffraction spectra from a cathode charged to different potentials.

1.2 X-rays

From a general point of view, this thesis is an investigation of some aspects of microscopic properties and the dynamics of ion transport in solid (condensed) matter. As I indicated above, it concerns the electrochemistry as well crystallography of some chosen ternary lithium compound for battery applications. If we would have a suitable 'microscope' or some device at hand which enabled us to 'look' at the structures on the atomic level in the same way as we observe events in our daily perception (also matching the time scale) then much of this work would have been superfluous.

Due to the lack of physical methods helping us to visualize physical processes in battery cathode compounds we have to resort to methods where we shine some very particular light on the object. Our ideas how light interacts with solid matter have been improved and refined to a degree where identification of pure chemical

samples are routine in research, medicine and in industry. Since 1911, after William Bragg published his first crystallographic studies on sodium chloride, the field of X-ray crystallography has been well explored. Two decades later a rigorous formalism had been formulated and a solid base of experimental data had been accumulated in order to identify atomic as well as molecular structures. The methods have become so powerful that even the analysis of complex structures found in living organisms are no exception anymore as it is for example the case for proteins or DNA.

As for the subject of this thesis, Lithium-Ion Batteries, we chose, for the above mentioned reasons, to shine light in the form of X-rays on powder samples, in order to find answers to questions like how a crystal structure changes as it is subject to electrochemical manipulations.[3] Thus we were employing the body of powder X-ray diffraction methods to find answers to questions of dynamical change in compounds which are known and (fairly) stable under ambient conditions.

Apparently this journey into the structure of matter is rather a difficult one if we realize that the 'image' produced by our light is of statistical nature. The powder method relies on the very large number of scattering events stemming from spatially randomly distributed and randomly oriented crystallites in the powder sample. Moreover, the entire scattering process is incoherent. We lose the phase information for scattered light and have no hope to easily reconstruct the 'true' three dimensional structure.

We find ourselves therefore at the heart of X-ray crystallography if we want to say something about these 3D structures, in particular to comment on their dynamical change upon removal and insertion of Li^+ in cathode compound.

1.3 *In Situ* – 'look inside'

In explaining this term I leap ahead. By measuring the weight of the cathode and by recording the current in charge or discharge experiment it is then possible to calculate how much of the intercalant is in the compound (the 'x' in $Li_{(1-x)}Mn_2O_4$ for example). If we want to look at what changes occur in a compound like $LiMnO_2$ if we remove lithium atoms there are in principle two ways in which this can be done. The first method is to charge or discharge an assembled battery stack and then take

[3]Neutron diffraction provides another means of structural analysis, very similar to X-ray diffraction. It has the advantage that weak X-ray scatterers like Li^+ are much more visible.

it apart, to access the modified cathode compound, remove it and do subsequent X-ray analysis on whatever is there. The problem here is that after this is done it is usually impossible to do further charge or discharge experiments on the compound with the required accuracy. This is because the disassembly exposes the cathode compound and electrolyte at some point to air and a number of secondary reactions can occur, forming undesired phases which will appear in the X-ray diffraction pattern. Common electrolytes are known to crystallize in air and any manganese oxide is prone to undergo what is commonly called *disproportionation*, a surface oxidation process, typically found at the surface of the crystallites. Water vapor in air causes further trouble. It is clear that we cannot avoid exposure to air since powder diffractometers are usually not found in an inert atmosphere (He, Ar etc.). If we want to find out about the structure at different compositions, we are forced to manufacture a series of ideally identical test cells which can all be charged to different concentrations of intercalant. These cells are then subsequently taken apart and must be discarded for further intercalation, after the X-ray analysis.

The second method is to find a way to 'look' into the battery without altering the state of the compound too much, and in fact there is a way to avoid any secondary side reaction. All we need is a window to 'look' into a battery, or to be more precise to see the cathode (or anode) in a sealed fully assembled test cell.

Beryllium is mostly transparent for X-rays. It scatters weakly[4], and has very few but sharp diffraction lines in a typical diffraction pattern. Beryllium is a conductor, so electrical contact to the cathode can always be established. A holder needs to be machined, which places the sealed cathode into the scattering plane of a typical powder diffractometer. Now we can attach the electrodes and charge the battery to the desired amount of cumulative charge transfer, which corresponds to a particular concentration of intercalant in the cathode. Subsequently we let the intercalation process settle into equilibrium and take a 'snapshot' of the structure, of known composition, by starting an X-ray scan.

All of the previous mentioned problems are avoided. The trade off is that we have to live with interference from peaks belonging to the beryllium window. However the decisive advantage is that we have real evidence for the evolution of the crystal structure as we change the composition in one and the same cathode. We can even take continuous 'snapshots' as we charge and discharge the cathode. If the rate of charge

[4]compared to manganese and oxygen, not lithium however.

is low and adjusted well, we can monitor changes in the battery at *quasi-equilibrium* conditions.

The first record of *in situ* X-raydiffraction for monitoring compositional changes in battery compounds was found in 1978 by Chianelli [12]. Chianelli proposed a method of 'Dynamic X-ray diffraction' using thick compacted electrodes of Li_xTiO_2. As pointed out by Jeff Dahn [13], the problem with Chianellis' method was that the rather bulky electrodes displayed no consistent equilibrium behavior which is necessary to correlate the cell potential in a meaningful way.

Jeff Dahn, M.A. Py and R. Haering developed the method further. By inventing a new cell design and assuring quasi-equilibrium conditions in a flat cathode, they succeeded in measuring the lattice parameters of Li_xTiS_2 during charge and discharge to high accuracy. In the recent past, Jan Reimers and Wu Li [14] did similar work on $LiMnO_2$ and $LiNiO_2$ as cathode compunds and Tao Zheng [15] (and other members of the lab) studied carbon anodes respectively.

1.4 Contribution of this Thesis

The objective of this thesis was to repeat Reimers' experiment, but improve on the experimental conditions in a number of ways and to identify mechanisms for the capacity loss. The contribution of this thesis is to provide an accurate confirmation for the irreversible transition on initial charge. If we understand the initial transformation processes better, we gain valuable insight for the explanation of the subsequent charge and discharge properties. The thesis explores the *in situ* method and documents many important aspects which have to be considered in the analysis of recorded X-ray data. The thesis is in this respect meant to be a handbook (although bulky) for the next person to conduct a similar experiment. Scientifically, little insight was gained since the interpretation of X-ray data from disordered compounds is inherently difficult.

1.5 Structure of the thesis

Apart from the first chapter, the structure of the thesis is chosen in a way to provide an account of the chronology of the study. A survey of the crystallographic properties of the compounds is necessary in order to understand the correlation between the electrochemical state and the structural state of the the powder cathode. It is provided

in chapter 2. In chapter 3 those experiments we did the fall of 1994, which were an empirical study of the electrochemical properties of $LiMnO_2$ cathodes, which lead up to the question of how to correlate the structure to the charge state of the cathode, are reviewed. Chapter 4 and chapter 5 introduce the method used to study the structure of $LiMnO_2$ cathodes. The experimental apparatus is also described there, including the design and assembly of *in situ* X-ray cells. The refinement of X-ray powder diffraction patterns will be addressed separately in chapter 6.

In chapter 7 we report on the most important *in situ* X-ray experiments done, and discuss our refinement results. A final and very short chapter summarizes and concludes the work and suggestions are made for the research ahead.

Chapter 2

Crystallography of Lithium Manganese Oxides

As pointed out in the introduction, there are in theory strong physical constraints for finding good intercalation host materials suitable for high energy density battery systems. Since solid matter is held together by attractive and repulsive forces mediated by the electromagnetic interaction, we are searching for compounds which can accommodate the extraction of one sort of ion, but yet maintain their electrostatic balance. Obviously we cannot expect that a simple rocksalt structure as found in NaCl will allow for such a process to occur. However if two different kinds of cations are present in place of sodium in NaCl, as is the case for many ternary oxides, we expect in some cases that the extraction of one sort of cation is possible. Two conditions have to be satisfied. First the ionic mobilities must allow for transport of the 'extracted' cations but not for the 'remaining' cations (at ambient temperatures). Second the 'remaining' cations must allow a change in the average oxidation state to balance the electrostatic forces in the crystal over an appreciable range.

In practice we find that the 'mobile' cations are light and monovalent such as Li^+. The 'remaining' cations are usually transition metals, heavier elements, like nickel, cobalt, manganese or iron, which are less mobile due to their mass and are seldom monovalent. The electrons in the 3d shell of transition metals are normally less tightly bound compared to 2p electrons in oxygen, for example, and there are (in principle) five energetically degenerate orbitals over which the valence electrons can be distributed. Thus transition metals are candidates in the search for cations with highly variable valency. Moreover the ionic radii of many transition metals are

approximately equal to that of Li^+ ions, which is another condition for the formation of regular crystal structures.

$LiMn_2O_4$ is a typical intercalation host. In this compound, oxygen occupies one sublattice and manganese and lithium ions will occupy a second sublattice very much like in rocksalts (i.e. NaCl). One goal of this chapter is to elaborate this important property. In order to provide for good isotropic ionic transport through the crystallite, lithium ions must be located on sites where they can access neighboring sites of the same kind without crossing high potential barriers, and these sites must be connected throughout the entire crystal.

Clearly if we want to learn about these mechanisms in more detail we need first to survey the various structures of Lithium Manganese Oxides in some detail and learn about their crystallography. The following three subsections will characterize separately the main crystal structures which were of fundamental importance in this study. The last subsection will stress common features and the similarities of these structures and will address more general issues such as stability and conductivity as well as phase transitions between these structures.

2.1 Orthorhombic $LiMnO_2$

$LiMnO_2$ was first synthesized by Johnston and Heikes [8] who studied the $Li_xMn_{1-x}O$ system for crystallographic and magnetic properties. Their samples where obtained by heating intimate mixtures of Li_2O_2 and MnO according to the reaction

$$\frac{x}{2}Li_2O_2 + (1-x)MnO \longrightarrow Li_xMn_{(1-x)}O \quad (600-850^oC). \tag{2.1}$$

under exclusion of air. $LiMnO_2$ was obtained for $x = \frac{1}{2}$ with mass density of approximately 4.23 gcm^{-3}. By means of powder X-ray diffraction[1] the authors succeeded to index all lines to an orthorhombic unit cell. A more detailed description of the crystallographic properties of $LiMnO_2$ was given by Hoppe, Brachtel and Jansen [10], who confirmed an orthorhombic unit cell with [Pmnm] space group symmetry. The unit cell parameters and atomic coordinates taken from [10] are displayed in Table 2.1 below. The method of synthesis is different compared to Johnston and Heikes. $LiMnO_2$ is obtained by using other precursors according to

$$1.4LiOH + MnO_{(1+\delta)} \longrightarrow LiMnO_2 + H_2O \quad (750^oC). \tag{2.2}$$

[1] See chapter chapter 4.

Figure 2.1 shows a single unit cell containing eight atoms which are shifted with respect to the origin so that lithium occupies the corners of the cell. The octahedron encloses a single manganese ion and is stretched along the < 001 > direction (c-axis). Continuation of the unit cell along the b-axis shows that each lithium ion is likewise sixfold coordinated by oxygen. This observation suggests a representation of this structure consisting of closed packed oxygen octahedra as shown in Figure 2.2.[2]

$LiMnO_2$					
Space group: Pmnm ; a=2.80_5 b=5.75_7 c=4.57_2 [Å]					
Atom	Position	x	y	z	n*
Li	2a	0.25	0.126(4)	0.25	1
Mn	2a	0.25	0.6347(2)	0.25	1
O	2b	0.25	0.144(1)	0.75	1
O	2b	0.25	0.602(1)	0.75	1
*) denotes fractional occupation of the site.					

Table 2.1: Structural parameters of $LiMnO_2$

Jahn-Teller distortions

According to Hoppe, Brachtel and Jansen [10], the stretch along the < 001 > direction compared to the two other axes in the (001) plane amounts to 14%. This phenomenon is quite remarkable, and can be explained by *crystal field theory*, considering that Mn^{3+} ions are coordinated not in spherical, but octahedral symmetry. In this case the degeneracy of the 3d orbitals in transition metals is removed. Contour plots of constant electron density of these orbitals are shown in Figure 2.3. The axes of the lobes of the d_{xy}, d_{xz} and d_{yz} orbitals do not coincide with the principal axes of the $[MO_6]$-octahedra[3] where the oxygen ions are found. These orbitals are collectively referred to as t_{2g} orbitals. The remaining orbitals are referred to as e_g-orbitals. The electron density of the $d_{x^2-y^2}$ orbital obeys a four-fold rotational symmetry around the z-axis and the d_{z^2} orbital obeys full rotational symmetry around the z-axis. As can

[2]This drawing and those of the following sturctures were generated with the program 'ATOMS' © [16].

[3] 'M' stands for a particular transition metal ion.

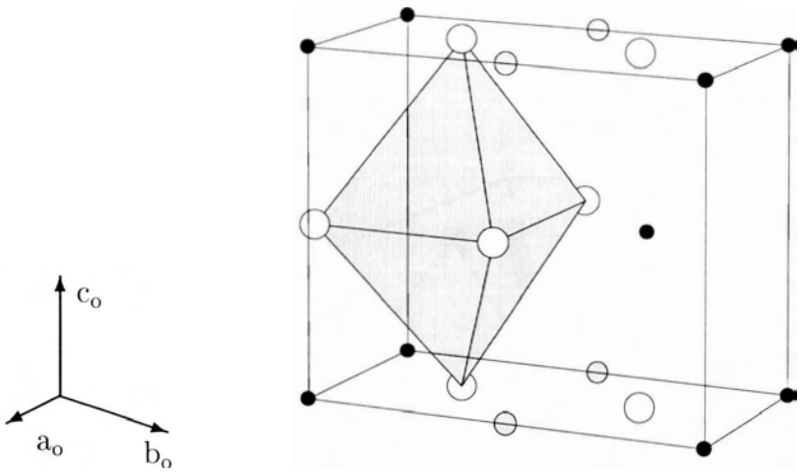

Figure 2.1: Unit cell of $LiMnO_2$ with lithium at corners. Large white atoms are oxygen and medium grey is manganese. The octahedron encloses a Mn^{3+} ion in the center.

be discerned from Figure 2.3, their lobes are centered between approaching oxygen atoms. Manganese has five d and two 4s electrons. For Mn^{3+} ions we have to distribute four electrons over the t_{2g} and $e_g$orbitals according to *Hund's rule*. We place one electron in each t_{2g} orbital and one electron in an e_g orbital. Now we consider the interactions of the electrons along the pricipal axes (x, y, and z axis in Figure 2.3) of the octahedreon. The electron density of the e_g orbitals is strongly centered around these axes whereas the density of the t_{2g} orbitals is minimal in the xy, xz and yz planes. As a consequence we find for the e_g orbitals in $[MO_6]$-octahedra a stronger repulsive interaction than for the t_{2g} orbitals. This leads to different bond lengths along the axes of $[MO_6]$-octahedra. In a crystal compound we will therefore find different lattice constants along the the corresponding axes, if in the majority of the Mn^{3+} the same e_g orbital is occupied.

The effect of an octahedral field on the energies of the d-orbitals is represented schematically in Figure 2.4 for this particular case, but can be generalized for any non-spherical crystal field.[4] The energy of the orbitals in a (negative) spherical symmetric charge distribution is *raised* with respect to a free ion. For an octahedral charge distribution some of the degeneracy is removed and if the symmetry of the octahedral

[4] with tetrahedral, trigonal or planar symmetric charge distributions.

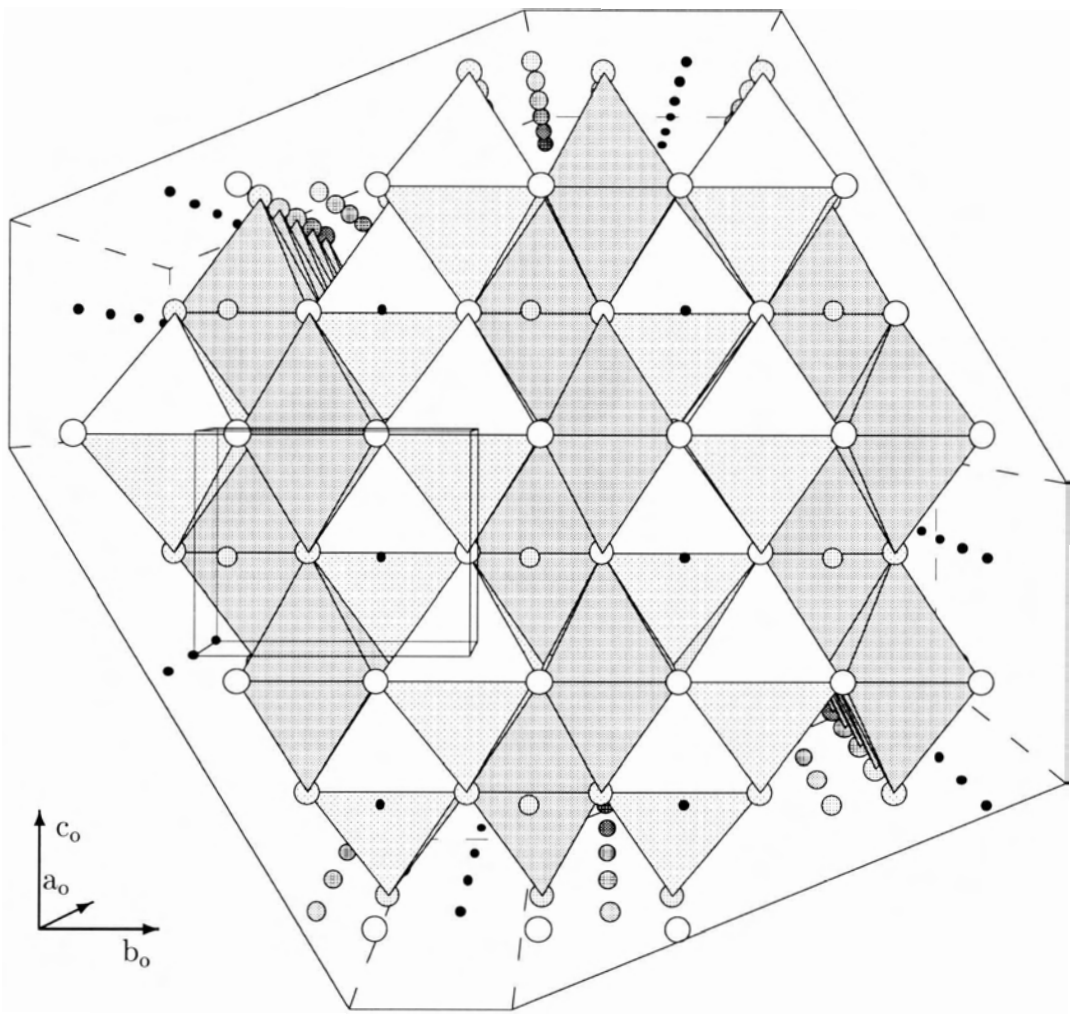

Figure 2.2: Crystal structure of $LiMnO_2$. The dark octahedra enclose manganese ions the white octahedra coordinate lithium ions. Linear chains of Li^+ and Mn^{3+} ions along the a-axis (into the paper) are visible at the edges of the crystal. Along $< 010 >$ (b-direction) are alternating layers of lithium and manganese.

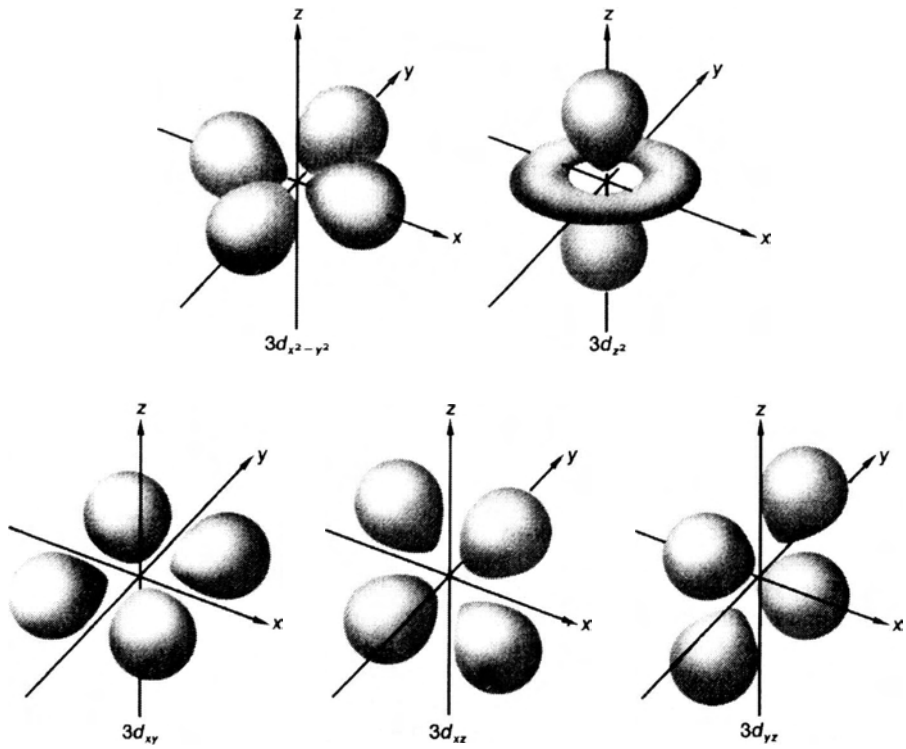

Figure 2.3: Contour plots of 3d orbitals in transition metals. The $d_{x^2-y^2}$ and d_{z^2}-orbitals have their lobes centered along the axis of the approaching ligands.

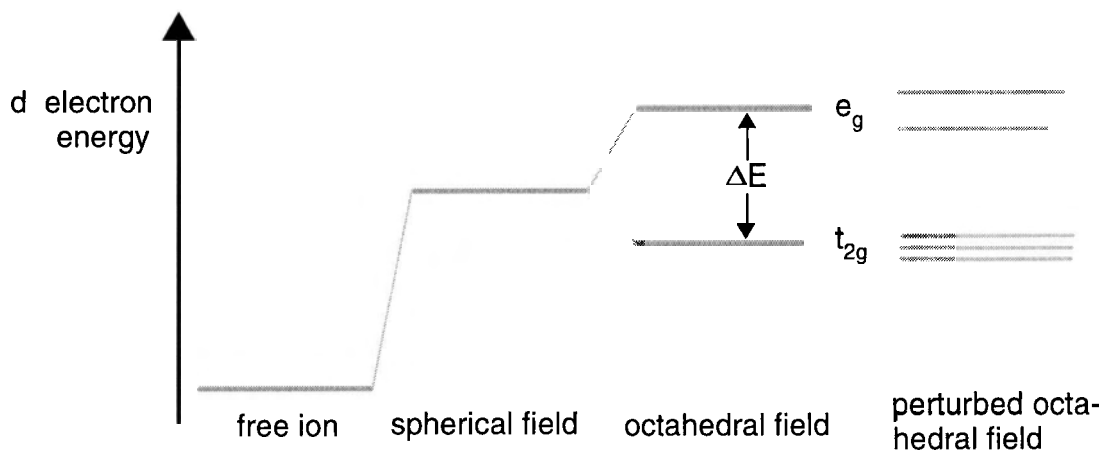

Figure 2.4: The effects on the energies of 3d electrons in a spherical, octahedral and perturbed octahedral field.

field is perturbed all of the degeneracy can be removed as indicated by the level splitting of the t_{2g} and e_g orbitals. Pertubations of the octahedral field symmetry are frequently found in crystal compounds in the form of lattice defects, vacancies and lattice strain.

The fact that $LiMnO_2$ is stretched along the $< 001 >$ directions, which corresponds to the z-axis in Figure 2.3, suggests that there is a preference for the occupation of the d_{z^2} orbital. This in turn must be a consequence of the (perturbed) symmetry properties of the actual charge distribution in which the Mn^{3+} ion is immersed in the crystal.

We remark that the symmetry breaking effect via the occupation of a single e_g orbital can only be understood in the conceptual framework of quantum mechanics. The theoretical basis for the removal of degeneracies in nonlinear molecular systems[5] is given by the *Jahn-Teller theorem*. This symmetry breaking effect is therefore often referred to as a *Jahn-Teller distortion*, which we will abbreviate by 'JTD' for subsequent reference. Jahn-Teller distortions lead to many interesting effects and properties in transition metal compounds.

$LiMnO_2$ as a Battery Compound

Using $LiMnO_2$ as a battery compound for lithium-ion batteries was considered more seriously a few years ago, after Ohzuku *et al.* [3] discovered a low temperature phase of $LiMnO_2$ synthesized at temperatures around 350°C, considerably lower compared to those reported by Hoppe *et al.* and Johnston and Heikes [10, 8]. Ohzuku demonstrated that most of the lithium could be extracted at high rates on the first charge and observed a reversible intercalation process for Li on subsequent charge-discharge cycles. From now on we will refer to the low temperature phase as as *LT-$LiMnO_2$* and the high temperature phase as *HT-$LiMnO_2$*. In section 3 we will report more about the electrochemical properties and synthesis of our LT-$LiMnO_2$ samples.

2.2 Cubic $LiMn_2O_4$

$LiMn_2O_4$ has the highest crystal symmetry of the structures discussed in this chapter. It has a cubic unit cell with a cell parameter of $a_c = 8.249$ Å[17] and has [Fd3m] space

[5] with nonspherical symmetry.

$Li_{(1-x)}Mn_2O_4$ Space group Fd3m ; a=8.249_1 [Å]						
Atom	Position	x	y	z	n†	x§
Li	8a	0.125	0.125	0.125	1-x	0-1
Li	16c	0	0	0	0	–
Mn	16d	0.5	0.5	0.5	1	–
O	32e	0.262	0.262	0.262	1	–
†) denotes fractional occupation and indicates possible solid solution range for the site. §) solid solution range.						

Table 2.2: Structural parameters of $LiMn_2O_4$

group symmetry. The crystal parameters, listed in Table 2.2 are compiled from the *International Tables of Crystallography* [18] and Wyckoff [19]. $LiMn_2O_4$ belongs to a crystal class commonly referred to as *spinel*. Many ternary compounds such as $MgAl_2O_4$, γ-Al_2O_3, Zn_2SnO_4 belong to the same crystal class including also many lithium compounds like $LiTi_2O_4$, LiV_2O_4, and $LiMn_2O_4$. In the latter a single unit cell consists of 56 atoms, so it is necessary to describe this rather complex structure in more detail.

Like in $LiMnO_2$, oxygen is also cubic close packed[6] in $LiMn_2O_4$ and occupies a face centered cubic[7] sublattice of unit cell parameter $\frac{a_c}{2}$. The oxygen framework provides two different kinds of octahedral sites, 16c and 16d and a set of tetrahedral sites on 8a. Here we used the Wyckoff site notation [19] for the space group [Fd3m] and we will do so in the following without further reference. Within the *regular* $LiMn_2O_4$-structure, manganese is octahedrally coordinated on 16d-sites and lithium tetrahedrally coordinated on 8a-sites. Based on approximate energy calculations by Miller [20] and by Goodenough *et al.* [21], there is a strong octahedral site preference for Mn^{3+} and Mn^{4+} over Li^+. Since a sphere inscribed in octahedral sites has a larger radius than the corresponding tetrahedral sphere radius, this agrees with the reported ionic radii which are tabulated in Table 2.3, and were taken from Shannon and Prewitt[8] [22, 23] and from Muller and Roy [24]. A single unit cell displaying

[6]often abbreviated as 'CCP'.

[7]abbreviated as 'FCC' subsequently.

[8]after Shannon and Prewitt [22, 23] ; there, the ionic radii are listed in terms of the coordination

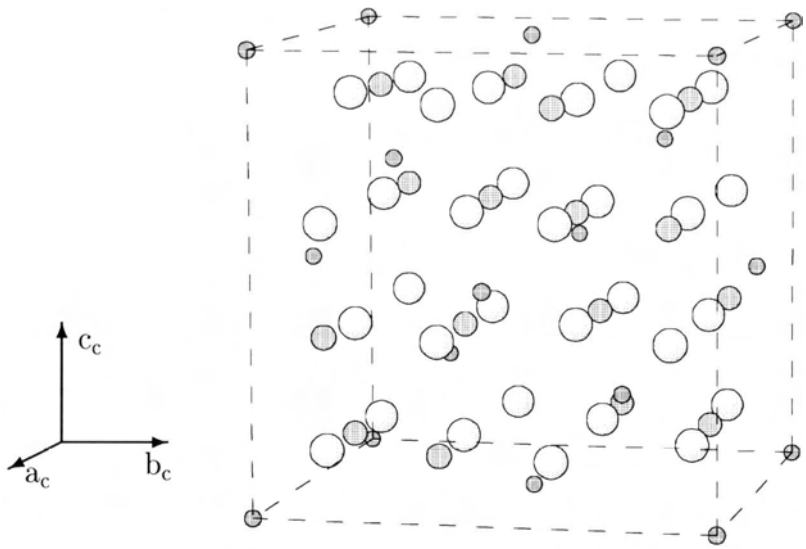

Figure 2.5: Unit cell of $LiMn_2O_4$. This structure corresponds to the 'true spinel' category. Lithium (small grey) on 8a sites, manganese on 16d (medium grey) and oxygen (large white) on a FCC sublattice.

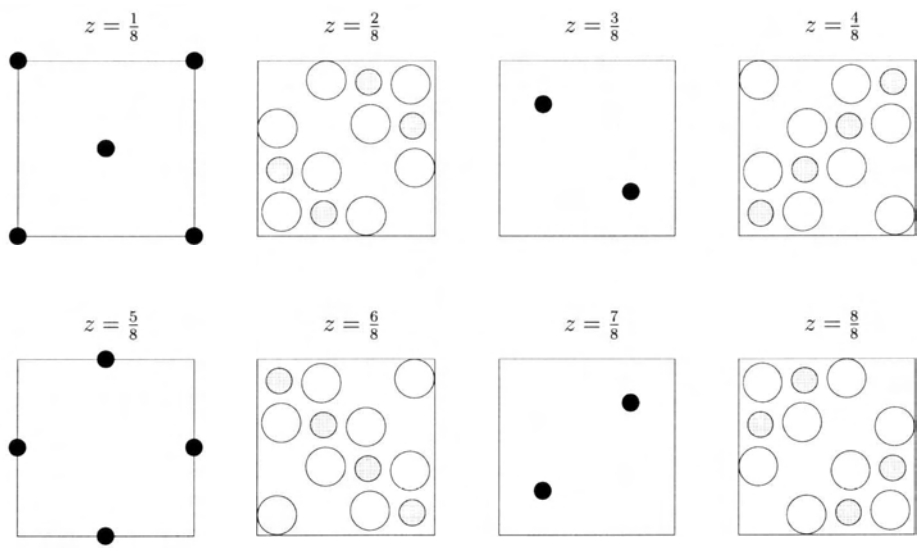

Figure 2.6: Successive layers of the spinel unit cell normal to (001) (c-axis). Lithium (small black spheres) occupies tetrahedral 8a-sites and manganese (medium black) octahedral 16d-sites. The cation layers are separated by 1/8 of the unit cell length.

the atoms is shown in Figure 2.5. In Figure 2.6 this unit cell has been sliced parallel to the c-axis in eight layers of equal thickness, beginning from bottom to the top of the unit cell. Obviously manganese and lithium cations are found in separate layers. Another view of the same unit cell is given in Figure 2.7 where only those octahedral and tetrahedral sites which fully fit in a single unit cell are plotted. Taking this

Ionic Radii after Shannon and Prewitt [22, 23] in [Å]					
coordination	Li^{+}	$Mn^{2+}HS^{\dagger}$	$Mn^{3+}HS^{\dagger}$	Mn^{4+}	O^{2-}
tetrahedral	0.73				1.24
octahedral	0.88	0.97	0.785	0.68	1.26
II					1.21
†) denotes High spin state .					

Table 2.3: Ionic radii of lithium and manganese in $LiMn_2O_4$.

representation one step further and replacing tetrahedra with the corresponding Li^{+} as little black circles one obtains again a very instructive view of the crystal structure as shown in Figure 2.8. Goodenough [21] states:

> The set of empty 16c octahedral sites form an interconnected three dimensional array of edge-shared sites identical to the 16d array, but shifted by $(\frac{a_c}{2}, \frac{a_c}{2}, \frac{a_c}{2})$. Each 16c site shares six edges (joining opposite faces) with other 16c sites forming intersecting $< 110 >$ chains; it also shares common faces with two 8a tetrahedral sites on opposite faces along a $< 111 >$ axis.

In order to illustrate this, Figure 2.9 shows the same crystal in an inverted fashion. Only octahedra corresponding to all 16c sites are plotted and manganese octahedra are replaced by the corresponding Mn^{3+}/Mn^{4+}ions on 16d-sites. This representation does in fact suggest that lithium ions can possibly diffuse along a system of 3D interconnected channels[9], provided the ions are mobile at ambient temperatures. We feel that it is very useful to have a number of different representations of one and the same

number.

[9]often referred to as *1x1 Tunnels*.

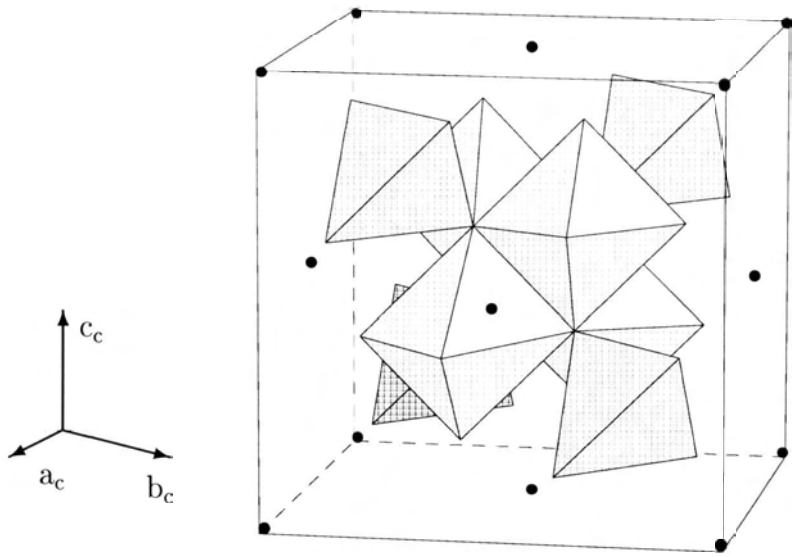

Figure 2.7: Unit cell of $LiMn_2O_4$ displaying manganese, sixfold coordinated by oxygen shown as brighter octahedral sites and lithium, fourfold coordinated by oxygen displayed as darker tetrahedra. The set of octahedra is not complete, only polyhedra which have all their atoms in the unit cell are shown.

crystal structure available, in order to visualize the complicated structural processes, which we will explore in the subsequent chapters.

So far only the *normal spinel* structure has been addressed. There are a number of other crystal structures very closely related to the spinel structure, of which two deserve mentioning here. The first is referred to as the *inverse* spinel structure. This is best explained by introducing the formal notation for ternary (ionic) compounds. Let A and B denote the cations and let X be used in place of the anions in the structure. Superscripts in roman letters symbolize the coordination. The $A_1B_2X_4$ spinels are classified as normal if the atomic distribution is of the $A_1^{IV}[B_2^{VI}]O_4$ type and as inverse if the distribution is of the $B^{IV}[A^{VI}B^{VI}]X_4$ type [24]. In the latter, cations need no longer be constrained to one particular site. In general however, each cation has preference for one of the cation sites, so that completely random distributions among the sites are quite rare.

The second structure is known as *atacamite*, and is best visualized by consulting Figure 2.10 (a): we only need to remove all the Li^+ ions (black). What remains are the sites occupied by the transition metal (Ti in this case) which are sixfold coordinated

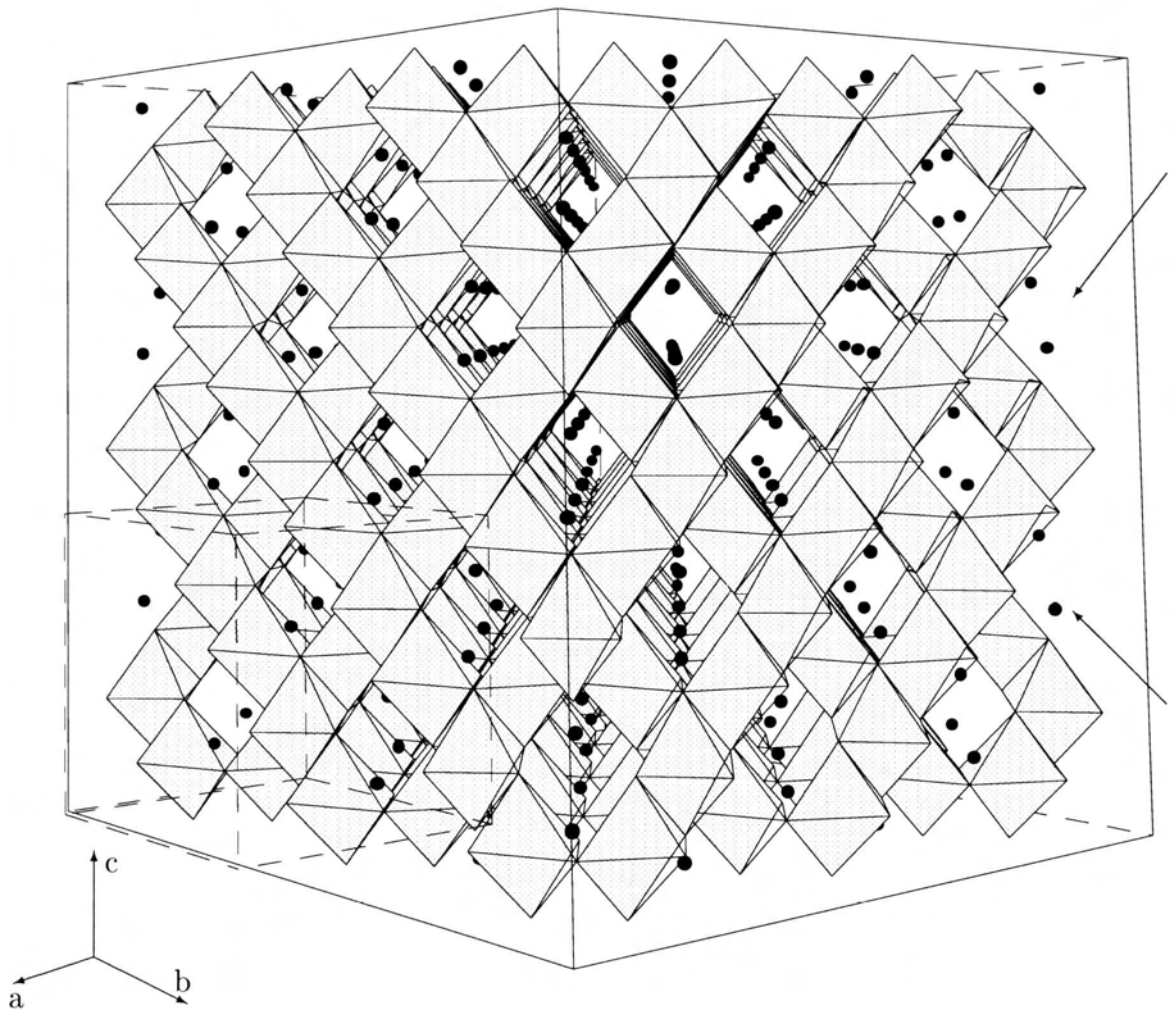

Figure 2.8: Crystal Structure of spinel, represented by oxygen octahedra. Each octahedron has oxygen at the corners and coordinates (sixfold) manganese in its center. The arrows point into the direction of the 3-dimensional system of empty 16c sites, which are also sixfold coordinated by oxygen. Lithium is shown as small black atoms, located on tetrahedral (8a) sites. For comparison a single unit cell is indicated by dashed lines in the lower left corner.

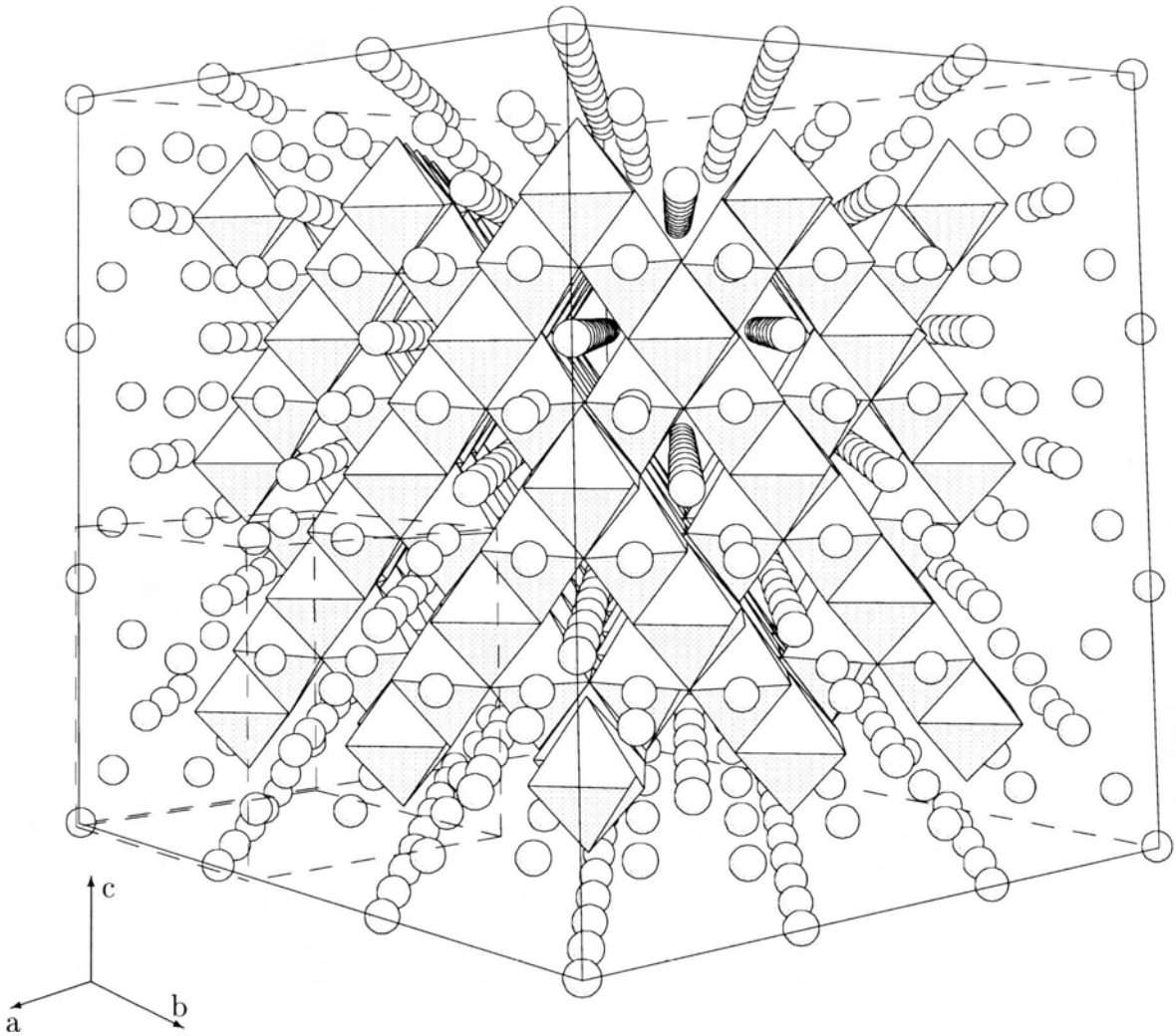

Figure 2.9: Three dimensional interconnected array of octahedrally coordinated 16c sites in $LiMn_2O_4$. The plot was obtained by replacing manganese octahedra by their corresponding Mn-ions on 16d sites (larger grey circles) and plotting octahedra for the (empty) 16c sites. For comparison a single unit cell is indicated by dashed lines in the lower left corner. The structure is often referred to as 3D 1x1 tunnel array.

by oxygen. These are the same oxygen [MO_6]-octahedra[10] which we referred to in the above discussion.[11] Conversely, by removing the Li^+ ions (type A cations) from 8a-sites in $LiMn_2O_4$ (black circles Figure 2.8) we obtain also the atacamite structure. In that sense we will refer to the term *atacamite* as the underlying framework of edge-sharing [MO_6]-octahedra and to the term *spinel* as the same structure where additional ions are distributed in an ordered or disordered fashion over the available octahedral and tetrahedral sites. The formation of a pure manganese oxide with the atacamite structure is known as λ-MnO_2, which is a particular modification of a variety of manganese dioxides (γ-MnO_2, Ramsdellite, α-MnO_2, β-MnO_2 ...).

Figure 2.10 (a) itself depicts a plot of the $Li_2Ti_2O_4$ structure which is most similar to NaCl. If all cations (Li^+ and Ti^{3+}) are replaced by Na^+ and all the O^{2-} are replaced by Cl^- we obtain the classic rocksalt structure of NaCl.[12]

2.3 Tetragonal $Li_2Mn_2O_4$

As will become apparent in this thesis, a corresponding structure with Mn in place of Ti in $Li_2Ti_2O_4$ has not been identified so far. This is a consequence of the Jahn-Teller distortion mentioned earlier in 2.1. By experiment [17, 25, 26], it was found that the cubic symmetry of the lithiated spinel phase is maintained until the average manganese oxidation state reaches values larger than 3.5 [13], at which a critical concentration of $Mn^{3+}(d^4)$ is reached, high enough to induce a *cooperative* Jahn-Teller distortion from cubic to tetragonal symmetry throughout the *entire* crystal. The phenomenon is called 'cooperative' because the distortion of the symmetry at one Mn^{3+} (d^4) site will inevitably influence neighboring sites in the array of edge-sharing [MO_6]-octahedra [27]. The value for the increase in the c/a-ratio ranges between 1.16 (Thackeray [28]) and 1.12 (Ohzuku [17]). Thus, $Li_2Mn_2O_4$ has a tetragonal unit cell and its space group symmetry is identified as [$I4_1/amd$] [28, 21]. The structural parameters for $Li_2Mn_2O_4$, as reported by Thackeray, are shown in Table 2.4. It is convenient to keep the site notation of the [Fd3m]-symmetry also for the [$I4_1/amd$]-

[10] M in [MO_6]-octahedra stands for transition metal ion.

[11] How these [MO_6]-octahedra are linked together in the atacamite *framework structure* is later shown Figure 2.13 (c).

[12] besides the fact that O^{2-}slightly deviates from the loci of the corresponding Cl^--ions.

[13] which corresponds to the *exact* stoichiometry of $Li_1Mn_2O_4$.

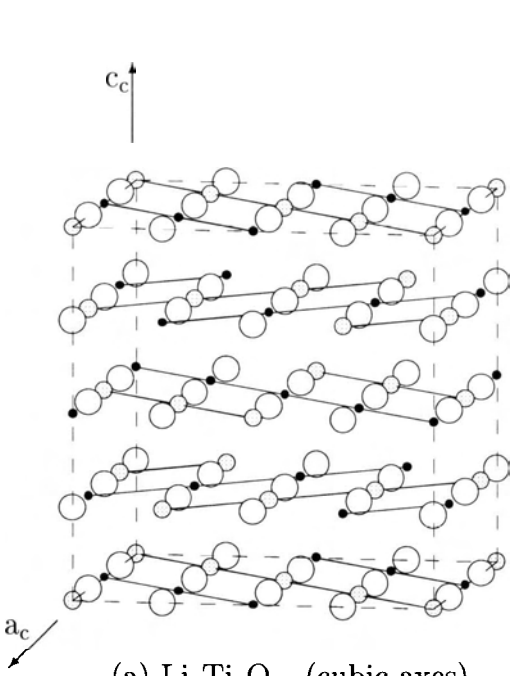

(a) $Li_2Ti_2O_4$ (cubic axes)

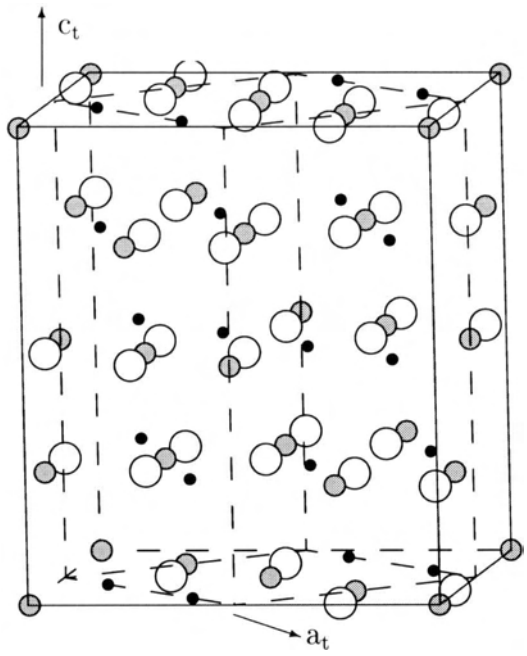

(b) $Li_2Mn_2O_4$ (tetragonal axes)

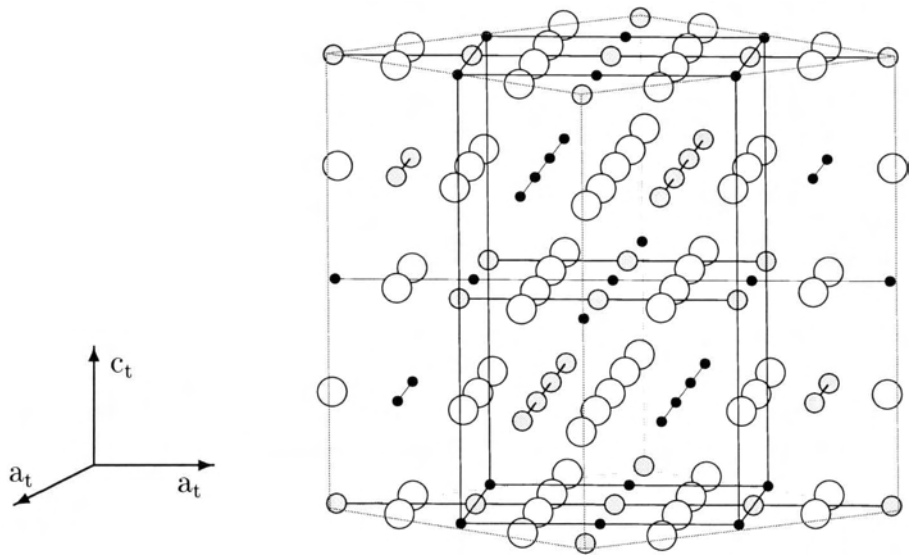

(c) $Li_2Mn_2O_4$ (rotated by 45 deg.)

Figure 2.10: In (a) the unit cell of $Li_2Ti_2O_4$ is shown where Li (black) occupies all 16c sites. A conversion from the cubic framework to the tetragonal distorted $Li_2Mn_2O_4$ structure is indicated in (b). The structure expands along the common c-axis. In (c) we rotated the structure by 45 deg. and indicated the shortest bonds for Li^+ and Mn^{4+}.

symmetry, since the two structures are closely related to each other (see 2.4.2). We note that (h,k,l) in [$I4_1$/amd] is equivalent to $(h+k, h-k, l)$ in [Fd3m].

$Li_2Mn_2O_4$ Space group [$I4_1$/amd] ; a=9.274_4 c=5.662_2 [Å]					
Atom	Position†	x	y	z	n§
Li‡	8a	0	0.75	0.125	1
Li	16c	0	0	0	0.5‡, 1
Mn	16d	0	0	0.5	1
O	32e	0	0.487(5)	0.252(3)	1

†) for easier comparison the site positions of the space group Fd3m are used; (h,k,l) in [$I4_1$/amd] is equivalent to $(h+k, h-k, l)$ in [Fd3m] .
§) denotes fractional occupation of the site.
‡) if lithium can be found on the 8a site.

Table 2.4: Structural parameters of $Li_2Mn_2O_4$

According to least squares refinements of powder diffraction data for $Li_2Mn_2O_4$, Thackeray *et al.* report that Li^+occupies *all* 8a (tetrahedral) sites and half of the 16c (octahedral) sites in the tetragonally distorted spinel structure. It is inherently difficult to refine for the Li^+ occupation in powder diffraction data, since the scattering cross section of Li^+ compared to Mn^{3+} is very small. In Figure 2.11 (d) we plotted the cation arrangement for this assumption. The distance between Li^+ ions on 16c sites (black) is 2.85Å, whereas the shortest distance between Li^+ on 8a and 16c sites amounts to 1.85Å. Although Mn^{3+} ions have a strong octahedral *site preference* [20] compared to Li^+, it is not clear to us why lithium ions move into sites where the repulsive Li-Li nearest neighbor interaction due to smaller bond lengths (1Å !) is strongly increased. We adopt therefore the picture that all Li^+ ions are found on 16c sites.

Therefore, we find that $Li_2Mn_2O_4$ is not a fundamentally new structure, it is the same as $Li_2Ti_2O_4$ except that the symmetry is reduced from cubic to tetragonal and that Li^+ might also be found on 8a sites. In order to illustrate the connection between the structures, we plotted the unit cells of $Li_2Ti_2O_4$ and $Li_2Mn_2O_4$ in Figure 2.10 (a) and (b) respectively, including the corresponding structure axes. In Figure 2.10 (c) the tetragonal axes are rotated by 45°C and the unit cell is inscribed into a complete spinel unit cell where all Li^+ is found on 16c sites. We indicated the smallest bond

lengths for Mn^{3+} and Li^+ ions and notice in contrast to the orthorhombic arrangement, that alternating layers of linear chains of Li^+ ions are rotated by 90°C .

As indicated at the beginning of this section $Li_2Mn_2O_4$ can be obtained by electrochemical insertion of Li^+into the host structures $LiMn_2O_4$ or λ-MnO_2 [29]. However, in place of electrochemical insertion, $Li_2Mn_2O_4$ can also be synthesized in this stoichiometry by chemical solid state reactions, or by other means of chemical synthesis as summarized in [26]. Some authors refer to $Li_2Mn_2O_4$ by the notation '$Li_{(1+x)}Mn_2O_4$ $(1 \leq x \leq 2)$' which is somewhat misleading since it suggests that a cubic spinel phase exists in which the lithium concentration can be any value in the range $(1 \leq x \leq 2)$. This, however, is not the case. $LiMn_2O_4$ is seen to convert to the tetragonal distorted phase upon *overlithiation.*[14] Therefore the above notation $Li_{(1+x)}Mn_2O_4$ is truly meaningful only for denoting the average lithium concentration in a two phase system. Converseley, upon *delithiation* of $LiMn_2O_4$ it *is* justified to refer to this system by $Li_{(1-x)}Mn_2O_4$ $(0 \leq x \leq 1)$, since intermediate stochiometries are found in the same cubic phase.

2.4 Comparison of the Structures

2.4.1 Crystal Structure

In Wells' *Structural Inorganic Chemistry*, [30] structures like $MgAl_2O_4$ are referred to as *complex ionic crystals*, in the sense that all pairs of neighboring atoms are essentially ionic in character. This viewpoint is commonly adopted in the electrochemical literature whenever lithium manganese oxides are described. So the idea is to regard the stuctures which were reviewed in this chapter as three dimensional assemblies of ions. As it turns out, this is a very successful approach for comparing these structures and as we have seen it is possible to regard all of the structures being derived from the classic rocksalt structure of sodium chloride[15] where anions and cations occupy FCC sublattices shifted by $(\frac{a_c}{2}, \frac{a_c}{2}, \frac{a_c}{2})$ with respect to each other. As demonstrated, all the reviewed Li-structures have a FCC oxygen lattice in common. What *distinguishes* these structures is the arrangement of the cations among the interstitial octahedral

[14] meaning that x in this notation can only be sightly larger than 1 or exactly 2.

[15] LiCl to be more precise. In NaCl the Cl^--ions are not really cubic close packed, whereas in LiCl they are due to the smaller ionic radius of lithium.

and tetrahedral sites, available in the oxygen sublattice. Due to particular cation distributions, the lattice might also be stretched in one direction (distortion) as we saw. This idea is presented in Figure 2.11 where the cation arrangements of the four important structures in this study are displayed.

Wu Li used these ideas recently [14] to calculate the order-disorder transition for solid solutions of $Li_xNi_{(2-x)}O_2$ as well as to predict the structures of $LiNiO_2$, $LiCoO_2$, γ-$LiFeO_2$ and $Li_2Ti_2O_4$ using a *lattice gas* model including nearest and next nearest neighbor interactions. This model is based on the assumption that differences in the oxygen sublattice are negligible[16].

It is important to keep in mind that in all electrochemical reactions done in this study, only Li^+ ions are displaced over larger distances (ideally). The oxygen lattice can be regarded as static except that bonding angles and distances in the oxygen array change dynamically as the overall cation distribution changes (sometimes irreversibly). By means of in-situ XRD we try to trace the phase changes in the cathode as a function of Li^+- concentration, which in turn is related to the electrochemical insertion potential of Li^+ in the host structure. Solid state reaction of this kind in inorganic compounds are often referred to as *topotactic* reactions, as defined in the following section.

2.4.2 Topotactic Phase Changes

In the discussion of the crystal structure of $Li_2Mn_2O_4$ in section 2.3 we already encountered a *topotactic* phase change. According to H. Manohar [31] a topotactic solid state reactions is defined as fol lows:

> A single crystal of starting material is converted into a single crystal of the product, the reaction taking place throughout the volume of the crystal, and there exists a definite three dimensional orientation relationship between the respective lattices.

If we ignore the fact that the transition metal cations in Figure 2.10 (Ti^{3+} and Mn^{3+}) are different, then for example does the mapping of the *structure* of $Li_2Ti_2O_4$ onto the *structure* of $Li_2Mn_2O_4$ as shown in Figure 2.10 (a) and (b), corresponds exactly

[16] The $[MO_6]$-octahedra may be distorted and also they may differ with their respective joining angles. Nevertheless these differences are regarded as small deviations from the 'ideal' FCC anion array.

to such a process. In the cubic and tetragonal unit cells the c-axes are parallel to each other, whereas the a axis of the tetragonal unit cell is rotated by an angle of 45 deg. with respect to the c-axis. Ohzuku *et al.* measured the lattice parameters for the transition from cubic [Fd3m] to tetragonal [$I4_1/amd$] symmetry [17], reporting their results by mapping the cubic parameter a_c to tetragonal lattice parameters a_t and c_t using the relations $a_t = a_c\sqrt{2}$ and $c_t = a_c$.

In the following we want to ask if a similar relationship can be established for the transition from the [Pmnm]-symmetry to [Fd3m]-symmetry, as it is observed for $LiMnO_2$ on the initial charge (delithiation). For this case, Gummow *et al.* suggested [5] the cooperative migration of every second Mn^{4+} ion in $LiMnO_2$ to a neighboring octahedral site in the oxygen lattice as shown in Figure 2.12. The top row displays two successive double layers of the orthorhombic lattice, (a) and (b), sliced parallel to the (100) plane. The two layers are isomorphic and have a thickness of $2a_o$ (5.61Å). In the lower panel two successive layers of the cubic spinel structure, parallel to (110) and of the same thickness are shown in (c) and (d). It is proposed that $< 012 >$ in [Pmnm]-symmetry and $< \bar{1}11 >$ in [Fd3m]-symmetry are parallel to each other. Consulting Figure 2.11 (a), where the orthorhombic unit cell is drawn with respect to the cubic axis, might clarify the situation. If the proposed assumption can be verified by experiment, then we have a complete set of relations for the orientation and length of the orthorhombic, cubic and tetragonal structure axes at hand. For the topotactic phase change from orthorhombic to cubic

$$a_c = 2\sqrt{2}a_o \; ; a_c = \sqrt{2}b_o \; ; c_c = 2c_o \quad (c_c \parallel c_o) \; , \tag{2.3}$$

for the phase change from cubic to tetragonal we have (as stated earlier)

$$a_t = \frac{a_c}{\sqrt{2}} \quad ; c_t = c_c \quad (c_t \parallel c_c) \; , \tag{2.4}$$

and the relation between the orthorhombic and tetragonal unit cell can be stated as

$$a_t = \sqrt{2}b_o \quad ; c_t = 2c_o \quad (c_t \parallel c_o) \; . \tag{2.5}$$

For all three relations we explicitly note that the c-axes are all parallel. Further, the orthorhombic b-axis and the corresponding tetragonal axis can be chosen parallel and finally we note that the tetragonal a-axis is rotated with respect to the cubic a-axis by 45 degrees. One might ask why it is meaningful to map orthorhombic parameters to cubic parameters, in particular when the numerical values, found in the tables of

this chapter, do not satisfy the above relationships. We will see that Equations 2.3 and 2.4 and Equation 2.5 bear significance for the interpretation of the many cycle behavior of the converted spinel phase.

2.4.3 Investigation of Lattice Mismatch at Phase Boundaries

Since we study in this thesis the removal of lithium from one phase which is known to convert to a different phase, the crystallographic conditions found at an interface are of fundamental importance. Moreover, phase transitions continue to occur in the repeated electrochemical charge-discharge experiments and it is therefore essential to discuss lattice mismatch at phase boundaries between all relevant phases. In the following, we investigate these phase boundaries in terms of the lattice parameters of the three main phases introduced in this chapter. We will also compare the volumes of unit cells and multiples of unit cells which contain the same number of oxygen ions.

In Tables 2.5, 2.6, 2.7 and 2.8, below we consider the conversion from one phase (A) to a second phase (B). We state the reported lattice constants and volume in the top line and calculate the corresponding parameters of B out of the measured parameters found in phase A using the relations in Equation 2.3 to Equation 2.5. The lattice mismatch is characterized by the RMS-deviation from the reported values found by measurement of single phase powders. For the conversion from $LiMnO_2$

$LiMnO_2$ to $Li_1Mn_2O_4$	a_c=8.24 Å; $V = 559.5$ Å^3		
topotactic relation	value	difference Δ [Å]	error [%]
$a_c = 2\sqrt{2}a_o$	7.93	−0.31	−3.75
$a_c = \sqrt{2}b_o$	8.14	−0.1	−1.18
$a_c = 2c_o$	9.14	+0.90	+10.92
$V = 8a_ob_oc_o$	591.1	+31.6	+5.64
The total cell volume contracts.			
RMS-deviation: $\sqrt{\sum \Delta^2} = 0.96$ Å.			

Table 2.5: Mismatch of lattice parameters, $LiMnO_2$ to $Li_1Mn_2O_4$.

to $Li_1Mn_2O_4$ which seems to be the most important mechanism on initial discharge, we find that the orthorhombic equivalent of $[MO_6]$-octahedra in $Li_1Mn_2O_4$ occupies significantly less space.

$LiMn_2O_4$ to λ-MnO_2 $a_{\lambda c}$=8.03 Å; $V = 517.8$ Å^3			
topotactic relation	value	difference Δ [Å]	error [%]
$a_{\lambda c} = \frac{8.03}{8.24} a_c$	8.03	−0.21	−2.55
$V = a_c^3$	559.5	+41.7	+7.45
The total cell volume contracts.			
RMS-deviation: $\sqrt{\sum \Delta^2} = 0.36$ Å.			

Table 2.6: Lattice contraction, $Li_1Mn_2O_4$ to λ-MnO_2.

Although the removal of Li^+ from $Li_1Mn_2O_4$ does not induce a phase transition where the symmetry changes, the resulting phase λ-MnO_2 is characterized by a considerable and uniform contraction of the cubic lattice. Mosbah [32] *et al.* report a lattice parameter of 8.029 Å. We included therefore Table 2.6 and want to point out that a volume reduction of 7.5% must have considerable impact on the crystal morphology at a phase boundary. In this table the difference Δ corresponds to the reported contraction of the cubic unit cell.

If we compare the three different tables for the volume mismatch, we find that the orthorhombic phase has almost the same cell volume as the tetragonal phase. Moreover, like in the orthorhombic phase, the tetragonal phase is also distorted along the common c-direction.

$LiMnO_2$ to $Li_2Mn_2O_4$ a_t=5.662 c_t=9.274 Å; $V = 297.3$ Å^3			
topotactic relation	value	difference Δ [Å]	error [%]
$a_t = 2a_o$	5.61	−0.05	−0.95
$a_t = b_o$	5.76	+0.10	+1.70
$c_t = 2c_o$	9.14	−0.13	−1.40
$V = 4a_o b_o c_o$	295.5	−1.78	−0.60
The total cell volume expands.			
RMS-Deviation: $\sqrt{\sum \Delta^2} \leq 0.17$ Å.			

Table 2.7: Mismatch of lattice parameters, $LiMnO_2$ to $Li_2Mn_2O_4$.

Between the orthorhombic and the cubic phase we find the strongest *overall* mis-

match. Not only the lattice parameters show a large RMS-deviation, also the cation arrangements of the two lattices are fundamentally different as pointed out earlier in this chapter. We expect for this reason, lattice strain at the interface, in particular, if the lattices are coherent, along the common c-direction.

$Li_1Mn_2O_4$ to $Li_2Mn_2O_4$	a_t=5.662 c_t=9.274 Å; V = 297.3 Å^3		
topotactic relation	value	difference Δ [Å]	error [%]
$a_t = \frac{a_c}{\sqrt{2}}$	5.83	+0.17	+2.90
$c_t = c_c$	8.25	+1.02	+11.00
$V = \frac{1}{2}a_c^2 c_c$	279.8	+17.5	+5.90
The total cell volume expands.			
RMS-Deviation: $\sqrt{\sum \Delta^2} \leq 1.06$ Å.			

Table 2.8: Mismatch of lattice parameters, $Li_1Mn_2O_4$ to $Li_2Mn_2O_4$.

Between the cubic and tetragonal structures there is also a strong mismatch along the common c direction. The RMS deviation is the largest. Despite the Jahn-Teller distortion, the positions of the Mn^{3+} and Mn^{4+} ions in the cation sublattice are identical, and only the occupation by Li^+ ions distinguishes the phases.

2.4.4 Mixed Valence and Conductivities

Electronic Conduction

Under *mixed valence* we understand the fact that manganese ions do not appear in only one oxidation state in the spinel structure. In $Li_{(1-x)}Mn_2O_4$ we find formally a valence of 4 if $x = 1$ and 3.5 if $x = 0$, the latter being the normal spinel stoichiometry. For $x = 0$ half of the manganese ions must be Mn^{3+} and the other half Mn^{4+}. The concepts of how to think about an average oxidation state of 3.5 are not so clear in the literature. Maybe the ionic view has to be abandonned one day, if better understanding of these compounds is found. The issue of mixed valence cations in similar transition metal oxides compounds is found to be important for questions concerning the electronic conductivity. According to Goodenough [21] and Mizushima [33], $LiMn_2O_4$-structures are good electronic conductors. In particular they are known as *small-polaron conductors* where the mechanism for conduction is attributed to

(electronic) impurity states in the gap between the valence and conduction bands. Assuming a regular distribution of Mn^{3+} and Mn^{4+}, electrons in Mn^{3+} d_4 states can 'jump' to neighboring Mn^{4+} d_3 states.

Ionic Conduction

A similar 'hopping' behavior is found for Li^+ ions. Under the influence of an electric field Li^+ ions can hop from one empty interstitial site in the lattice to another. This idea finds confirmation in the AC-impedance measurments [34] where Li^+ diffusion in a solid ionic conductor is considered to be a rate determining process for the insertion/removal of Li^+ in these phases.

Kanoh *et al.* [34] studied the diffusion coefficients of Li^+ in a Pt/λ-MnO_2 electrode with an aqeuous electrolyte using AC-impedance analysis. It is found that the diffusion coefficient of Li^+ in $Li_{(1-x)}Mn_2O_4$ drops by an order of magnitude at a concentration of $x = 0.2$ as compared to $x = 0.5$. The diffusion is slightly enhanced at intermediate stoichiometries (0.5) as compared to $x = 1$. The ionic conductivity is inversely proportional to the diffusion coefficient. A simplifying argument for this observation is that Li^+ ions encounter higher potential barriers for the hopping from one site to another as the lattice contracts.

For the ionic conduction of manganese, we did not find any reference. We assume that Mn^{3+} ions can change their sites only under the influence of strong internal electrostatic fields. Such fields sometimes occur if the local charge balance is adversely altered upon removal of lithium. Manganese is also far too heavy and its strong positive charge will not allow for ionic diffusion of Mn^{3+} even remotely similar to the diffusion of Li^+.

The diffusion of O^{2-} ions in a $LiMn_2O_4$ lattice is indirectly confirmed. In a recent publication by Croguennec *et al.* [6], the authors claim the recording of an oxidation current in a $LiMnO_2$ cathode at a battery potential of 4.18 V after the initial cycle. If oxygen is released from the lattice, it is known that O^{2-} can diffuse in a similar manner through the solid state matrix as Li^+ can. The question is however what triggers the release of oxygen from the lattice.

2.4.5 Stability

$LiMnO_2$

Finally we want to consider the issue of crystal stability upon extraction of Li^+. This can be done by electrochemical deintercalation of Li^+ or can occur to some degree by a surface oxidation processes which is mentioned in 3.9 in chapter 3 ahead. As stated at the beginning of this chapter, it is necessary to maintain the electrostatic balance in the host compound, upon removal of the 'mobile' cations. It is now straight forward to compare the two principal structures $LiMnO_2$ and $LiMn_2O_4$ under this aspect. In Figure 2.13 we adapted again the oxygen octahedra representation for these structures. It is apparent that any attempt to remove *all* of the Li^+ in $LiMnO_2$ will introduce a strong negative spatial charge distribution between the zigzag layers of the remaining manganese octahedra. The change in valence for manganese from Mn^{3+} to Mn^{4+} has to compensate for the negative spatial charges between the manganese layers. However, being localized in layers, Mn^{4+} ions will also polarize the lattice along these layers. The resulting fields destabilize the entire crystal structure and support the 'migration' of Mn^{4+} ions (of smaller radius) to empty neighbor sites (left behind by extracted Li^+) in order to compensate for these strong fields.

The above picture is of course simplified. We have not considered the Jahn-Teller effect due to the presence of manganese as a typical Jahn-Teller ion. If locally all Li^+ ions which surround a Mn^{3+} ion are removed, then the origin of the distortion found in $LiMnO_2$ is eliminated and Mn^{3+} is oxidized to Mn^{4+}. In order to restore full octahedral symmetry in an Mn^{4+} d_3 state the lattice must contract along the c-direction and must expand in a and b direction.[17] As consequence, local stress will be induced in the crystal structure due to the change of valence at the manganese site. This constitutes a second destabilizing factor for the orthorhombic framework under extraction of lithium. If a domain[18] of orthorhombic structure is sufficiently void of Li^+ this domain must collapse, most likely under migration of Mn^{4+} ions to sites where the overall free energy of the crystal lattice is reduced. These are rather qualitative arguments which need, strictly speaking, quantitative justification. Any attempt to include a simulation of these conditons in form of a lattice gas calculation would go far beyond the scope of this thesis.

[17] This can be verified by examining the lattice parameters with their given topotactic relations.

[18] The more precise meaning of 'domain', crystal, crystallite and grain are discussed in chapter 4.

$\mathbf{Li_{(1-x)}Mn_2O_4}$ $0 \leq x \leq 1$

$LiMn_2O_4$ is regarded as the most stable structure in the family of $Li_xMn_{1-x}O_2$ compounds [21]. When Li^+ is deintercalated, there are no strong polarizing fields, pulling Mn^{3+}/Mn^{4+} ions in a particular direction, which can destabilize the crystal framework as a whole. As the average oxidation state reaches 4 in $Li_{(1-x)}Mn_2O_4$, and the ionic radius of Mn ions decreases, we do observe in fact a decrease of the cubic unit cell parameter. As we will discuss in chapter 7 later, there is a direct, almost linear relationship between x in $Li_{(1-x)}Mn_2O_4$ and the cubic lattice parameter a_c.

$\mathbf{Li_{(1+x)}Mn_2O_4/Li_2Mn_2O_4}$

Upon overlithiation of $Li_1Mn_2O_4$, a critical concentration is reached where an abrupt change from cubic to tetragonal symmetry takes place. The exact critical concentration has been reported by Goodenough *et al.* around $x = 0.1$ [21], but depends of course strongly on the *exact* stoichiometry of the spinel compound. In particular the oxygen or manganese deficiencies are the determining factors.

We mentioned the driving force for this mechanism as the Jahn-Teller effect. At the stoichiometry of $Li_1Mn_2O_4$ the average valency is 3.5. If more lithium is inserted into the phase, the repulsive forces along the c-axis at Mn^{3+} sites[19] must be stronger than the attractive forces at fewer Mn^{4+} sites. The entire crystallite undergoes a distortion to tetragonal symmetry. As mentioned in 2.1, this effect can only be understood by the knowledge of discrete energy levels in atomic systems.

Intermediate and Disordered Phases

The distortion of $Li_1Mn_2O_4$ to $Li_2Mn_2O_4$ depends strongly on the *symmetry* and *crystallinity* of the specimen. The cooperative distortion along the common c-direction is a *result* of the regular ocatahedral symmetry.[20] I believe that any impurities, vacancies or defects will weaken the bundled effect of repulsive forces along the same direction.

---

[19] where electrons occupy d_{z^2} orbitals.

[20] The symmetry of the crystal is of course cubic. By octahedral symmetry we mean the symmetry of the $[MO_6]$-octahedra. That symmetry must be perturbed in a way to favour the occupancy of the d_{z^2} orbitals in Mn^{3+}.

For example, if the lattice is strongly oxygen deficient, we have some experimental evidence that the repulsive forces due to an increased interaction of half of the Mn-ions (Mn^{3+}) along the c-axis are too weak to trigger the transiton. Richard *et al.* [35] studied the behaviour of $Li(Li_{1/3}Mn_{5/3})O_{4-\delta}$ for different oxygen deficiencies ($0 \leq \delta \leq 0.25$). $Li(Li_{1/3}Mn_{5/3})O_4$ itself is a structure close to an inverse spinel. Some of the Li^+ are found on 16c sites instead of 8a sites and possibly some of the Mn-ions occupy 8a sites. In that sense we can call the structure also disordered. Richard showed that oxygen vacancies can be obtained by ammonia reduction of the spinel electrode materials. The electrochemical cycling data suggests that it is increasingly difficult to intercalate Li^+ in a tetragonally distorted phase. The alternative interpretation is simply to state that a lattice with many oxygen vacancies cannot undergo a distortion from cubic to tetragonal symmetry. The bundled and directed effect of Mn^{3+} ions contributing strong repulsive interactions along the common c-axis in the crystal is disturbed by the symmetry breaking effect of many oxygen vacancies and the disorder on the cation lattice.

The latter interpretation assumes of course that the distortion affects larger domains in a crystallite all at once. This is in contrast to the picture of a moving phase boudary in a (single-) crystalline domain which separates the cubic and tetragonal phase.

I assume that a similar argument can be applied for the case where we have a strongly disordered phase and not necessarily many oxygen vacancies. The disorder is however restricted to the cation sublattice.

2.4.6 Crystal Structure and Chemical Potential

In order to establish a link to the following chapter, which reports the electrochemical experiments, I would like to add a few remarks about the influence of the crystal structure on the chemical potential.

In the following chapter we will define the chemical potential in a mathematical expression involving the *Gibbs free energy*. For a more intuitive understanding I think it is helpful to regard the the crystal structure primarily as an assembly of charged ions. For *any* given stoichiometry of a crystalline material there is a net balance of repulsive and attractive forces. The lattice parameters and the symmetry are the solutions to that balancing problem. Changing the stoichiometry in any way must

neccessarily affect either the lattice parameters or the symmetry[21] or both. Lithium intercalation systems are good examples of this. The addition of Li^+ to $Li_{(1-x)}Mn_2O_4$ is accompanied by the reduction of a Mn^{4+} ion to Mn^{3+}. Reduction of any transition metal oxide (=TMO) involves an expansion of the ionic radii. Moreover, the inclusion of Li^+ requires space. We expected therefore an expansion in lattice volume.

If the lattice suddenly expands (in volume), as in the cubic/tetragonal distortion case, some of the internal energy in the system is released to do work against the electrostatic attraction. The work which is required to insert or remove an ion must now be lower, since the charges are on average more separated in space than before.

Different insertion potentials ('plateaus') for Li^+ in the same compound reflect on a finer scale the different available interstitial sites and their respective interactions with nearest and next nearest neighbours (for example the two phases of spinel at 4.0 V). To first order it reflects however the lattice parameters and the physical space which is available for an ion at given intercalation site (for 3 V, 4 V and 5 V plateau in spinel compounds).

[21] Symmetry of the underlying lattice. Changes of the stoichiometry alter of course the local symmetry at many sites in the lattice.

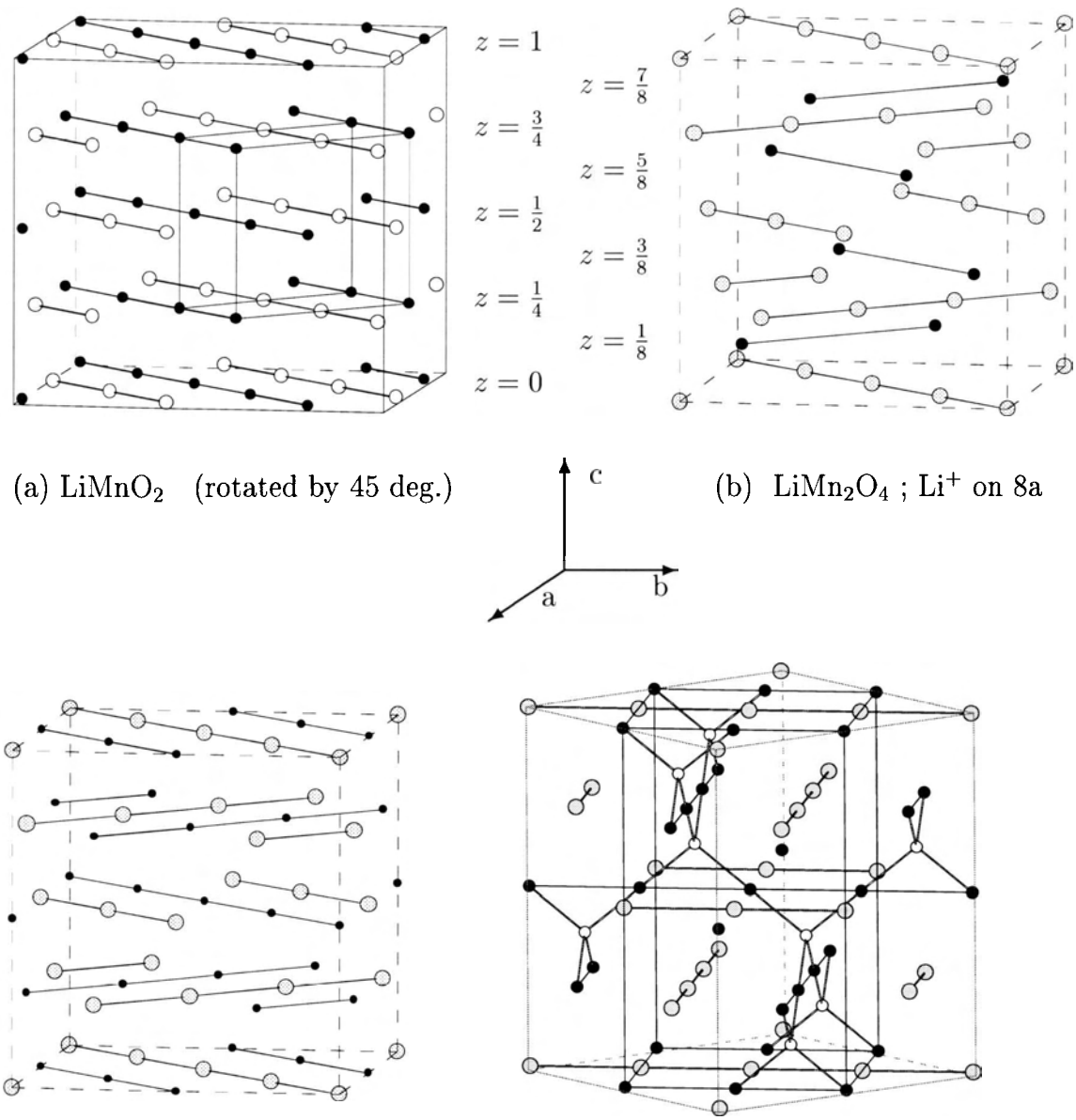

(a) $LiMnO_2$ (rotated by 45 deg.)

(b) $LiMn_2O_4$; Li^+ on 8a

(c) $Li_2Ti_2O_4$; Li^+ on 16c

(d) $Li_2Mn_2O_4$; Li^+ on 8a and 16c

Figure 2.11: Cation arrangements of various lithium transition metal oxides. (a) $LiMnO_2$ unit cell; (b) regular $LiMn_2O_4$-spinel with Li^+ on 8a; (c) $Li_2Ti_2O_4$ with all Li^+ on 16c. This structure has the same cation arrangement as $Li_2Mn_2O_4$, despite the fact that the unit cell is distorted along the common c-axis. In (d) we show an alternative arrangement for $Li_2Mn_2O_4$ with Li^+ ions placed on 8a *and* 16c (n=0.51).

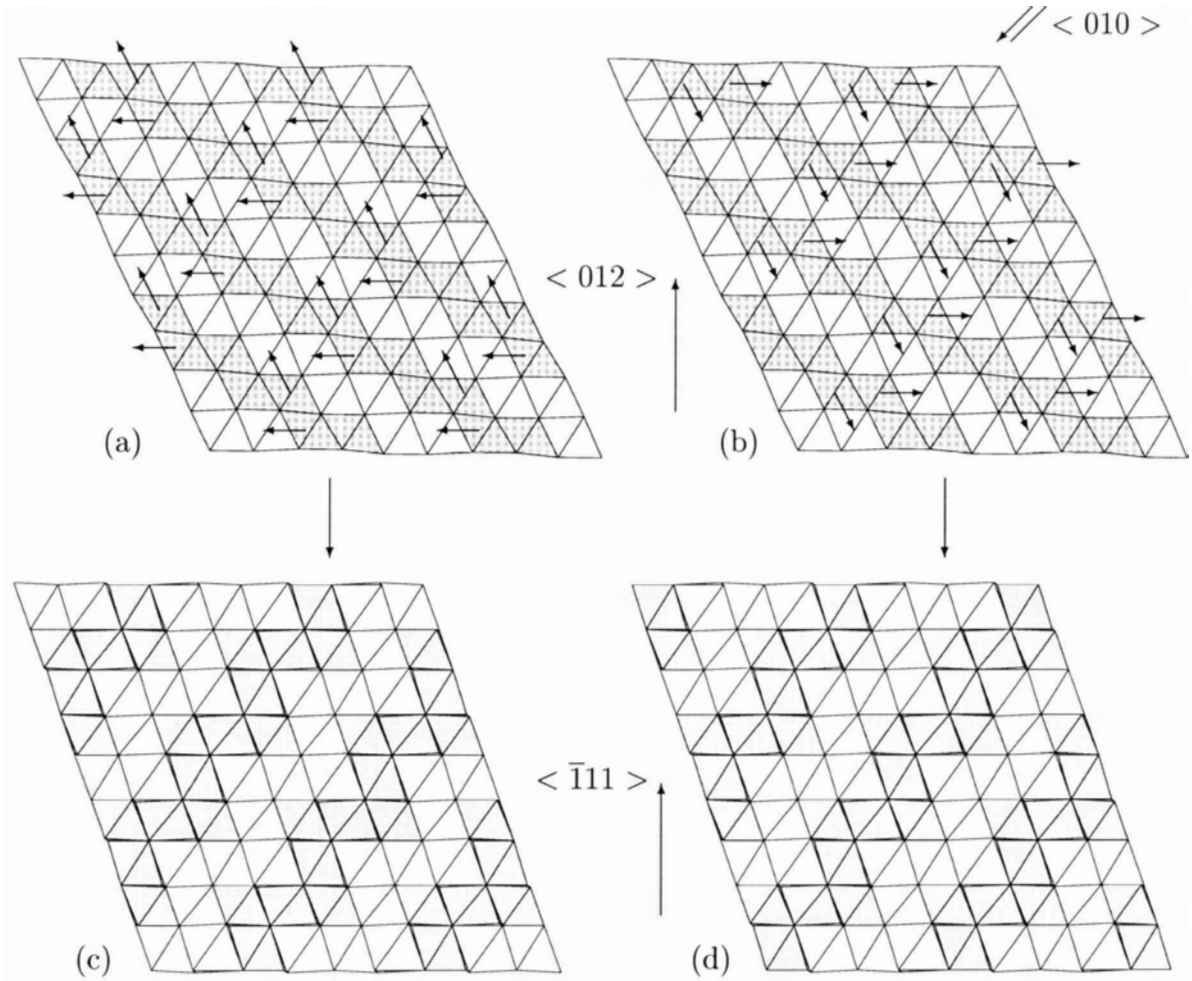

Figure 2.12: The irreversible transition from $LiMnO_2$ to $LiMn_2O_4$ (λ-MnO_2 on charge) can be explained if we assume that Mn^{4+} can migrate from one octahedral site to a neighboring site. In (a) and (b) the orthorhombic framework was sliced parallel to (100) planes and a scheme of cooperative 'jumps' of Mn^{4+} to nearest neighbor sites was applied to both layers, as indicated by little arrows. Below, in (c) and (d), the cubic spinel structure is sliced parallel to (011) planes. The assumption is, that layers (a) and (c), as well as layers (b) and (d) map onto each other in the phase transition from $LiMnO_2$ to $LiMn_2O_4$. The large arrows between the graphs indicate directions in the crystal lattices which are parallel to each other. The figures were adopted from Gummow [5]. The arrows on the top right corner of (b) indicate an alternative movement of Mn^{3+} ions causing disorder in the cation sublattice.

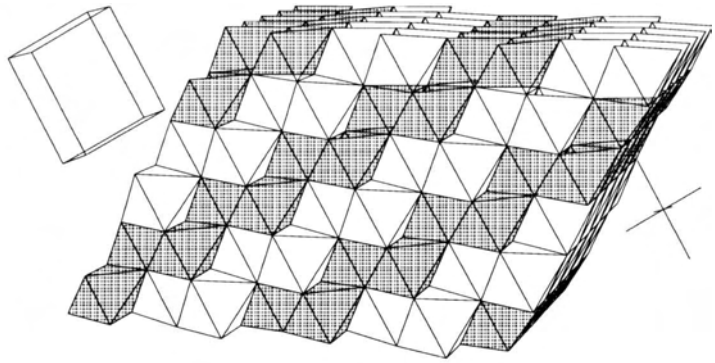

(a) $LiMnO_2$

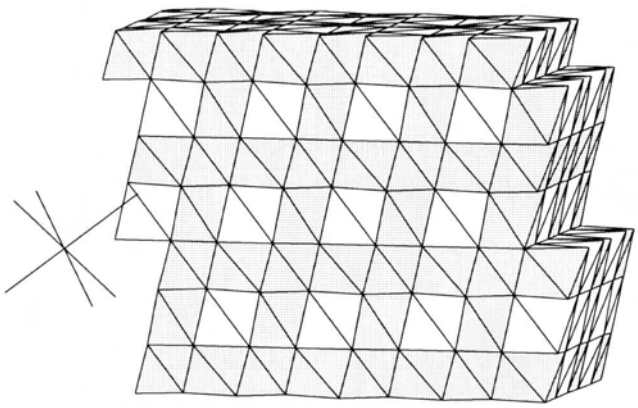

(b) $Li_2Ti_2O_4$; Li^+ on 16c

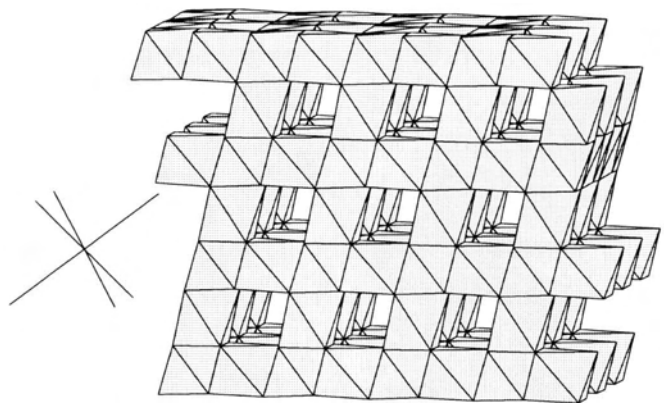

(c) λ-MnO_2 ; only Mn on 16d

Figure 2.13: Lithium transition metal oxides in the oxygen octahedra representation. The orientation of the crystal axes is indicated for each case. In (a) the zigzag layers of $LiMnO_2$ are apparent whereas in (c) the regular interconnected array of 3D channels, also referred to as 1x1 tunnels, dominates.

Chapter 3

Electrochemical Study

In this chapter, we will first review basic electrochemistry background. Later, we report on the samples used in the study and how test batteries were assembled. Finally we report on the experiments which led up to the *in situ* X-ray study of $LiMnO_2$ powder cathodes.

3.1 Electrochemical Essentials and Terminology

3.1.1 Cell Potential

When lithium metal is placed in a polar liquid, we observe the tendency of lithium to dissociate. Lithium ions go into solution and a negative charge is left behind in the metal. This process continues until the (attractive) forces between Li^+ in solution and the negative charges on the metal balance the tendency for lithium dissociation. The cumulative charge on the lithium metal electrode is a (relative) measure of the chemical potential of lithium metal. Compared to other metals and lithium transition metal oxides (TMO), metallic lithium dissociates very rapidly and a strong negative charge is left behind in the metal. Lithium atoms in lithium metal are less tightly bound than in typical Li-TMO compounds. The cell potential can be attributed to the differences between the binding energy of lithium in the anode and in the cathode.

Given a counter electrode where the dissociative tendency of lithium is considerably lower, we can build an electrochemical test cell. For this, it is necessary to ensure that lithium ions in the solution have appropriate mobility. This can be achieved by choosing the right *electrolyte*. Connecting the two electrodes through a wire, we can

allow the entire system to lower its overall *Gibbs free energy*. Electrons do work in the wire, and Li ions are simultaneously intercalated in the TMO, where they are more tightly bound than in the metallic Li anode. The net work done by n transferred electrons is

$$\Delta W = n \times e \times \Delta V \quad , \tag{3.1}$$

where e is the charge of a single electron and ΔV is the potential difference between the two electrodes. If the thermodynamic potential is known, which in this case is the Gibbs free energy, we can write an expression for the chemical potential:

$$\mu = \frac{\partial G(N,T,P)}{\partial N} \Bigg|_{T,P\ const.} \quad , \tag{3.2}$$

where N denotes the number of Li atoms. In combining equations 3.1 and 3.2 we find an equation for the potential difference between the electrodes,

$$V = -\frac{\mu_{cathode} - \mu_{anode}}{e} \quad . \tag{3.3}$$

3.1.2 Voltage Curves

For the electrochemical testing of the batteries, computer controlled battery cyclers were used in all cases. The test cells were always cycled at constant temperatures of 30.0±0.3°C. There are generally two modes in which the batteries can be charged or discharged:

1. The *galvanostatic* mode: the external current is fixed so that ideally during constant times the same amount of charge is transferred.

2. The *potentiostatic* mode: the external voltage is fixed, so that ideally a current flows proportional to the internal potential gradient. If no current flows, the battery is in electrochemical equilibrium.

In both cases the transferred charge can be calculated as the area under the I-t curve according to

$$Q(t) = \int_{t_1}^{t_2} I(t)dt \quad . \tag{3.4}$$

Throughout this thesis we assume that the external current is matched by an ionic current in the electrolyte, which is only attributed to the process of Li intercalation. This of course is never exactly satisfied. For the electrolyte, numerous secondary side

reactions are known, which can obscure the recorded currents. However, it is believed and widely accepted that these secondary effects are small and provided the separator is placed properly to insulate the two electrodes, conduction of lithium ions should dominate.

For later convenience in the analysis of V-t or I-t curves, a number of common conventions and technical terms are introduced. The capacity is usually specified in units of mAh/g with respect to the *active mass*[1] of the electrode. Upon the (sometimes false) assumption that all lithium in the cathode can be deintercalated, the theoretical *maximum specific capacity* of any $Li_x[MO]_y$ composition is calculated according to:

$$c_{max} = \frac{x \times F}{3.6 \times y \times m} . \tag{3.5}$$

In the above equation F denotes Faraday's constant (96480 Coulomb/mole) and m is the molecular weight of the stoichiometric TMO-unit (=[MO]) in the compound. The factor 3.6 arises from conversion of seconds into hours and mA to A. If we postulate, as stated above, that *all* ionic conduction in the electrolyte corresponds to intercalation, we can express the amount of charge transferred as a mole fraction in the composition of the cathode compound using Equations 3.4 and 3.5:

$$x(t) = \frac{Q(t)}{c_{max} \times m_A} , \tag{3.6}$$

where m_A is the active mass of the cathode. The quotient of Q(t) and m_A represents the specific absolute charge transfer[2] for the cathode and quite frequently, for example in many cycle experiments, we will report voltage curves where the time axis is transformed according to

$$c_{sp}(t) = x \times c_{max} \quad \text{(mAh/g)} . \tag{3.7}$$

It is necessary to point out that the mole fraction as calculated in Equation 3.6 is not related in any way to the structure of the compound, it is just a statement about the average composition in the cathode.

If we charge a battery galvanostatically, the current in an experiment is fixed. Rather than report the absolute current, it is useful to specify the current by a *charge rate*. For example if a battery is charged at a 25 hour rate (C/25), we understand that

[1] where the weight of the binder and carbon black (5-10% of cathode weight) is subtracted.

[2] and is sometimes referred to as the 'magic number' of the intercalation host.

the battery will be fully charged in 25 hours. Sometimes the current is specified with respect to the electrode mass (units of mA/g), but we will not use this convention in this thesis.

In many cases it is beneficial to consider derivative curves since the details in the voltage *vs.* capacity curves (V-Q curve) are rather weak. Taking the derivative of Q with respect to V amplifies these features. A *voltage plateau* in the V-Q curve, will appear as a strong peak (with proper scaling) in the derivative curve and the area under the peak is proportional to the number of intercalation sites in the host at the given cell potential. This is one way in which the equation

$$I(t) = \frac{dQ}{dV}\frac{dV}{dt} \tag{3.8}$$

can be interpreted.

3.2 Electrochemical Test Cells and their Assembly

3.2.1 Samples

As mentioned in chapter 2, the first successful synthesis of LT-$LiMnO_2$ was reported by Ohzuku *et al.* [3]. Compared to the synthesis temperatures reported there, 300-450°C, our LT-$LiMnO_2$-samples were prepared at temperatures near 100°C by the Belgian company Sedema [36]. The process for the synthesis of our samples is similar to that reported by Reimers *et al.* [4]. It involves mixing of stoichiometric amounts of reactants, dissolving them in an aqueous solution and subsequent drying at low temperatures in air. Details cannot be disclosed here for reasons of confidentiality. The material is available to all interested researchers from the above mentioned company [36]. The X-ray diffraction pattern of the main sample which we used later in all of our *in situ* experiments is shown in Figure 3.1 (b).

Compared to the samples received from Sedema, Reimers *et al.* reported rather poor crystallinity of their samples synthesized at low temperature. The samples appear as a brown-olive colored compound and have a fine powder texture. On a time scale of the order of weeks LT-$LiMnO_2$ seems to be stable in air. We stored the compound in a polyethylene bottle under ambient conditions. However, during this study we noticed a significant conversion, apparent in change of colour from brown-olive to almost black. This change was also apparent in the diffraction pattern. The underlying chemical process is surface oxidation. Carbon dioxide and oxygen (in air) will

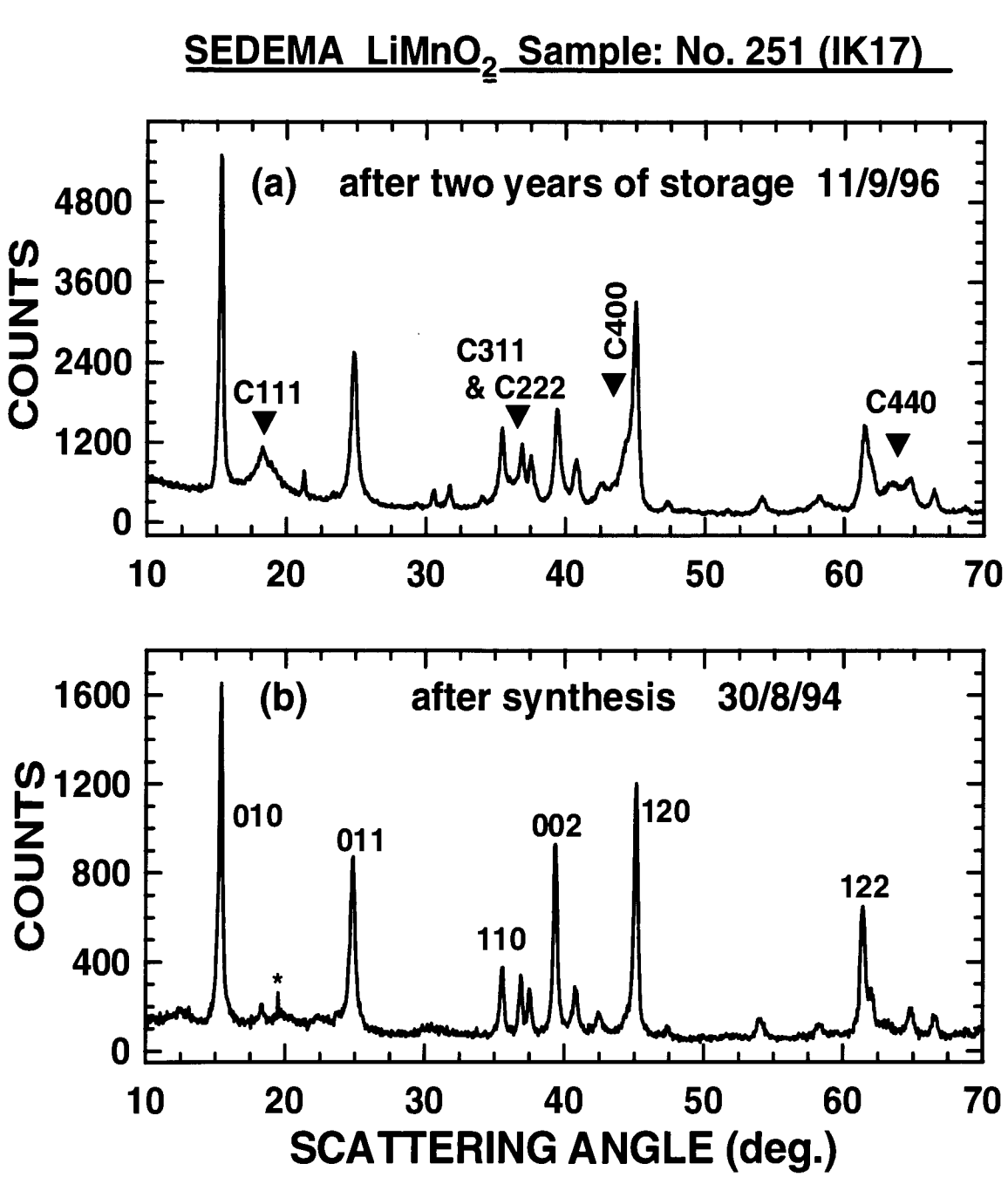

Figure 3.1: X-ray powder diffraction patterns of the sample IK17 which was used later in all in-situ experiments. The pattern in the bottom panel was acquired a few weeks after we received the samples. Major Bragg peaks are indexed with respect to the orthorhombic unit cell. The pattern in the top panel was taken two years later. The positions and indices for the most prominent peaks of the cubic spinel phase are indicated. The little star in (b) marks an impurity peak.

react with lithium on the surface of the tiny crystallites to form lithium carbonate according to equation

$$4LiMnO_2 + \frac{1}{2}O_2 + CO_2 \longrightarrow Li_2CO_3 + 2LiMn_2O_4 \quad . \tag{3.9}$$

The lithium deficient orthorhombic lattice of $LiMnO_2$ converts to the stable spinel framework, $LiMn_2O_4$, as explained in the previous chapter. This was evident from the diffraction pattern taken from the same sample 48 months later, displayed in Figure 3.1 (a). For comparison, the colour of spinel $LiMn_2O_4$ is predominantly black, given that the stoichiometric ratios are well matched. These early X-ray diffraction patterns were refined after *Rietveld* (see chapter 6) and showed good evidence for the presence of the orthorhombic phase of $LiMnO_2$. The refinement procedures are explained in chapter 6, here we report just the results to complete the physical characterization of our samples. All known physical parameters are summarized in Table 3.1.

$LiMnO_2$ samples (supplied by Sedema)				
Parameter		Units	No. 251	No. 652
Lattice	a	Å	2.805±0.001	2.804±0.001
	b	Å	5.746±0.001	5.742±0.001
	c	Å	4.572±0.002	4.576±0.002
Composition	x	-	0.99	0.97
(in $Li_xMn_yO_z$)	y	-	1.01	1.03
	z	-	2.06	2.06
Density	bulk	g/cc	n.m.	0.60
	tapped	g/cc	n.m.	0.98
SSA†	-	m^2/g	15.3	11.1
Diameter	(mean)	μm	4.2	2.0
H_2O §	600°C	%	1.52	0.98
†) SSA: specific surface area, after Brunauer, Emmett and Teller. §) residual water content in mass percent.				

Table 3.1: Physical parameters of the $LiMnO_2$ powder samples.

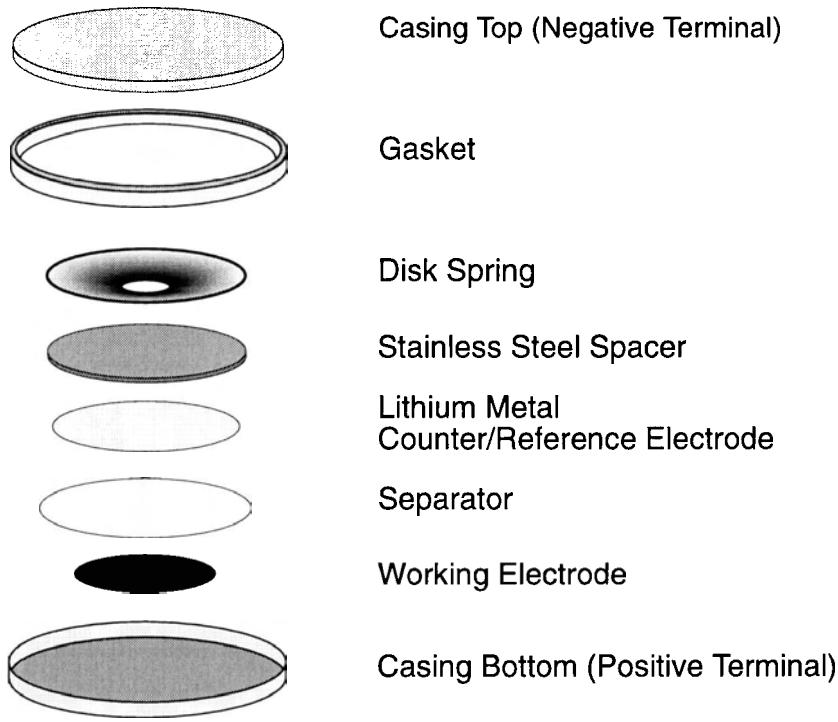

Figure 3.2: Exploded view of regular coin cell adapted from Oliver Schilling [37].

3.2.2 Assembly of Test Cells

In this section we briefly describe the standard method used to assemble small batteries, which were used in all our electrochemical tests. In Figure 3.2 we show an exploded view of a test cell. We used commercially available coin-cell hardware (type 2320) supplied by Moli Energy. A mild steel disk spring and a stainless steel contact plate were used to maintain a constant force of about 200 N on the electrode stack. In order to avoid corrosion at high voltages (4.5 V *vs.* Li at 30°C) a special stainless steel can (Shomac 30-2) was used on the cathode side. Since the stacking of the electrodes was reversed in some experiments, the spacer normally used on the anode side (see Figure 3.2) also has to be anti corrosive. In order to rule out any electronic conduction across the stack, a polypropylene separator (Celguard No. 2400) is used, which is microporous, so it allows mechanical transport of lithium ions in microscopic trucks. In cells with Li metal anodes, 12.5mm squares cut out of 125 μm lithium foil were used.

Cathode electrodes where made by mixing the powdered cathode material with carbon black (Super S, MMM Carbon, Belgium) in order to increase the conductivity

and with PVDF (polyvinylidene fluoride) binder for the formation of a solid film. In addition excess solvent NMP (n-methyl pyrrolidone) was added so that thin slurries could be spread on an aluminum substrate (Al-foil) using a *doctor blade* spreader. The electrodes were dried at 105 °C in air and afterwards compacted with a mechanical hydraulic press. Finally, square electrodes[3] (12.5mm) were cut using a precision cutting jig and their weights were recorded in order to calculate the expected total charge of the battery according to

$$Q_{tot} = m_A \times c_{max} \quad , \tag{3.10}$$

where m_A is the *active mass* of the cathode, without the mass of binder and carbon black and c_{max} is the *maximum specific capacity* for the TMO as defined in the previous section. Typical cathode weights range around 10-20 mg which corresponds to a total charge of the order of 2-4 mAh. The preparation of $LiMnO_2$ cathodes was done under ambient conditions, whereas the subsequent assembly and the preparation of Li anodes was done either in an argon-filled glove box or in a dry room. By counting individual drops, approximately 0.05 ml electrolyte was added using a syringe. The type of electrolyte is discussed in the section below.

The assembly of X-ray *in situ* cells is very similar. A hole is cut in the steel can and a beryllium disk of proper diameter is inserted into the stack. Details for the assembly of X-ray in-situ cells are discussed in chapter 5.

3.2.3 Electrolyte

The electrolyte is one of the main 'ingredients' in most battery applications. Since it is very important, we will devote a separate section to it. The electrolyte has to meet a large number of requirements of which the most important are the following :

1. sufficient supply of Li^+ at proper concentration to the system,
2. must display high *ionic conductivity* at room temperature,
3. must be stable at high potentials and must withstand large potential difference in order to avoid decomposition of the electrolyte,
4. must be *chemically inert* with respect to all other components in the battery, and if possible,

[3]Figure 3.2 shows however a round working electrode.

5. should be non-toxic and cheap to synthesize.

The first three requirements are not too difficult to satisfy in practice. In general the ionic conductivity of aqueous electrolytes is much higher compared to non-aqueous electrolytes [14] (at room temperature). However, the use of aqueous electrolytes in conjunction with metallic lithium is impossible, so that non-aqueous electrolytes must be employed in Li battery applications. For example, in all of our experiments we used a non-aqueous electrolyte where 1 mole of $LiPF_6$ was dissolved in a 30/70 mix (by volume) of ethylene carbonate/diethyl carbonate (EC/DEC). Non-aqueous electrolytes however, are not chemically inert, when brought into contact with metallic lithium and it is very hard to satisfy requirement number four. In fact, all of the known non-aqueous electrolytes do react with metallic lithium to form a passivating and insoluble, ionically conducting film, often referred to as *solid electrolyte interphase* (SEI), [38]. If these batteries are used as rechargable batteries, this film will not promote regular and even *electroplating* of Li^+ on the passivated surface. On the contrary, it is found that lithium grows in thin dendrites, as a consequence of the fact that the passivation layer has to be somehow 'pierced' in order to deposit a lithium ion on the surface. Upon subsequent cycling of the battery, the surface area of metallic lithium increases very rapidly, which can lead to poor behavior. Researchers are now focusing on concepts whereby the Li metal anode is replaced by another intercalation compound. This type of Li-Ion battery is reviewed in the following section.

3.2.4 Lithium Ion Batteries

A common replacement for lithium metal anodes in commercial applications are anodes made of carbons. In order to understand this we refer to Figure 3.3, where the binding energies of Li *vs.* graphite, coke and various TMO's are shown [1]. The energies are defined with the binding energy of Li metal as (zero) reference point on the energy scale. As we can see, the binding energy of Li in graphite is very close to the binding energy of Li in lithium metal, and hence it is the first choice for maintaining a large potential difference in the battery. Insertion of Li in graphite can also be characterized as an intercalation process and the *insertion potential* must then be a function of average Li-concentration. Since both electrodes are intercalation compounds, the overall voltage *vs.* time curve will change compared to a cell with Li metal anode. For a given state of charge in the battery, the resulting potential is then given as the difference between the two binding energies.

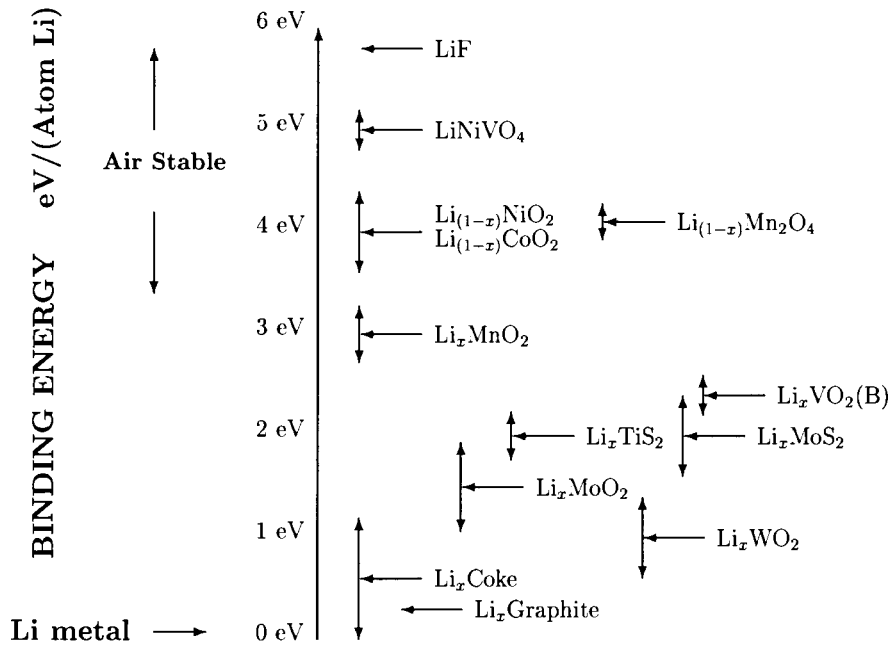

Figure 3.3: Binding energies of lithium in various lithium transition metal oxide compounds. The binding energies are referenced with respect to the binding energy of lithium in metallic lithium and correspond to the insertion potentials if Li-metal is the reference electrode. Graphite and Coke are also included as intercalation hosts.

Maximum concentrations of Li in carbons usually do not exceed the stoichiometry Li_xC_6 with $x = 1$. The lithiated phase of carbon is found to be unstable in air, oxygen will react with Li at the surfaces of the carbon host. From Figure 3.3 we find generally that hosts with binding energies below 3 V are likewise unstable. For assembly of Li-Ion cells in air, a lithiated transition metal oxide is chosen with binding energies preferably above 3 V. That means that all the Li in a Li-Ion battery is initially supplied by the TMO intercalation host. As a consequence the batteries have to be charged after assembly.

Surface passivation as found on lithium metal anodes (SEI) can still occur due to a similar reaction of the electrolyte with Li on the surface of carbon. However, in carbon anodes, Li is intercalated and this leaves the total surface area unaffected (no dendritic growth). For this reason Li-Ion batteries are considerably safer. A major drawback in the Li-Ion concept is that not all Li supplied by the TMO can be used for reversible cycling. Even if all Li could be removed on initial charge some fraction (up to 20%) of Li is lost to a passive insoluble layer similar to the SEI.

As stated above, the overall potentials of a Li-ion battery is given as the difference between the insertion potential of the two intercalation hosts. In particular, the potential of Li in carbon decreases rapidly at low but increasing concentrations of lithium in carbon. For concentrations above $x = 0.2$ the potential is close to 0 V against a lithium metal anode and remains relatively constant. For further details on lithium insertion into carbon, I refer to the extensive work done by my colleagues Brian Way, Hang Shi, Yinghu Liu, Tao Zheng and Alf Wilson [39, 40, 41, 15, 1].

It remains to mention that Li-Ion batteries are often referred to as *rocking chair* batteries, with the idea in mind that Li rocks back and forth between the two intercalation hosts[4]. Frequently we will also refer to these systems as carbon/$LiMnO_2$ cells, and batteries with Li metal anodes as Li/$LiMnO_2$ cells.

3.3 Experimental Study of $LiMnO_2$

3.3.1 Full Charge/Discharge Tests for Li/$LiMnO_2$ Cells

Figure 3.4 shows voltage *vs.* time graphs for three Li/$LiMnO_2$ cells. Figure 3.4 (a) shows a typical result for a Li/$LiMnO_2$ battery charged and discharged over ten full cycles using a constant current corresponding to a C/25 rate. Between the first charge ($\leq$ 15 h) and all subsequent charge cycles we find an apparent change in the shape of the V-t curve. On all subsequent charge and discharge cycles we observe two dominant *plateaus*: one at 3 V and one at 4 V. Careful observation shows that the upper plateau becomes flatter and increases slightly in length. The lower plateau also becomes flatter but it decreases in length. The latter is rather difficult to observe in a linear graph like this. All of the above mentioned is much better visible, if the time variable is transformed according to Equation 3.7 and multiple cycles are mapped on the same abscissa as shown in Figure 3.5 a. Here the first, fourth and nineteenth cycle are shown. As pointed out in chapter 2, the removal of lithium from the orthorhombic phases leaves an unstable layered structure behind. The change between the first charge and all subsequent cycles in the voltage *vs.* capacity graph corresponds to the *irreversible phase transition* from the orthorhombic phase to the spinel phase as reported by Reimers *et al.* [4] in 1993. In fact, Figure 3.5 (a) confirms

[4]which is a simplified picture. Particular Li-Ions go either in or out of solution and the electrolyte serves as a reservoir.

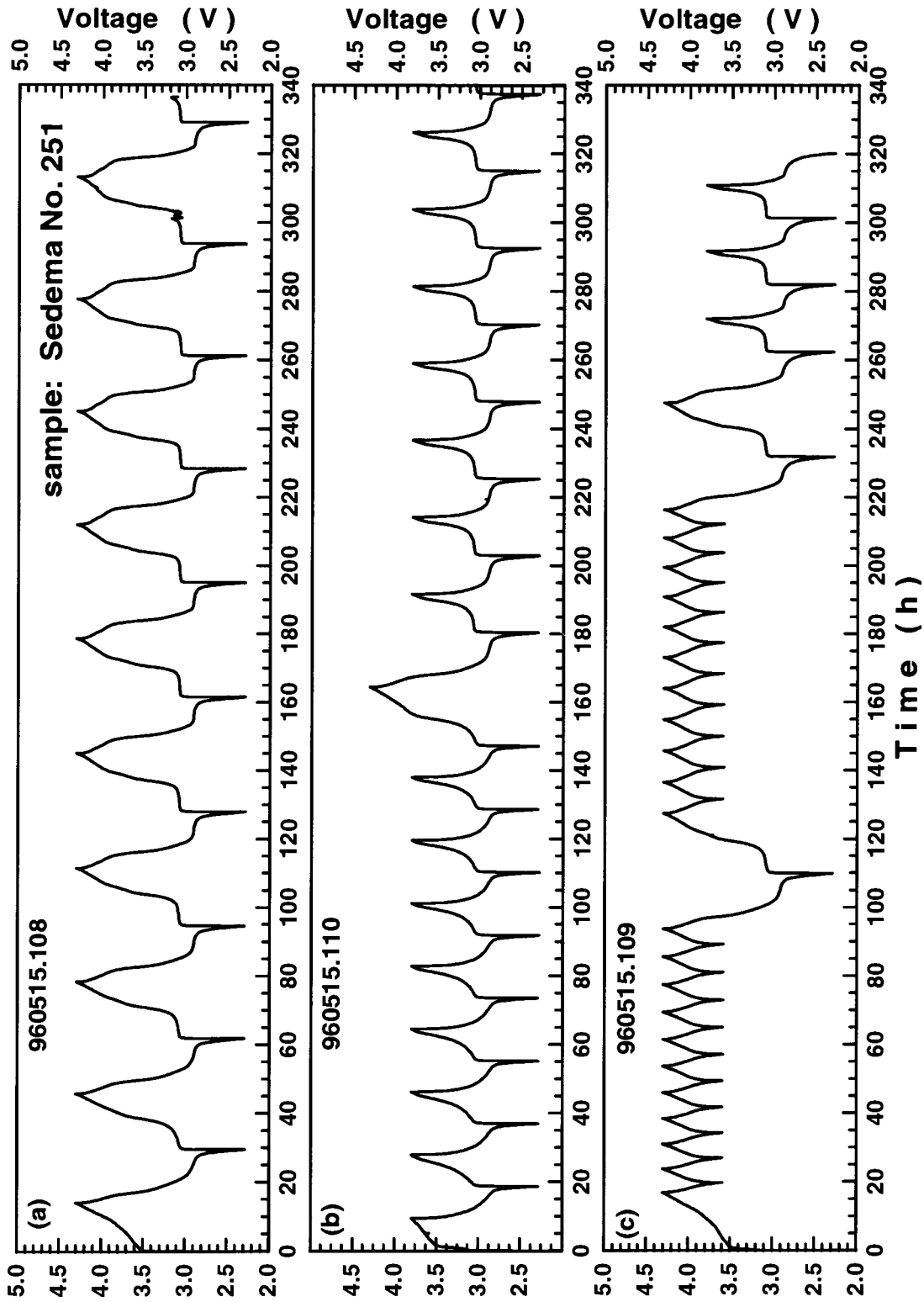

Figure 3.4: Voltage *vs.* time graphs of three $Li/LiMnO_2$ cells.

(a)

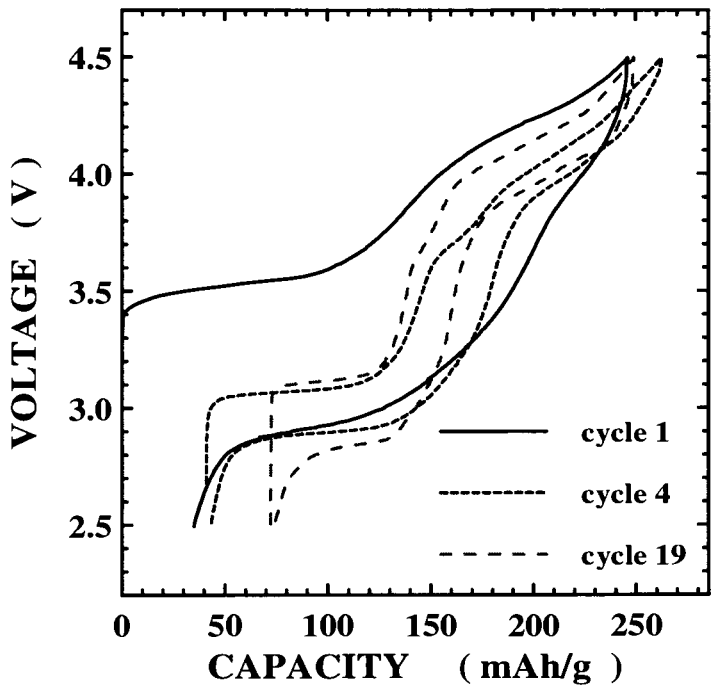

(b)

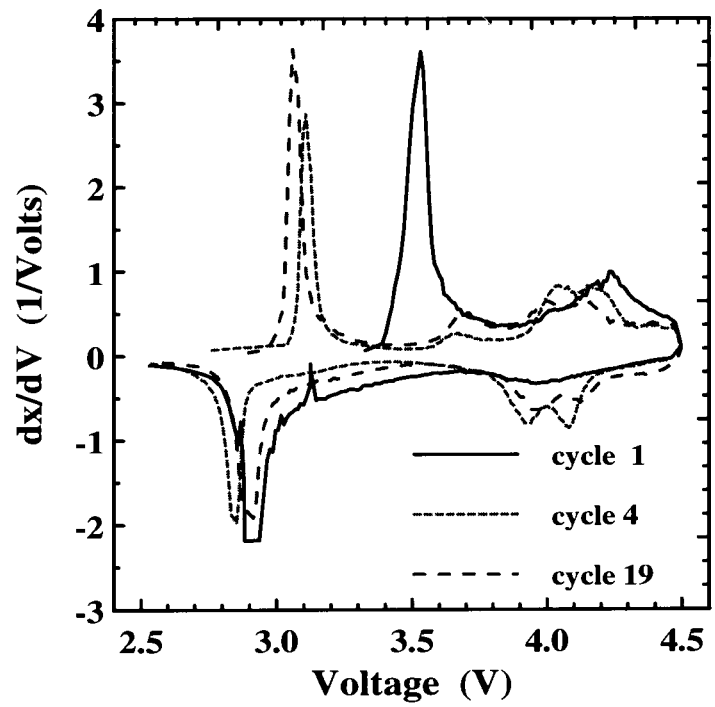

Figure 3.5: In (a) voltage *vs.* specific capacity is shown for the first, fourth and 19th cycle of a Li/$LiMnO_2$ cell. Below, the derivative curve dx/dV, with x in $Li_{(1-x)}MnO_2$, is plotted for the same cycles.

the continuous evolution of the two plateaus upon subsequent cycling, as proposed in the above. Moreover we read off easily that the initial charge of the battery amounts to approximately 230 mAh/g. In terms of the theoretical maximum capacity (Equation 3.5), we find that approximately 80% of the Li in $LiMnO_2$ was transferred on the first charge. Here this value will be referred to as *depth of charge*[5]. In the same figure we show in (b) the derivative curve dx/dV, with x as in $Li_{(1-x)}MnO_2$, for the corresponding cycles. Bearing in mind that the area under a peak is proportional to the number of intercalation sites in the host at a given potential, we find a dramatic redistribution of available intercalation sites over the whole voltage range. This must correspond to significant changes in the structure of the host.

As can be seen for this battery in Figure 3.6 (a), the discharge capacity for Cell 2 is much lower than its initial charge capacity. We notice in particular that the *discharge* capacity *increases* during the next three cycles whereas the *charge* capacity *decreases* during these cycles. After cycle three we observe that both capacities rapidly decrease with cycle number. It seems that the discharge capacity is always smaller than the charge capacity for a given cycle. We do not understand why the two capacities differ in the indicated manner during the first four cycles.

The battery was taken off the charger after cycle 14 because of *shunting*. An internal short occurred most likely due to dendritic growth of Li on the anode (see section 3.2.4), a problem which we encountered frequently in $Li/LiMnO_2$ battery experiments. This can also be seen in Figure 3.4 (a). After 300 h we find 'spikes' at the end of the 3 V plateau, the typical indicator for shunting. Capacity *vs.* cycle number of a nominally identical cell (Cell 1) is also shown in Figure 3.6 (a), which lasted almost for 20 cycles before shunting occurred. Below in (b), we included for better comparison multiple voltage *vs.* time plots for this cell. The first, third and 19th cycle were superimposed, so that the upper *trip points* at 4.5 V coincided. From this figure it is evident that the capacity fade can predominantly be attributed to the shortening of the lower plateau at 3 V.

Capacity Retention

In order to study the capacity retention *vs.* cycle number of this cathode material, we used Li-Ion cells, for which shunting is not a problem. The voltage curves will be altered compared to $Li/LiMnO_2$ systems as discussed in the previous section.

[5]although it is more common in the literature to refer to the *depth of discharge* of a battery.

(a)

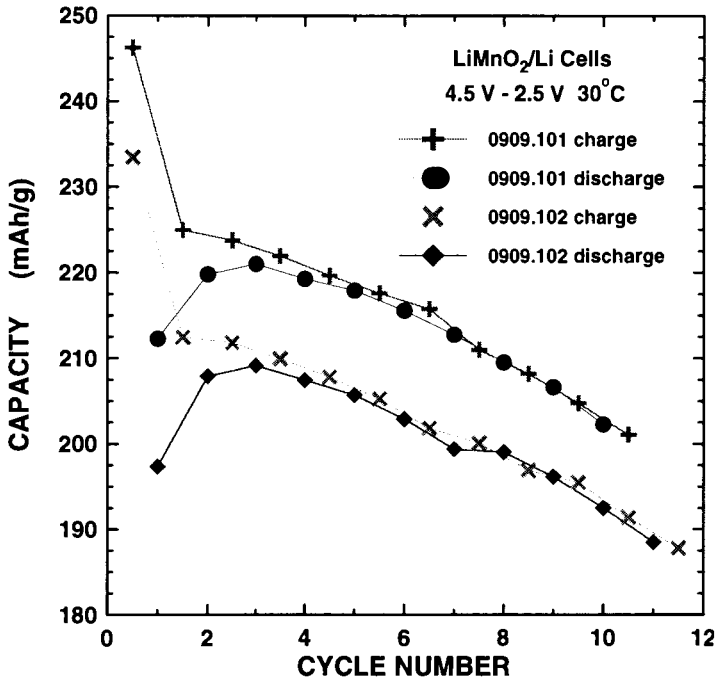

(b)

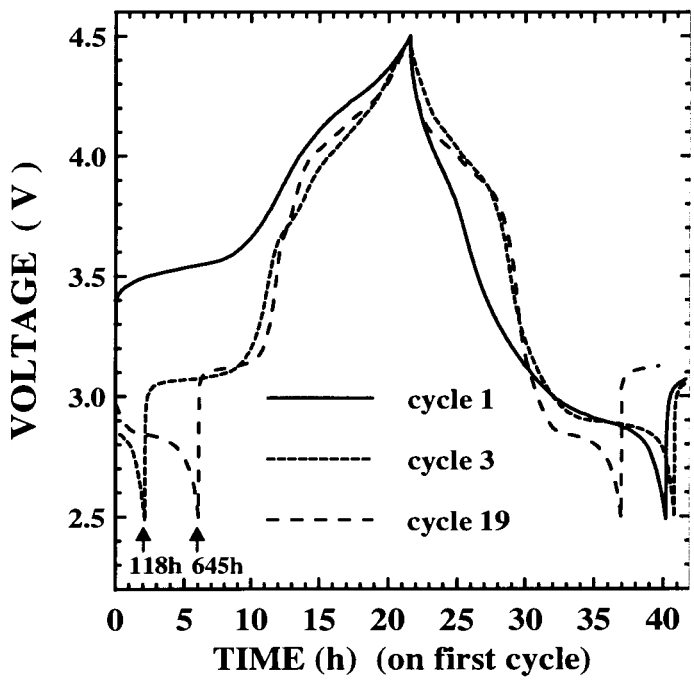

Figure 3.6: (a) charge and discharge capacity *vs.* cycle number for the cell in (b) (Cell 1: 0909.101). The second cell in (a), (Cell 2: 0909.102), is a nominally identical cell. In (b) voltage *vs.* time is shown for the first, third and 19th cycle of a Li/$LiMnO_2$ cell (# 0909.101).

Moreover, lithium is lost in the cathode for the process of intercalation due to the passivation layer (SEI), formed on initial charge of any Li-ion battery. Figure 3.7 (a) shows a carbon/$LiMnO_2$ cell for cycles one to four and in (b), cycles 35 to 38 are shown. The current used was 11.4 mA/g (C/25-rate) and the temperature was fixed at 30°C. Because the voltage profile of the carbon electrode is relatively flat, the 3 V and 4 V plateaus are clearly observed. In Figure 3.8 (a) the capacity *vs.* cycle number is shown for this cell. The cell was cycled 75 times and we find an almost uniform fade in the capacity. The drop in capacity at cycle 17 may be attributed to a power failure, where the battery may have been shorted for a brief period of time on the order of minutes.

Comparison with Regular $LiMn_2O_4$ Cells

The following arguments are qualitative and are not meant to be conclusive up to this point. What we are trying to establish here is a qualitative understanding for possible structural changes in an unstable cathode compound. It is reasonable to compare the converted structure ($LiMnO_2$ after the first cycle) to known structures of the same stoichiometry.

In order to demonstrate the correspondence of the upper plateau found in our cells after the first cycle and the plateau in an original $LiMn_2O_4$ cell, we have included voltage *vs.* capacity data for a typical $LiMn_2O_4$ cell in Figure 3.9 (a). Below, in (b), the derivative curve is shown for the same cell. In (a) we see that there are two long plateaus, closely spaced around 4 V. The derivative curves shown in (b) reveal that these plateaus are truly distinct. Comparing Li/$LiMnO_2$ cells with $LiMn_2O_4$ cells is best done consulting the derivative curves. Figure 3.5 (b) and Figure 3.9 (b) are provided for such a comparison and we see that cycle 4 in the Li/$LiMnO_2$ cell also displays two plateaus much like the $LiMn_2O_4$ cell.

Not apparent from Figure 3.9 is the 3 V plateau in $LiMn_2O_4$ electrochemical cells. It is usually 50-100 mV below 3 V. The presence of the 3 V plateau has been confirmed recently by Bates *et al.* [42] in a study of the proposed 5 V plateau in $LiMn_2O_4$. Thin film $LiMn_2O_4$ cathodes were deposited by electron beam evaporation and annealed at different temperatures (400-800°C). Initially the batteries where charged to 4.5 V followed by a full discharge to 1.5 V. Subsequently the batteries where charged to 5.3 V.[6] In a final step the cells where discharged to 3.8 V in order to measure the

[6]using phosphorus oxynitride electrolyte which the authors report to be stable up to 5.5 V.

(a)

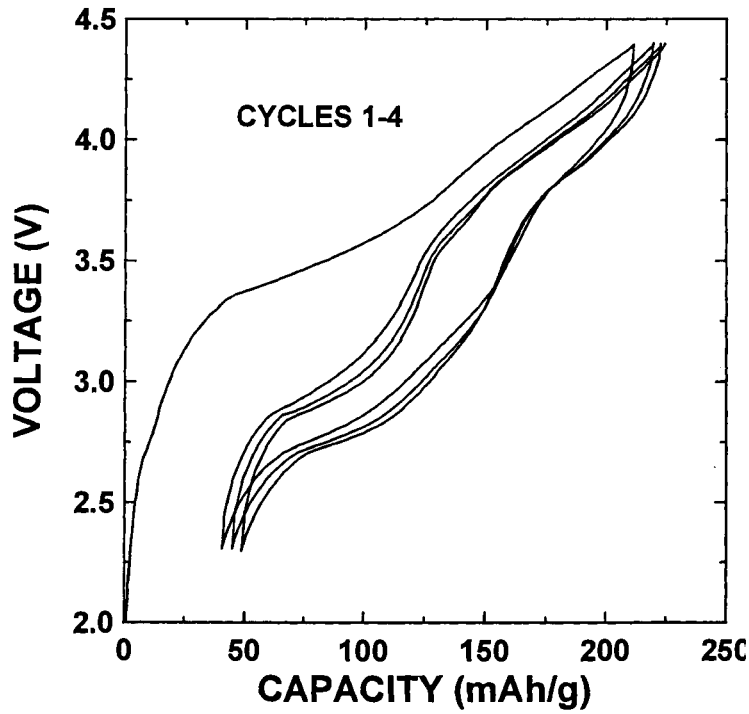

(b)

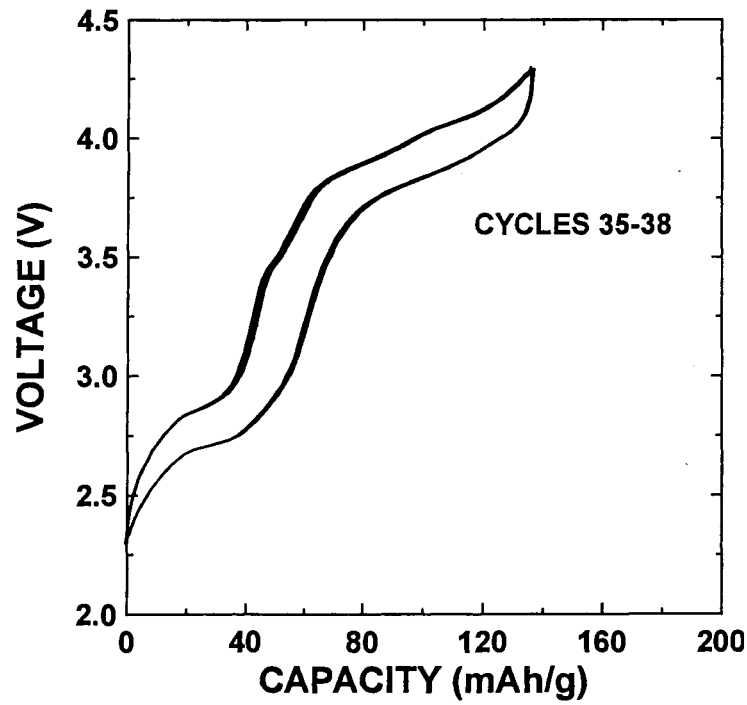

Figure 3.7: In (a) the voltage *vs.* capacity is shown for a carbon/$LiMnO_2$ Li-ion cell during the first four cycles and in (b) cycles 35 to 38 of the same cell are displayed.

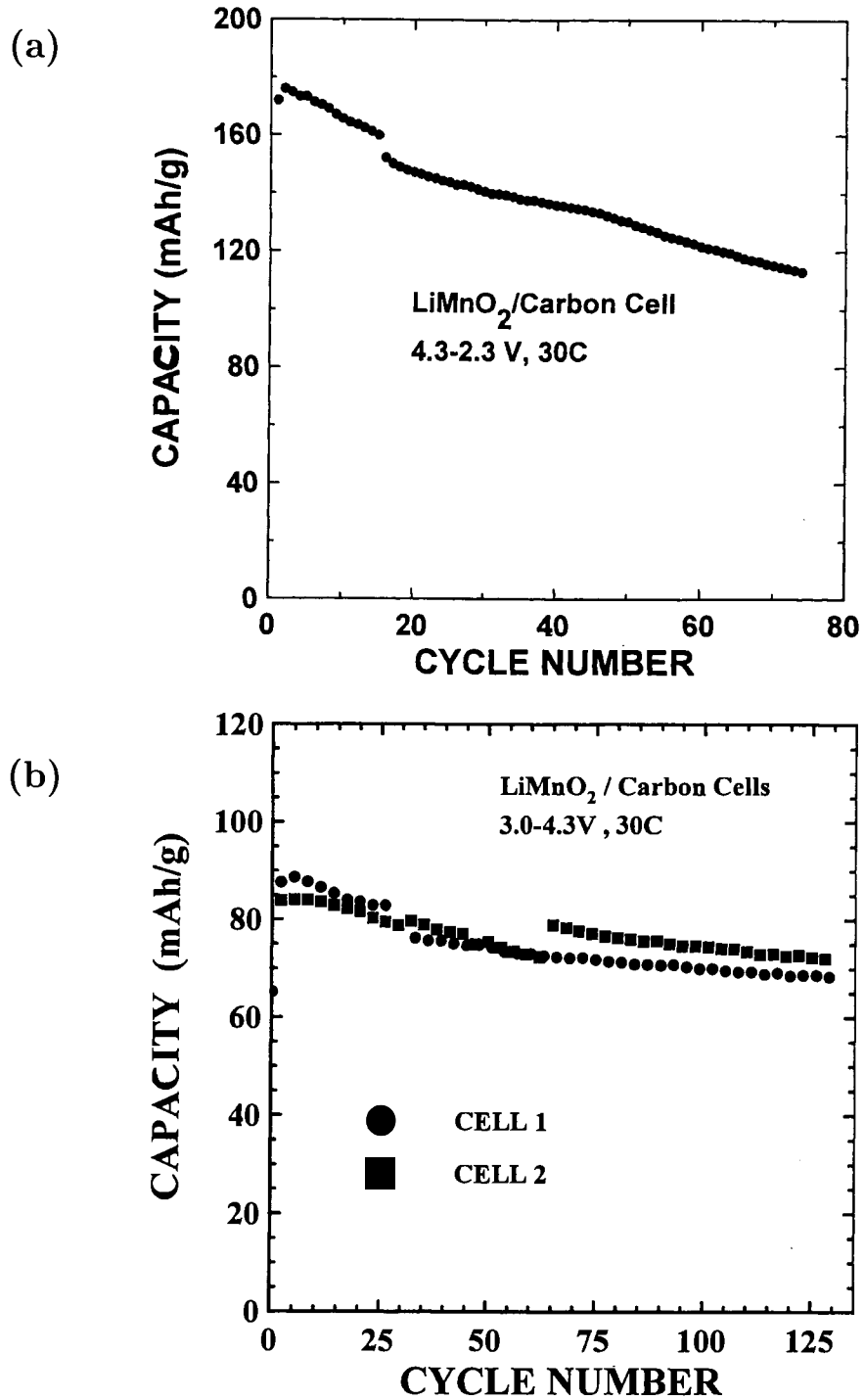

Figure 3.8: The capacity fade of a $LiMnO_2$ cathode cycled over both plateaus is evident from (a) where the many cycle behavior of a carbon/$LiMnO_2$ cell is shown. In (b), a pair of carbon/$LiMnO_2$-cells were restricted to the upper plateau. The recorded capacity fade was considerably lower.

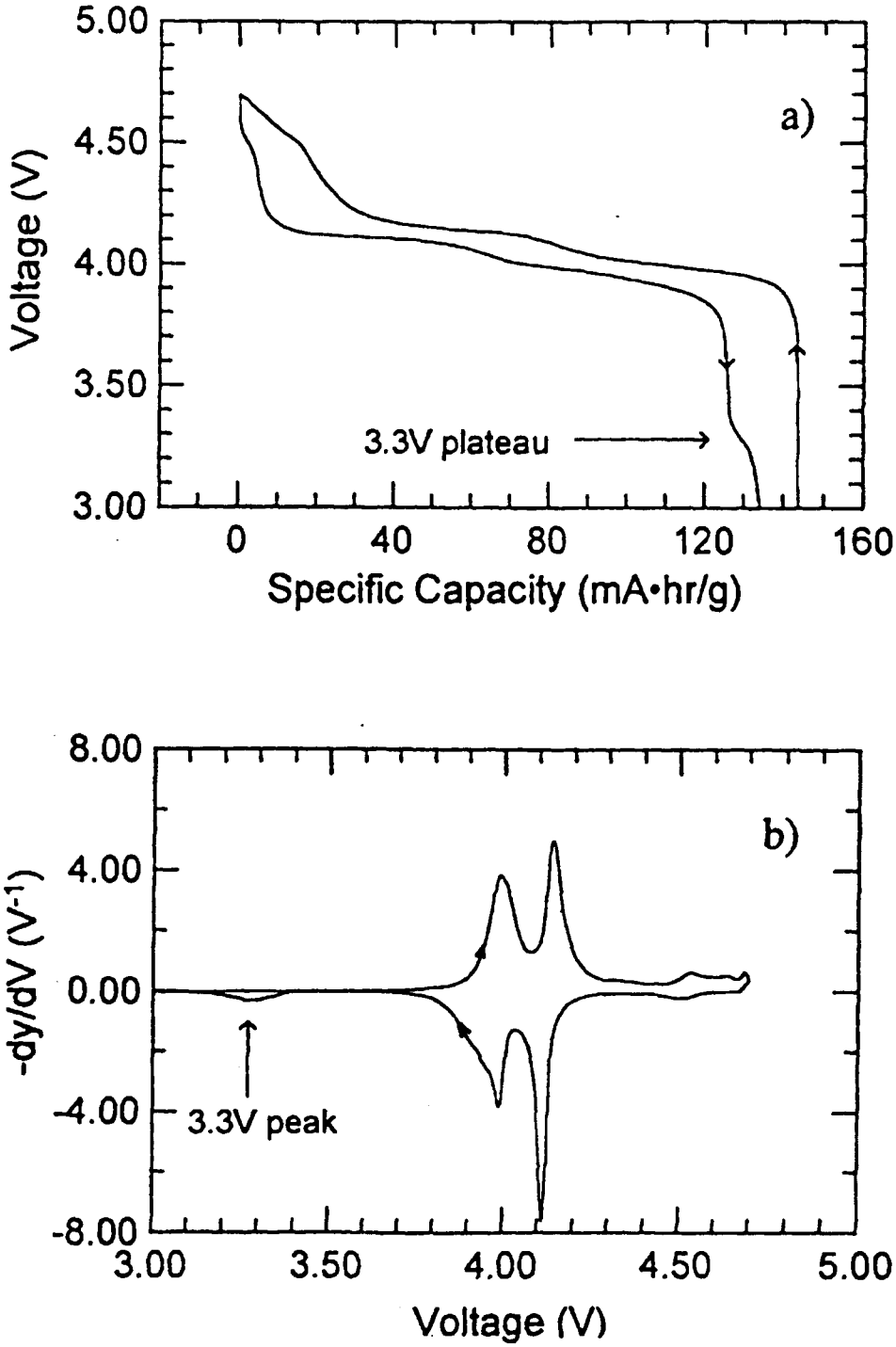

Figure 3.9: In (a) voltage *vs.* capacity is shown for a $Li/LiMn_2O_4$ cell (first charge and discharge). Below, in (b) we plot the corresponding derivative curve.

capacity retention in the 4 V and proposed 5 V plateau. The 3.0 V plateau was observed in all samples when the battery was charged close to equilibrium conditions.

Some other interesting facts concerning $LiMn_2O_4$ are reported by Bates *et al.* which we like to mention here. One observation is, that the capacity in the 3 V region, depends on the annealing temperature. At lower temperatures the capacity is considerably larger. A second observation is, that cells which show clearly the two closely spaced plateaus in the 4.0 V region, mentioned earlier in this section, display very little capacity in the proposed 5 V plateau. On the other hand, cells with a short and steep 4 V plateau show large capacities in both the 3 V and 5 V regions.

Common to all test cells is the poor capacity retention in the 5 V region. If a 5 V plateau is observed on charge, subsequent discharge does not display a corresponding flat 5 V plateau. The discharge curve is steep and not flat and considerably shorter than the charge plateau.

Another interesting effect is that on discharge at higher (non equilibrium) rates the capacity in the 3.0 V plateau is small. As the insertion of lithium progresses the potential drops down to 2.2 V. Conversely on subsequent charge the potential reaches quickly 3 V and as Li^+ removal progresses, the potential rises to 3.8 V. This non-equilibrium behavior is addressed in end of the following section.

Hysteresis

Between the charge and discharge recording for cycles 4 and 19 in Figure 3.6 there exists a considerable *voltage offset*. This 'hysteresis'-like behavior can be understood if we consider that lithium insertion takes a finite time and is hampered by scattering processes. The insertion of Li^+ in the host is determined by the temperature dependent *diffusion coefficient* and the electric field. Hence we find for the intercalation of Li^+ a finite *resistance* at the electrolyte/host interface. If the externally applied potential and the equilibrium potential of the host do not match we find a current flowing and according to Ohms law the potential drops at the interface. The potential difference at the electrolyte/host interface is reversed upon current reversal, and hence we see a difference in the overall potential between charge and discharge. If the currents are chosen infinitely small, equilibrium conditions are present and the potential difference between charge and discharge vanishes.

However, in practice we will find that even at equilibrium conditions the charge and discharge potentials do not always meet as they should. By dimensional analysis

we find that any area enclosed in a voltage *vs.* capacity curve has units of energy and must correspond to physical work. Since we are looking for (ideally fully) reversible processes, going around a closed path in a V-Q diagram at constant temperature and pressure must correspond to either of two options: the system[7] does net work on the environment[8], or the environment is doing work on the system. The latter is the case if the crystal structure undergoes changes which are not reversible and some of the energy required for this process cannot be recovered.

In the experiments reported by Bates *et al.* we have an example of a system where a very large offset of almost 2 V is observed between the charge and discharge voltage in the 3 V plateau. For one, there is definitely a kinetic diffusion barrier for Li^+ in the crystallites. However, rather than having just a potential drop due to a large diffusion coeffient, there is the effect that forced insertion of Li^+ favours at the diffusion boundary the reduction of Mn^{4+} to Mn^{2+} instead of Mn^{3+} (high Li^+ concentration, insertion potential drops to 2.2 V). Mn^{2+} ions are rather large (see Table 2.3). Along the diffusion front the lattice might therefore expand beyond the regular tetragonal distortion. If the cell is allowed to equilibrate, Li^+ diffuse and Mn^{4+} and Mn^{2+} disappear in favor of Mn^{3+} and the insertion potential reaches 3 V again. Obviously the system exchanges to a much larger extent elastic energy when subject to non-equilibrium currents. The work in the V-Q diagram was therefore not only dissipated by an increased ohmic resistance, some fraction of it went into the expansion and contraction beyond the equilibrium values.

We do not know whether the process reported by Bates *et al.* is fully reversible. Important in my opinion is the observation that a large hysteresis in the charge discharge curve, can also indicate excess mechanical stress in the crystallites of the cathode.

3.3.2 Restricted Charge/Discharge Experiments

As I pointed out in the previous section, the physical processes associated with the two distinct plateaus in the converted $LiMnO_2$ structure were quite different. The 4 V region was considered the domain where Li ions are inserted or removed from a λ-MnO_2 host structure and the 3 V region was reported as a two phase region, where

[7] the crystallites in the cathode.

[8] the rest of the coin cell including the electronic circuit.

$LiMn_2O_4$ and $Li_2Mn_2O_4$ coexist. This is as much as one can 'guess' from analyzing electrochemical cycling data of test cells. What is rather puzzling, is that we find a monotonic decrease in capacity if the cells were charged or discharged over many cycles and that this fade can almost entirely be attributed to the shortening of the lower plateau. One explanation found in the literature is that cycling over the 3 V region, where crystallites distort from cubic to tetragonal symmetry, causes fracturing of the crystallites and subsequent disconnection from the conducting part of the electrode. This hypothesis however cannot explain why we observe a stable upper plateau and a shortening in the lower plateau. Fracturing would imply a corresponding decrease in both plateaus. Obviously there is some insight missing into what the true nature of the structural and compositional changes in the cathode is.

Although we cannot deduce the structure from electrochemical cycling data, we continued our empirical electrochemical study, in particular to investigate the capacity retention of $LiMnO_2$ cells. We found it worthwhile to test the charge retention of the two plateaus separately and to test the impact of 'full' charge/discharge cycles.

In order to put these ideas into a controlled format, we restricted the voltage range over which the batteries were cycled in three different ways:

1. Successive cycling over the lower plateau only. This corresponds to restricting the initial deintercalation of lithium in the cathode (on charge) by fixing the upper trip-point at an intermediate voltage between the two observed plateaus (2.3-3.8 V).

2. Successive cycling over the upper plateau only. This was meant to remove as much Li from the cathode initially as possible and restricts the subsequent intercalation of lithium (on discharge) in the transformed cathode structure (3.6-4.4 V).

3. Cycling of the cell in either one of these modes but insertion of a single full charge and discharge cycle after a number of upper (or lower) plateau cycles. After this cycle the initial cycling range was restored in order to compare subsequent cycles to cycles prior to the full charge/discharge cycle.

Figure 3.4 (b) shows the voltage *vs.* time graph for a battery initially restricted to the lower plateau. Displayed are the first eight cycles over the lower plateau, one full charge/discharge cycle and seven more cycles over the lower plateau. In Figure 3.4 (c)

we charged the cell up to 4.3 V and restricted the cycling for the following 10 cycles to the upper plateau after which a full discharge/charge cycle was inserted. The subsequent 10 cycles were again restricted to the upper plateau. Finally we inserted a full discharge/charge and another discharge cycle, in order to test the available capacity on the lower plateau. In both cases the insertion of a full charge/discharge cycle was found to increase the capacity available for the particular plateau compared to the capacity measured before the full cycle.

In order to see this better we show in Figure 3.10 (a) an enlargement of the time axis around the full charge/discharge cycle for the lower plateau experiment. The data corresponds however to a different cell than shown in Figure 3.4 (b). Displayed is the tenth cycle over the lower plateau, the full charge/discharge cycle and the next cycle over the lower plateau. During the full charge/discharge cycle we restricted the battery potential between 2.3 and 4.5 V. In Figure 3.10 (b) we display the capacity *vs.* cycle number for the whole test of this battery. For the restriction over lower plateau we find an initial capacity near 100 mAh/g before the full charge/discharge cycle was inserted. After this cycle the capacity increased to almost 140 mAh/g and sustained that level for the next 8 cycles done at 30°C. Since the full charge/discharge cycle increased the capacity we coined the name *'boost' cycle*, which is shorter than always writing 'full charge/discharge cycle' and we will use it subsequently as a synonym. Unfortunately, the battery had to be moved out of the temperature controlled environment to room temperature conditions, due to necessary maintenance of the charger equipment. We attribute the capacity drop of almost 10 mAh/g to a change in impedance. Due to a higher impedance at a lower temperatures the battery will reach the upper trip point earlier than in the temperature controlled 30°C environment. However, for the subsequent 23 cycles the reversible capacity remained almost constant and the insertion of a second boost cycle did not increase the capacity any further.

In the complementary experiment for the upper plateau, we found the same tendency. And we also provide an enlargement of this situation with Figure 3.11. Initially we could cycle over the upper range moving a total capacity of 50 mAh/g with slight increase upon subsequent cycling. After the tenth cycle a full discharge/charge cycle was inserted and the reversible capacity for the subsequent cycles increased by almost 10 mAh/g. The second boost cycle caused further marginal increase in the capacity. After cycle 27, we decided to switch the cell to the lower plateau in order to measure the capacity retention on the lower plateau cell. The lower plateau capacity of this

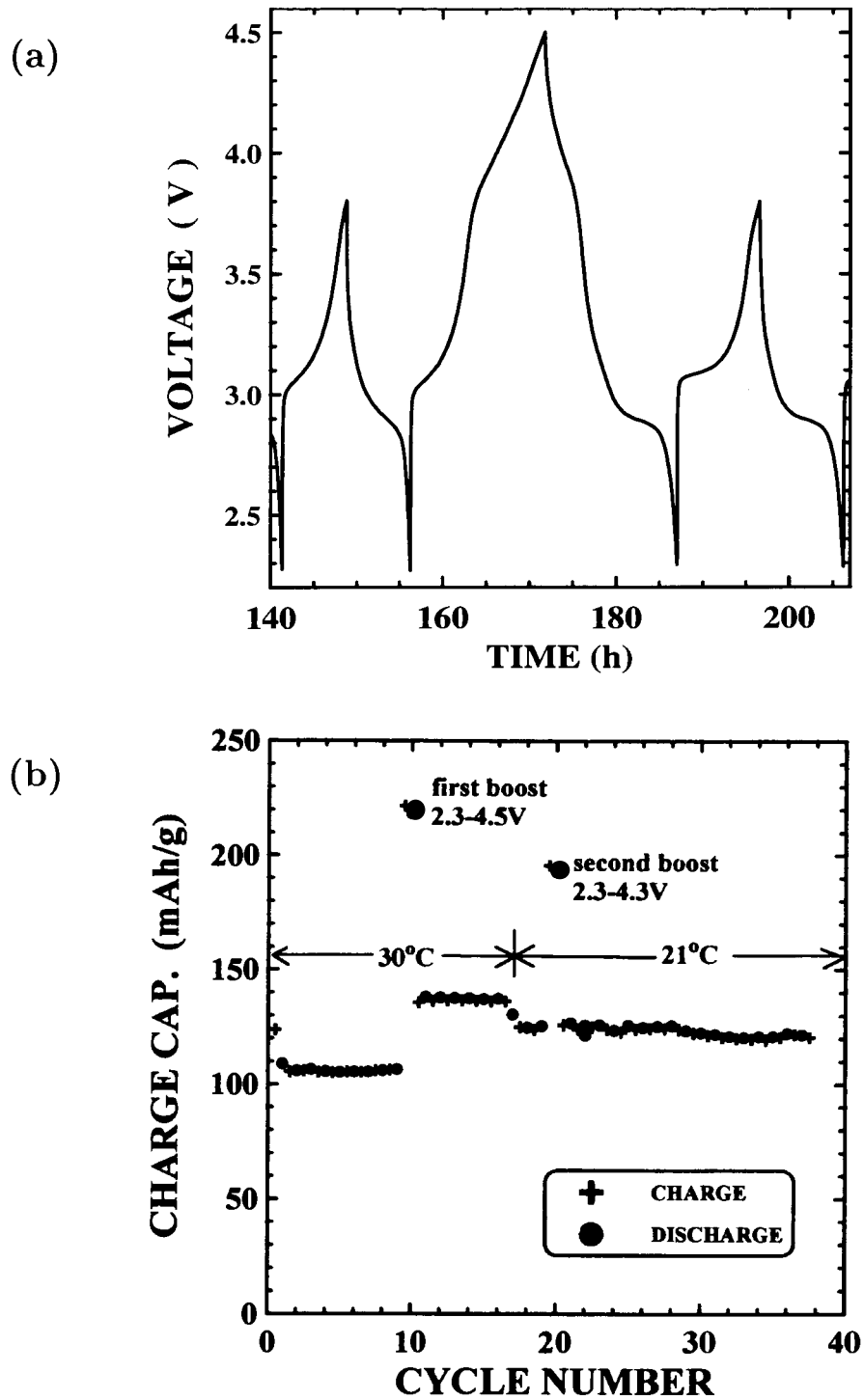

Figure 3.10: In (a) the cycle range was restricted to the lower plateau. Displayed is the 10th cycle, a 'boost' cycle, and the 11th cycle again on the lower plateau. In (b) the corresponding capacity *vs.* cycle number for the whole test of the cell is shown.

(a)

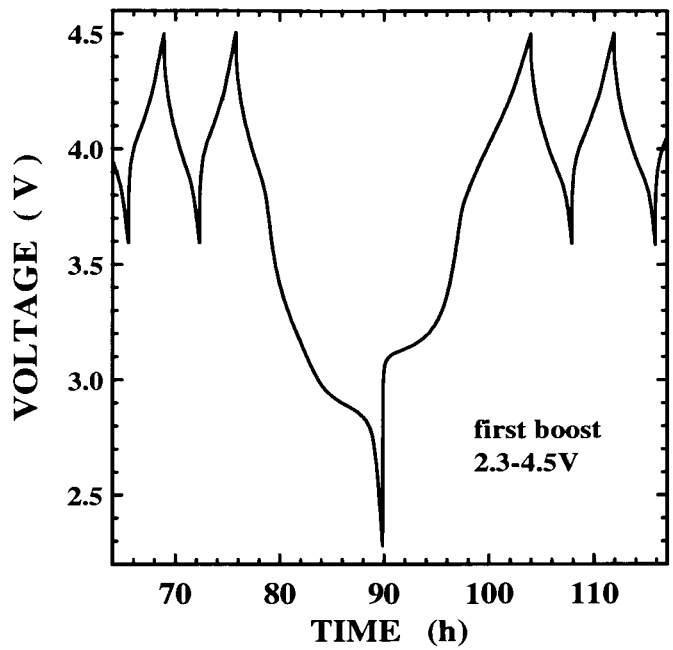

(b)

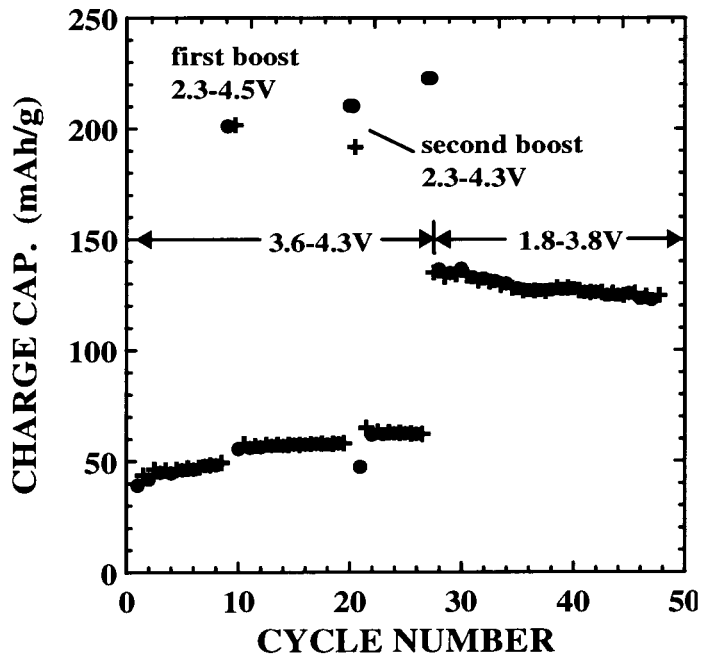

Figure 3.11: In (a), the cycling range was restricted to the upper plateau. Displayed is the tenth cycle on the upper plateau, a 'boost' cycle and the 11th cycle on the upper plateau. In (b) the corresponding capacity *vs.* cycle number is shown for the entire test of the cell. The cell was switched to the lower plateau after cycle 27 out of curiosity.

cell did not differ significantly from the experiment described above (Figure 3.10). However we found that the capacity fade for subsequent cycles seemed larger compared to the fade visible in Figure 3.10 (b), but not as large a compared to the full charge/discharge experiment, see Figure 3.8 (a) which necessarily was carried out using Li-ion cells.

It was very interesting to carry out long-term cycling studies with carbon/$LiMnO_2$ cells restricted to a wider range for the upper plateau. In Figure 3.8 (b) the capacity *vs.* cycle number is shown for two carbon/$LiMnO_2$ cells restricted to 3.0 to 4.3 V. The lower trip-point for such a cell is still above the main part of the lower plateau as can be discerned form Figure 3.7 (b). This is to assure that we do not cycle the battery over the critical two phase region. Compared to the full range (2.3-4.3 V) experiment shown in Figure 3.8 (a) we find the capacity fade for the upper plateau (3.0-4.3 V) considerably lower.[9] The capacity increase near cycle 65 for cell 2 occurred because the upper trip-point was increased from 4.3 to 4.4 V. The cells have a capacity of about 80 mAh/g and presumably, although not tested, another 80 to 90 mAh/g could be accessed by cycling as well over the lower plateau, although with larger fade in overall capacity.

In section 3.2.1, we mentioned that the powder samples suffered long-term instability. We proposed a reaction affecting the surfaces of the crystallites, thus leaving the bulk of the material unchanged. Data displayed in Figures 3.10 and 3.11 were taken in September 1994 just after we received the freshly synthesized samples. In order to confirm that the electrochemical behavior has not been altered significantly we show in Figure 3.12 a typical lower plateau test taken almost two years later with cathodes made from the same sample. The depth of charge equal to $x = 1$ (in $Li_{(1-x)}MnO_2$) corresponds to the theoretical maximum capacity of 285mAh/g. The capacity removed during the first boost cycle (No.9) was about 185mAh/g, considerably lower compared to the experiment shown in Figure 3.5. This has two reasons. The first is that the upper trip-point was at 4.3 V and not at 4.5 V and second we expect to measure a lower overall capacity on the initial charge, since some fraction of the $LiMnO_2$ structure has already converted to the cubic spinel structure. In summary however we find qualitatively similar behavior.

[9]We point out that the ordinate axes on Figure 3.8 (a) and (b) are different: 80 cycles are compared to 125 cycles.

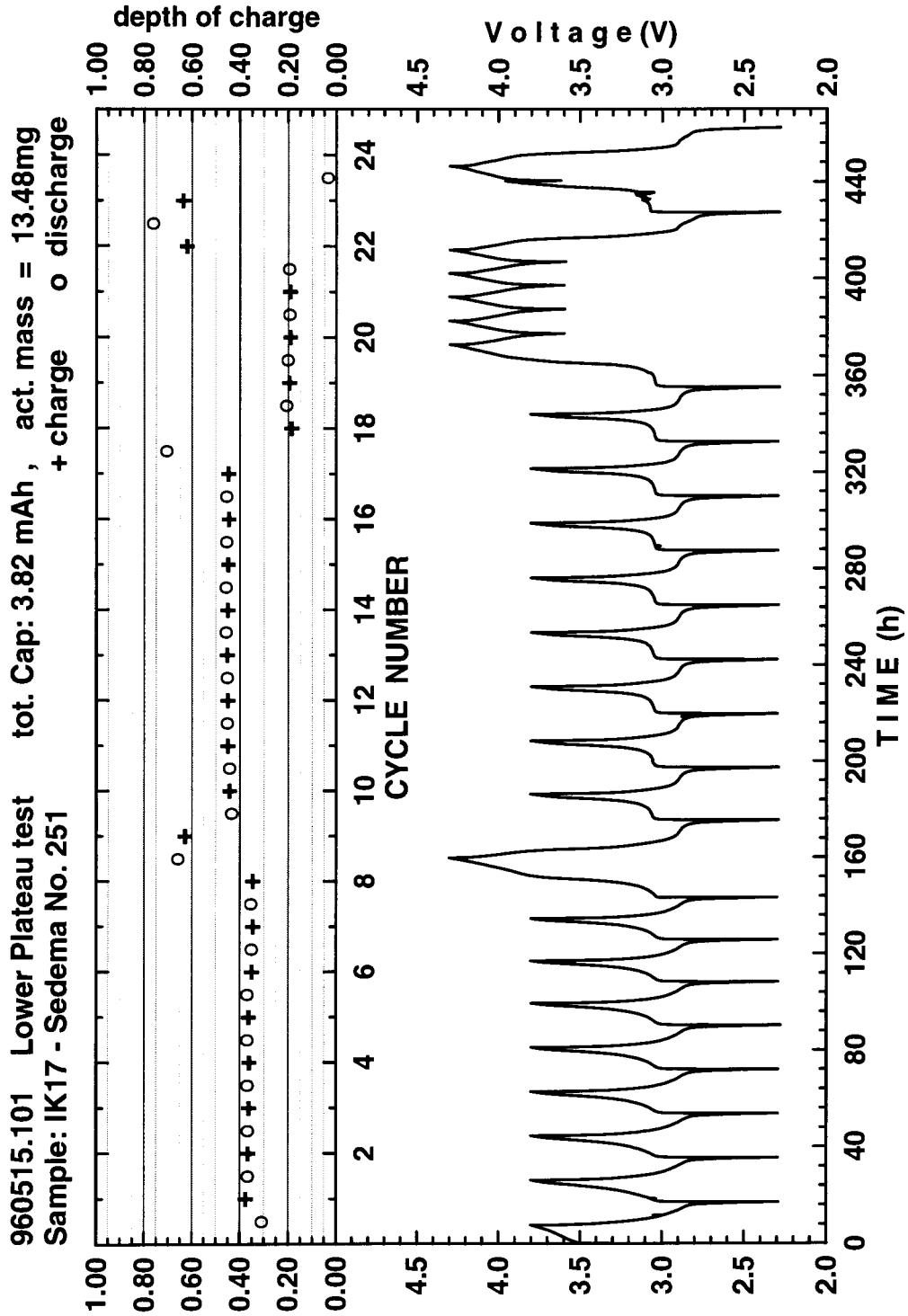

Figure 3.12: Voltage *vs.* time graph for a $Li/LiMnO_2$ cell restricted initially to the lower plateau taken June 1996. The depth of charge is displayed in the upper panel for each cycle.

3.3.3 'Cut off' - Voltage Test

So far we have confirmed in all the experiments that the $LiMnO_2$ structure is unstable and does not allow for any reversible insertion of Li in the host structure. The careful reader noticed however that we always started the cells on a charge cycle instead of discharge. From an empirical point of view it is legitimate to ask, whether it is possible to *insert* Li into the $LiMnO_2$ structure as found in a freshly made cathode. The open circuit voltage (OCV) of a freshly assembled test Li/$LiMnO_2$ cell was usually between 2.8 and 3.4 V depending upon how long the cell was shorted during assembly[10]. Since Li in lithium metal is still at a much higher potential, we expect to test for Li insertion into $LiMnO_2$ if we initially switch the cell on a discharge cycle.

I tried a number of experiments and found always a negative answer. No significant amounts of Li can be inserted on an initial discharge cycle into the $LiMnO_2$ structure. Confirmation is found in Figure 3.13 (a) where the cell reached a potential of 2.3 V within less than two hours. This is very little time compared to the C/25 rate current and amounts to an overall capacity below 10% of the theoretical maximum capacity of 285mAh/g. But Figures 3.13 and 3.14 and Figure 3.15 show more than the first two hours of a discharge experiment. In an attempt to identify the effect of varying the upper trip-point of the lower plateau experiment I set up this test series where the upper trip-point was increased by 0.1 V for each cell over the range from 3.2 to 3.9 V. For each trip-point setting the cell was cycled at least seven cycles on the lower plateau. Then a boost cycle was inserted to complete the conversion from orthorhombic to cubic spinel ordering. Subsequently the cell was switched back to the lower plateau with the particular upper trip-point. In all experiments we find confirmation for a conversion which allows subsequent insertion of lithium in the 3 V plateau. The amount of lithium which can be intercalated in the 3 V plateau depends of course on the upper trip-point voltage. The length of the remaining orthorhombic V-t characteristic on initial charge shrinks with increasing upper trip-point. This is most evident from Figure 3.13 (c) and Figures 3.14 (a) and (b) (upper trip-point 3.4 V to 3.6 V). For the latter figure we switched back to charge the cell initially since it was obvious that Li cannot be intercalated in the $LiMnO_2$ structure. If we compare the boost cycle for 3.8 V in Figure 3.15 (b) to subsequent cycles full charge/discharge cycles in Figure 3.4 (a), we find that most of the initial charge

[10]shorting cannot always be avoided if test cells have to be handled with metallic tweezers in a glove box.

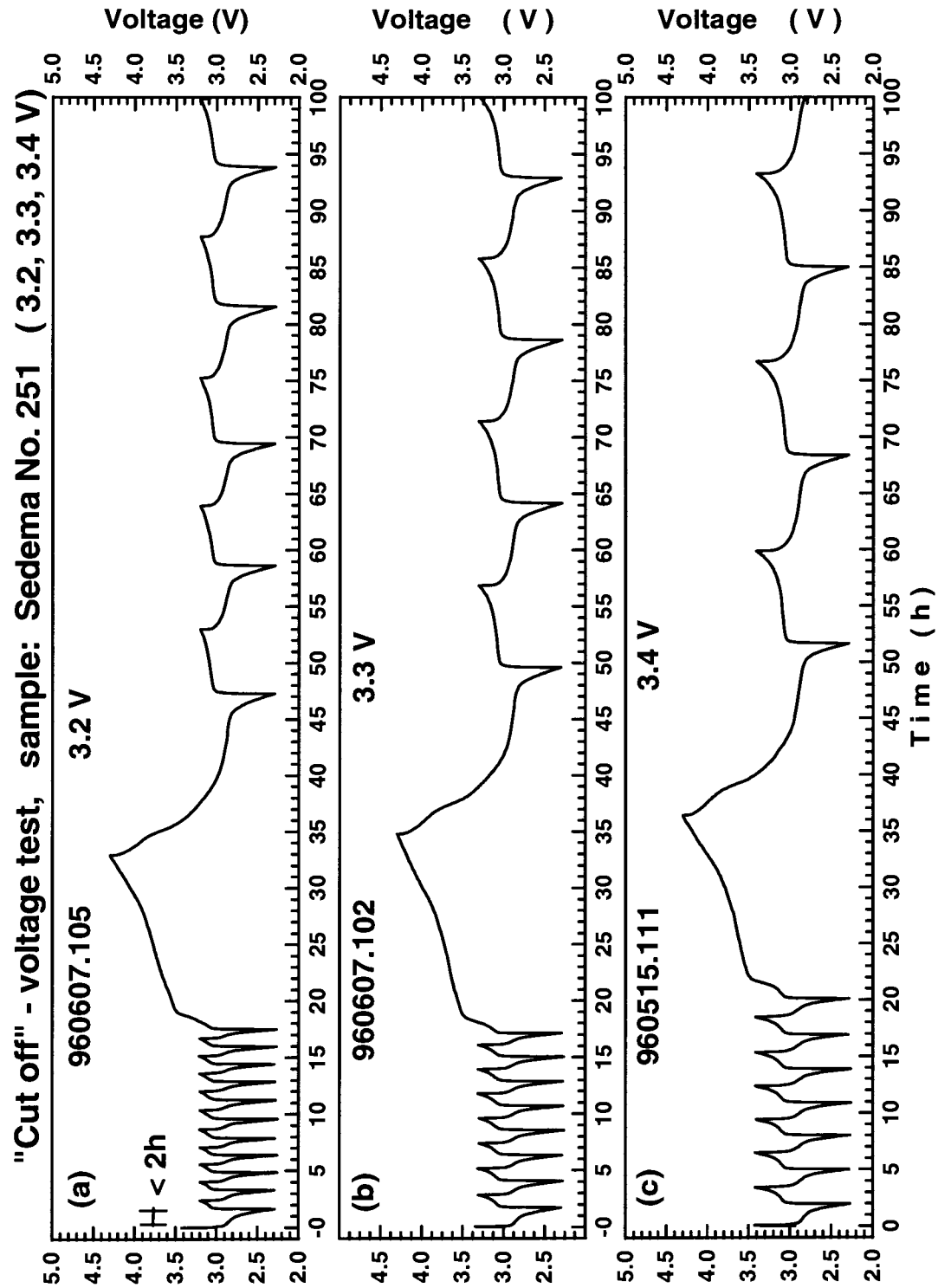

Figure 3.13: Voltage *vs.* time graphs of $Li/LiMnO_2$-cells with variable upper trip-point voltage ('cut off') at 3.2, 3.3 and 3.4 V.

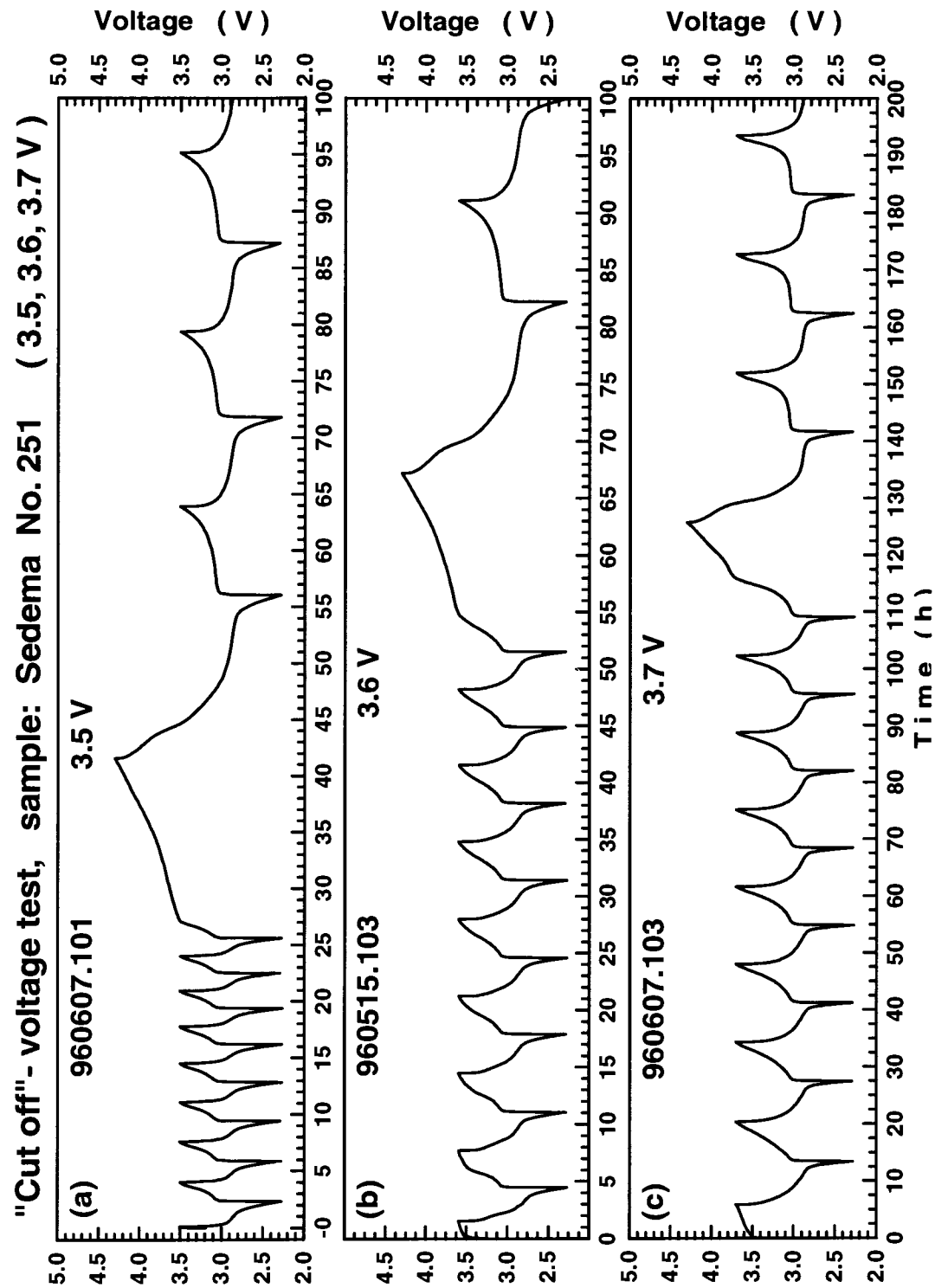

Figure 3.14: Voltage *vs.* time graphs of $Li/LiMnO_2$ cells with variable upper trip-point voltage ('cut off') at 3.5, 3.6 and 3.7 V.

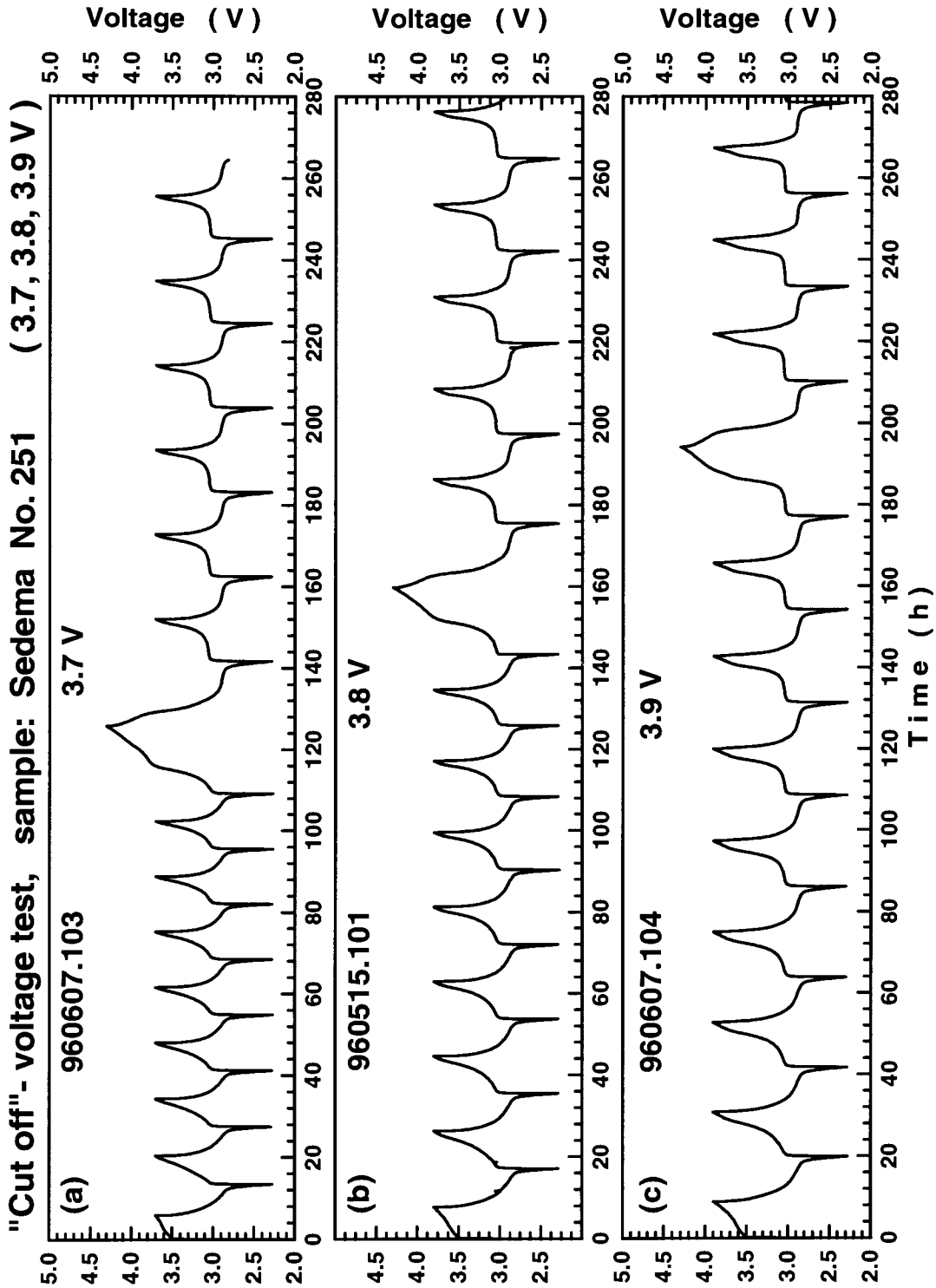

Figure 3.15: Voltage *vs.* time graphs of Li/$LiMnO_2$-cells with variable upper trip-point voltage ('cut off') at 3.7, 3.8 and 3.9 V.

characteristic of orthorhombic $LiMnO_2$ is gone. In Figure 3.15 (c) this is even more evident, which suggests that subsequent cycles up to a critical upper trip-point 3.9 V are enough to convert the *all* of the orthorhombic structure to cubic spinel if the cell is cycled indefinitely.

3.3.4 Summary

In the following I would like to summarize the most important results of this empirical study.

1. no reversible intercalation process for the orthorhombic $LiMnO_2$ phase was observed.

2. The electrochemical data confirm the suggested transformation from orthorhombic to the cubic spinel phase on initial charge of a $LiMnO_2$ cathode.

3. The more lithium is initially removed from the $LiMnO_2$ phase, the more complete is the conversion. In particular, capacity available on the 3 V plateau can be increased by inserting a single full charge/discharge cycle .

4. It is possible to cycle the cell similarly to a regular $Li_{(1-x)}Mn_2O_4$ cell ($0 \leq x \leq 1$) for many cycles without significant capacity fade. However, the available capacity is much less than the theoretical maximum capacity of 'pure' $LiMn_2O_4$ cathode material (149mAh/g).

5. There is a strong discrepancy between the charge and discharge capacities over the first four cycles. The charge capacity is always larger than the discharge capacity. However, the difference between charge and discharge capacity becomes smaller.

6. After an initial increase in (discharge) capacity over the first three cycles, strong capacity fade occurs when the cell is cycled continuously over both plateaus (3 V and 4 V). It seems that for many cycles the maximum capacity for a $Li_{(1-x)}Mn_2O_4$ system is approached.

7. The observed fade can be predominantly attributed to the shortening of the lower plateau.

8. The fade in capacity retention is less severe when the cell is cycled over the lower plateau only and initially approximately 140mAh/g are available in this potential range.

For the lower plateau experiments, we find that only the fraction of $LiMnO_2$ which was converted during initial charge, can be accessed for the discharge process occurring at a potential of 3 V where most likely the tetragonal phase and the cubic phase coexist. We propose that a single boost cycle will convert *residual* orthorhombic domains (in the core of the crystallites) which remained intact while cycling the battery over the 3 V plateau with an upper trip-point below 3.8 V into the cubic phase. Thus a boost cycle increases the available capacity in this *potential region*. We may also speculate that the capacity fade on the 3 V plateau will initially be obscured for the first 10 to 30 cycles. This may be due to the fact that each charge to the upper trip-point (3.8 V) will supply additional capacity for the tetragonal phase region up until all residual $LiMnO_2$ is used up ('reservoir' idea).

For the upper plateau experiments we do already allow for a full conversion of all $LiMnO_2$ to $LiMn_2O_4$ on the first two or three cycles, since we are always above the upper trip-point for the lower plateau (3.8 V). However we find also an increase in capacity for subsequent boost cycles, although smaller in magnitude. This increase cannot be attributed to a growth in the fraction of available $LiMn_2O_4$ structure. The experiment suggests that this increase must rather be attributed to a mechanism which is linked to the discharge and charge process in the 3 V region.

3.3.5 Conclusions

As the previous summary reveals there are many observations, but few definite answers. We may speculate about 'mechanisms' in the tetragonal/cubic two phase region, but so far we cannot really identify any such mechanism and it may also be possible that structural changes are caused when the cathode is fully charged (delithiated) at high voltages. Due to the speculative nature of our understanding we make a suggestion.

Knowledge of the structure at any instant of the charge/discharge process, would ideally allow the prediction of electrochemical data such as a voltage *vs.* capacity graph. Predictions of this kind, based on first principles calculations are rare and complicated. For $LiMnO_2$ we are not aware of any first principle calculations which

allows the prediction of electrochemical properties and comparison to experimental data. Setting such a calculation up is beyond the scope of a Master's thesis. However any real understanding of the electrochemical behavior is always based on knowledge of the structure involved for a given intercalation process.

At this point of the thesis project, we felt that only an experimental method which gives accurate information about the structure of the cathode material at different charge states could help to further our understanding of the observed intercalation processes during and after the initial charge of a $LiMnO_2$ cathode. An *in situ* experiment, where the battery is charged in quasi equilibrium conditions, can give conclusive evidence for the proposed structural transformations. Further, questions about the crystallinity of the particles in the cathode after the irreversible phase change cannot be answered without a method of structure analysis.

Reimers *et al.* did a X-ray *in situ* study on $LiMnO_2$ in 1993. As mentioned in the introduction, problems with the hermetic seal of the *in situ* battery and limited control options made this study not as detailed as would be required for an accurate analysis of the interesting processes in the tetragonal/cubic two phase region. The need for a more detailed study is evident.

In order to understand the the interpretation of the *in situ* experiments that followed this experimental study, we need to know all that can be potentially learned from powder X-ray diffraction patterns. In the following chapter the basic ideas relevant to our experiments are reviewed.

Chapter 4

Powder X-ray Diffraction

When X-ray radiation interacts with solid matter a large variety of phenomena are observed. This is to be expected since the energy of X-ray photons from Cu-K_α-radiation *is* of the order of the energy of an electron dipole transition from the L-shell to the K-shell (for a metal). If matter is bombarded by X-rays of this kind, the observed interactions range from fluorescence radiation to the emission of Auger electrons. A summary of the different kinds of phenomena is given in Figure 4.1.

In powder X-ray diffraction only the unmodified coherent portion of scattered radiation is considered for the purpose of structure determination on the basis of *Bragg's law*. In order to distinguish between elastically scattered radiation and any other form of primary or secondary X-ray radiation, a monochromator crystal filters the scattered radiation before it enters the detector.

In the following, the basis of powder X-ray diffraction, the Bragg law, is stated in vectorial form. This helps to introduce some necessary nomenclature. Next the calculation of peak intensities and integrated peak intensities will be discussed. In the last two sections, peak width and error sources are considered.

4.1 The Bragg Law

Two coordinate systems of complementary nature prove to be an effective means to describe crystal structures. Let (a_1, a_2, a_3) be the set of axes which span the smallest repeating unit in a crystal, the unit cell. A second set of axes, (b_1, b_2, b_3) can be defined by requiring

$$a_i \cdot b_j = \delta_{ij} \qquad i, j = 1, 2, 3 \qquad (4.1)$$

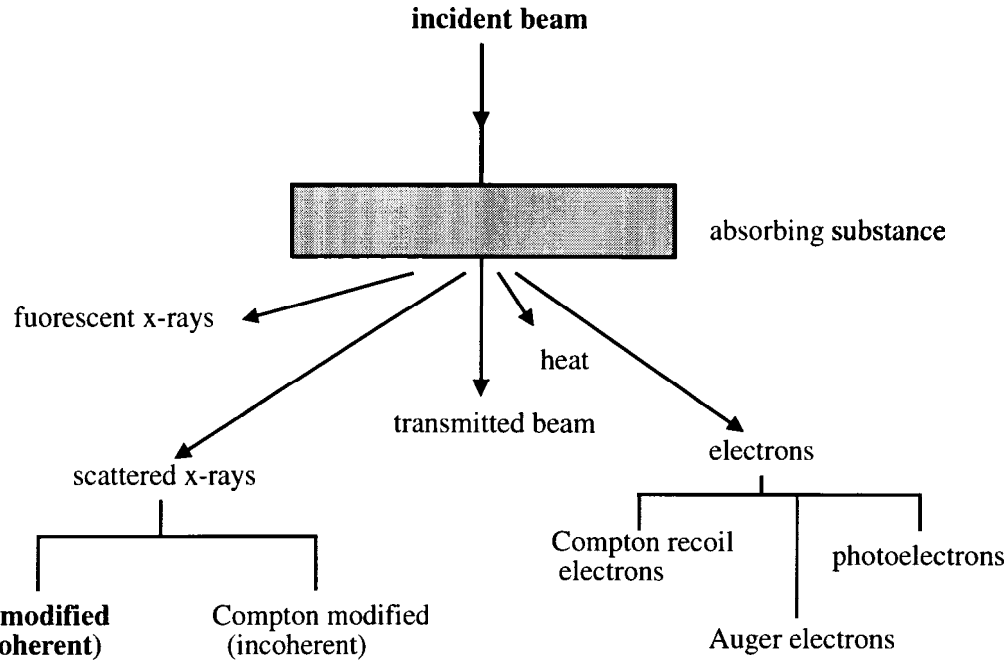

Figure 4.1: Effects of X-ray radiation passing through solid matter (i.e. a powder sample) after Henry *et al.* [43].

$$v_a = (a_1 \times a_2) \cdot a_3 \;\; = ((b_1 \times b_2) \cdot b_3)^{-1} = v_b \quad \textit{and cyclic.} \tag{4.2}$$

Here v_a and v_b are the volumes spanned by each set of coordinate axes. The set of points,

$$\{\; \vec{r}_n \mid \vec{r}_n = n_1 a_1 + n_2 a_2 + n_3 a_3 \;;\;\; n_i \in \mathbb{Z}_o \;\} \tag{4.3}$$

defines a regular infinite *lattice* in *real space*. A single unit cell in a crystal can be referenced uniquely to one lattice point. However, it is necessary to point out that a crystallite consists of a finite number of unit cells. The set of points,

$$\{\; \vec{H}_{hkl} \mid \vec{H}_{hkl} = hb_1 + kb_2 + lb_3 \;;\;\; h,k,l \in \mathbb{Z}_o \;\} \tag{4.4}$$

constitutes another regular lattice in *reciprocal space*. Any point in reciprocal space corresponds to a set of parallel planes in real space. The indices (h,k,l) are known as *Miller indices*. If (a_1,a_2,a_3) and (b_1,b_2,b_3) are defined as above then for a given element $\vec{H}_{hkl}$ of reciprocal space the distance d_{hkl} between two parallel planes is given as

$$|\vec{H}_{hkl}| = \frac{1}{d_{hkl}}. \tag{4.5}$$

By stating Bragg's law in vectorial form, the connection between the two spaces is easily established. Let $\vec{s}_0$ and $\vec{s}$ be unit vectors of the incoming and the scattered radiation on a crystal corresponding to the reflection of the *hkl*-planes. The situation is pictured in Figure 4.2. Then according to Bragg's law we have

$$\frac{\vec{s} - \vec{s}_0}{\lambda} = \vec{H}_{hkl} \quad , \tag{4.6}$$

where λ is the wavelength of the X-ray radiation. The direction $\vec{H}_{hkl}$ in reciprocal space is normal to the set of parallel (hkl) planes in real space.

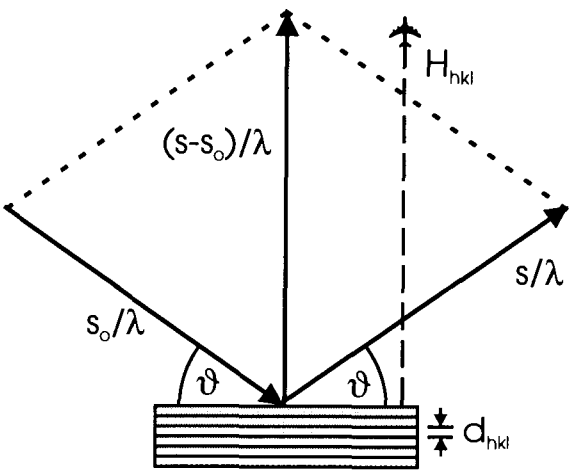

Figure 4.2: Geometrical relation for the vector representation of the Bragg law.

4.2 Calculation of Peak Intensities

Depending upon the position of atoms in the unit cell, varying intensity ratios will be found for different *hkl* reflections. The *relative intensity*[1] of a powder X-ray diffraction pattern is proportional to the product of

$$I_R = m_{hkl} \cdot |F_{hkl}|^2 \cdot \frac{1 + \cos^2 2\theta}{2} \cdot \frac{\cos\theta}{sin2\theta} \quad . \tag{4.7}$$

Here m_{hkl} denotes the *multiplicity* of the particular reflection. Since the crystallites are randomly oriented in the powder sample we have to count multiples of symmetry

[1] comparing different *hkl*-reflections of the same powder pattern

related planes of a particular reflection. The first trigonometric factor arises if we assume *unpolarized* X-ray radiation incident as a (quasi) plane wave on the powder sample. The second trigonometric factor is related to the particular geometry of powder X-ray diffraction. The factor F_{hkl} is known as the *structure factor* of a particular reflection. In crystal structures with more than one atom per unit cell, the coherent scattering of separate atoms will add to the amplitude at the detector. Depending on the spatial distribution, the relative phases of these contributions will be shifted with respect to each other. If the fractional coordinates (u_n, v_n, w_n) of the atoms in a unit cell are known, then we can write the structure factor as

$$F_{hkl} = \sum_{n=1}^{N} f_n e^{2\pi i(hu_n + kv_n + lw_n)} \tag{4.8}$$

where the sum is carried over all N atoms belonging to a single unit cell. Here, f_n is called the *atomic scattering factor* and arises for the same reason as the structure factor. The spatial distribution of electrons around the nucleus leads to dephasing of coherent scattering, when scattering is not exactly in the forward or the backward direction. Thus f_n is angle dependent, and for convenience it is normalized to the scattering strength of a single (localized) electron. The atomic scattering factor is therefore often stated as the ratio between scattering of all electrons of an atom[2] and the scattering of a single electron. In the same sense we can view the structure factor as the ratio between scattering of all electrons in a unit cell and a single electron [44]. Another useful concept is to regard the structure factor as the Fourier transform of the electron density in the unit cell.

Equation 4.7 is only valid for the case where Bragg's law is exactly satisfied. The intensity at angles close to the Bragg angle is however strongly varying. Practical measurements of powder diffraction patterns measure scattered radiation averaging over a finite solid angle. The size of this solid angle is determined by the width of the *receiving slit*, an aperture before the detector as indicated by '**R**' in Figure 4.3. Further, the data acquisition requires the measured intensities to be binned and the data bins are of the same width as the step size of the goniometer. It is therefore extremely difficult to measure the relative peak intensity directly, by setting the goniometer to the desired angle. Again, in practice the *integrated* intensity is measured for a particular reflection and corresponds to the finite area under the peak in a

[2]in an ionic solid, the corresponding ion.

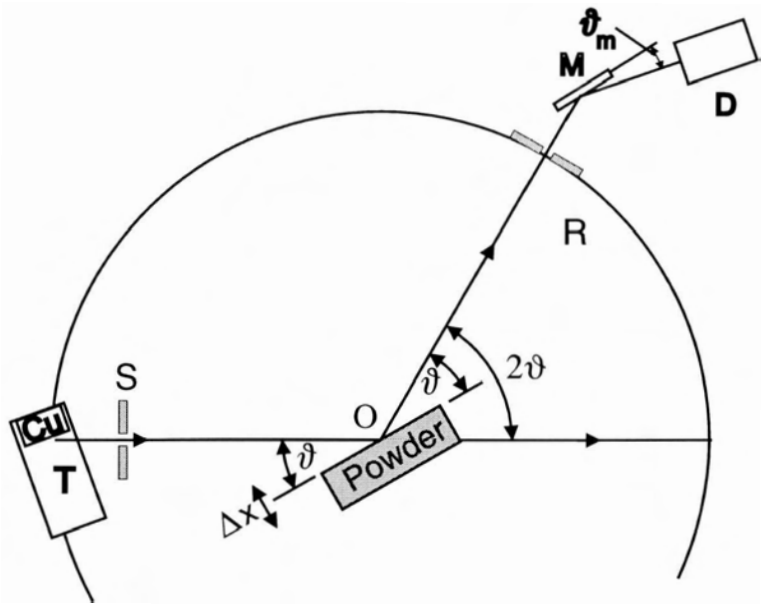

Figure 4.3: 2Θ geometry for powder X-ray diffraction. T = X-ray tube, S = source slit, R = receiving slit, D = detector, O = scattering center, M = graphite monochromator. A possible *off-axis* shift of the powder sample from the ideal scattering plane is indicated by Δx.

real diffraction pattern (see for example broad peaks in Figure 3.1). Roughly the integrated intensity corresponds to the maximum measured intensity times the half width at half maximum intensity.

In theory it is therefore of interest to predict the integrated intensity based on the knowledge of the positions of all atoms in a crystal. It is possible to integrate over the contributions of a single reflection if the scattering intensity is considered over a small interval up to and below the Bragg angle, see for example Warren [45]. The result is very similar to that found in Equation 4.7, and in theory only an additional factor of $(\sin 2\theta)^{-1}$ has to be included. This result can be rearranged as

$$I_R = m_{hkl} \cdot |F_{hkl}|^2 \cdot \frac{1 + \cos^2 2\theta}{\sin^2 \theta \cos \theta} \quad , \tag{4.9}$$

which is directly proportional to the peak intensity for a given *hkl*-reflection. The entire trigonometric factor is known as the *Lorentz polarization factor* (LP). In practice the LP factor has to be modified. In order to suppress undesired fluorescence background radiation, the outgoing X-rays are scattered off a graphite monochromator before they can reach the detector. If the monochromator is included as a

second scatterer whose incident radiation is partially polarized, then the numerator of Equation 4.9 will change to

$$1 + \cos^2 2\theta \cos^2 2\theta_m \quad , \tag{4.10}$$

where θ_m is the Bragg angle of the monochromator reflection[3].

4.2.1 Calculated Intensities for the Three Main Phases

Based on Equation 4.9, we calculated the intensity patterns for the three phases of lithium manganese oxide which where introduced in chapter 2. The results are shown in Figure 4.4.

The fractional coordinates for the individual atoms are listed in chapter 2 for each phase. Atomic form factors were taken from the *International Tables of Crystallography* [18]. The oxidation state of oxygen was fixed at -2, for manganese the oxidation state was fixed between $+3$ and $+4$, depending on the stoichiometry. Lithium was always treated as Li^+. For all calculations we used the wavelength of Cu-K_α radiation (1.54059 Å). These and the following calculated intensity patterns serve as a reference for the identification of the different phases in our in-situ studies which we describe later.

4.2.2 Li_2MnO_3 and Shift of Cubic Peak Positions

In chapter 2 we introduced only the most important structures which are observed in our *in situ* X-ray study as we show later. Another phase of lithium manganese oxide has not been mentioned yet: Li_2MnO_3. It is similar to the layered $LiCoO_2$ and $LiNiO_2$ stuctures [37]. Since all manganese atoms are in oxidation state IV, removal of Li^+ causes the oxididation of Mn^{4+} to Mn^{5+}. The extraction potential is also higher than 4 V, which is difficult to realize with electrolytes which decompose at potentials above 4.5 V. It is also not known whether deintercalation actually takes place, or whether other processes, like oxygen release, occur in parallel. We introduce its calculated intensity pattern here for later reference when we try to identify mechanisms for capacity loss in our $LiMnO_2$ batteries.

Although the Li_2MnO_3 unit cell is monoclinic it is difficult to distinguish from the cubic and tetragonal phases by considering the intensity patterns. Distinct peaks

[3]For the PW1730 (Philips) diffractometer, we have a graphite monochromator with $\theta_m = 13.3\ ^\circ$.

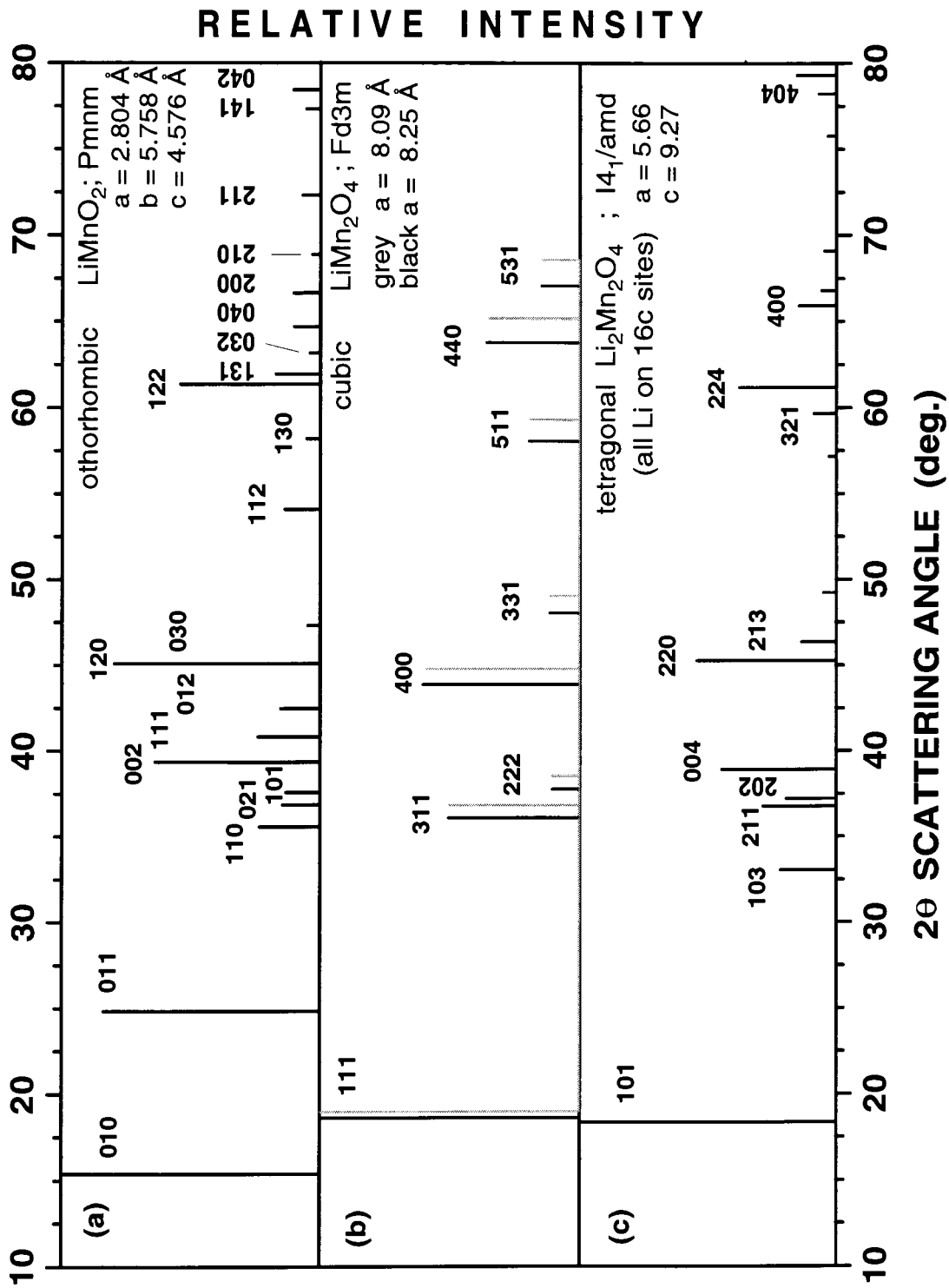

Figure 4.4: Calculated relative integrated intensities for three phases of lithium manganese oxides. The most prominent peaks are indexed to the corresponding unit cells.

are usually weak and the strong peaks coincide with the strong peaks positions of $LiMn_2O_4$ and $Li_2Mn_2O_4$ shown in Figure 4.5 (a), (b) and (c).

If Li is removed from the cubic phase, the cubic lattice contracts. Mosbah *et al.* reported lattice parameters as small as 8.029 Å for $Li_{(1-x)}Mn_2O_4$ with $x = 0.97$. This corresponds to a significant change in the position of the peaks of this phase and is probably only realized in very pure and highly crystalline phases to this extent. In our experiments we report cubic lattice parameters as small 8.10 Å, which is still a considerable change. We calculated the positions of a $LiMn_2O_4$ phase for a = 8.10 Å and included the intensity calculation of the original phase (a = 8.25 Å) for comparison in Figure 4.5 (b). The peak shift for the C111 amounts to 0.37 deg. and is much larger for the C440 peak with 1.41 degrees.

4.2.3 Peak Shifts from Tetragonal to Cubic Symmetry

In order to illustrate the effects of lattice contraction on the peak positions we calculated a series of intensity patterns for decreasing c/a ratio of the tetragonal phase. The result is shown in Figure 4.6. In (a) we plot the intensity pattern for the tetragonal phase as reported by Goodenough *et al.* [21] and include a calculation for slightly modified parameters a=5.71 Å, and c=9.00 Å. The directions of the peak shifts are indicated with arrows. In Figure 4.6 (b), (c) we display patterns for the same unit cell with decreasing c/a ratio. In (d) the ideal c/a ratio for a cubic unit cell is used ($\frac{c}{a} = \sqrt{2}$). As expected we find that separate reflections of the tetragonal phase merge into symmetry related reflections in the cubic phase (T220 and T004 into C400; T224 and T400 into C440 etc...). However the T101 and T211 peaks, equivalent to C111 and C222 in [Fd3m] notation, shift very little compared to all other tetragonal peaks. The dashed line in Figure 4.6 is included for easier comparison. In (f) we display a pattern of an extreme case for a 'reversed' c/a ratio. Compared to a cubic unit cell, the c axis is now shorter and the a axis longer compared to the ideal cubic parameter for $Li_1Mn_2O_4$.

If we consider the relative *intensities* in Figure 4.6 (d), we find good agreement to the pattern calculated for $LiMn_2O_4$ in Fd3m symmetry. The differences stem from Li^+ which are all placed on 16c.

Since we calculate the intensities assuming [$I4_1$/amd] symmetry we have to be careful with the inclusion of symmetry related positions. Although the change to higher [Fd3m] symmetry does not matter here, we employed for the more general case

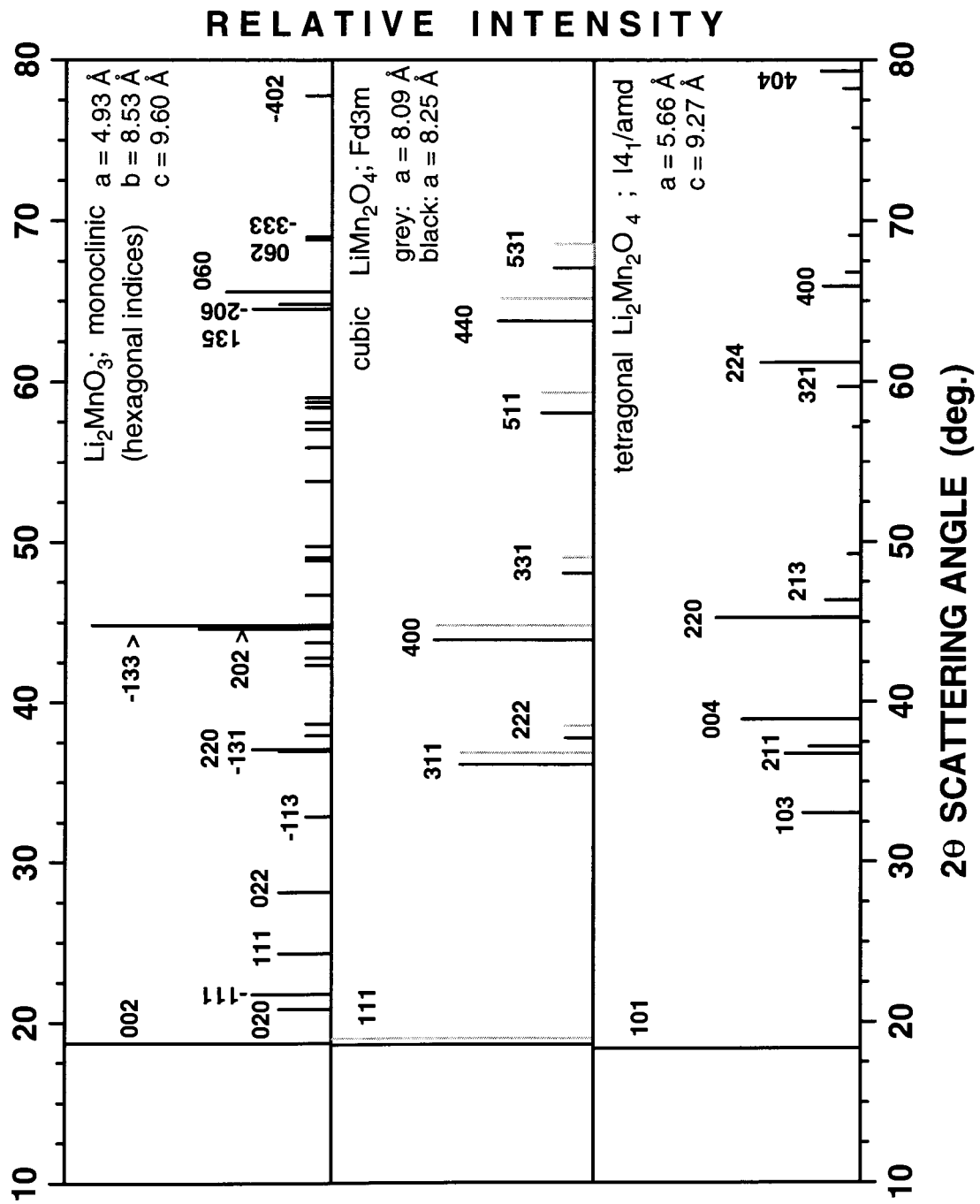

Figure 4.5: (a) calculated relative intensities for the Li_2MnO_3 phase. In (b) we calculated the $LiMn_2O_4$ phase with two lattice parameters to demonstrate the shift of the peak positions. The Li_2MnO_3 phase is difficult to distinguish from the cubic and tetragonal phases. Most of the distinct peaks are weak and the strong peaks coincide with the positions of the phases shown in (b) and (c).

a modified algorithm. Structure factors are calculated for all possible permutations of hkl-indices and symmetry related reflections are thus summed explicitly. This consideration is important if intensity patterns are calculated where the symmetry in the unit cell is broken by fractional occupation of symmetry related sites.

We do not imply by these calculations that tetragonal phases with these c/a ratios are physically realized or found. The significance of these patterns is to help interpret some puzzling results which are presented later in chapter 7.

4.2.4 Absorption and Finite Temperature

Two effects have not been accounted for. Any powder sample will absorb scattered radiation. The deeper the scatterer is below the surface of the powder sample the stronger the absorption[4] of scattered radiation. An exact treatment shows however, that absorption does not affect the relative intensities for peaks at different angles. This is only correct if the sample is large and thick enough, so that the X-ray-beam is always focussed on the sample[5].

We have also not taken into account the effects of finite temperature. So far we assumed that all atoms or ions are fixed at their exact positions on the crystal. However, at finite temperature, the ions and atoms will oscillate around their equilibrium positions. Assuming a random model where the displacement, u, of an ion from its ideal (=equilibrium) position follows a Gaussian distribution, it can be shown that the intensity of a reflection is decreased for peaks at higher diffraction angles. The net contribution to Equation 4.9 is a single exponential factor

$$e^{-2M} \qquad M = B\sin^2\theta/\lambda^2 \qquad B = \frac{8\pi}{3} < u^2 > \ , \tag{4.11}$$

is often referred to as *Debye-Waller temperature factor*. The mean square displacement B is generally not trivial to calculate from first principles. The second effect of finite temperature is to increase background radiation. In most cases the intensity of the background radiation progresses linearly with diffraction angle. It is counter intuitive that finite temperature has no effect on the half-width of a diffraction peak as the above result suggests. In the following section we will ask the question what influences the width of a diffraction peak.

[4]Here we address only the absorption of the sample. Absorption due to beryllium is addressed elsewhere.

[5]and not on the holder or anything else.

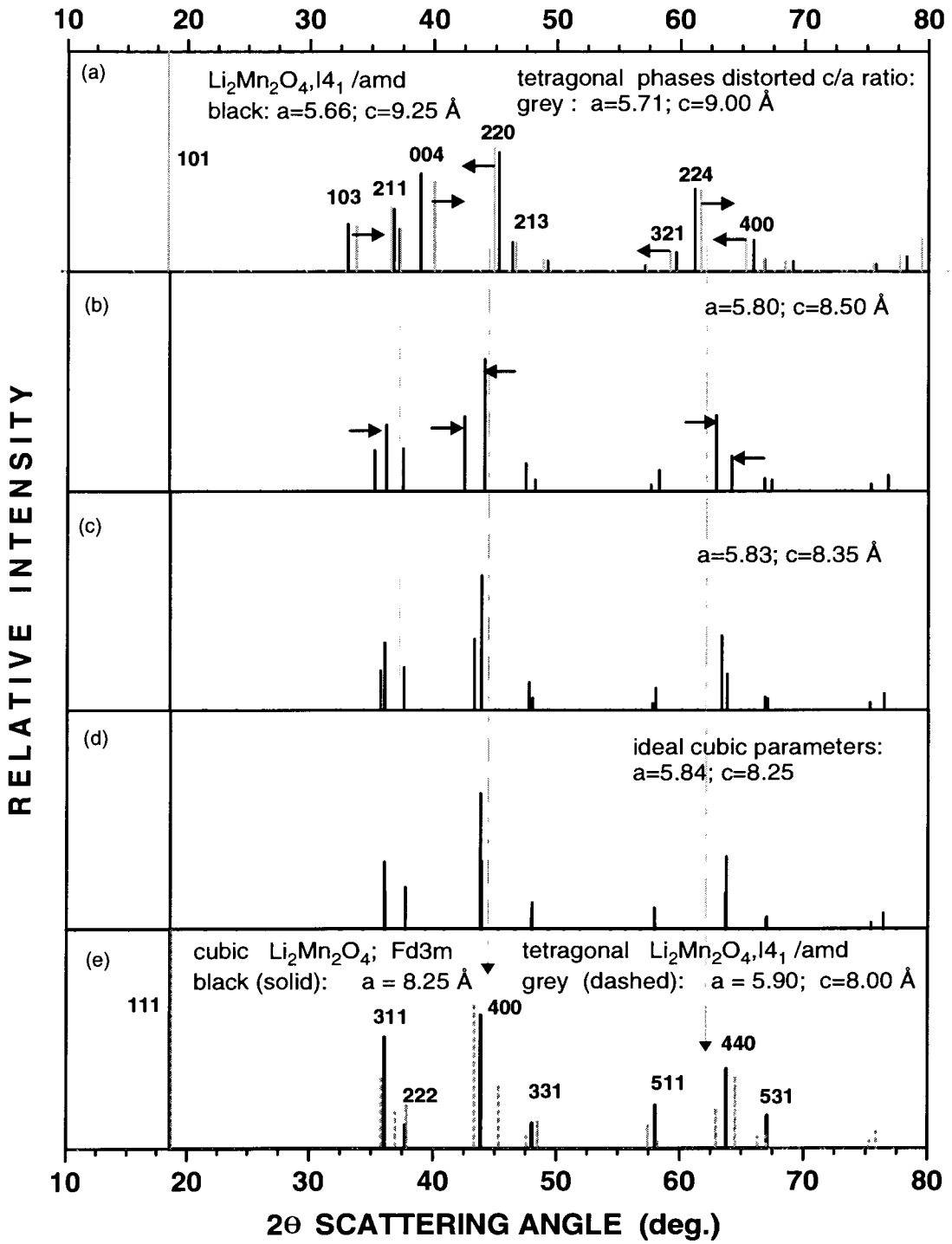

Figure 4.6: In order to illustrate the effects of lattice contraction on the peak positions we calculated a series of intensity patterns for decreasing c/a ratio of the tetragonal phase. of Cu-$K_\alpha$radiation (1.54059 Å).

4.3 The Width of a Peak

In Figure 4.7 (a) we consider the scattering of X-rays from a finite domain of n layers of parallel hkl planes. Scattering from atoms in subsequent planes lined up along the plane normal, have a phase difference of 2π if the Bragg condition for the hkl reflection is exactly satisfied. A small difference in scattering angle $\Delta\theta$ will introduce an additional phase difference for ions in neighboring planes.

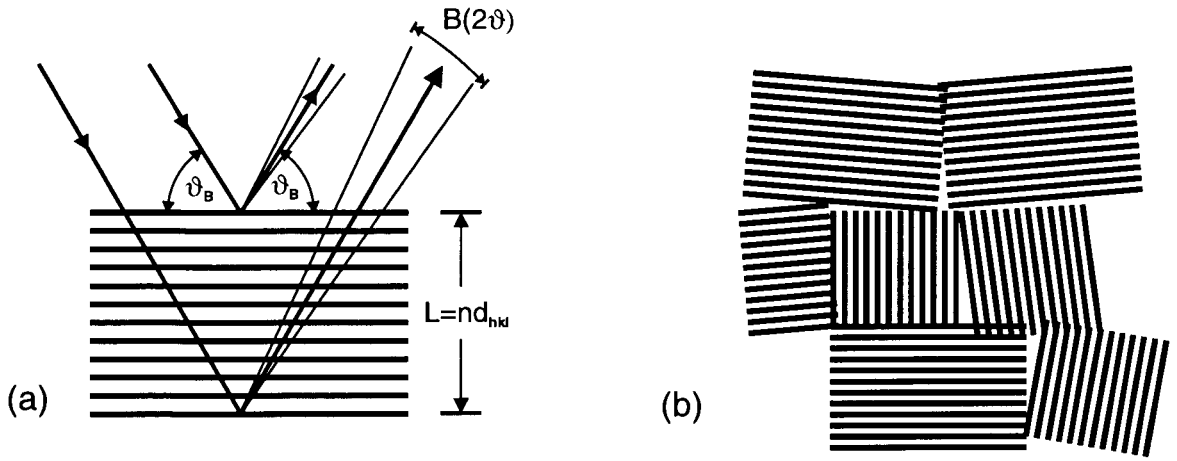

Figure 4.7: A finite number of n parallel hkl planes in a crystal (a) has length $L = nd_{hkl}$ along the plane normal. The intensity of a reflection is therefore still appreciable for a range of scattering angles $B(2\Delta\theta)$ around the Bragg angle of the reflection. Tiny blocks (b) of imperfectly aligned crystallites are found in a single grain of a powder sample.

If the incoming and the outgoing radiation[6] subtends the same (but arbitrary) angle with the refection plane, then scattering from any two atoms of this plane is always in phase. Hence for fixed $\Delta\theta$, the *number* of scatterers lined up along the plane normal will determine whether pairs of destructively interfering rays can be found. Since the number of scattering planes is always finite in a real crystallite, we can always find a smallest range $\Delta\theta$ where the scattered radiation is not entirely cancelled due to destructive interference. Conversely if the width $B(2\Delta\theta)$ of a peak at half maximum is known, one can infer the number of coherent scatterers along the H_{hkl} direction. This idea is used to estimate the size of crystallites in a powder

[6]If the radiation is approximated by a plane waves.

sample. The result is the well known Scherrer Equation

$$B(2\Delta\theta) = \frac{K_s \lambda}{L \cdot \cos\theta_B} \quad , \tag{4.12}$$

where $L = nd_{hkl}$ is the size of the crystal domain and K_s is an additional correction factor. The width $B(2\Delta\theta)$ is measured at half maximum in radians. This simple result needs some qualifying remarks.

1. An exact treatment according to Scherrer is based on the assumption that the crystallites are of cubic symmetry. There, an additional factor $K_s = 0.89$ is applied to the right hand side of Equation 4.12, which reflects to some degree the shape of the crystallites[7].

2. The estimation of the physical size of crystallites is not necessarily the same as the estimation of the grain size of a powder sample. This is illustrated in Figure 4.7 (b), where a grain is built up a number of imperfectly aligned ideal crystal domains.

3. Since L corresponds to a physical dimension normal to the diffraction planes, we will refer to this parameter as the 'length of coherent scattering normal to the (hkl) plane (which is equivalent to the $< hkl >$ direction), regardless of the grain size. In later parts of this thesis we will refer to this parameter as *domain size*, for brevity.

There exists another derivation for the calculation of peak width due to Stokes and Wilson [46]. The resulting equation is the same as Equation 4.12, but is independent of the shape of the unit cell. Moreover, the result is independent of the distribution in size and shape of the crystals making up the powder sample [45]. Since there are no other effects than corrections for *instrumental broadening*, we believe that the peak width is a good parameter for the estimation of the volume average (entire sample), of the length of coherent scattering normal to the reflecting planes. In particular, the relative comparison of widths of one and the same peak in two different XRD patterns should be valid, as long as the crystal structure itself has not significantly changed. We will make extensive use of these ideas in chapter 7. In order to demonstrate the usefulness for our powder samples we refer to the XRD patterns shown in Figure 3.1

[7] a two dimensional array of scatterers which is in plane with the incoming and outgoing radiation is corrected by a factor $K_s = 1.84$, (Warren 1990, [45]).

where the average peak width can be estimated to be of the order of 0.1 deg. Below in Table 4.1 we list some values for the Scherrer equation assuming a plane spacing of 1 Å for a reflection at $\theta_B = 45$ deg. using Cu-K_α radiation.

$L = nd_{hkl}$	B(2Θ) (deg.)	Number of planes n
1 mm	1.12×10^{-5}	10000000
1 μm	1.12×10^{-2}	10000
1 nm	$1.12\times10^{+1}$	10
$\lambda = 1.5409$ Å ; $\Theta_B = 45$ deg. ; $d_{hkl} = 1$ Å		

Table 4.1: Relation between length of coherent scattering normal to the scattering planes and peak width, calculated by using the Scherrer equation.

4.4 Errors

We need to address a number of error sources which are of significance if real data is compared with calculations.

So far we have assumed that all scatterers lie in the ideal scattering plane. If the sample has a macroscopic thickness (1-5mm), as illustrated in Figure 4.3, scattering can occur below the ideal scattering plane. This will affect the positions of the recorded peaks. However, our samples contain manganese which has nominally 25 electrons. Over macroscopic distances lithium manganese oxide will act as an effective absorber and the detector records scattered radiation from a very thin layer at the top of the powder sample. This holds even for the case when the powder is compressed to a thickness of 125μm as in a typical $LiMnO_2$ electrode, described in chapter 3, so that reflections from the aluminum substrate are not expected.

More serious is the case when the entire powder sample or the electrode is shifted off axis by an amount of Δx as shown in Figure 4.3. The correction for the peak positions depends on the diffractometer and is given by

$$\Delta\theta = \frac{\Delta x \cos\theta_B}{R} \quad , \tag{4.13}$$

where R is radius of the diffractometer circle and $\Delta\theta$ is the correction in radians, which has to be added to the observed scattering angle, θ_B.

There is also an effect due to the imperfect focusing on a flat-faced specimen. The irradiated area on the sample is angle dependent. This is also referred to as the *footprint* of the beam on the sample. We will address this issue in chapter 6 where it applies directly to our experiments.

Another source of errors affecting the intensities of the peaks is due to a *preferred orientation* of grains in a powder sample. Electron micrographs of $LiMnO_2$ show that the powder grains have no particular texture. A preferred orientation in the powder sample is therefore not expected. However, in the case of a compacted electrode, crystallites could be aligned along a preferred face. In that case it is actually necessary to confirm by experiment that preferred orientation is negligible. We have not corrected for this effect, since we do not rely so much on the ratios of the relative intensities in our analysis. However the agreement between observed and calculated intensities for pure powder XRD patterns was satisfactory for our needs.

These are all the important sample and method specific error sources. There are of course a number of error sources which are apparatus and detector specific. We will also address these where it is appropriate.

Chapter 5

In Situ XRD Measurement Setup

This chapter deals with the technology which we developed to carry out *in situ* X-ray measurements on $LiMnO_2$ powder cathodes. Two problems were central during the development phase. At first is was necessary to improve the seal of *in situ* cells. Second it was necessary to centralize the control for charging or discharging the *in situ* cell and for switching of the X-ray diffractometer. Some questions regarding absorption of X-rays in an *in situ* cell need also to be addressed.

5.1 *In Situ* Cell Design

In chapter 3, we discussed briefly the assembly of test cells used in the electrochemical characterization of $LiMnO_2$ as a cathode material. In order to study the structural properties of $LiMnO_2$ during specific electrochemical manipulations it is necessary to find a way to simultaneously place the cathode in a diffractometer. We require that the interference of the casing of such a cell on the XRD profile is minimal and we require that the casing houses the cathode constitutes an electrochemical environment which is very similar to the environment found in the electrochemical test cells. An early design which meets such a task was described by Jeff Dahn [13]. In Figure 5.1 we display an exploded view of the electrochemical cell. In this design, the bottom of the electrode stack is at the same time the holder which is mounted in the diffractometer. A cell top machined out of brass is screwed down on bottom with nylon screws in order to ensure insulation. Between the two parts, the beryllium window, coated on one side with the cathode material, is inserted together with the gasket, separator and lithium metal anode. This *in situ* cell design proved suitable for many shorter

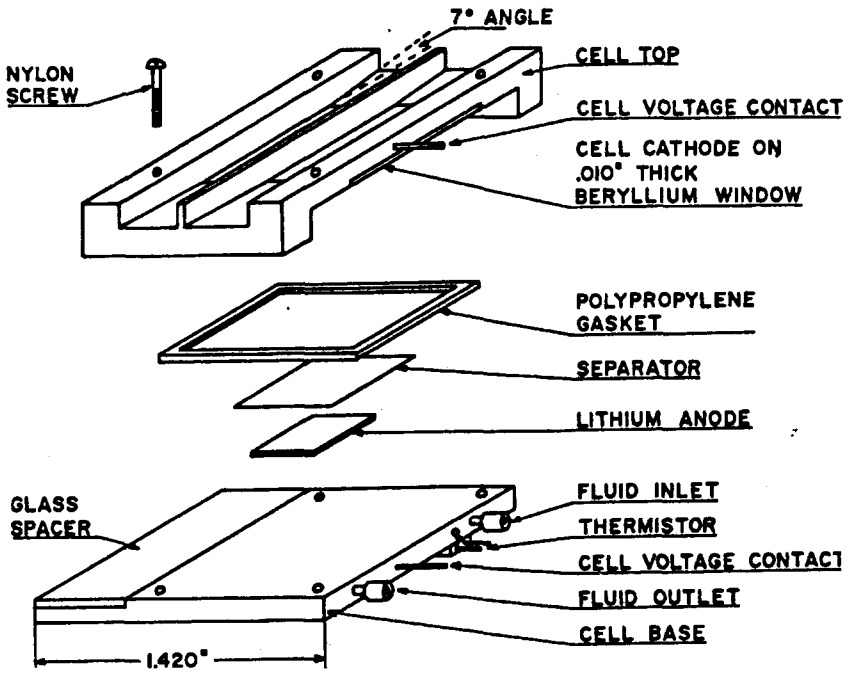

Figure 5.1: Exploded view of *in situ* cell design used in studies prior to this thesis. The electrodes are arranged in reverse stacking order.

in situ X-ray studies and was used up until recently in our lab, see for example Wu Li [14] or Tao Zheng [15].

However, as soon as one tries to study structural changes under quasi equilibrium conditions, the time span over which the the *in situ* cell has to be intact exceeds easily two weeks. An inherent problem with the design is the vacuum integrity of the cells. The brittleness of beryllium and the use of nylon screws set limits to the degree these cells could be sealed using a polypropylene gasket. Although in some cases it was possible to continue experiments for many months without problems with the seal, as reported by Tao Zheng, the vacuum integrity was difficult to reproduce consistently with the existing design. Another problem is the fact that the metals used in the casing were not the same as in coin cells and that this constitutes a different electrochemical environment compared to the electrochemical test cells. Side reactions, particularly at high voltages, may occur which over the course of a long-term experiment are highly

undesired.

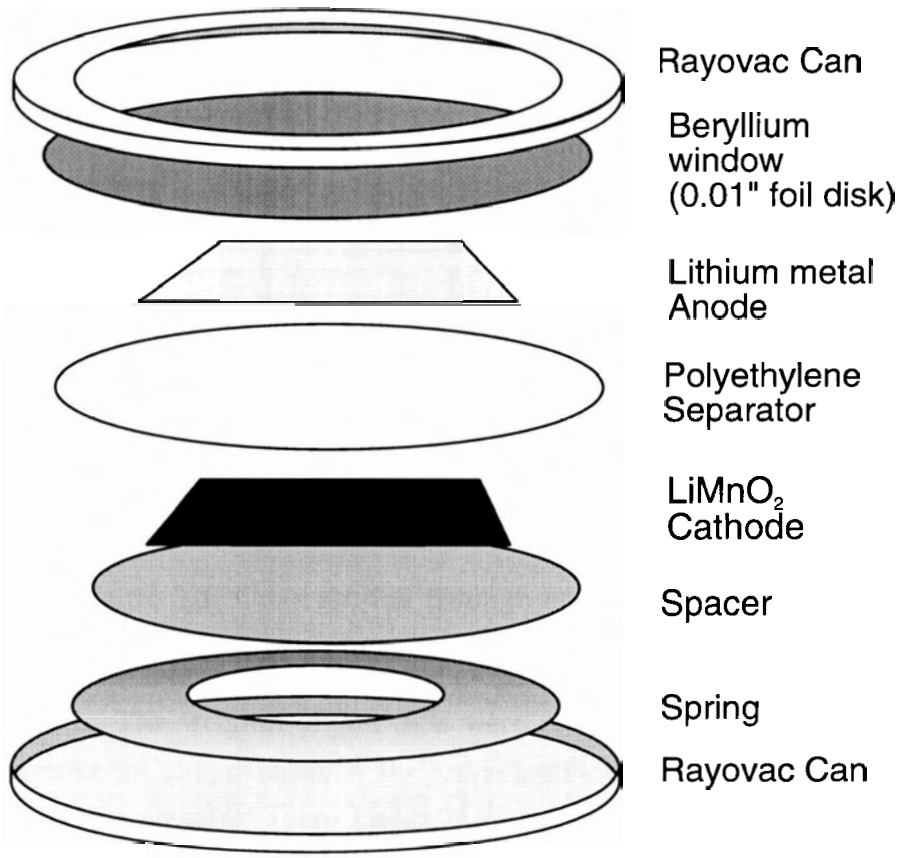

Figure 5.2: Exploded view of an *in situ* cell in regular stacking order.

These problems stimulated us to improve the existing design. The result is shown in Figure 5.2. In order to keep the electrochemical environment the same we simply tried to modify the coin cell hardware (2325, Rayovac) used for the electrochemical experiments. Plain steel cannot be used for the entire top casing, since X-ray radiation would suffer strong attenuation and the 'inside' of such a battery cell would not be 'visible'. The use of beryllium as a window is therefore paramount. The solution is to cut a hole into the cell top, to insert a 2.16 cm diameter beryllium window (Brush Wellman Electrofusion Products, Fremont CA 94538, material grade PF-60, Ø2.16 cm and 0.25 mm thickness) and to use the conventional method to crimp top and bottom together in order to prevent air from leaking into the cell. The order of the remaining components of the electrode stack is shown in Figure 5.2. What is not shown in this figure is the gasket, which is attached to the bottom can and provides a seal by pressing to the inside of the beryllium window and the inner edge of the

steel rim on the cell top. We included therefore a cross-sectional drawing of an *in situ* X-ray cell in Figure 5.3, where the sealing technique can be better understood.

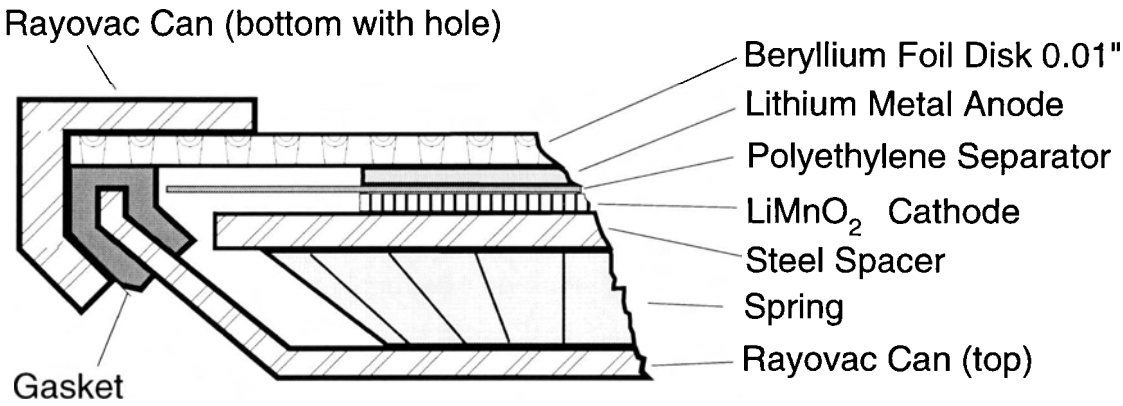

Figure 5.3: Cross section through an *in situ* X-ray cell.

These cells were fabricated in the same glove box where the conventional test cells were assembled. The weights of the cells were recorded and in order to test their vacuum integrity we placed them in the ante-chamber of a second glove-box and let the pressure drop below 10^{-2} Torr. The cells where considered 'short term leak-tight', if no visible traces of electrolyte were found on the outside of the cells after 12 hours exposure to low pressure. Subsequently the cells were left under ambient conditions and their weights were recorded roughly every two weeks.

A number of trials were necessary to find a suitable sealant after we found that most of the *in situ* cells showed traces of electrolyte leakage after the low pressure test. The sealant has to be electrochemically inert and must be removable for subsequent recycling of beryllium windows. Silicone vacuum grease (Dow Corning) was the first choice. However the long-term vacuum integrity was still intermittent as can be discerned from Table 5.1 (Batches 1 and 2) below, where we display the results of three studies for different sealants. Finally we found that using Roscobond, a water soluble pressure sensitive adhesive (Rosco, Port Chester, NY 10573), gave satisfactory results (Batch 3). In order to avoid the edge of a separator being caught between gasket and beryllium window, it was also necessary to reduce the size of the separator.

The astute reader may have noticed that we used *Rayovac* coin cell hardware (No. 2325) instead of the hardware supplied by Moli Energy for the assembly of *in situ* cells. The reason for this choice was that the rim of a Rayovac can is slightly higher

Test	number of cells	Δ days	Ø loss [mg]	± stdev. [mg]	min [mg]	max [mg]	% loss percent	sealant
1	4	46	30.9	± 17.7	4.3	41.4	≤ 62	Vac. grease
2	4	42	15.0	± 18.2	1.3	40.7	≤ 30	Vac. grease§
3	6	80	3.4	± 2.3	≤ 0.1	6.9	≤ 7	Roscobond§

§ used small separators.

Table 5.1: Weight loss study for X-ray *in situ* cells for various sealing techniques. The average weight loss is complemented by the minimum and maximum loss observed in the batch of test cells. The percentage loss is calculated by assuming that each cell contained no less than 60 mg of electrolyte.

compared to the hardware supplied by Moli Energy (No. 2320). This is desirable since we included an additional layer in the electrode stack by inserting a beryllium foil disk of 0.25 mm (0.01") thickness. Using the old hardware would have increased the *stack pressure* exerted by the spring and might have caused breaking of the beryllium window during the crimping process. The Rayovac 2325 cell hardware was chosen to avoid this problem and the force on the electrode stack remains at approx. 200 N as in a regular test cell. The steel used for the 2325 cell hardware is almost identical to the material used for 2320 cell hardware so we expect the electrochemical properties to be very similar.

In order to test the equivalence of the electrochemical environment we compared the cycling behavior of two selected $LiMnO_2$ cathodes *vs.* lithium metal anodes. The resulting voltage profiles for the first six cycles are shown in Figure 5.4. The new cell design does not adversely affect the electrochemical behavior of the $LiMnO_2$ material.

Finally we need to address the *stacking order* of the *in situ* cell shown in Figure 5.2. As shown, the lithium electrode is placed below the beryllium window and X-rays scattered from the electrode have to traverse three layers twice: beryllium, lithium metal and separator. This stacking sequence, which we will refer to as *regular stacking*, seems rather awkward since we expect strong attenuation of the scattered radiation. The reverse configuration, referred to as *reverse stacking*, where the cathode is mounted directly below the beryllium window would result in much higher intensities and less interference from other phases in the path of scattered X-rays.

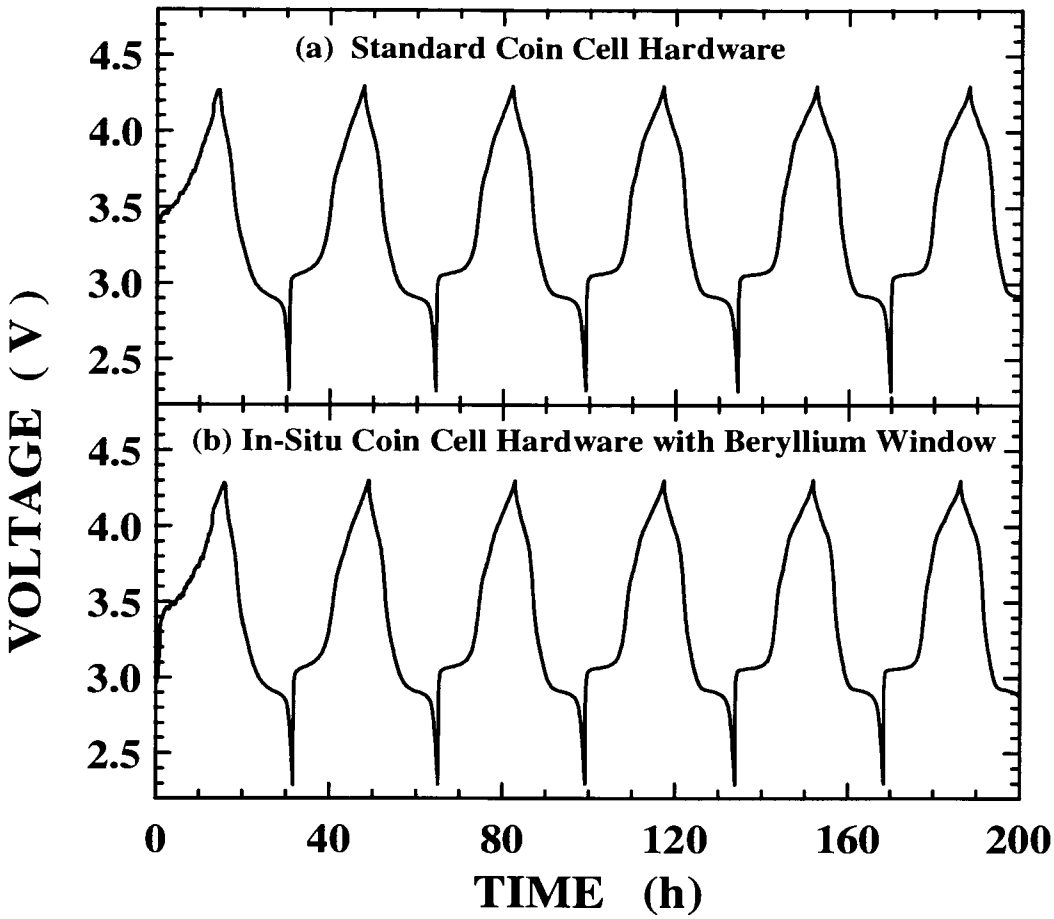

Figure 5.4: Comparison plot of electrochemical behavior of $LiMnO_2$ in regular coin cell hardware and *in situ* coin cell hardware. The cells were cycled at a 25 h rate.

There are two problems which do not permit reverse stacking for $LiMnO_2$ cathodes. The first is that beryllium dissolves in the electrolyte at voltages above 3 V and this constitutes a secondary side reaction which falsifies the measured currents. Moreover, the electrochemical environment is altered irreversibly. The second difficulty is that compacted powder cathodes on the substrate are very brittle. As a consequence the $LiMnO_2$ cathode coating has to be either deposited directly on the beryllium window, or a different way has to be invented in order to obtain a cathode 'film' which is not too brittle and can be cut and handled like the lithium metal anode.

Plastic Electrodes

Both problems have been addressed by Monique Richard *et al.* [47] using a novel technique involving plastic film electrodes based on a patent from Bellcore Corporation [48]. $LiMnO_2$ powder[1] is mixed with a polymer (Kynar Flex 2801, VdF-HFP, Atochem) and the usual 'ingredients' (see chapter 3) plus EC/PC (ethylene carbonate/propylene carbonate) to obtain flexible films from slurries after the solvent (Acetone) has evaporated. The EC/PC can be removed by soaking the electrode in ether, leaving pores behind in which the electrolyte will later move. A separator made with the same polymer is fabricated in a similar way. The major advantage of porous polymer electrodes and separators is that *all* the electrolyte needed in the cell, will be contained in the separator and plastic electrode itself. In this way it is possible to build cells in reverse stacking order, discussed in detail in reference [47], which allow charge to voltages above 3 V. An exploded view of an *in situ* X-ray cell based on Bellcore plastic electrode is found Monique Richard's M.Sc. Thesis [49]. The technology is very promising and it has been demonstrated that structural information from the powder cathode can be obtained without much interference from other phases. We will come back to this shortly in chapter 6. However in this thesis we still used the old way to make electrodes as described in chapter 3, since the plastic electrode technique was still in a developmental stage at the time I fabricated the *in situ* cells studied in here.

Cell Holder

Compared to the old *in situ* cell design, the cell is no longer directly attached to a holder. A series of special holders were designed and machined for mounting X-ray *in situ* cells of the new design onto the different X-ray diffractometers. The holder used exclusively in this study was designed for the Philips PW1730 with a Philips goniometer and is shown in Figure 5.5.[2]

[1] any powdered compound can be used.

[2] The drawing was done using the program 'AutoCAD' © [50].

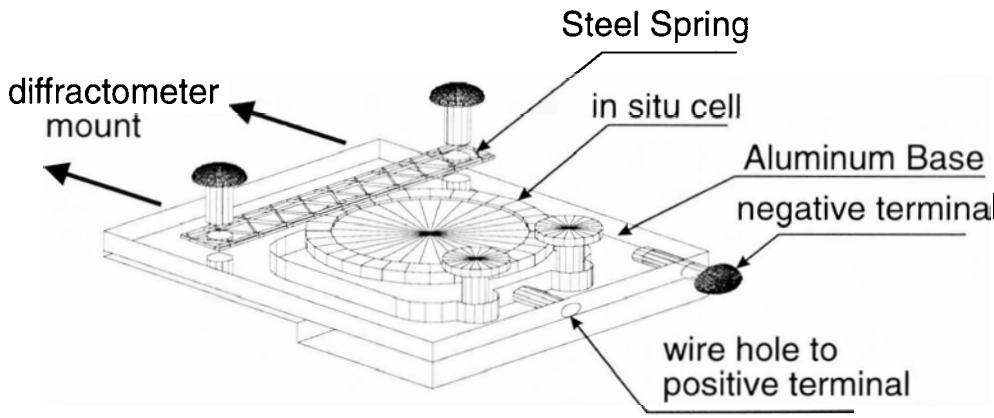

Figure 5.5: Technical drawing of *in situ* cell holder for PW1730. A 0.1" plastic piece insulates the bottom of the coincell from the aluminum base (not shown in figure).

5.2 Absorption

The issue of X-ray absorption and attenuation needs definitely to be addressed in a technique where X-ray spectra are acquired through a beryllium window. In view of the geometry of 2θ scattering setup, we need to consider that scattering from crystallites in the powder cathode has to traverse two times the same path through a slab of absorbing material. The path length is angle dependent, particular at glancing incidence, and therefore we expect large variations in the attenuation of the detected scattered radiation. Adopting a linear absorption coefficient for the fractional decease in intensity, then the transmitted intensity through a slab of uniform material is given as (Cullity, [44])

$$I_x = I_o e^{(-\mu/\rho)\rho x} \ . \tag{5.1}$$

The traversed distance is x, and μ/ρ is the *mass absorption coefficient*, listed for the all elements in the *'International tables of Crystallography'* [18]. The coefficient ρ denotes the actual density of the absorbing substance. Keeping the density separate from the mass absorption coefficient allows one to calculate μ/ρ for a substance containing more than one element. If the weight fractions w_1, w_2, etc. of the elements 1, 2, etc. and their respective mass absorption coefficients are known then

$$\frac{\mu}{\rho} = w_1 \left(\frac{\mu}{\rho}\right)_1 + w_2 \left(\frac{\mu}{\rho}\right)_2 + \ldots \tag{5.2}$$

denotes the mass absorption coeffient of the substance.

Based on Equation 5.1 we estimated the absorption of the X-ray beam in an *in situ* X-ray cell in regular stacking order. The beam has to traverse the beryllium window, the lithium anode and the separator twice before any radiation scattered from the cathode can be detected. Since the mass absorption coefficient of beryllium is twice that of lithium for Cu-K_α radiation and that of polyethylene (separator, nC_2H_2) is twice that of beryllium, we approximated the absorbing stack by a single beryllium layer of 0.5 mm thickness[3] and used its mass absorption coefficient (1.007 cm^2/g). Using Equation 5.2 for the $LiMnO_2$ stoichiometry and the *tapped* powder density of 0.66 g/cm^3 for the compacted[4] cathode we obtain $\mu/\rho = 161.4\ cm^2/g$, which is much larger compared to beryllium. This is not surprising since the cathode contains manganese which is a strong absorber. Since the absorption in $LiMnO_2$ is quite strong, we did not include it as an absorbing layer of fixed thickness. Instead we calculated the *penetration depth* of an X-ray beam at given angle for which the scattered beam intensity dropped by a factor of e^{-4} compared to the incoming beam at the surface of the cathode. This corresponds to an attenuation of 98 % and larger. The results are listed in Table 5.2. The table reveals that even though the cathode is only 125 μm

2θ (deg.)	peaks	depth† Δx (μm)	path§ L (mm)	$e^{(\mu/\rho)\rho L}$
15	O010	22.9	7.66	0.24
30		48.4	3.86	0.49
45	O120	71.5	2.61	0.62
60	O122	93.5	2.00	0.69
75	O211	114	1.64	0.74
90		132	1.41	0.77
† penetration depth; § path in the absorbing stack (Be/Li/Sep)				

Table 5.2: Penetration depth of X-ray radiation in $LiMnO_2$ for various angles of the incoming X-rays. The attenuation of X-rays on the path into the and out of the cell is also calculated for the same angular positions.

in thickness, hardly any scattering will reach the detector from the layers *below* the cathode. This is an advantage for cells in both stacking orders. However, considering

[3]Foil disk: 250 μm ; lithium anode: 125 μm ; separator: $\leq$ 10 μm .

[4]If the cathode is compacted the density is *larger* and hence the absorption also greater.

the rather small penetration depth at low angles, we find that if the stacking order is reversed (cathode at Be-window), we sample effectively only the upper half of the cathode at angles below 30 degrees. Since diffusion and concentration gradients play a significant role, intercalation processes at the Be-surface of the cathode can differ from processes at close to the cathode/separator interface. Consequently we have to keep in mind that peaks at low angles and peaks at high angles do not sample the same material of the cathode. In particular, we gather significant radiation from the cathode-separator interface, only at higher angles. This problem does not arise for cells with normal stacking. There we have, however, more peaks and stronger background due to the separator and lithium anode.

The attenuation due to the path in the layers above the cathode is also quite large at low angles. Peaks at angles higher than 50 deg. should therefore appear much stronger than in the calculated pattern. The intensity ratio between O122 and O010 can deviate by a factor of 0.36 according to our estimates. This is a lower limit for cells in normal stacking order. For cells in reverse stacking we only need to include the beryllium window and obtain a factor of 0.53 for the change in intensity ratio of the two peaks.

Attenuation of X-rays passing through a small $LiMnO_2$ powder grain is negligible. From the penetration depth calculation for $LiMnO_2$ it is evident that X-rays completely penetrate the powder grains in the cathode. Over the length scale of a typical grain (1 μm) the attenuation of X-rays is less than 1 %.

Due to the finite size thickness of the steel rim (0.254 mm) of the coin cell, there is a lowest angle, for which X-ray radiation will not reach the cathode any more. Taking the crossectional Figure 5.3 drawing of an *in situ* X-ray cell into account we find by a conservative approximation that peaks below 10 deg. (2θ) are generally not detectable. That means that peaks like O010, at 15.5 deg. fall well in the detection range.

5.3 The Data Acquisition Circuit

The schematic diagram of the data acquisition circuit is displayed in Figure 5.6. Four distinct units are shown each of which I would like to address separately.

Computer and Source-Measure Unit

In the upper left corner is the central computer control unit ('PC-386') which is connected to the X-ray equipment and to a remotely controlled precision *Source-Measure Unit* from Keithley Instruments (Keithley 236). The computer is a running custom-made software interface named 'CH236' (Charger for Keithley K236). The source-measure unit (SM-unit) is used as a current source either in potentiostatic or galvanostatic mode and is connected to the PC via a standard *IEEE* interface cable. The computer is equipped with an appropriate interface card and the program encodes control sequences which automatically switch the instrument in the desired mode.

In the potentiostatic mode we fix the potential at the terminals and record the current. There are of course limits, and the unit allows programming these limits. There is also a *compliance value* for the current. This will be the maximum value for the current and the terminal voltage will deviate from the programmed value if the necessary current is beyond this compliance value in order to adjust the mismatch. Conversely the galvanostatic mode allows the currents to be fixed at a constant value and the voltage is recorded within the programmed compliance limits. If necessary, the unit will adjust the current if the compliance for the potential is reached. Taking measurements is done by an interrupt request issued by the computer. Each time the computer polls the instrument, only a single measurement is recorded, either current or voltage.

Diffractometer and Detector

The grey shaded elements in the upper right corner symbolize the X-ray diffractometer in the 2θ geometry which was described earlier in chapter 4. The generator running the X-ray tube is a Philips PW1730 and the goniometer is from the same manufacturer. The X-ray tube is a standard water-cooled Copper line source with four beam ports of which two are equipped with goniometers. The goniometers are high precision mechanical instruments both equipped with a stepper motor. In little box ('D') on the upper right half circle is a standard scintillation detector amplified by a photo-multiplier tube. Not shown in the graph is the *discriminator*, the electronic circuit which filters the photo-multiplier signal appropriately. I will not describe the signal processing here, details can be found in Cullity [44] for example. In the diffraction plane we have the *in situ* X-ray cell which is connected to the source measure unit.

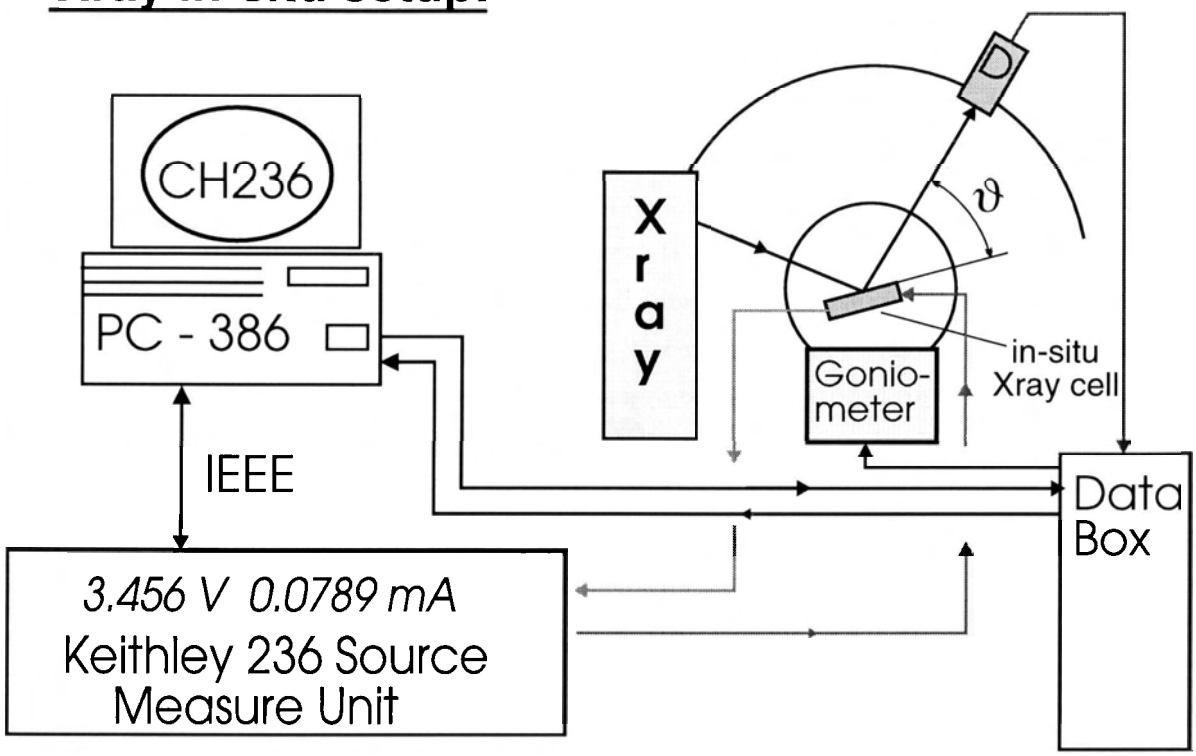

Figure 5.6: Schematic diagram of X-ray *in situ* setup. The computer program 'CH236' controls simultaneously charge and discharge of the battery and the timing and settings for the acquisition of XRD profiles.

'Data Box' and 'TALK'

In the lower right corner we find the fourth unit, a temporary storage device called *Data Box*. The 'Data Box' itself is equipped with enough memory to record the maximum number of steps which can be acquired in a single XRD profile scan. Beyond storing counts, it is equipped with a serial computer interface and a couple of electronic switches to signal to the stepper motor.

'TALK' is the standard software used for single XRD profile acquisition and was developed in the late eighties by Radix Corporation specifically for the 'Data Box' applications. The interface is kept simple and communication between the 'Data Box' and the PC is established via a serial connection sending standard ASCII sequences.

Operation of 'TALK'

The 'TALK' software allows the user to program up to 32 independent *sequences* encoding each initial and final angle, step size and count time per step ('channel'). The operator programs the desired sequences and at the beginning of a scan all the information is uploaded to 'Data Box'. Next the goniometer is reset to the starting angle of the first programmed sequence and once the data acquisition is running all counting events are temporarily stored in the 'Data Box'. After all programmed sequences are measured, data can be downloaded and stored in the PC in a new 'TALK' session. A typical XRD scan usually extends over a few hours, for example measuring a XRD profile from 10 to 90 deg. with 0.05 deg step size and 10 s counting time per step, takes 4 hours and 24 minutes. Having the PC not preoccupied with data collection is made possible by storing data in the 'Data Box'.

In order to acquire a whole series of sequential XRD profiles of the same type, 'TALK' has an option which allows the user to run batch files . By this it is possible to continuously measure XRD profiles[5], while an *in situ* X-ray cell is being electrochemically manipulated. The correlation between charge state and scan number has to be done manually by keeping accurate records and frequent checking of the battery and X-ray control units.

Different Modes of Operating *In Situ* X-ray Equipment

The above method was used in the *in situ* X-ray experiment on $LiMnO_2$ carried out by Jan Reimers *et al.* in 1993, using the early *in situ* cell design on the PW1730 diffractometer. Due to problems with the seal, the currents were adjusted[6] so that one full cycle was completed after five days. Since the Bragg scattering from *in situ* cells is rather weak, long scan times of about 10 h each are necessary. The number of XRD scans was therefore limited to about 12 per full charge/discharge cycle and as a consequence the resolution into which voltage range a particular scan falls was low.

Our goal was to increase the number of scans in order to get a more accurate picture of the crystal transformations, particularly in the two phase region at 3 V. With a leak-tight battery this can in principle be accomplished by charging and discharging the battery at a very low rate. For example, at a 400 h rate one can expect to obtain

[5] all stored in separate data files.

[6] and kept fixed afterwards.

40 XRD profiles which yield sufficient resolution for the given cell voltage range.

This way of operating the *in situ* X-ray equipment is called the *continuous charge* mode since the battery is continuously charged or discharged and not really in thermodynamic equilibrium. There are, however, different ways of operating the *in situ* X-ray equipment conceivable, which are more suitable for the study of phase transitions: In *step scan* mode, one switches the SM-unit in potentiostatic mode and increments the voltage by small amounts (10-100 mV) while recording the changing current. The battery will eventually settle into equilibrium and at this point of time we want to take an XRD profile. Once the scan is complete the voltage is incremented by the next (possibly different) step.

In Situ X-ray experiments can take up to eight weeks and during most of this time one is simply waiting until equilibrium conditions are met at the battery terminals. In an attempt to make the X-ray diffractometer accessible to other users, it should be possible to remove the *in situ* cell temporarily from the diffractometer and keep it at a constant potential in equilibrium. The voltage must be continuously monitored and any deviations from equilibrium have to be recorded. However, in order to avoid peak shifts due to errors introduced by different mounting positions, it is more desirable to keep the battery mounted and not to move it.

We saw that there is a trade off between scan time and charge rate. If one knows which peaks in the XRD profile are of particular interest, one could program an XRD scan which is restricted to the angular ranges in which these peaks occur. Hence the time for a scan of these particular peaks can be as little as 1 h but still as accurate as the 10 h scan over the full 2θ range between 10 and 90 deg.. This is particularly useful if one tries to follow a phase transition and to check that one does not miss any intermediate phase changes during faster charge and discharge operations. The mode where we continuously charge (or discharge) and scan over a restricted range is abbreviated by 'CDS-mode' (**C**harge or **D**ischarge and **S**can continuously).

Problems with Independent 'TALK' Operation

The major drawback of 'TALK' is that one has either the choice between controlling the XRD machine for each scan manually or that one acquires continuously XRD profiles of the same kind. In the former, the experimenter has to be present most of the time for switching the X-ray equipment based on the charge discharge state of the battery. In the latter, one has to hope that one can manipulate the charge and

discharge of the battery such that XRD profiles at the desired trip-points are taken. In both cases the experimenter basically switches two devices independently and must keep record of the time of recording of each scan. It is also difficult to respond quickly to emergency situations like a power failure. Restarting the whole X-ray batch mode operation is very tedious and requires meticulous record keeping since the interruption of batch mode operations with 'TALK' will require programming the schedule for the following XRD profile scans.

Another problem which arises in long-term studies is the failure of the water cooling system for the X-ray tube. This can occur any time if the water pressure falls below a minimum threshold[7] and will cause the generator to shut down, while the X-ray counting electronic is still running, recording zero counts for each channel.

The conclusion of the analysis is that although measurements are not impossible, the existing 'TALK' software is not convenient for long-term *in situ* X-ray studies. In particular if one embarks on a long-term research program one is always interested to improve the experimental conditions.

Combined Control System

Rather than having two computers controlling independently the battery charger and the X-ray machine respectively it was highly desirable to have one single control computer which gives the experimenter full flexibility in determining the course of *in situ* X-ray data acquisition. The requirements for such a system are the following:

1. Switching of the charge-discharge unit and continuous monitoring of battery potential and charge or discharge current.

2. Switching of the 'Data Box' for specific acquisition of XRD profiles. The program must allow the user to access the data after each scan.

3. Maintaining a continuous record for voltage, current and XRD scan information as a function of time. Keeping a record reflecting any changes in the control protocol.

4. Allow quick response in emergency situations: halting of the charge/discharge process, in order to have time for fixing the problem. Restarting the system

[7]which happens if the water filter clogs up due to unexpected repairs in the SFU water pipe system ...

after a power failure should be a routine operation.

5. Graphical support for viewing data at any time, without any prior data manipulation and graph preparation, while the control program is running,

6. and along with this, options for flexible response for changing the course of the charge/discharge protocol.

The program 'CH236' was developed by the author to meet these specific demands. It was long and tedious but nevertheless an extremely useful learning experience. In writing the code, many problems in interface programming had to be solved and without techniques of structured modular programming the task would have never been successfully completed. I will not describe the program structure in any further detail in this thesis. At this point I would like to show an example of a typical *in situ* X-ray mmeasurement which could only be conducted using the new software.

5.4 Example of an *In Situ* X-ray Experiment

Figure 5.7 is a printout of a test protocol, generated by CH236 for a many cycle *in situ* X-ray experiment which I called *'Doberman'* for easier and quicker reference[8]. In Figure 5.8 we display the voltage *vs.* time, current *vs.* time and XRD status *vs.* time which was obtained by following the programming in the protocol. It is the second cycle of a twenty cycle experiment and all the cycles are shown in Figure 5.9. In order to conclude this rather technical chapter, I would like to go through the test protocol step by step and explain a number of details:

Header

In the top section we find information for data storage and control parameters for the electrochemical data acquisition,

- `Xray Data` : the format and name of the numbered XRD profile data files,
- `CTRL FILE` : file used to store this control protocol,

[8]Naming experiments will save a lot of awkward formulations...

CH236 TEST-PROTOCOLL 10:30:24

TEST TITLE : 0701-144 Doberman Last Revision: 08-05-1996

XRay Data : X144p(scannumber).RAW
CTRL FILE : DOBERMAN.236
DATA FILE : 144-1.DAT
Vsteps : 0.0200 V
Isteps : 0.500 *f*A
Failsafe : 0.2500 V
Timeout : 900 sec

SQ	MODE	DIR	SOURCE	LOWER	UPPER	CY	LO%	File.XSR	TIME
1	MVOT	C	0.00 nA	0.000 V	9.999 V	0	-----	--------	0.10
2	MVOS	C	0.00 nA	-9.999 V	9.999 V	0	-----	10-90s12	05:49
3	CD	C	+170.55 *f*A	2.300 V	4.300 V	0	-----	--------	-----
4	CD	C	+ 85.26 *f*A	2.300 V	4.310 V	0	-----	--------	-----
5	HS	-	4.305 V	Compl: *q*	341.10 *f*A	0	7.50	four12s	02:10
6	CD	D	-170.55 *f*A	4.000 V	4.300 V	0	-----	--------	-----
7	CD	D	-341.11 *f*A	3.100 V	4.300 V	0	-----	--------	-----
8	CD	D	-170.55 *f*A	3.020 V	4.300 V	0	-----	--------	-----
9	CD	D	- 85.26 *f*A	2.995 V	4.000 V	0	-----	--------	-----
10	HS	-	3.000 V	Compl: *q*	341.10 *f*A	0	5.00	two12s	03:45
11	CD	D	-170.55 *f*A	2.850 V	4.300 V	0	-----	--------	-----
12	CD	D	-341.10 *f*A	2.310 V	4.300 V	0	-----	--------	-----
13	CD	D	- 85.26 *f*A	2.295 V	4.300 V	0	-----	--------	-----
14	HS	-	2.300 V	Compl: *q*	341.10 *f*A	0	7.50	four12s	02:10
15	CYCL	-	----------	--------	-------	3	50.00	--------	-----
16	UNDF	-	----------	--------	-------	0	-----	--------	-----

XSR - FILES

XSR-File	Reg	Init - Final	Step	Count	Scan Time	HKL - Remarks
10-90s12 :	1	10.00 - 90.00	0.05	12.0	05:42:56	--- --- ---
four12s :	1	24.20 - 26.70	0.05	12.0	00:10:43	--- --- ---
	3	35.00 - 47.50	0.05	12.0	00:53:35	--- --- ---
	5	60.00 - 67.50	0.05	12.0	00:32:09	--- --- ---
	7	75.50 - 81.50	0.05	12.0	00:25:43	--- --- ---
two12s :	2	23.00 - 47.50	0.05	12.0	01:45:01	--- --- ---
	4	55.00 - 81.50	0.05	12.0	01:53:36	--- --- ---

CH236 end of Records.

DATE/TIME: C O M M E N T S saved Data Files

10:20:00 Start for Doberman: O.K.

Figure 5.7: Test protocol displaying the charge/discharge programming for the many cycle *in situ* test 'Doberman', generated with the program 'CH236' ('Compl: q 341.10 fA' should read 'Compl: $\pm$ 341.10 μA').

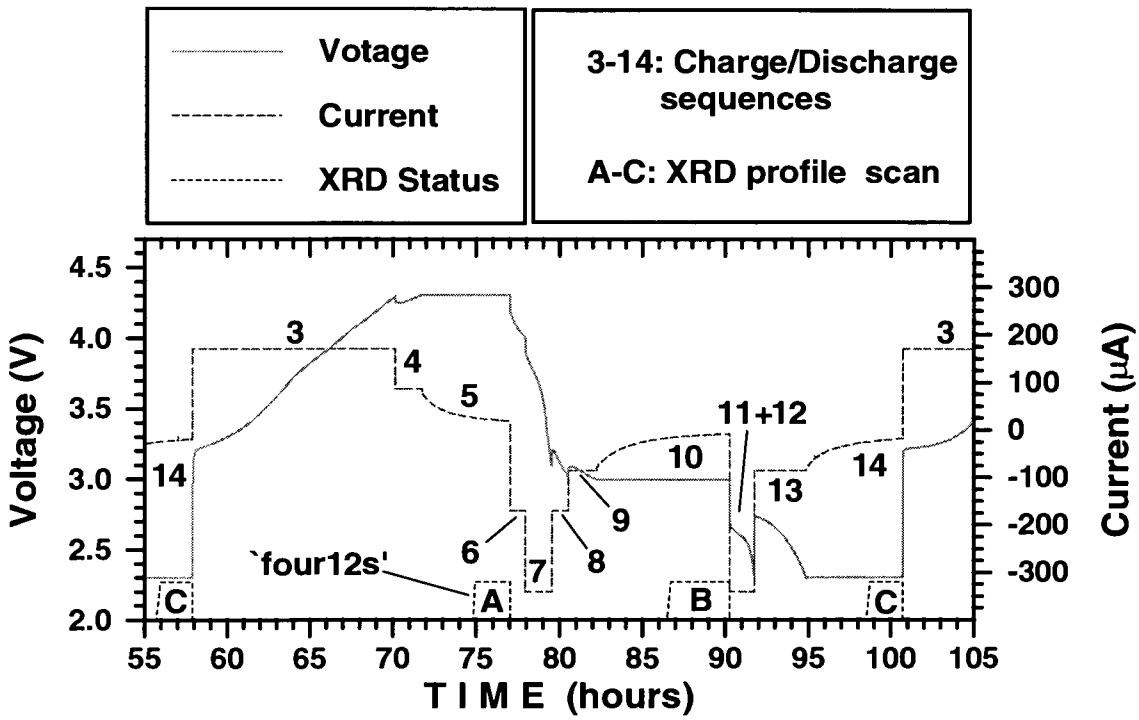

Figure 5.8: Cycle 2 of Voltage *vs.* time, current *vs.* time and XRD profile acquisition *vs.* time for *in situ* test 'Doberman'.

- `DATA FILE` : name of the data file containing voltage, current, time and XRD status information; it also writes comments for when the course of the experiment was altered,
- `Vsteps, Isteps:` the precision increment for data recording in galvanostatic and potentiostatic mode respectively,
- `Failsafe:` voltage bracket for recording errors in constant current mode; not always activated,
- `Timeout:` time after which the program forces the recording of data if no change larger than the precision increments occurred during this time span.

Sequences 1-16

- `1 MVOT:` Measure the voltage only and wait for a given time, 0.1 h in this case.
- `2 MVOS:` Measure voltage only and take an XRD profile according to the modalities stored in the 'XSR-File' `10-9012s.xsr`.

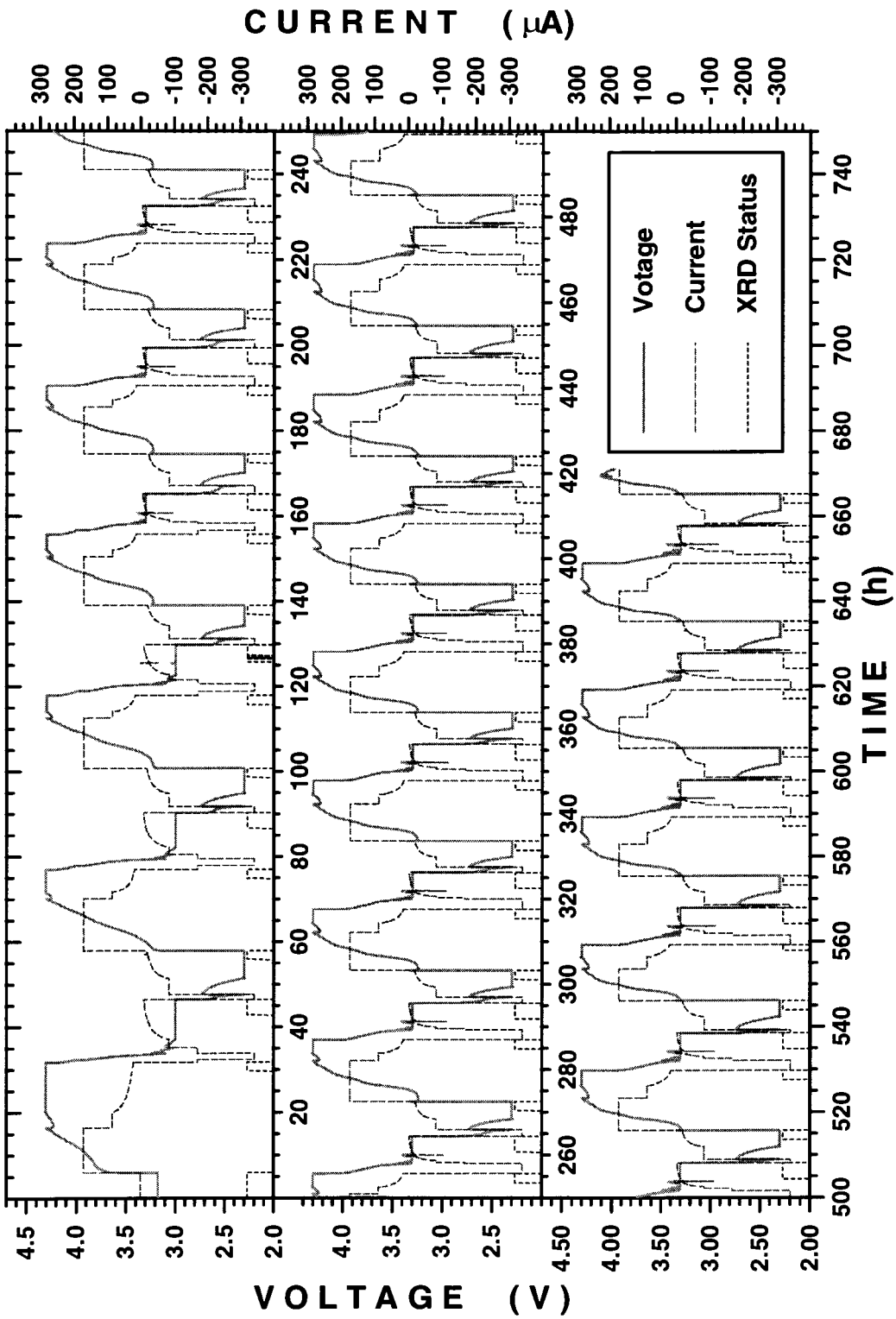

Figure 5.9: All cycles of Voltage *vs.* time, Current *vs.* time and XRD profile acquisition *vs.* time for *in situ* test 'Doberman'.

- `3 CD`: Charge or Discharge. Here we charge with $+170.55\mu$A, up until the upper trip point of 4.300 V is reached. Then we proceed with the next sequence.

- `4 CD`: Same as above with different limits. The current is reduced in an attempt to approach equilibrium. Notice that we increased the upper trip-point by 10 mV, in order to compensate for hysteresis effects.

- `5 HS`: Hold and Scan. Now the SM-unit is switched to potentiostatic mode, and the voltage is fixed at 4.305 V. The computer polls now for current in the bounds which are determined by the *compliance value* for the current, `Compl: q 341.10 fA` , which should read as 'Compl: $\pm$ 341.10 μA'. After the current settles below 7.5% of the compliance current, a detailed XRD profile is acquired according to the XSR-file `four12s.xsr`. The total scan time is 2 h and 10 min. .

- `6 CD ... 9 CD`: These are a number of sequences determining the details of the discharge up to 3.000 V. As one can see in Figure 5.8 it is advantageous to slow down the charge transfer. Although the lower trip-point is already reached on discharge at 341.11 μA, it is still possible to discharge the cell at voltages above this trip-point if the current is considerably lower. Again this effect is only present since the battery is discharged far away from equilibrium conditions.

- `10 HS`: Here we 'equilibrate' the battery at 3.000 V and we wait until the current drops below 17 μA, before we take a more detailed scan over 3.45 h, according to the scan modalities stored in file `two12s.xsr`.

- `11 CD ... 14 HS`: These sequences are the program for the discharge in the lower plateau region much like the discharge in the upper plateau region. At the end, a less detailed scan is taken at 2.3 V as it was done at 4.305 V in sequence 5.

- `CYCL`: This is a 'dummy sequence', which tells the program to start again with sequence No. 3. This loop is executed for a maximum of 50 cycles.

- `UNDF`: As soon as CH236 encounters an undefined sequence the test is finished. There are however other means to terminate or halt the experiment.

XSR - Files

This is a formatted printout of the sequences which will be uploaded to the 'Data Box' each time before an XRD profile of this time is acquired. It is possible to encode up to eight regions each with data for

- `Inil` initial angle, 2θ,
- `Final` final angle,
- `Step` 2θ increment for the goniometer,
- `Count` number of seconds to count at each position.

The total `Scan time` is calculated and includes an estimate for the time it takes to reset the goniometer arm to the desired start position. `HKL - Remarks` are fields to document and mention the most important reflections of a particular phase measured in this region, for example `311 531 440` .

Chapter 6

Refinement of XRD Patterns

This chapter describes how we obtained quantitative data from XRD patterns which were taken from in-situ X-ray cells. By 'data' we mean quantities like intensity, width and position of a peak or even the presence of an entire crystallographic phase with its characteristic XRD pattern. These quantities can, in principle, be measured by eye and ruler. However, such measurements are not as reliable and instead a more sophisticated process called *refinement* is invoked. The refinement of XRD patterns includes three stages:

1. An elaborate 'guess' which explains the origin of a particular peak or a number of peaks in the observed powder pattern. This can be obtained by comparison to powder data where the structure is known.

2. The formulation of a mathematical model, which generates a calculated diffraction profile. The model contains parameters like lattice constants, space group, intensity wavelength of used radiation etc. ... .

3. Extraction of these parameters by minimization of the difference between calculated and observed quantities.

Refinement of the lattice constants of a single phase crystal powder sample is standard. Refinement for site occupations and and lattice defects in powder samples are usually more involved. There are programs available which are made for refinement of entire phases of crystal powder samples, they will be discussed in the section *Rietveld refinement*. The strategies used to extract data from patterns that show more than one phase is discussed in the second section.

6.1 Rietveld Method

In 1969 H.M. Rietveld proposed a method for the refinement of neutron powder intensity profiles which could be applied as well to X-ray powder diffraction profiles [51]. The author distributed a program which does the task and his code is the basis of many improved versions of profile refinement programs. The program minimizes the quantity

$$S_y = \sum_{i=1}^{N} w_i (y_i - y_{ic})^2 \quad , \tag{6.1}$$

where y_i is the observed intensity for the i-th data bin of a total of N observations. The calculated intensity is y_{ic}, and w_i is a weighting factor chosen to be proportional to the inverse of the observed intensity. The program calculates an intensity profile based on the knowledge of the space group and fractional atomic coordinates of a given powder sample. Parameters included in the refinement model are a function for the background $\sum_{i=1}^{4} c_n (2\theta)^n$, an overall scale factor, and overall temperature factor, lattice constants, peak profile parameters and wavelength and off-axis shift as global parameters. The total number of all possible parameters can be quite large, but we will not list them here. Details can be found in Young [52] and in [51]. A figure of merit is the *'goodness of fit'* (G.O.F.), defined as

$$\chi^2 = \frac{S_y}{N - P} \quad , \tag{6.2}$$

where N is the number of data points and P the number of parameters included in the refinement. A number close to 1 indicates good agreement between model and observation. There is a whole range of merit functions, of which the *'Bragg-R'* factor

$$R_B = \frac{\sum_k |I_k(obs.) - I_k(calc.)|}{\sum_k |I_k(obs)|} \quad , \tag{6.3}$$

is also frequently used. The Bragg-R factor is less reliable since the calculation the observed integrated intensities $I_k(obs.)$ is based on the refinement parameters themselves. The total integrated intensity has to be distributed by an algorithm to the individual reflections (see Young, [52]).

In order to identify the single phase of orthorhombic $LiMnO_2$ (after synthesis), we refined the powder intensity profile shown in Figure 3.1 (a) by using Hill and Howard's version [53] of the Rietveld program. The result is shown in Figure 6.1, where the raw data, the calculated fitting profile and the difference between the two are plotted.

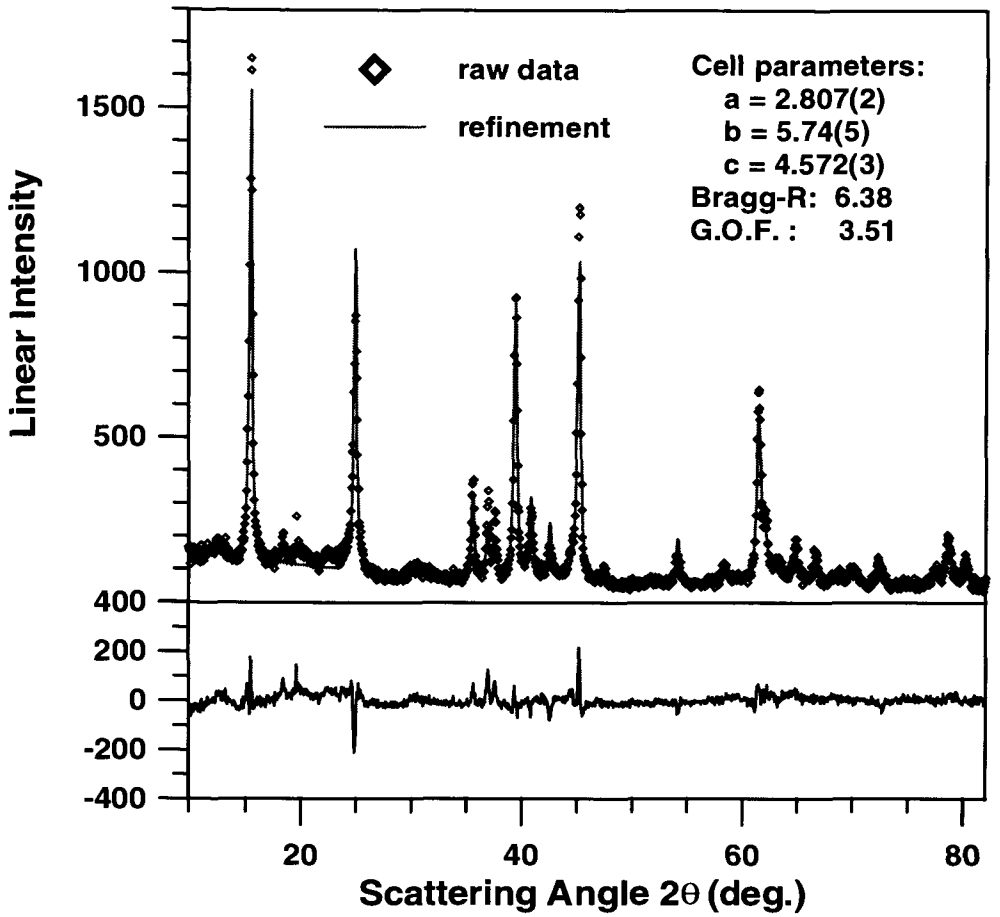

Figure 6.1: Rietveld refinement of the $LiMnO_2$ XRD powder profile, taken two months after synthesis. The difference between observation and calculated pattern is shown in the lower panel.

The G.O.F was 3.51, and for comparison to previous data we stated the refined lattice parameters. In chapter 3 we did mention that $LiMnO_2$ is not stable in air (for long times) and that a surface reaction causes conversion to another (cubic) phase. This effect is also apparent in the XRD profile from the sample after synthesis, but less profound (see Figure 3.1 for comparison) and this explains the rather poor G.O.F. of 3.51. However, combined with the calculated line intensity pattern (see chapter4, Figure 4.4), we find this convincing evidence that we have predominantly single phase orthorhombic $LiMnO_2$ as starting material for making cathodes.

6.2 A Typical XRD *In Situ* Diffraction Profile

In Figure 6.2 we show a typical X-ray diffraction pattern as obtained from one of our in-situ cells. The plot also displays peak intensity patterns, which were retrieved from a CD-ROM database compiled by the *International Center for Diffraction Data* [54]. Identified are three separate phases. The first is due to the beryllium foil disk, which acts as a window for X-rays. The second phase belongs to the lithium metal anode, directly under the beryllium disk and the third phase is scattering from the $LiMnO_2$ cathode which we seek to analyze.

There is at least one other phase present which was not identified as peak intensity pattern on the plot in Figure 6.2. Due to surface oxidation we observe reflections from *beryllium oxide*, also referred to as *bromelite*. For comparison we have taken a diffraction profile of a single beryllium foil disk, Figure 6.3 which we could directly mount in the diffractometer. We identified the phases of beryllium and bromelite by matching the corresponding positions of the *powder* profiles of these substances. Since we compare in this case solid metallic phases to powder diffraction data we should not be surprised if the relative ratios of the observed intensities do not match.[1] In general, the manufacturing of thin foils has an effect on the preferred orientation of the crystallites in the metal.

The polyethylene separator which is between the lithium metal anode and the cathode, contributes six peaks in the range between 15 deg. to 30 degrees.[2] In order to identify the latter we acquired the XRD profile for a single layer of separator which was mounted on a microscope glass slide. The profile is shown in Figure 6.4 (a) for comparison. The broad 'hump' at 20 deg is due to scattering from the liquid electrolyte phase.

Naming and Labeling Conventions

In order to simplify the following discussion, we classify the various observed reflections. Peaks which belong to the hardware such as beryllium, steel and the aluminum of the cell holder, are referred to as *constant background* peaks. Peaks belonging to the crystal compounds in the cathode are called *variable peaks*. Peaks emerging from the lithium metal anode are *variable background* peaks, since their intensity

[1] This argument also applies to the lithium metal phase in Figure 6.2.

[2] All subsequent angles are referring to 2θ-values unless otherwise stated.

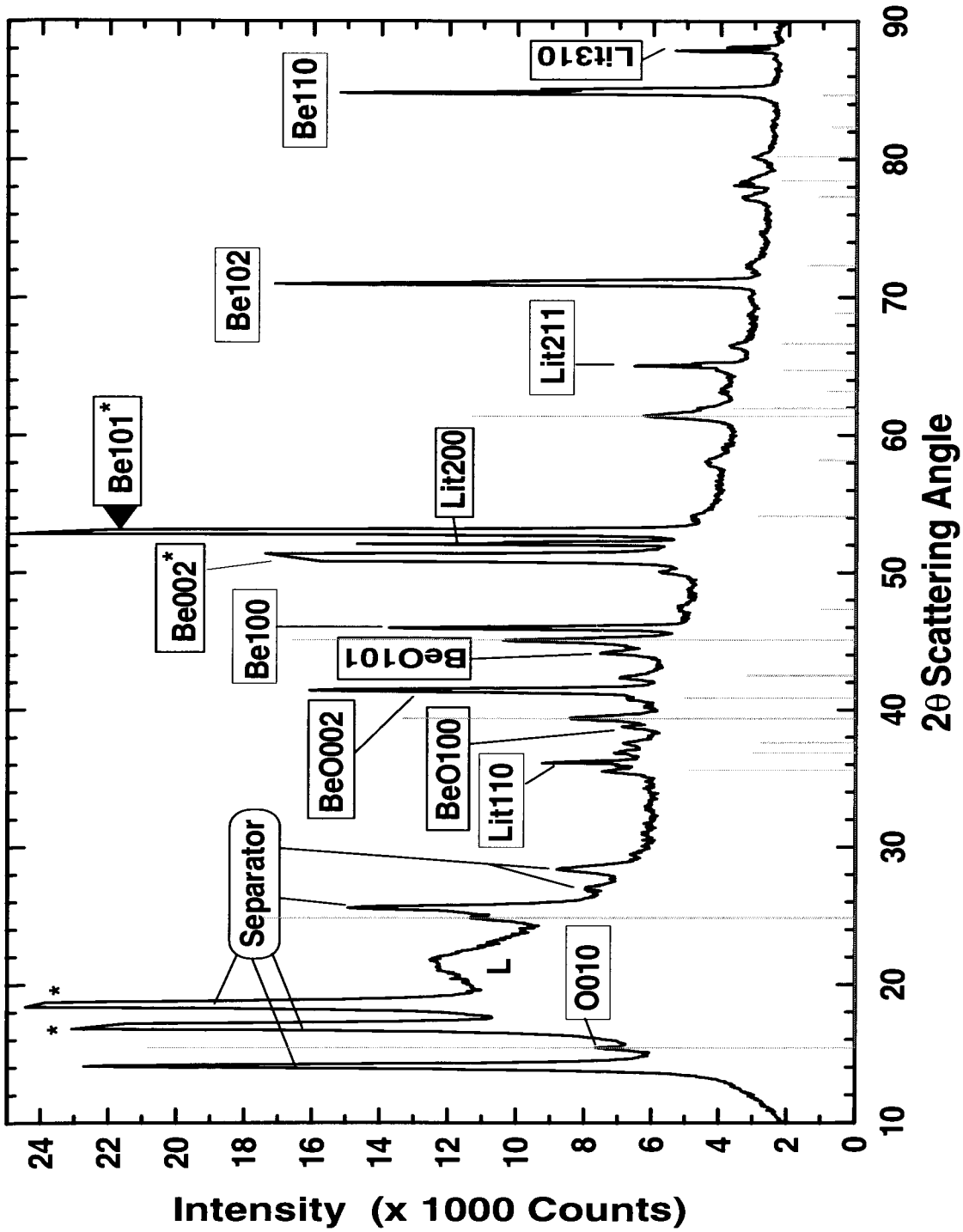

Figure 6.2: Plot of a typical X-ray in-situ powder diffraction profile, identifying peaks belonging to other phases. The calculated intensity pattern is also shown (thin lines). Peaks labeled with a star do not fit on the scale.

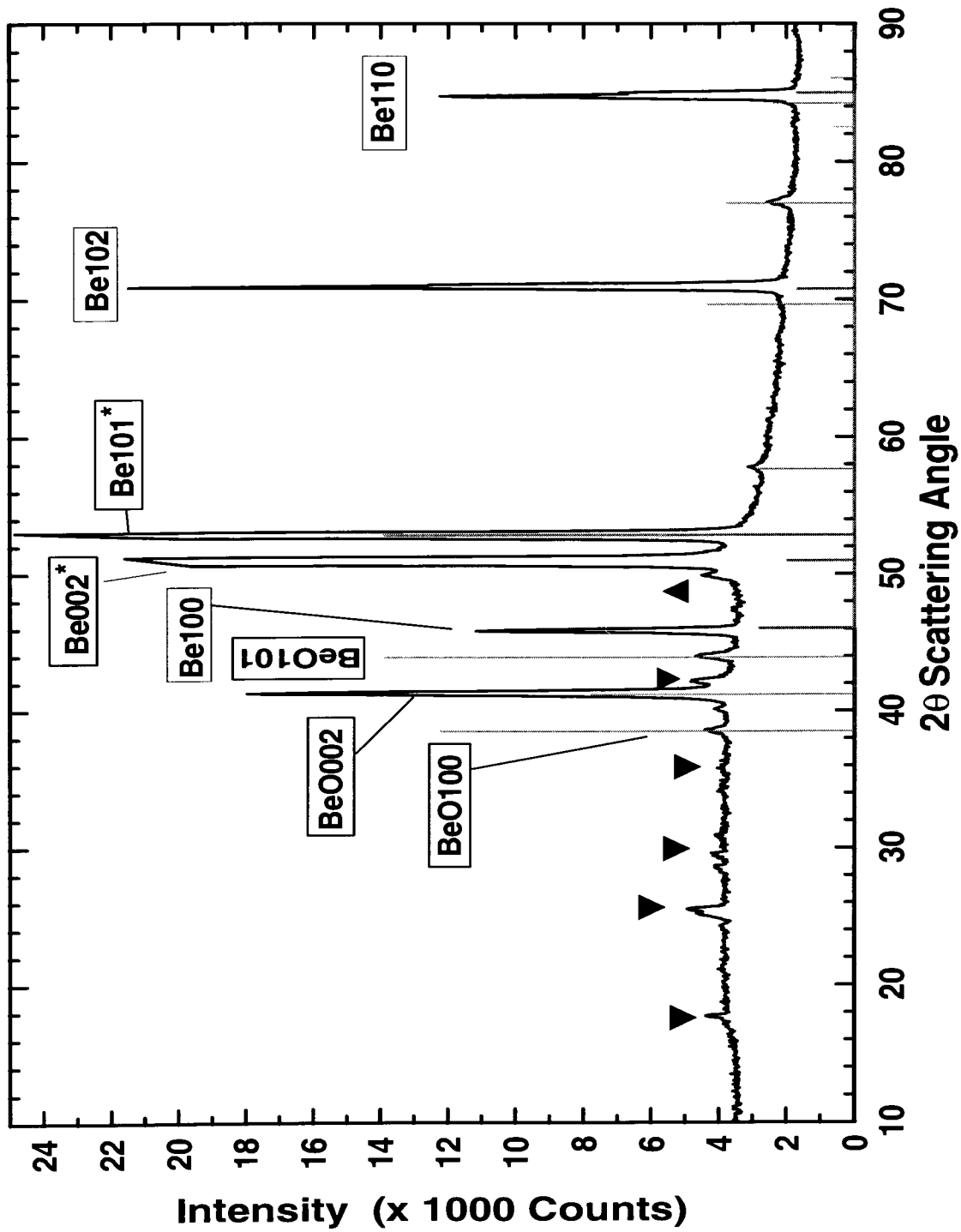

Figure 6.3: X-ray diffraction profile of the beryllium foil disk used to seal the *in situ* batteries. The black triangles indicate unidentified peaks. The intensity patterns for beryllium and for bromellite as found in the database are also shown.

fluctuated strongly as the cells were charged and discharged. Scattering due to the presence of liquid phases (electrolyte) and diffuse scattering at finite temperatures of crystal phases is simply called *background*.

In order to distinguish peaks belonging to different phases in diffraction profiles we either refer explicitly to the phase such as 'the 010 peak of the orthorhombic phase of $LiMnO_2$', or we use a short notation like 'O010' or 'ort010' where the context allows it. The three phases of lithium manganese oxide are then distinguished by 'C400' or 'cub400' for the 400 peak belonging to the cubic phase $LiMn_2O_4$ and 'T211' or 'tet211' for the 211 reflection belonging to the tetragonal phase $Li_2Mn_2O_4$.

Unidentified Peaks

There are a few, little, constant background peaks which we could not identify in the XRD profiles of in-situ cells. For example there is a little peak exactly at 50 deg. which is on the left hand side of a broad beryllium (002) peak. Although it would be of interest to know their origin, we did not attempt to further identify them if we were certain that they did not belong to the phases of interest like $LiMnO_2$ or $LiMn_2O_4$. Such is the case for the above mentioned peak, as can be seen in Figure 6.3, it must be a peak belonging to the beryllium foil disk.

Strategy

In principle it should be possible to generate a given observed diffraction pattern by refining the appropriate model. We would have to consider all relevant phases and model the absorption properties of the layered stack. If the refinement works we have solid confirmation that our picture of the scattering process is correct. But apart from this being a very ambitious task, we do not really gain anything, since we have to tell the program initially which phases are present. What rather interests us are the *incremental* changes in the crystal structure of the cathode only, when the electrochemical state is altered. If the crystal structure of the cathode is affected, then this must become apparent in at least a few of the peaks belonging to this single phase. Some peaks might be more accessible than others since there is always the possibility of overlap with reflections of other phases. In Figure 6.2 for example the strongest reflection of the orthorhombic phase, 010 (15.3 deg.), is totally obscured by the separator and weaker peaks like the 111 (40.61 deg.) and 112 (54.0 deg.) overlap significantly with peaks from phases belonging to the cell hardware. Thus if we want

to find out about changes in the cathode alone we can only analyze a few particular peaks which are accessible.

Example

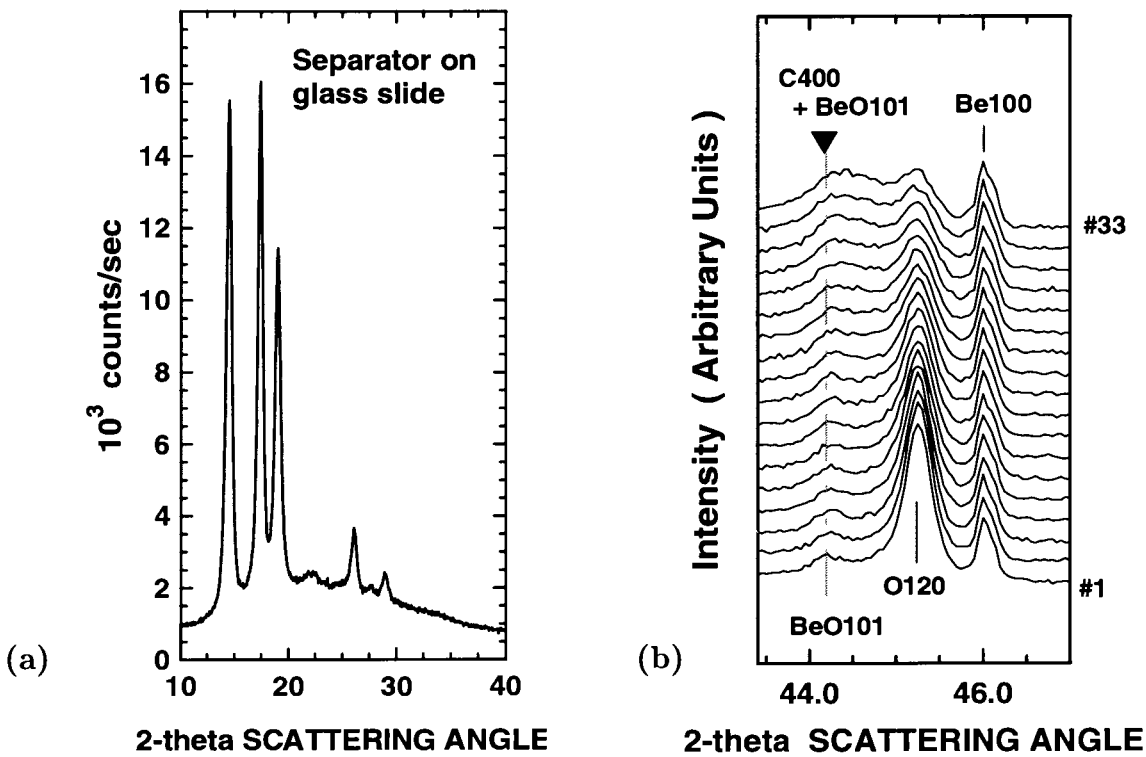

Figure 6.4: (a) XRD pattern of a polyethylene separator mounted on a glass slide . (b) multiple XRD patterns for a small region. O120 belongs to the orthorhombic phase, and C400 is a reflection from the cubic phase. Be100 is a constant background peak from the beryllium window and BeO101 is a peak belonging to the beryllium Oxide.

A series of subsequent diffraction profiles for the charge of a $LiMnO_2$ cathode in a cell where the stacking order was reversed, is shown in Figure 6.4 (b). Here we can see how the 120 peak of the orthorhombic phase dissapears and the 400 peak of the cubic phase emerges next to it. We observe changes of the integrated intensities, of the position of the 400 peak and we see that the half widths for the cubic and the orthorhombic peaks are quite different. We notice a strong constant background reflection of the beryllium foil disk ('Be100'), which is very close to the O120 reflection.

There is also a small constant background peak belonging to the beryllium oxide phase ('BeO101'), which can be inferred from comparison with Figure 6.3. What we are seeking is the extraction of the position, intensity and half width data for the peaks (O120 and C400) belonging to two separate phases of the same substance. The method we used is described in the following.

6.3 Single Peak Refinement

Instead of modeling the diffraction profile of the entire electrode stack including the beryllium foil disk and the separator, we were simply defining an 'ad-hoc' model for each particular 2θ region of interest. The model included a constant and a linear background parameter and the individual i-th peak found in the region ($2\theta_{min} \leq x \leq 2\theta_{max}$) is formulated by

$$\begin{aligned} p_i(x) &= \alpha_i[(1-\gamma_i)G(x) + \gamma_i L(x))] \\ L(x) &= \frac{w_i}{\pi w_i^2 + (x-\beta_i)^2} \\ G(x) &= \sqrt{\frac{\log 2}{\pi w_i}} \cdot \exp(-\log(2)\frac{(x-\beta_i)^2}{w_i^2}) \quad . \end{aligned} \tag{6.4}$$

Here α_i is a parameter proportional to the linear maximum intensity, β_i is the position of the peak center on the 2θ axis, w_i is the half width at half maximum and γ_i determines the peak shape to be either pure Gaussian ($\gamma_i = 0$) or pure Lorentzian ($\gamma_i = 1$) or any intermediate linear combination. The overall model function for the region is given by

$$f(x) = a_1 + a_2 x + \sum_{i=1}^{k} p_i(x) \quad , \tag{6.5}$$

where k is the number of peaks and a_1, a_2 are the constant and linear background parameters respectively.

Using a nonlinear least square fitting algorithm, taken from *Numerical Recipes* [55] and known as the *Levenberg-Marquardt* method, the observed intensity profile was refined by minimizing the G.O.F. as a merit function.

The method is quite sensitive to local minima, and in order to reach a global minimum for the refinement one usually does a number of strategically chosen refinement steps. Once the model function agrees well with the observed intensity profile, parameters for the peaks of interest are extracted and all allowed parameters are refined

once more and a routine which calculates the covariances between the parameters is used to estimate errors on refined parameters.

It turns out that the refined model function is of great use for refinement of subsequent XRD profiles which are very similar to the initial one. In fact, the differences are incremental if the electrochemical manipulations are applied in a slow and controlled manner. To extract parameters of the new profile, we kept the constant background peaks fixed and refined only the parameters of the electrochemical phases (cathode and anode) and allowed for the refinement of the constant linear background parameter, as the overall intensity may fluctuate for different XRD profiles of the same region. The resulting changes are then attributed to changes in the structure of the cathode[3] only.

This method proved very successful as we shall see in the experimental chapters following this chapter. Problems arise when we encounter a phase transition and one peak of the initial phase is obscured by the peaks emerging from a newly formed phase. There is no simple way to deconvolute uniquely two overlapping reflections if none of the peak parameters are known. Refinements in the intermediate region of phase transitions lack therefore accuracy and have to be interpreted with caution.

Another problem is the interference of constant background peaks. There are two strategies to surmount this problem. If the overlap is not too strong and one can guess the shape of the background peak reasonably well we can just fix these parameters and measure relative changes as outlined above. If the background peak is too strong we tried to guess the shape by trial and error by refining a number of representative XRD patterns from this region. A 'guess' for background peaks could be obtained from XRD patterns taken from a 'dummy cell' where we omitted the inclusion of the cathode, in favor of a plain aluminum foil strip. If the guess seemed reasonably good, we subtracted the intensity of this single peak from all subsequent XRD patterns and used the manipulated data for further analysis. These matters will be addressed when I discuss the data where I had to do this, and further justification of this method will be given.

[3]and in part in the lithium metal anode if 'visible' in the electrode stack.

Chapter 7

Experimental II
In situ X-ray Study

Three major experiments were carried out after the development of the new *in situ* technique, in order to inquire about the questions raised at the end of chapter 3. The purpose of the different experiments is presented below.

Irreversible Phase Transition: Test 'Safari'

The goal in the first experiment was to establish a precise record of the irreversible phase transition proposed by Reimers *et al.* [4]. For this particular purpose we used a cell built in reverse stacking order. The cell was charged using quasi equilibrium conditions (400 h rate) up to 4.02 V. The central questions were, whether any intermediate phases occur and how well the cubic phase forms and what the lattice constant of the new phase is. This experiment is subsequently referred to as the 'Safari' test.

Two Phase Region at 3 V: Test 'Hero1'

In the test 'HERO1' we also cycled the cell at a very low rate (200 h). The cell was built in regular stacking sequence in order to complement the reverse stacking experiment 'Safari' for the initial charge. We charged the cell up to 4.3 V and discharged it to 2.3 V for two full cycles. Particular attention was given to the behavior in the interesting two phase region at 3.0 V.

Crystallinity *vs.* Cycle Number: Test 'Doberman'

The third experiment was fundamentally different. Here, the goal was to analyze the crystallinity of the different phases as a function of cycle number. Knowing that shunting is always a big problem for lithium metal cells, we included three layers of separator and succeeded to charge and discharge the cell for 20 cycles before shunting most likely ended the test. The trade off in this experiment was that the signal from the cathode was rather weak. The test was given the name 'Doberman' for short reference. We already introduced the test protocol of 'Doberman' in chapter 5.

7.1 Test 'SAFARI'

7.1.1 Charge Protocol

For a detailed study of the irreversible phase transition on the first charge it was desirable to use an *in situ* cell having reverse stacking order. Our goal was to measure the peaks of the disappearing orthorhombic phase and the emerging cubic phase as well as possible; this could only be done by placing the cathode directly under the beryllium. We were able to separate the compacted cathode from the standard aluminum substrate and with some care it was possible to include the brittle cathode in the electrode stack. The active mass of the cathode was 11.37 mg which corresponds to a total charge capacity[1] of 3.24 mAh. The open circuit voltage (OCV) after assembly was 3.26 V. Figure 7.1 shows the current *vs.* time, voltage *vs.* time, and XRD status for the entire *in situ* X-ray test. Plots of this kind will be abbreviated as 'IVS-plots' subsequently. The cell was charged using a very low current. In order to approach quasi-equilibrium conditions we chose a 400 h rate (8.1 μA). The first nine hours of the IVS-plot need however some further explanation. Before mounting the cell in the *in situ* holder we measured an OCV of 3.1 V, slightly lower than the voltage after assembly six weeks before this test. After mounting the cell in the holder, the holder was accidentally placed on a metallic surface which caused an outside short of the battery for approximately, but no more than 15 min. The cell was discharged during this time to an OCV of 2.17 V. In order to assess the total charge transfer during this period, I decided to charge the battery at a 100 h rate up to 3.3 V, which is just 40 mV above the initial OCV. The total charge transfer was below 0.13 mAh, which is

[1] all lithium removed.

less than $0.05x$ in $Li_{(1-x)}MnO_2$. The results in chapter 3 also suggested that it is not possible to intercalate lithium in orthorhombic $LiMnO_2$ and we saw that the battery potential dropped rapidly when discharged at a 25 h rate to 2.3 V. The XRD profiles of scan No.1 to No.4 also did not show any significant differences compared to XRD profiles taken from *in situ* cells during the developmental stages of this project. This gave me enough confidence to continue the experiment as planned. The battery was ramped up to a voltage of 3.42 V in 'CDS-mode' which is explained in the following: The *in situ* cell is charged (or discharged) to a particular trip-point while the control program continuously acquires XRD profiles. If the trip-point is reached and the X-ray data acquisition is still in progress, the *in situ* cell is switched to potentiostatic mode and the potential is fixed at the trip-point voltage. In due course the electrochemical system should reach equilibrium after waiting for a long enough time. Scan No.4 in Figure 7.1 is a perfect example of such a control process.

The current spikes at 8.33 h, 116 h, 167 h and 204 h are due to problems switching the SM-unit remotely, without disconnecting the *in situ* cell from the terminals of the instrument. During a brief time period of the order of milliseconds the terminal connectors are shorted by the SM-unit. These current spikes look more dangerous than they actually are. No significant amounts of charge can be transferred in such a short time compared to the time scale of the entire experiment.

The battery was charged with a current of 8.10 μA in CDS-mode, as soon as scan No.4 was complete. Since the current at the end of scan No.4 was still 14.62 μA , the electrochemical potential adjusted itself over the time when scan No.5 was taken. Subsequently the cell was charged first to 3.70 V (115 h), then to 3.90 V and finally to 4.02 V since the experiment progressed to our satisfaction.

7.1.2 Reverse Stacking

A question which remains is whether beryllium, which dissolves at voltages above 3.0 V, would significantly falsify the recorded current. The only check available to me at the given time was to screen the beryllium surface for traces of corrosion after the cell was taken apart two months after the test in October 1996. Traces of corrosion appear as little dark spots on the originally unmarked surface as was learnt from other experiments. I screened the surface under a magnifying lens and compared it to the surface of a new foil disk from the same batch. The beryllium foil disk for test Safari did not display any traces of corrosion. This may be attributed to a protective surface

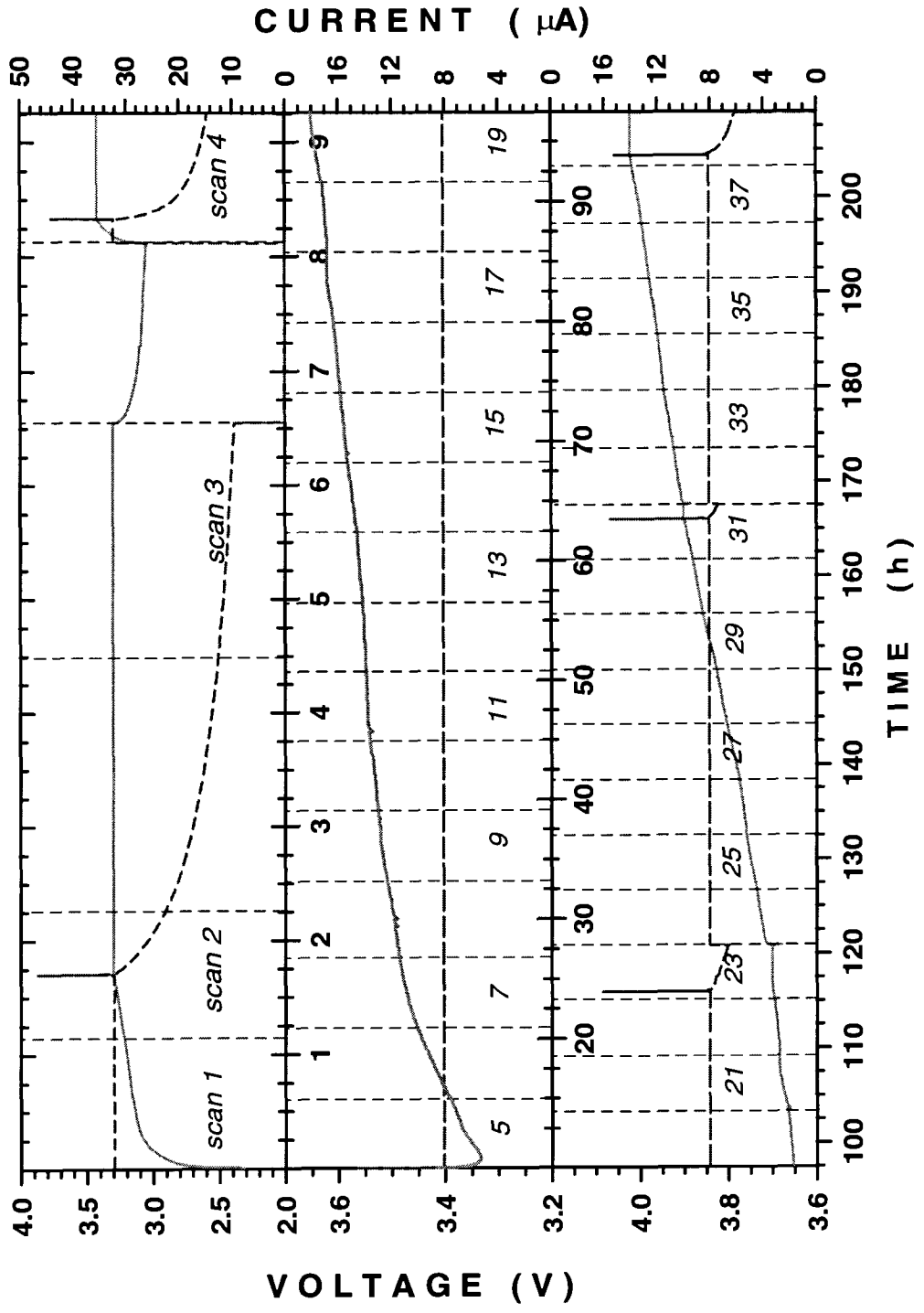

Figure 7.1: Voltage *vs.* time (solid line), current *vs.* time (dashed line) for test 'Safari'. The XRD scan status is indicated by vertical dashed lines.

film of beryllium oxide. We concluded that dissolving beryllium did not significantly effect the cumulative charge record of test Safari.

7.1.3 XRD Profiles

A summary of all XRD profiles taken for this test is shown in Figure 7.2. Individual profiles are offset by 1000 counts each. Figure 7.3 is a view of of the initial scan (No.1), an intermediate scan (No.19) and the final scan (No.34). We marked the strongest peaks from beryllium and beryllium oxide in scan No.19. It is clearly visible that very little of the orthorhombic phase is left, if about half of the lithium is removed from this phase. Before we proceed with more detailed analysis, it is necessary to address some important points which arise out of a general analysis of Figures 7.2 and 7.3.

Orthorhombic Phase

We notice that for the initial scans the relative intensities for the peaks of the orthorhombic phase are not in good agreement with the calculated pattern (Figure 4.4, chapter 4). In particular the 010 peak, usually the strongest reflection, is smaller than the 002 and 120 reflection and the 122 peak is exceptionally strong. This effect is due to the varying thickness of the absorbing beryllium window as was shown in section 5.2 . At low angles the path through the foil disk is much longer than at high angles. Consequently, peaks at lower angles appear attenuated. We estimated the attenuation of the O010 peak with respect to the O122 peak. The calculated ratio of their respective intensities is 100:54 whereas their observed intensity ratio is approximately 50:54. This corresponds to an attenuation factor of 0.5 for peaks below angles of 16 deg. compared to peaks at above 60 degrees. This agrees with the estimate of 0.53 which we calculated in section 5.2 for an *in situ* cell in reverse stacking order.

Now we consider the changes in the pattern as lithium is removed. If the orthorhombic phase converts entirely into a different phase, then the intensity of all peaks should dissapear uniformly. Their relative intensity ratios should *not* vary as lithium is removed.[2] Scan No.19 in Figure 7.3 however suggests the opposite. The ratio of O010 and O122 is almost reversed. In scan No.34 we notice that O122 and

[2]By this we mean that the two phases are physically separated by a well defined domain boundary. One side contributes scattering of the orthorhombic phase, the other side gives rise to scattering from the newly formed phase. The influence of the (extended) domain boundary is neglected in this picture.

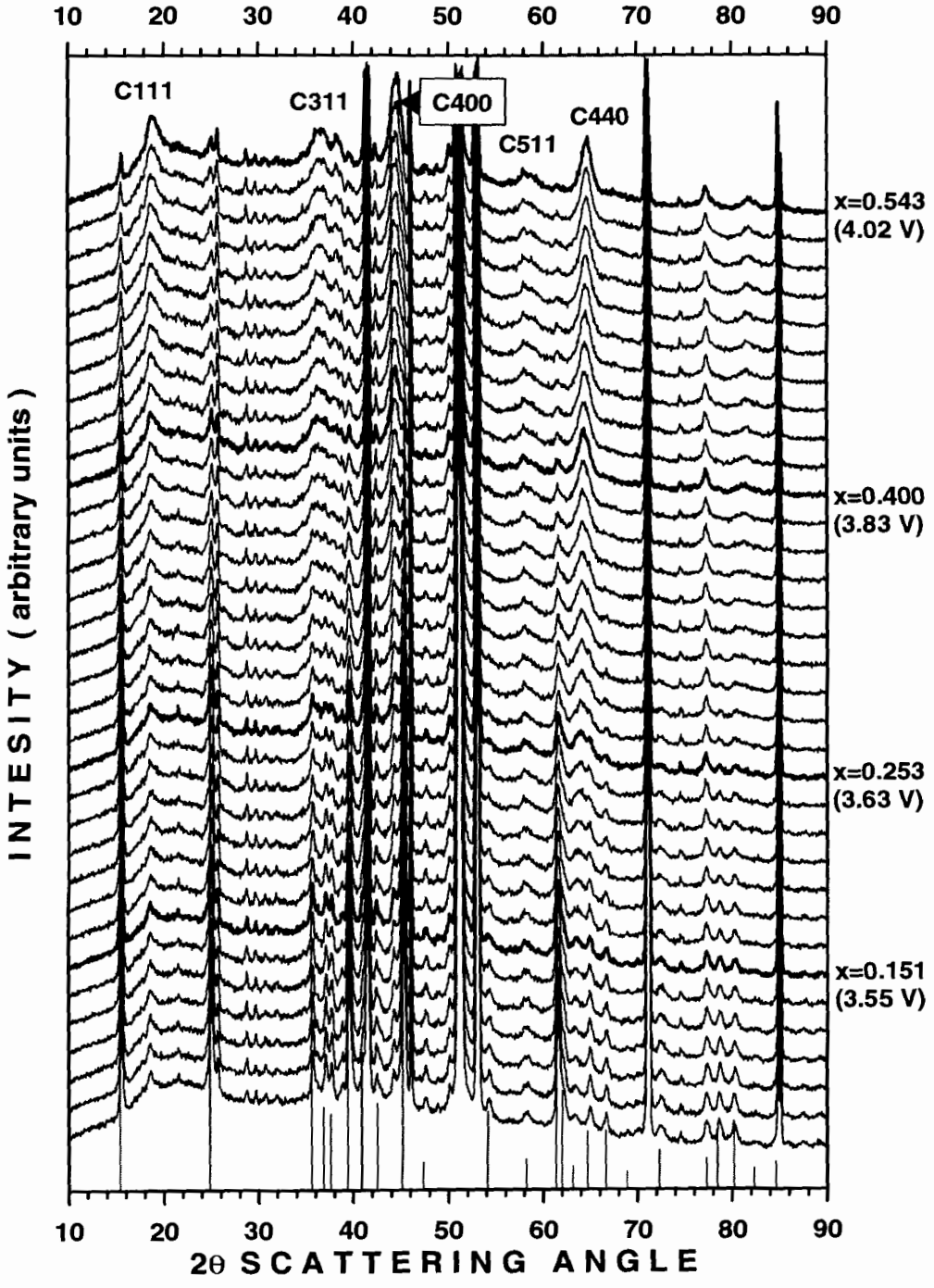

Figure 7.2: 'Safari': XRD profiles No.1 to No.34. The line intensity pattern on the lower 2θ axis is the calculated line pattern from chapter 4 for the orthorhombic phase. The strongest peaks of the cubic phase are labeled on top of the last scan. The approximate voltage and x in $Li_{(1-x)}MnO_2$ is shown on the right ordinate for selected scans.

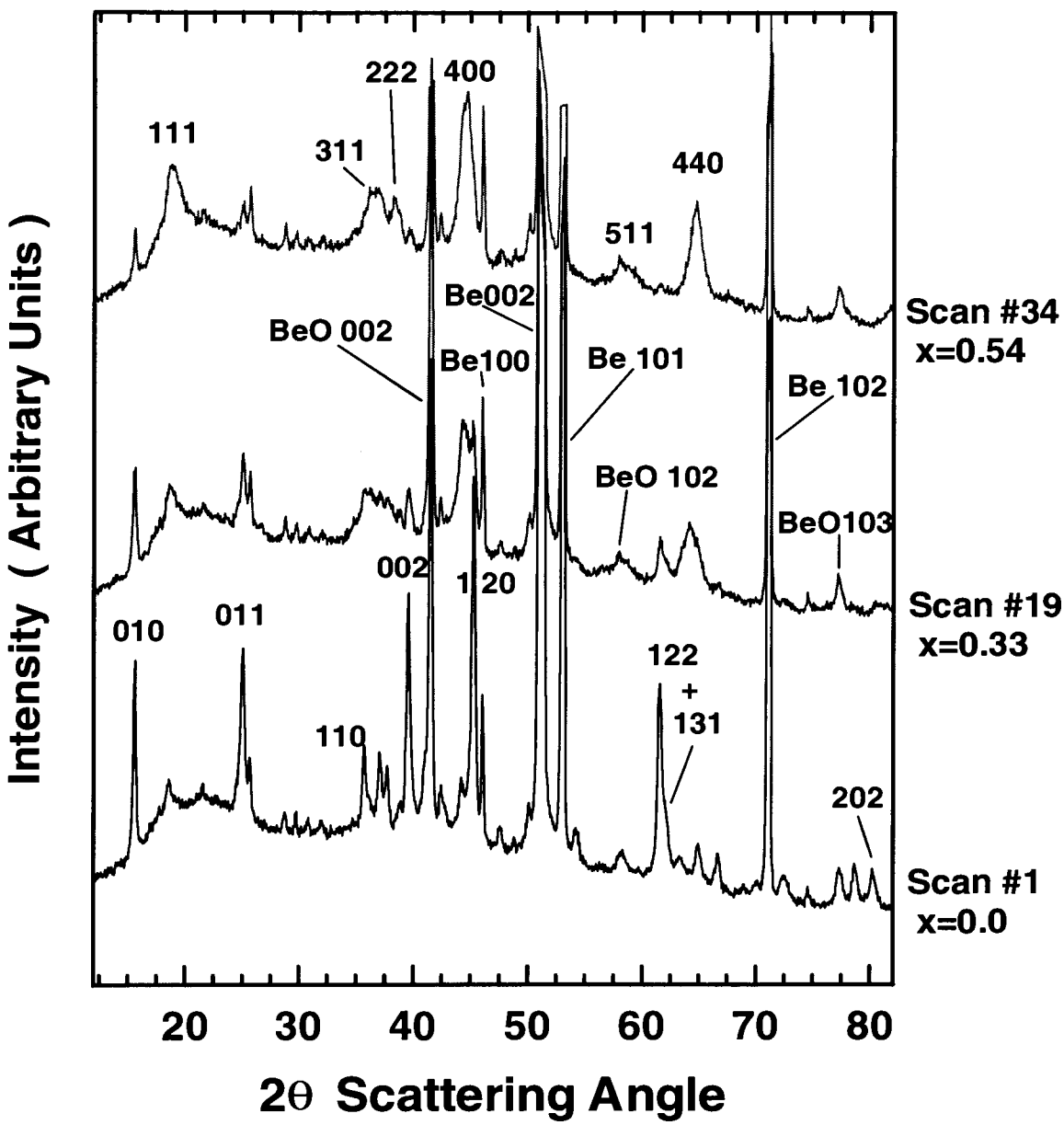

Figure 7.3: XRD profiles of the first, 19th, and 34th scan of test 'SAFARI'. In the first scan the most prominent peaks of the orthorhombic phase are labeled, in scan 19 we labeled peaks originating from beryllium and beryllium oxide and in scan 34 the strongest features of the cubic phase are indexed. The variable x refers to $Li_{(1-x)}MnO_2$.

all the other peaks of the orthorhombic phase above 30 deg. are almost not visible, whereas the O010 and O011 peaks are still well defined.

Inactive Cathode Material

These observations could be explained independently of changes of the atom arrangement in the orthorhombic unit cell[3] if we assume that larger sections of the cathode are electrochemically inactive. We mentioned that the compacted cathode is very brittle and it is possible that small fractures at the edges of the cathode introduce high resistance paths or total disconnection from the active cathode material. Figure 7.4 (a) and (b) depict a view of the top of an *in situ* X-ray cell. Figure 7.4 (c)

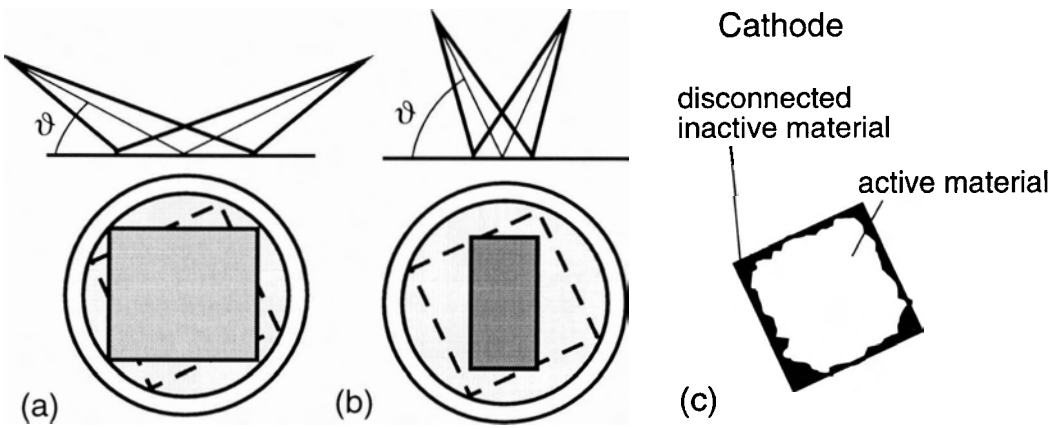

Figure 7.4: Scattering from disconnected cathode material of a square powder cathode is much stronger at low angle (a) since the area of scattering (grey shaded rectangles) is much larger compared to higher angles (b). In (c) the cathode is drawn showing disconnected inactive material.

shows a damaged cathode, where large fractions of material at the edges are disconnected. The grey shaded rectangles map the region of the incident X-ray beam. At low scattering angles the X-ray beam covers a large area, hence a large amount of the scattering arises from inactive cathode material. At higher angles the center of the cathode is preferably probed, hence the fraction of scattering arising from disconnected material is lower. The square shaped cathode may be rotated with respect to the incident radiation zone, as indicate in Figure 7.4. We tried, however, to keep

[3]which is responsible for the relative intensities of the peaks and not the positions.

track of the cathode orientation at assembly time in order to orient the coin cell in the holder for maximum scattering efficiency.

Penetration Depth Argument

The second argument for the non-uniform decrease of the orthorhombic peaks is the strong absorption of the cathode material. As demonstrated in section 5.2, at low angles the scattering from the cathode emerges from a thin surface layer of the cathode at the beryllium cathode interface. The bulk of the cathode is not probed. Only at higher angles is the penetration depth large enough that crystallites in the bulk contribute to the intensity pattern.

If intercalation processes are delayed at the top of the cathode then the acquired X-ray patterns may be interpreted as follows: O010 and O011 represent an earlier stage in the extraction process of lithium. O122 and O211 contain more information about the more recent state of lithium extraction. The crystallites at the separator/cathode interface are the most 'advanced' scatterers in this picture.

Discussion

The arguments above are important considerations. However to attribute the non-uniform behavior of the intensities in the orthorhombic phase entirely to these processes is problematic for the following reasons:

- The material closest to the beryllium window still contributes the strongest scattering, even at high angles. The penetration depths in section 5.2 were calculated for 98% attenuation.

- We charge the cell at a very slow rate (400 h) in order to ensure equilibrium conditions. Kinetic resistance for Li^+ diffusion over 125 μm should be minimal.

- Lattice parameters of the cubic phase as a function of x for two entirely different *in situ* cells with *opposite* stacking order agree well. In experiment 'Hero1' (see section 7.2.5, Figure 7.22) the cathode surface at the separator is predominantly screened. If diffusion gradients alter the charge state across the thickness of the cathode by an order of $0.1x$ then[4] the lattice constants of the cubic phase as a

[4]This would be required to explain the delayed disappearance of O010 and O011. The composition at the surface is $Li_{0.8}Mn_1O_2$, and in the bulk $Li_{0.7}Mn_1O_2$, the latter corresponding to a more

function of x must differ by a fixed amount.[5]

- The fraction of disconnected cathode material must be less than 10 %. This estimate is based on a comparison of the predicted capacity and measured charge transfer for test 'Hero1' the assumption that the maximum depth of charge in $LiMnO_2$ is 0.80.

The above arguments might explain the non-uniformity in the relative intensities of the orthorhombic phase. Therefore it is not possible to unambiguously identify the changes in the intensities as an important characteristic of the phase transition itself.

Cubic Phase

As lithium is removed from the cathode, we see in the patterns of Figures 7.2 and 7.3 that very broad and strong peaks emerge. In particular the C400 and C440 peaks are very strong and the C400 peak stands out as the strongest peak belonging to the cathode phases. Comparing the ratios of the relative intensities we find poor agreement with the calculated pattern of $Li_1Mn_2O_4$ in Figure 4.4, as was seen in the disappearing orthorhombic phase. In particular if we compare the 111 peak with the 440 peak we should expect an intensity ratio of 100:36 according to the calculated pattern. Taking attenuation into account and applying a factor[6] of 0.5 to the intensity of 111 (which is even at higher angle than O010), we still expect to find an observed intensity of 50:36 for the two peaks.[7] Scan No.34 of Figure 7.3 however suggests that the ratio is almost reversed. Moreover the intensity of the 111 peak appears rather small in scan No.19 compared to the C400 and C440 peaks.

Another problem arises out of the discrepancy between the observed and calculated relative intensities of the 311 and 222 peaks. Normalizing the strongest peak to 100, their calculated ratio should be 51:11. The appearance of a rather strong and well-defined 222 peak is an odd feature. Attenuation due to different angles should be negligible for a comparison of the 311 and 222 peaks.

---

advanced state.

[5]The above arguments comparing 'Safari' and 'Hero1' can however not rule out the possible cancellation of two error sources.

[6]Taken from the O010/O122 comparison.

[7]C440 is only 3 deg. higher than O122, thus we expect the same attenuation ratio.

Summary

The presence of peaks at the approximate positions of the cubic phase suggests that the newly formed phase(s) have (a) cubic unit cell(s). Broad peaks indicate either extremely small domains or the presence of a number of phases with different lattice parameters.[8] We pointed out some problems with the relative intensities. Strong absorption at low angles and inactive cathode material render a discussion of the discrepancies difficult. For the three strongest peaks (400, 311 and 440) we find that the integrated intensities are approximately correct. This suggests that the atoms in the unit cell are roughly at their ideal positions. However we have to be careful in the analysis of these patterns due to the possibility that the cubic phase is not formed like an ideal $Li_1Mn_2O_4$ compound.

7.1.4 Refinements

Using single peak refinement as described in chapter 6 we followed the tendencies of individual peak intensities of the two phases. This is possible if the number of scans per mAh of transferred charge is large. This is the case in a 400 h rate experiment (for a single charge) where consecutive scans are separated by 7 h, and as we can see in Figure 7.2, the changes in subsequent scans are indeed incremental. In general we want to remark that features in the XRD profiles not belonging to the cathode are reproduced remarkably well in each scan and differences can be classified as random 'noise' in the signal. There are no systematic tendencies visible, for peaks not belonging to the cathode phases in the whole set of XRD spectra. This gives confidence that the following method used to extract selected parameters for consecutive scans gives reliable answers.

Successive Refinements

Peaks in a particular region were modeled by a function according to Equation 6.5. Once we obtained satisfactory agreement, the same function was used as a starting model for the subsequent scan. A number of strategically chosen refinement steps were selected and stored in a command script. After application of these steps to the new data file, the desired parameter was extracted from the modified model function.

[8]Each crystallite may have a well defined lattice parameter. The broadening stems from the averaging over the cathode.

The latter served as initial fit for the next data file and so on, until the last profile was reached or the model was not appropriate anymore[9].

In order to obtain consistent results for refinements of a particular peak in subsequent data files, the shape parameter which determines the ratio between Gaussian and Lorentzian (gl-ratio), was usually not included in the refinement. In doing so, a rigid model assumption was imposed for the refinement of particular peaks. If the peak height changes drastically over a number of successive scans, than the modeled peak shape could become inappropriate and was indicated by a bad G.O.F. Re-defining the model at any intermediate scan, for example by including the gl-ratio in the next refinement in order to minimize the G.O.F., will lead to inconsistent results. Comparison of the intensities or halfwidths before and after the re-definition of the assumed model for the peak will not be meaningful anymore.

It was our strategy therefore, trying to be as consistent as possible in the method of extracting one and the same parameter from separate X-ray data files. That meant necessarily that we did not minimize the G.O.F. by all means for subsequent XRD data files. This strategy gave the most consistent results for comparing intensities, and halfwidths.

Refining peak positions however, are an exception to this practice. Since the gl-ratio, the halfwidth and the intensity are usually independent of the position parameter[10], we included this parameter and tried to obtain best fitting results (minimizing the G.O.F.) for subsequent data files. However the obtained set of parameters was only used to extract the position values. In order to refine the halfwidth and intensity, we usually adopted the procedure outlined above, independently of the position refinements, even though this meant doubling the amount of work.

7.1.5 Intensity Refinements

In Figure 7.5 shows the refinement results for the decreasing orthorhombic phase. In the upper panel (a) we plot the voltage *vs.* x in $Li_{(1-x)}MnO_2$ for comparison. The relative intensity values in (b) were normalized to a value of 10 for each peak in the initial XRD profile. At 4.02 V the O010 and O011 reflection are still more than twice as large compared to reflections at higher angles; O002, O120 and O122.

[9]for example in the case of a vanishing phase.

[10]This is rigorously only true, if the peak is symmetric to the ordinate axis.

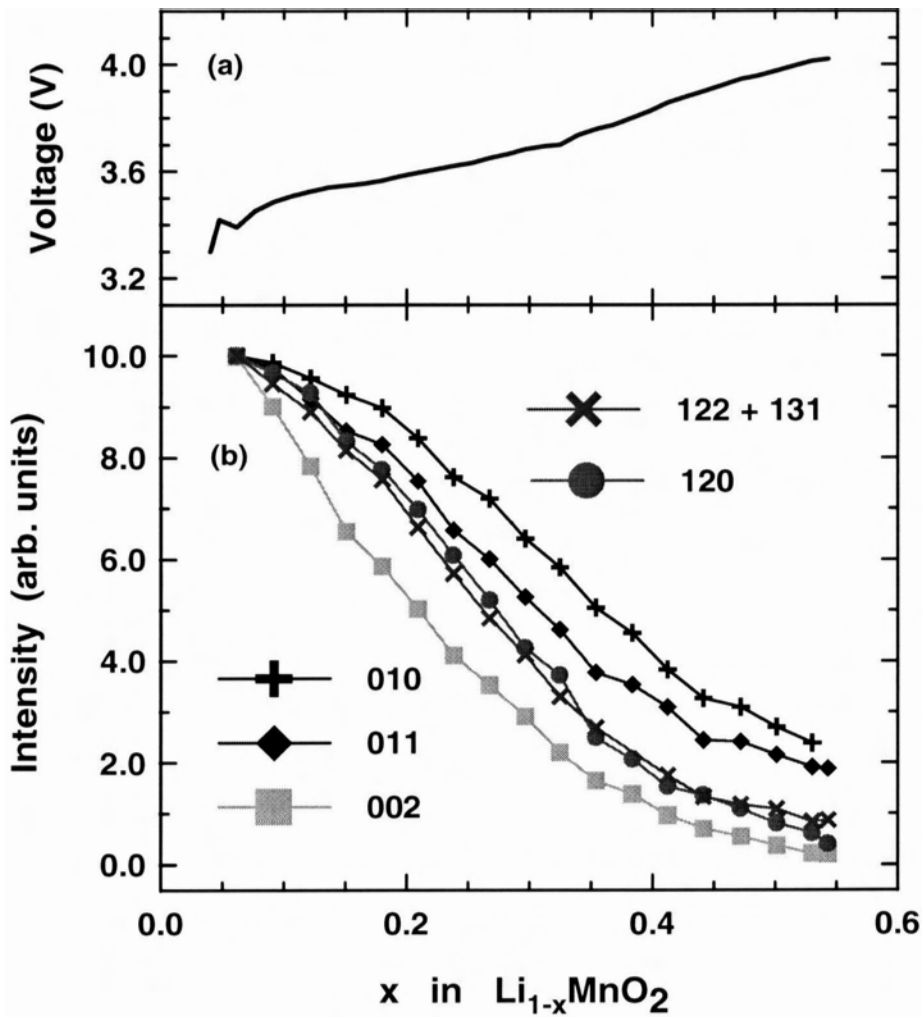

Figure 7.5: 'Safari': (b) Intensity *vs.* x in $Li_{(1-x)}MnO_2$ for the vanishing orthorhombic phase. The top panel (a) displays the voltage *vs.* x for comparison.

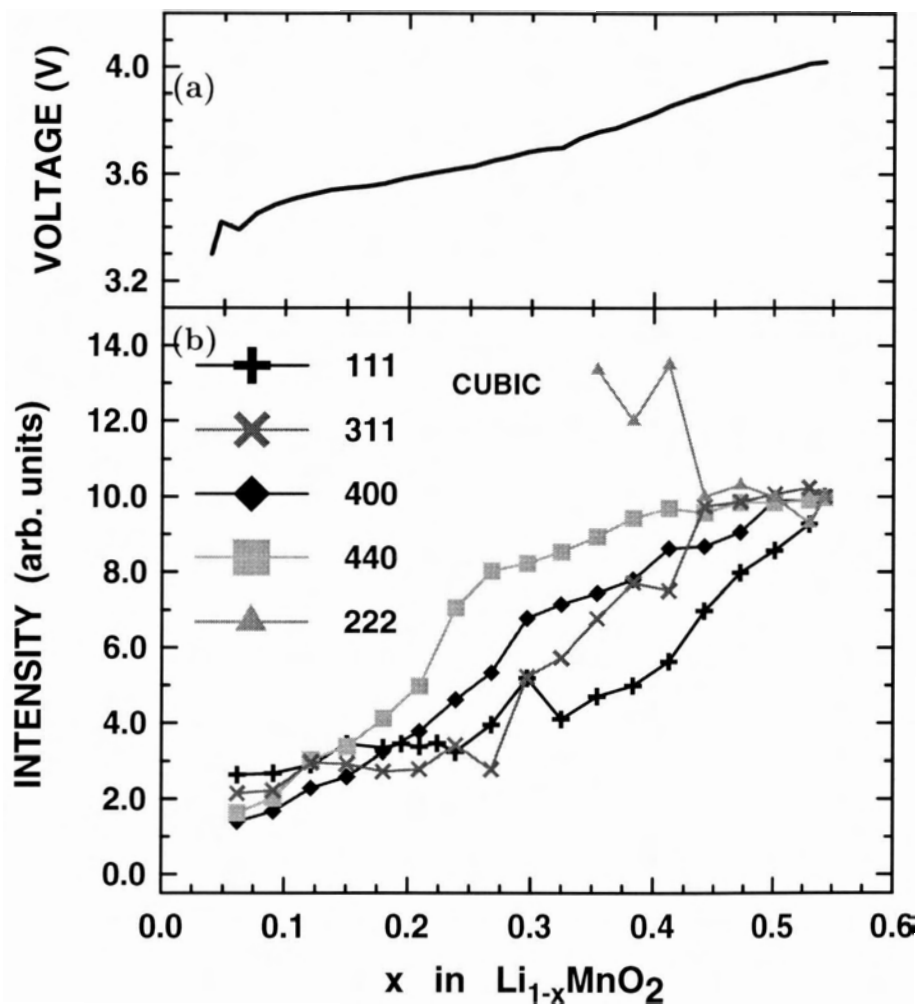

Figure 7.6: 'Safari': (b) Intensity *vs.* x in $Li_{(1-x)}MnO_2$ for the newly formed cubic phase. The top panel (a) displays the voltage *vs.* x for comparison.

This is a larger deviation and we attributed this already to disconnected cathode material which is predominantly screened at low angles. The deviation for O010 is larger than for O011 at higher angle as one would expect. Despite the non-uniform decrease in intensity, we find however that the orthorhombic phase vanishes rapidly on charge. Important for the discussion of the dynamics of the phase transition will be the observation that after half the lithium is removed from the cathode, only small traces of the original orthorhombic phase are detectable in the X-ray profiles.

Refinements of intensities *vs.* lithium content for the strongest peaks of the cubic phase are shown in Figure 7.6 (b). The results for the C400 and C440 peaks are most reliable (high SNR) whereas the refinements for C311 are less accurate since the peak is very broad and we are not sure whether the assumption of a single peak is correct. Throughout this study we found that the cubic phase does not form well along this direction, the observed peaks are very always broad. Moreover, in the region of the C311 peak we find also a lot of other interfering peaks from the vanishing orthorhombic phase. The C111 reflection displays a local maximum at $x = 0.3$. Whether this is rather an artificial result and stems from a necessary re-definition of the model function at this point, or whether this is something physical cannot be decided at this point. The trend for higher and lower angle peaks is similar compared to the findings for the orthorhombic phase. We normalized the intensities with respect to the *last* XRD profile. Here the higher angle peaks gain intensity before the lower angle peaks. Most striking is that the C111 peak is almost constant up to $x = 0.23$. The C111 peak correlates strongly to the largest lattice spacing for the strongest scatterer, which is manganese.

7.1.6 Refinement of Positions

Orthorhombic Phase

In Figure 7.7 (a)-(e) we display the positions of the strongest peaks of the orthorhombic phase as a function of lithium content. As we have seen, the phase disappears quite fast and some peaks are obscured by the emerging cubic phase, and could not be refined for $x \geq 0.4$. The important result of this analysis is that the positions of the peaks do not vary in any uniform fashion for $0 \leq x \leq 0.4$. We deduce that the orthorhombic unit cell does neither expand nor contract.

The strongest peak of this phase O120 is not included in Figure 7.7. It is too

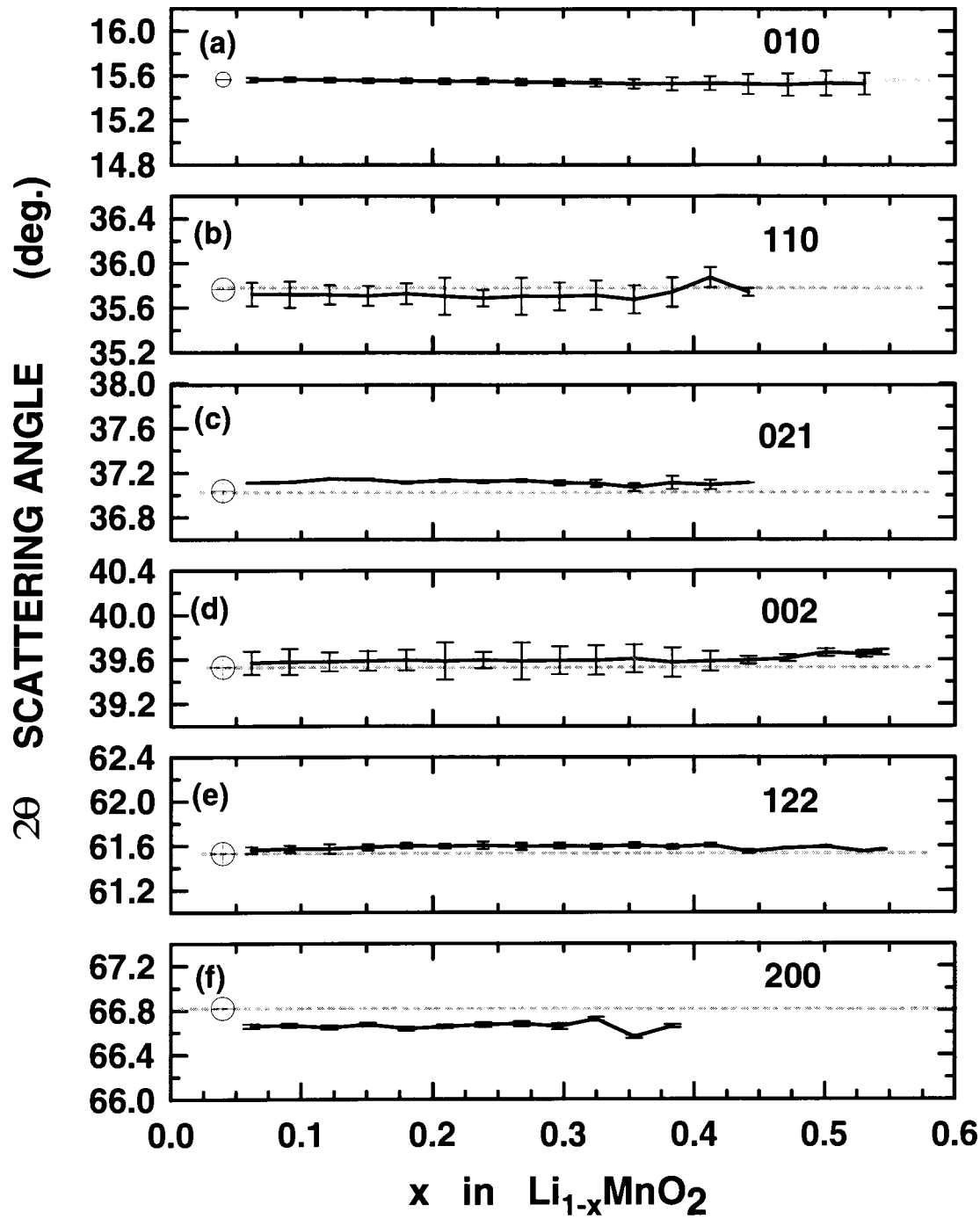

Figure 7.7: (a)-(f) refinements of the positions the disappearing peaks of the orthorhombic phase *vs.* x in $Li_{(1-x)}MnO_2$. The dashed lines indicate the off-axis corrected, calculated positions. The scale on the ordinate axis is for all peaks the same. No significant uniform trends for peak shifts are apparent.

close to the C400 peak for obtaining an accurate position refinement. We also did not include data for O011, but there we also did not observe any significant shift.

Cubic Phase

In Figure 7.8 (a)-(e) we display the positions of the strongest peaks of the cubic phase as a function of lithium content. The position parameters for the 111 and 440 reflection are more reliable. Refinements for the 400 reflection suffer some interference with overlapping peaks and so does 311, but to a larger degree. The peaks for the cubic phase are quite weak in the beginning and we regard the errors for the refinements in the region $x \leq 0.3$ as being too small. However we see clearly that there is a uniform trend in the shift towards higher angles as we remove lithium further and, as the peaks gain intensity the error bars shrink in size. The shift to higher angles corresponds to a contraction of the lattice of the cubic phase. This can only be explained if this new crystal phase itself is subject to electrochemical manipulations.

This is already a very significant result which allows us to draw first conclusions upon the nature of the phase transition. As lithium is removed from the orthorhombic phase the structure becomes unstable and forms a cubic framework. However, these cubic domains are not in the form of completely delithiated spinel phase λ-MnO_2, we must have some form of $Li_{(1-x)}Mn_2O_4$ which is then further delithiated in a second step.

The extracted values for all refined positions of the cubic phase for a particular XRD profile can be used in a separate routine to obtain refinements of the lattice parameter a. The result is shown in Figure 7.8 (f) where we plot the lattice constant a in Å *vs.* x in $Li_{(1-x)}MnO_2$ for the cubic phase. As the peaks of the cubic phase gain intensity, the errors for the determined lattice constant decrease. The same result is reproduced in Figure 7.9 (A), where we included a linear least squares fit, and for better comparison the voltage *vs.* lithium content is plotted below in Figure 7.9 (B). The non uniform behavior for the lattice constant for $x = 0.33$ could be an indicator for a poor model or a particular bad refinement for this particular dataset. However as we already saw in the Figure 7.6 for the intensities, there is also a 'kink' visible at $x = 0.3$. Refinements of the intensities and position where usually separate, which makes a poor fit less probable. The best indicator for a poor model at this stage is the fact that the charge curve itself has a 'kink' at the same lithium concentration. It is therefore very unlikely that a refinement error for that particular dataset is

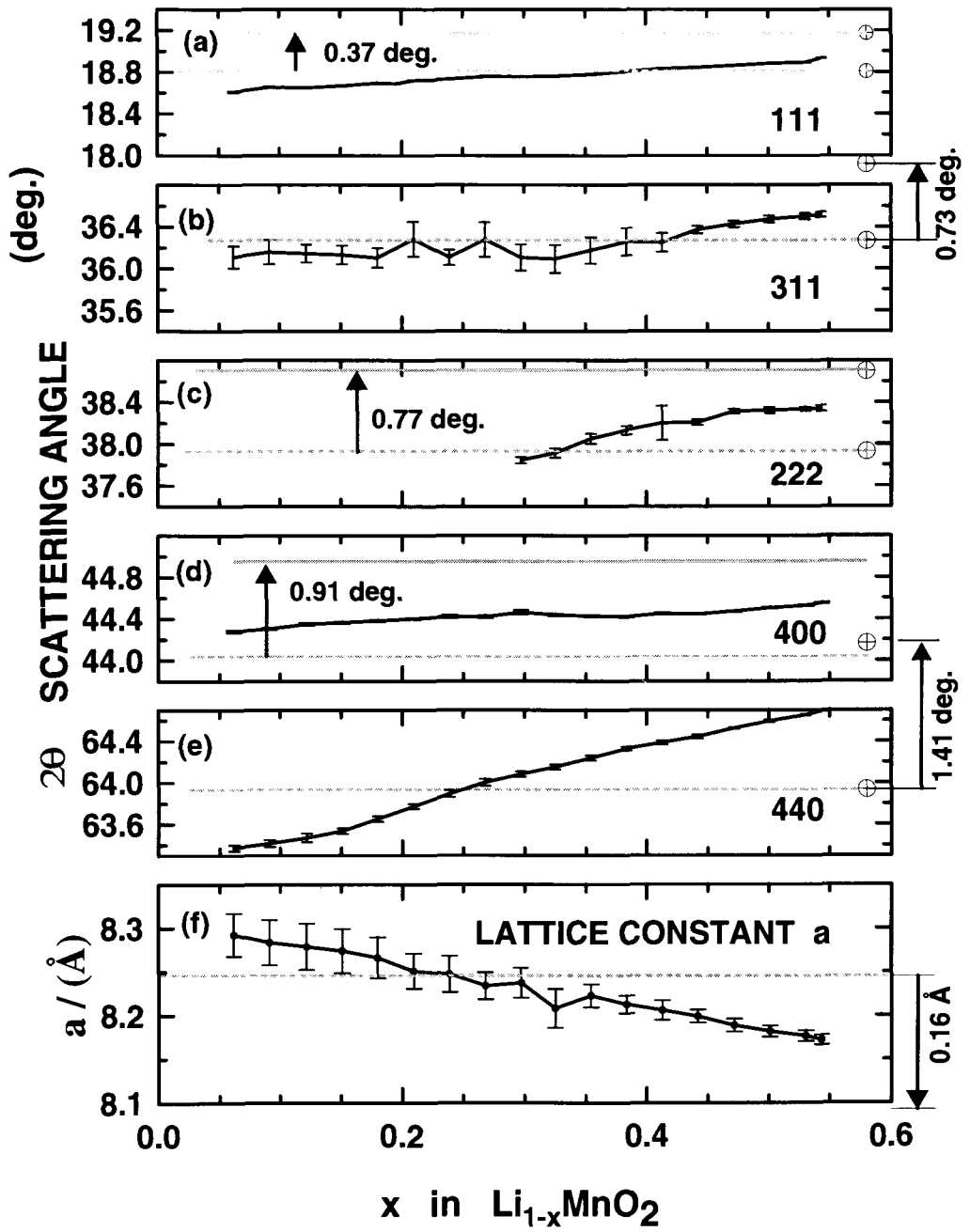

Figure 7.8: (a)-(e) refinements of the positions of cubic peaks *vs.* x in $Li_{(1-x)}MnO_2$. In (f) we show the lattice constant of the newly formed cubic phase *vs.* x in $Li_{(1-x)}MnO_2$, calculated by a refinement procedure. The dashed line indicates the off-axis shift corrected, calculated position for $Li_1Mn_2O_4$. The solid line and arrows indicate the anticipated shift for a uniform cubic phase with $a = 8.09$ Å.

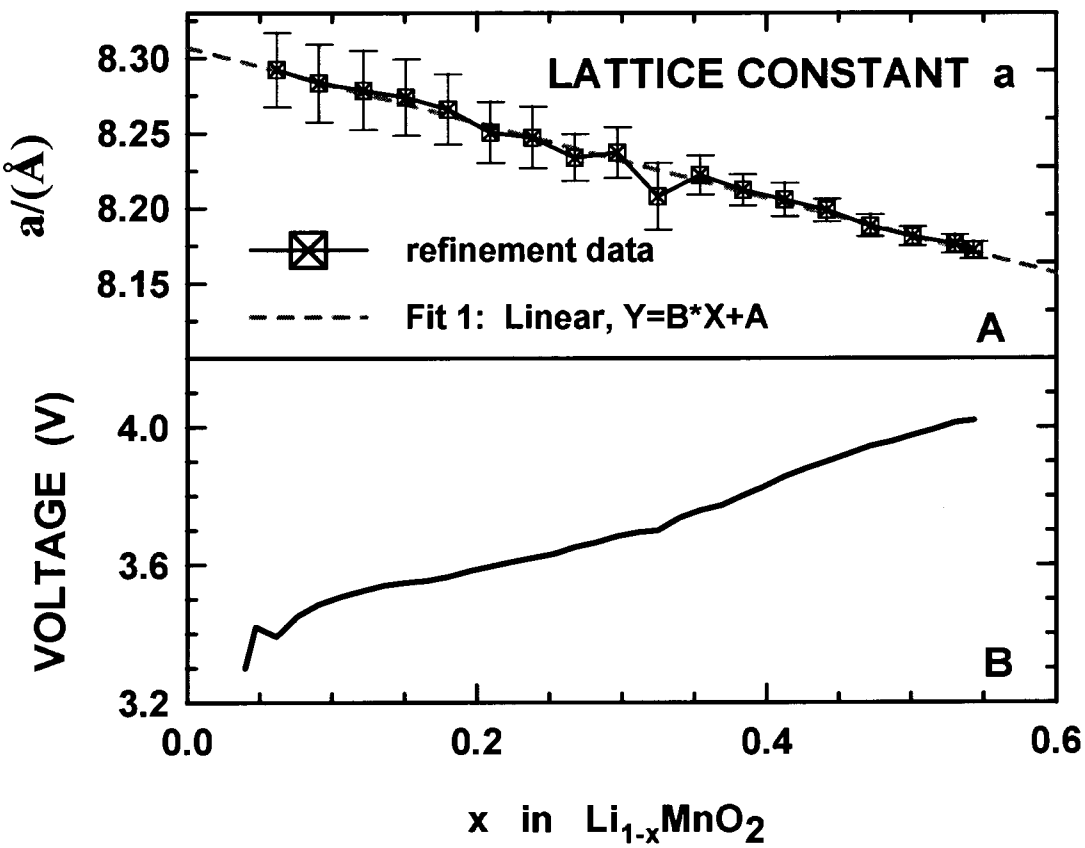

Figure 7.9: (A) lattice constant of the newly formed cubic phase *vs.* x in comparison with the cell potential (B) as a function of x in $\mathrm{Li}_{(1-x)}\mathrm{MnO}_2$.

responsible for the 'kink's in the refinement data. Inconsistencies occur also for the halfwidth parameters at that concentration, as we shall see in the following section.

Maybe it is possible that the assumption of a single cubic phase for our refinements is not appropriate. However due to lack of better insight, it is the best we can do at this stage of the analysis.

7.1.7 Refinements of Halfwidths

Orthorhombic Phase

In Figure 7.10 (a) we plot the halfwidths of the strongest peaks of the decaying orthorhombic phase as function of x in $Li_{(1-x)}MnO_2$. Although the halfwidth of these peaks also contain the broadening due to the instrument, we use these values to find lower limits on domain sizes and to follow the general trend when lithium is removed. For this purpose we plot in Figure 7.10 (b) the correlation length of coherent scattering in the direction normal to the respective lattice planes. The correlation length is calculated using Equation 4.12 for the values of the refined halfwidths. We also included a number of linear least squares fits to selected data. The fits did however not include any data for $x \geq 0.3$. As we can see in Figure 7.10 (a) the reported errors on the parameters for $x \geq 0.3$, are getting rather large, indicating strong cross correlations due to a poor model or weak peaks with low signal to noise ratio (SNR). These fits are only included to empahsise the trends in the data set. In fact as the orthorhombic phase disappears, except for the 010 and 011 reflection, the peaks are getting very weak and the SNR is large.

Although individual peaks measure strictly speaking the *correlation length* in a particular direction one can get an estimate of the *domain size* of crystallites if many different directions are taken into account. Extrapolating the fit to the average at $x = 0$, we obtain an estimate of 270 Å for the domain size of crystallites in the powder cathode. For the domain size at $x = 1.0$, after all lithium from the orthorhombic phase is removed, we obtain an estimate of 65 Å. This is an indicator that we must have contamination due to inactive cathode material. Taking only the data for the (less reliable) 011 reflection into account, we still find a decrease in the correlation length to about 165 Å. In any case the domain size of the crystallites is getting smaller as lithium is removed as one expects.

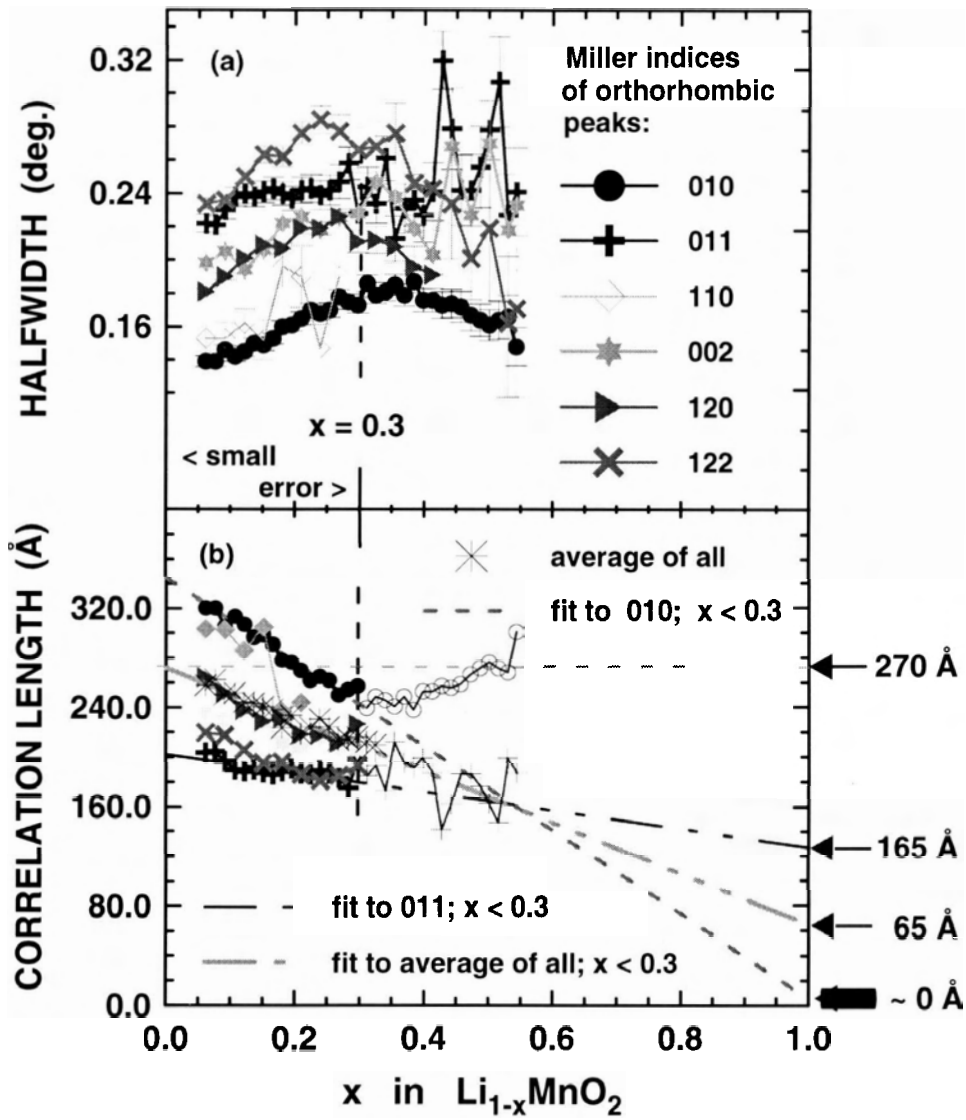

Figure 7.10: Halfwidth (a) and correlation length (b) *vs.* x in $Li_{(1-x)}MnO_2$ of the orthorhombic phase. Linear least squares fits include only data for $x \leq 0.3$ where the errors are still small. The fit to the average of all peaks serves to estimate the *domain size* of the crystallites at the beginning (x=0; 270 Å) and at the end of charge (x=1; 165 Å). Using the width of the 010 reflection we actually predict that the correlation length approaches 0 Å for $x = 1$. A pessimistic estimate uses the (less reliable) 011 reflection to estimate only a decrease in the correlation length to about 165 Å.

Cubic Phase

The same analysis for the cubic phase is not so clear. Figure 7.11 (a)-(b) is a graph which displays halfwidths for the cubic phase. We see immediately that the trend for the different directions is not uniform. As already mentioned at the end of section 7.1.3, the measured halfwidths are not uniform at all. In particular, we find that the 311 peak is *very* broad with a halfwidth of 1.20 deg and larger. On the other hand there is the 222 peak which starts at a halfwidth of 0.5 deg and becomes the narrowest peak of the cubic phase with 0.25 deg. for $x = 0.54$. The halfwidth of the 111 reflection also increases but less dramaticly than 311 does. The absolute value (0.7 deg.) agrees within error with the 400 and 440 reflections. What is particularly puzzling are opposite trends for the 222 and 111 peaks, since 222 and 111 have the same planes and 222 is just the 2nd order reflection 111.

In Figure 7.11 we plot the corresponding correlation lengths. Taking only data values for $x \geq 0.4$ into account we an estimate of the domain size of 75 Å is we exclude the 'outlier' peaks 311 and 222. Taking all peaks into account we confirm an increase in domain size to about 115 Å for $x = 1$. Whether 311 and 222 are truly 'outliers' or whether they represent physical meaningful processes cannot be answered yet.

Discussion

If we assume that that the cubic phase grows uniformly in size and is well defined by a sharp domain boundary, we expect to find (within refinement errors) the same absolute value for the halfwidths and that all the peaks show decreasing halfwidth. This is clearly not the case. We rule out that our refinements[11] are not accurate enough. Since the intensities and positions also show discrepancies, we rather conclude that our refinement model of a single ordered cubic phase is inappropriate.

Ohzuku *et al.* [17] found in XRD experiments with delithiated spinel phases that the two plateaus close to 4.0 V correspond to a *two phase region*, where two cubic lattices with slightly different lattice (difference: 0.1 Å) parameters coexists. It is explicitly stated there that for $0.4 \leq x \leq 0.65$ no *intermediate* lattice parameters are found.

The difference of 0.1 Å in the lattice constant could explain broad peaks if we have scattering from two distinct regions. For example the outer surface layer of a

[11] Single peak refinement with an 'ad hoc' model for each region.

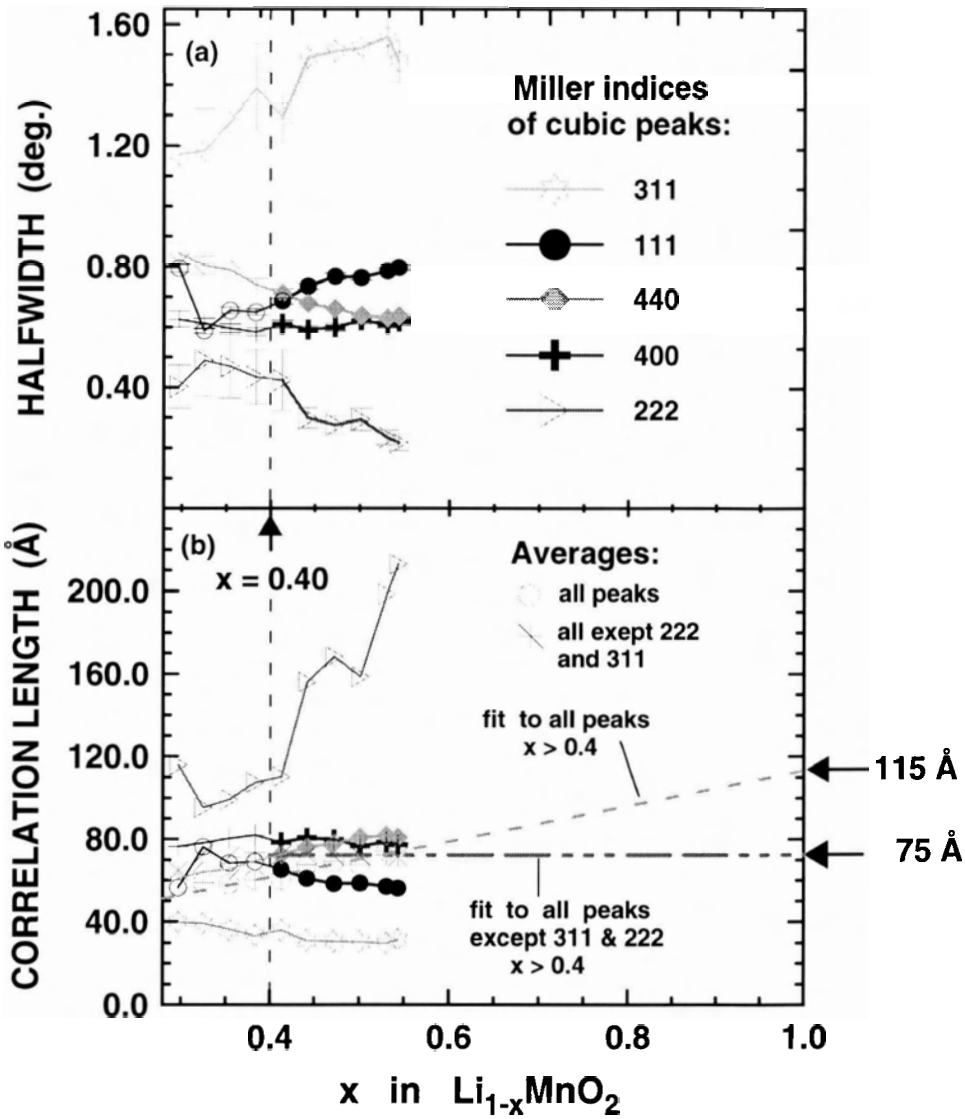

Figure 7.11: Halfwidths (a) and correlation lengths (b) *vs.* x in $Li_{(1-x)}MnO_2$ of the strongest peaks of the newly formed cubic phase. Linear least squares fits include only data for $x \geq 0.4$ where the errors are small and overlap with orthorhombic peaks is marginal. The strong discrepancies in the trends suggest a poor model. It is likely that the cubic domains are not single phase. In this case the estimate of 75 Å for the *domain size* of the forming cubic serves only as a lower bound.

crystallite has a lattice constant close to 8.10 Å and at an inner shell we measure 8.20 Å, assuming that extraction of lithium creates a concentration gradient towards the center (steepest increase).

The broadening of the peaks in the pattern due to two cubic phases should nevertheless appear in a way that peaks to higher angles are broadened stronger[12] for all peaks. We have still the problem that the odd peaks (311,111) increase in halfwidth, and that the even peaks (222,440 and 400) decrease in intensity. We have yet to identify another explanation for the non uniform behavior of *all* parameters.

7.1.8 Off Axis Shift

The correction for an off axis shift of the cathode (see Figure 4.3) is usually the first analysis done on any *in situ* X-ray dataset of this kind. We took two independent XRD spectra, scan No.1 and No.5 of test 'Safari' and refined all accessible peaks of the orthorhombic phase. The refined positional parameters for the individual reflections were then used to refine the lattice constants and an off axis parameter. The input and the results for scan No.5 are given in Table 7.1. The 141 reflection was not further included since it gave always large $\Delta 2\theta$ values. As can be seen in Figure 7.3, it overlaps strongly with the BeO103 reflection. For scan No.2 we found an off axis shift of 288.4 μm, which is in excellent agreement with the first refinement. The off axis of test 'Safari' was therefore fixed at 290 μm.

In principle we can do the same analysis for the newly formed cubic phase. However, the number of accessible peaks is much lower and as we have seen, we may not have a single cubic phase. The resulting broadening in the peaks makes position parameters also less reliable.

In Table 7.2 we display the results for refining the lattice constant and off axis of scan No.15 ($x \simeq 0.26$), just when the cubic phase forms. This is a compromise, since intensities are rather low and the cubic phase still interferes strongly. However, it is at the onset of the formation of the cubic phase where we hope to have a stoichiometry close to $LiMn_2O_4$. The obtained off axis shift of 164 μm is considerably lower compared to the refinement of the orthorhombic phase. Since the refinements for the cubic phase are generally less accurate than refinements of peak positions of the orthorhombic phase for $x \leq 0.15$, we adopted the following method to extract

[12]Ignoring effects of texture.

off axis = 291.5 μm						
hkl	2θobs.‡	2θcorr.	2θcalc.	$\Delta 2\theta$	refined	d-space§
010	15.566	15.385	15.393	−0.008	1	5.7560
011	25.027	24.849	24.863	−0.014	1	3.5810
110	35.720	35.564	35.474	0.008	1	2.5254
021	37.118	36.945	36.899	+0.046	1	2.4359
101	37.694	37.521	37.561	−0.040	1	2.3945
002	39.568	39.396	39.398	−0.001	1	2.2870
111	41.057	40.866	40.814	+0.072	1	2.2108
120	45.252	45.084	45.088	−0.004	1	2.0107
122	61.543	61.386	61.394	−0.008	1	1.5101
131	62.030	61.847	61.975	−0.102	1	1.4973
040	64.942	64.788	64.784	+0.004	1	1.4390
200	66.662	66.509	66.543	−0.033	1	1.4052
211	72.462	72.315	72.219	+0.096	1	1.3081
141	77.326	77.183	77.365	−0.182	0	1.2334
042	78.710	78.569	78.534	+0.035	1	1.2180
202	80.261	80.121	80.164	−0.043	1	1.1973
Space group: Pmnm ; a=2.8104 b=5.7560 c=4.5740 [Å]						

‡Angular values in degrees. § Denotes the calculated distance of lattice planes in [Å].

Table 7.1: The off axis shift (top) and refinement of lattice parameters (bottom) of the orthorhombic phase.

lattice parameters for the cubic phase. We used the off axis parameter as obtained from refining the orthorhombic phase to correct the observed 2θ values of the cubic phase(s), by suppling the off axis as a fixed parameter to the lattice parameter refinement routine. The shift of the individual reflections is angle dependent and given by Equation 4.13. In Figure 7.12 we plot the peak shift (2θ) *vs.* the 2θ scattering angle for test 'Safari'. These curves depend of course on the particular goniometer.

off axis = 163.7 μm						
hkl	2θobs.‡	2θcorr.	2θcalc.	$\Delta 2\theta$	refined	d-space§
111	18.536	18.435	18.631	−0.196	1	4.7623
311	36.315	36.218	36.114	+0.104	1	2.4871
400	44.259	44.164	43.904	+0.260	1	2.0622
440	63.750	63.663	63.831	−0.169	1	1.4582
Space group: Fd3m ; a=8.2486 [Å]						

‡Angular values in degrees. § Denotes the calculated distance of lattice planes in [Å].

Table 7.2: The off axis shift and refinement of lattice parameter (bottom) of the cubic phase.

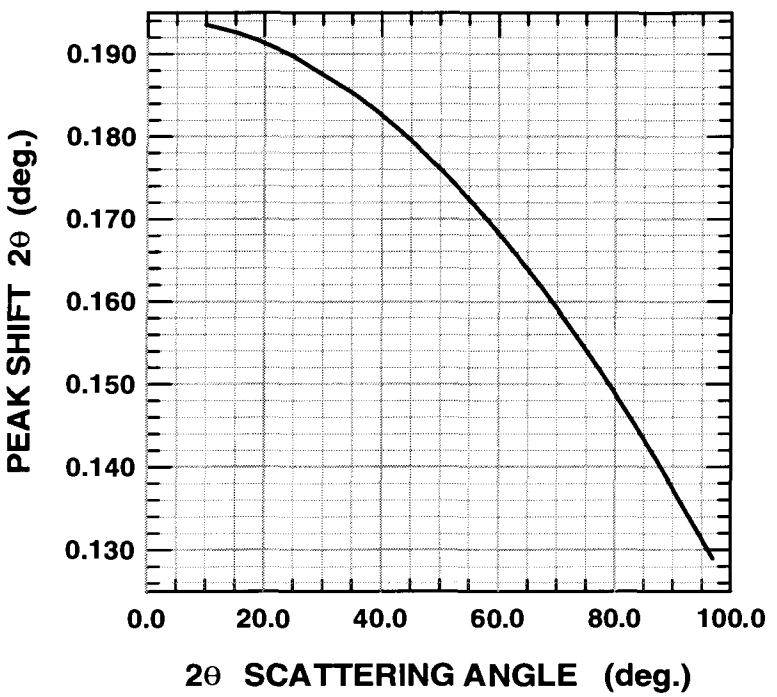

Figure 7.12: Peak shift *vs.* 2θ for an off axis of Δx=290 μm for test 'Safari'. The Curve was calculated using the diffractometer radius R=173 mm for the Philips PW1730 Diffractometer.

7.1.9 Discussion

On the surface, the orthorhombic to cubic transformation appears to take place in a simple manner. The orthorhombic phase disappears and the cubic phase appears as lithium is removed. However, the cubic phase which forms is not so simple, as indicated by two features of its diffraction pattern. First, the halfwidths of the peaks vary in an anomalous way across the pattern. Second, the positions of the Bragg peaks do not correspond exactly to those expected for a simple cubic system. This is clear based on the fact that the 400 peak shifts less than expected as x varies (see Figure 7.8).

The oxygen atom lattice is a cubic close packed framework in both structures, and the major structural difference is the repositioning of the manganese atoms. If the manganese atoms begin to reposition into 16d sites in a small area of the crystal and into 16c sites in another nearby region, then a 'stacking fault' will result at the interface between these two regions. Stacking faults are known to cause complex diffraction patterns (See Henricks and Teller, [56] and H. Shi [40]), with features similar to those observed here.

7.2 Test 'Hero1'

7.2.1 Charge Protocol for 'Hero1'

The active mass for the cathode in test 'Hero1' was determined as $m_A = 10.33\ mg$. The current for a 200 h rate is accordingly 14.72 μA . Directly after assembly the OCV was 3.231 V. I used two layers of separator for safety and, as mentioned earlier, the cell was assembled in regular stacking order. The entire test took 23 days and there was no problem regarding the seal of the cell. Over the course of three months we determined a loss in weight of approximately 1.6 mg. In Figure 7.13 we show the corresponding IVS-plot for the entire test. A total of 119 individual XRD profiles were recorded.

During the startup procedure the battery was short circuited while switching the SM-unit in the desired mode. The battery potential dropped down to an OCV of 0.6 V, but recovered over the course of minutes to about 2.6 V. I decided to proceed with the test for the same reasons mentioned earlier for test 'Safari'. A number of other 'incidents' during the test need mention.

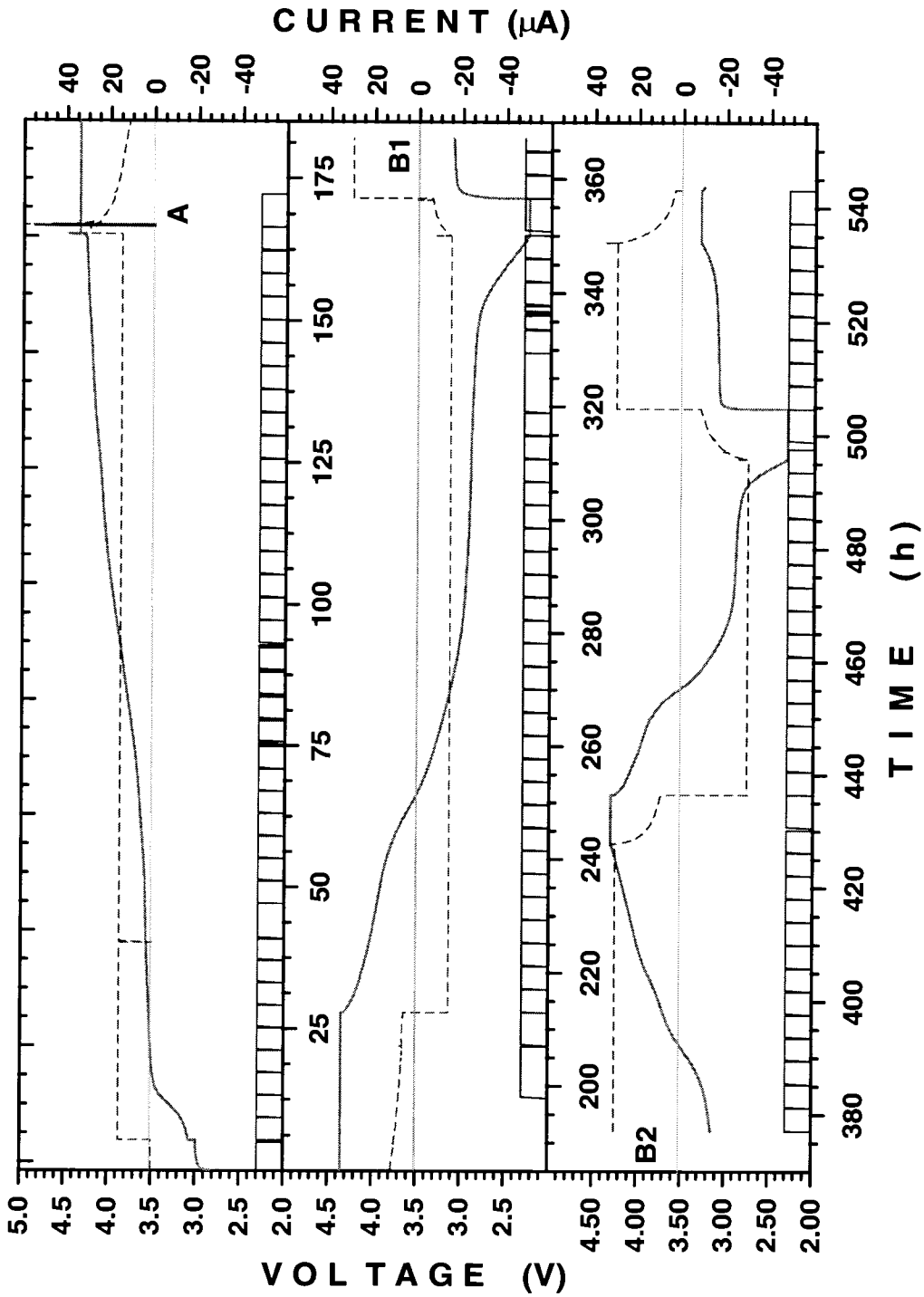

Figure 7.13: Voltage *vs.* time (solid line), current *vs.* time (dashed line) for test 'Hero1'. The XRD scan status is indicated by the rectangular squares on the bottom.

In an attempt to avoid shorting during switching in emergency situations, I installed a manual switch, while the test was running at $t = 162$ h. Careful bridging of leads should allow in theory to do this without causing any disturbance while recording the voltage. However, the battery was disconnected for a few milliseconds, which caused the instrument to record a voltage above the programmed trip point, so that the charger program switched the cell to the next sequence. After this I had to reconnect a loose wire and this meant disconnecting the battery for approximately one minute. This explains the current spike at $t = 162.1$ h. The first charge-discharge cycle was complete after 355 hours. For the next cycle we halved the charge rate (from 200 h to 100 h rate) due to time constraints scheduling all X-ray *in situ* experiments.

The test proceeded after protocol up to $t = 365$ h (scan No.71), when a control error[13] paused the control program 'CH236' for 10 hours. During this time scan No.71 was completed, no voltage was recorded, but the charging of the battery was continued. The X-ray machine was also idle for about eight hours. After subsequent restart, the test was finished according to protocol without major interruptions[14]. Particular detailed scans were obtained at (approximately) $t = 200$ h, $t = 355$ h, $t = 430$ h and $t = 500$ h (scan numbers: 1, 44, 78, 95 and 110, respectively), when the cell potential was approaching equilibrium conditions either at 4.3 V or 2.3 V.

The off-axis refinement was done using the positions of the orthorhombic phase of the first and second XRD profile. The result indicated that the center of the scattering plane was 62.3μm *above* the ideal plane as compared to 290μm *below* for test 'Safari'.

7.2.2 XRD Raw Data

Figure 7.14 shows the raw data of all 119 XRD profiles for the region between 34 deg. to 47 degrees. The intensity axis scales from 0 to 130000 counts but is labeled as arbitrary units. Subsequent scans are offset by 1000 counts. The profiles appear rather 'compressed' and many peaks appear as very weak. The average background scattering for each scan was at 2000 counts in this region. I call these type of graphs multi-plots.

In the bottom of this multi-plot the calculated intensities for the strongest $LiMnO_2$

[13] An undetected bug in 'CH236'.

[14] Minor interruptions like the exchange of the water filter for the X-ray generator etc.

peaks in this region are also shown. At 36.25 deg. we have the 100 reflection of lithium metal. The intensity of this reflection is not constant, it represents a typical *varying background* peak. The strong constant background peak at 41.5 deg. is the 002 bromellite (BeO) reflection and the peak at 46 deg. is the 100 reflection belonging to the beryllium metal. These strong peaks serve as 'reference peaks' in the diffraction pattern. Their uniform appearance in each scan gives confidence that we can compare the raw data of subsequent scans without applying a normalizing procedure to adjust the overall scale. The features belonging to the cathode appear much weaker compared to test 'Safari', since we have stronger absorption due to regular stacking.

These multi-plots convey something which is not visible in a collection of 119 single profile plots. The experimenter can easily trace the shifts in peak position and the incremental changes in peak intensity. It is also possible to identify the constant background peaks which strongly overlap with reflections belonging to the cathode. Such is the case for the BeO101 reflection which overlaps with the C400 reflection. It is possible to estimate the magnitude for this reflection and to subtract if out from all 119 XRD profiles.

Along the right ordinate axis we indicate when the cell reached the upper and lower trip-point and the corresponding scans are emphasized with a thicker line. What is most important in this test, is the behavior in the 3.0 V region. In Figure 7.14 these are the scans before and after the scan at the lower trip-point at 2.3 V. If one examines this graph with care one finds that the 6th and 7th scan prior to the scan taken at 2.3 V (first cycle) displays clearly *two* peaks at 44.1 deg. and 45°, indicative for a two phase region. In scan at 2.3 V (thick line), we find that the strong reflection at 45.1 deg. appears simultaneously with a weaker reflection at 39.7 degrees.

In the following section we describe the subtraction method in more detail and address some interesting detail which we discovered accidentally by using this method.

7.2.3 Subtraction of Background Peaks.

Variable Background Peaks

In Figure 7.15 (a) we show a selection of 43 XRD profiles in the region between 31.8 deg. to 40.2 degrees. Plotting fewer profiles on the ordinate axis as in Figure 7.14, enhances the visibility of weaker peaks. In (b) we show the same data, where the Lit100 peak for each scan was subtracted from the raw data file. In order to accomplish

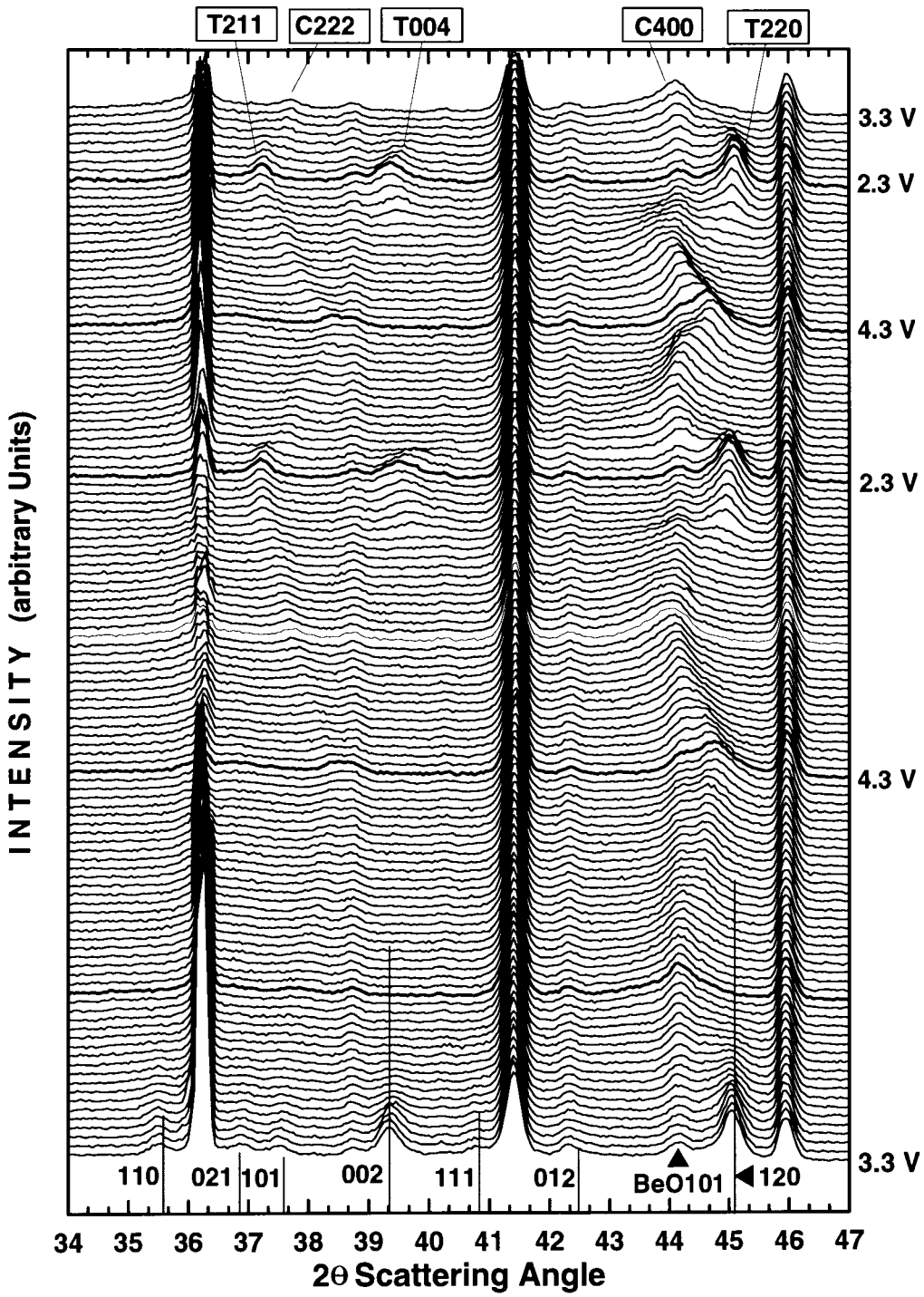

Figure 7.14: All 119 XRD scans for plotted for test 'Hero1'. At the bottom we show the calculated intensity pattern for $LiMnO_2$.

this we defined an artificial model for each profile, such that we place a number of broad peaks at the left and the right side of the Lit100 reflection. The lithium peak itself was modeled by three peaks spaced approximately at equal distance over its peak width. The peak width of the model peaks was rather narrow, compared to the peaks at the side. The peak positions were *not* refined and the slope of the linear background was also fixed, whereas the constant background was kept as a refineable parameter. Defining more than one peak for the Lit100 reflection allows one to generate a very accurate model function for this peak. The broad peaks left and right to Lit100, serve to pick up the broad background characteristic of the C311 reflection which is disrupted by the narrow Lit100 reflection.

With the help of a graphical interface it was possible to check the refinements for consistency. That means to plot the model function for the background peaks only and compare them to the raw data, or to plot the model function for the Lit100 peak only and compare it to the raw data.

The next step was then to subtract the calculated intensity of the model function of the Lit100 peak from the original raw data and copy the result into a new (modified) raw data file. This was done for each of the selected scans in Figure 7.15 (a) and the result is shown in (b). For most of the scans this method worked quite well and, as we can see the C311 reflection appears left of the C222 reflection. The simultaneous shift in position of the two peaks is due to expansion and contraction of the cubic lattice. We also deduce from Figure 7.15 (b) that the intensity of the 311 peak decreases as we approach the two phase region at 3.0 V (scans 77 and 111). However, before scan No.77 we find a number of profiles where the subtraction left a peak peak at 36.0 degrees. We are not sure whether this is an artificial result of the subtraction or whether this peak bears real significance. The modified set of profiles was then used for refinements of positions, intensities and half widths.

Constant Background Peaks and Mechanical Runaway

In Figure 7.16 (a) and (b) we show again all the 119 scans for the region between 38.5 to 47 degrees. In (a) we labeled the reflections belonging to the beryllium and the bromellite phases and in (b) we labeled the 400 reflection belonging to the cubic phase. Close to the scans taken at 2.3 V we labeled the peaks belonging to the tetragonal phase, T004 and T220 close to the scans taken at 2.3 V. We obtained an initial fit for the first scan in Figure 7.16 (a) for this region. The peaks of the initial model

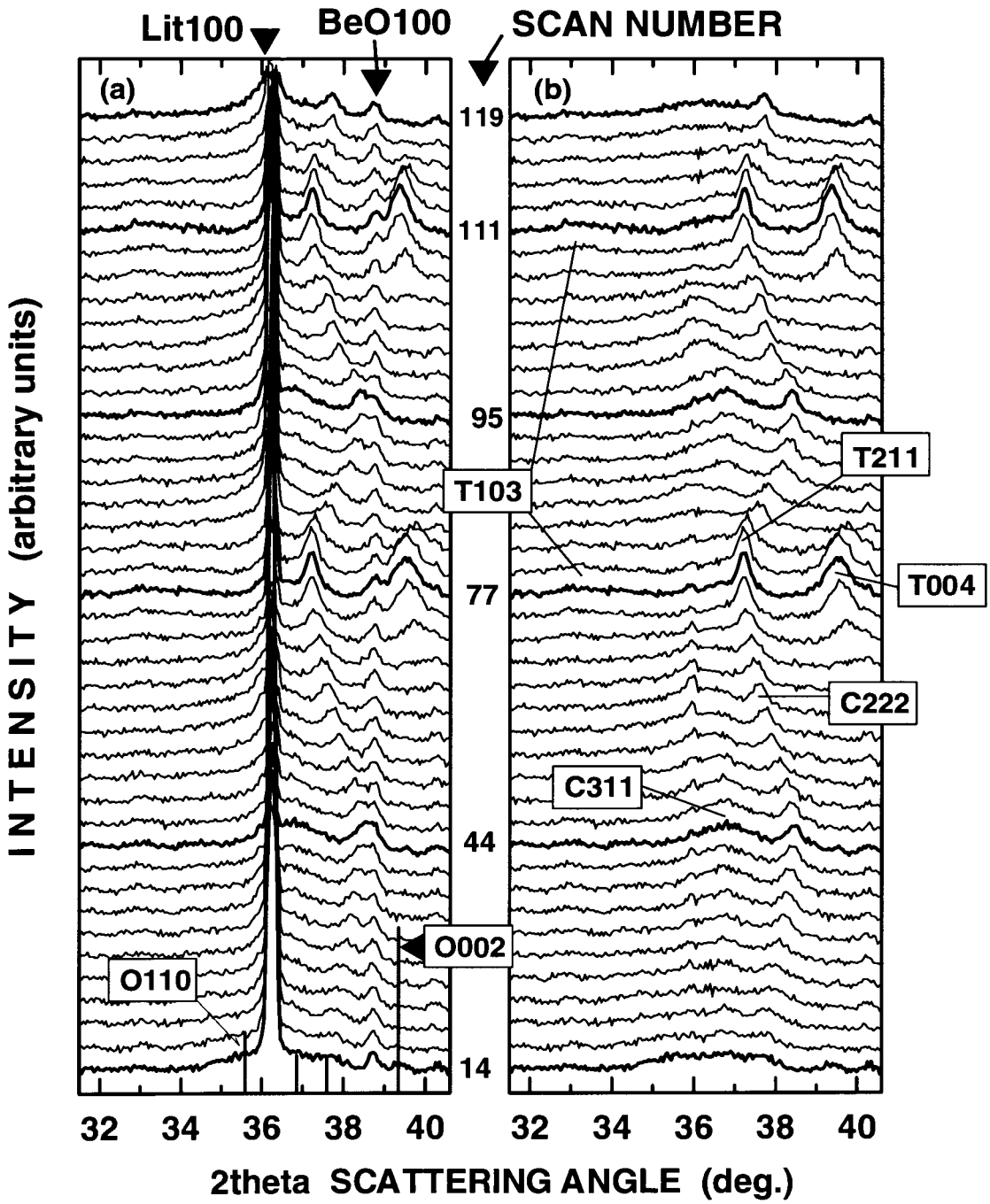

Figure 7.15: Selected XRD profiles before (a) and after (b) subtraction of constant BeO100 and variable Lit100 background peaks.

function which correspond to the beryllium and bromellite phases were subtracted from *all* the other subsequent scans to obtain a modified set of raw data. In (b) we notice immediately there two 'S-like' features where the Be002 and the Be100 peak used to be. These features become more pronounced with increasing scan number and they indicate that the position of these peaks shifted to higher angles with increasing scan number.

Although the magnitude of 0.03 deg. of the shift is rather small, we wanted to find out whether we have here a mechanical problem in the goniometer or an effect related to the *in situ* X-ray battery.

Mechanical runaway could appear if the zero setting of the goniometer shifts a little bit each time it is reset from 90 deg. to 10 deg. after each scan. Mechanical runaway can be traced by monitoring peaks of known substances in subsequent calibration scans. In Figure 7.17 we find the results of such calibration scans, performed on the two goniometers in use. Before and after each test we used a silicon wafer to acquire a scan at high precision[15]. The 311 reflection of silicon was refined and in Figure 7.17 we report the position of the Cu-$K_{\alpha 1}$ component of the 311 reflection for the different scans.

Experiment 'Hero1' was performed on channel 1 between July 27 and August 19. We find that the 311 peak position shifted by 0.005 deg. to a *lower* angle during the course of the experiment. This shift corresponds to recording of the same peaks at lower angle with increasing scan number, which is in contradiction to the observed shift in Figure 7.16 (b). Moreover, the magnitude is too small compared to the observed shift of 0.03 degrees.

In order to find out about effects related to the charge and discharge of the cathode, we refined the position of the strongest peak (BeO002) and plotted it against scan number in Figure 7.18. As we can see there is a strong correlation between the direction of the shift and the direction of the charge current. This effect can be explained if we consider the process of depositing lithium ions on the metallic lithium anode.

As described in chapter 3, lithium ions are not evenly electro plated on the metallic lithium substrate. We estimate the maximum thickness of the deposited lithium metal layer, by assuming that all of lithium in the cathode forms an even layer with the

[15]Source slit: $\frac{1}{2}^{o}$; Receiving slit $\frac{1}{15}^{o}$; Step size: 0.01 deg. and counting time 3 seconds at each step.

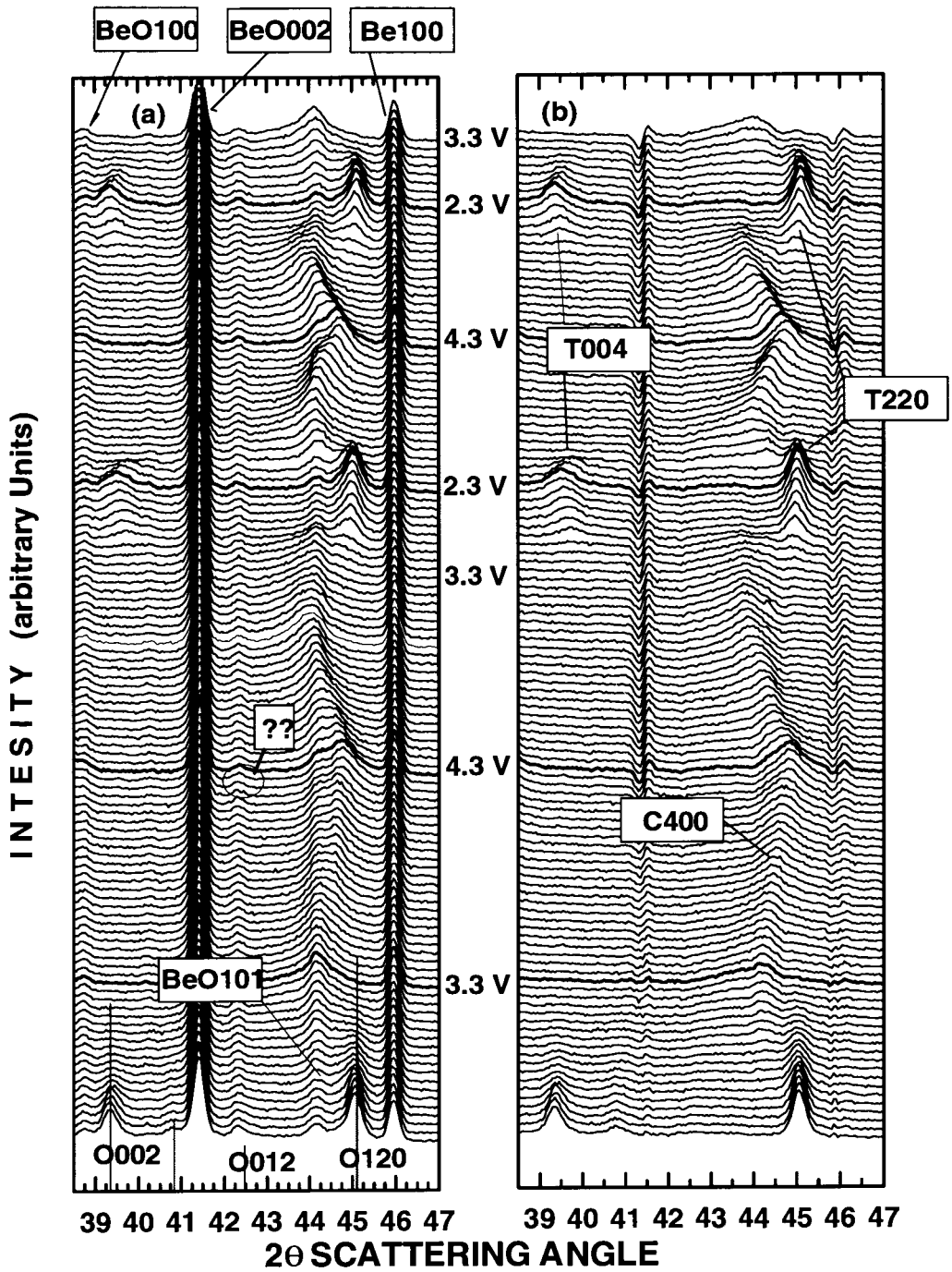

Figure 7.16: Selected XRD profiles for region 2 before (a) and after (b) subtraction of constant and variable background peaks. The increase in intensity of the 'S' feature in (b) indicated a shift in the scattering plane of the foil disk. The questionmark labels an unidentified constant background peak.

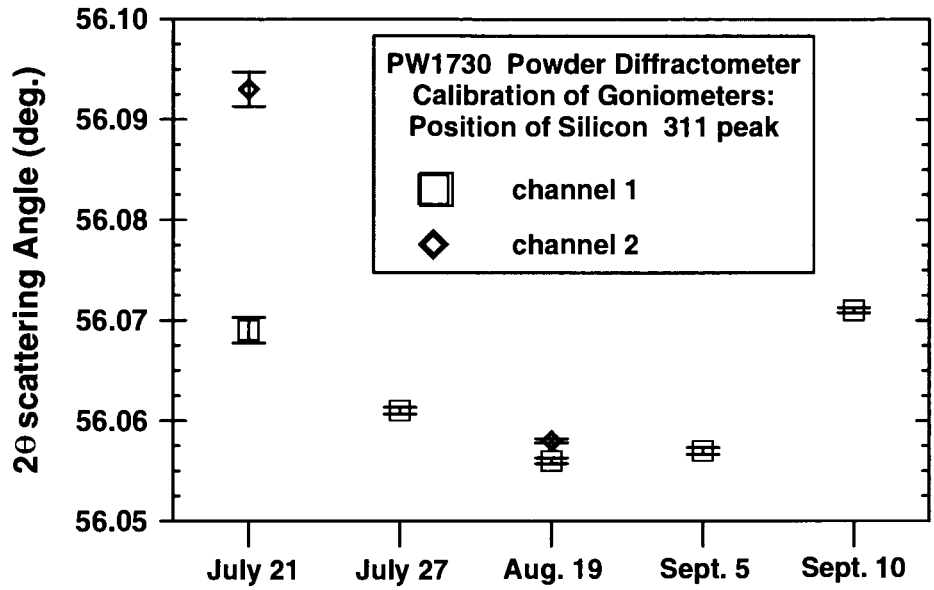

Figure 7.17: Calibration of goniometers by measurement of Si 311 peak positions.

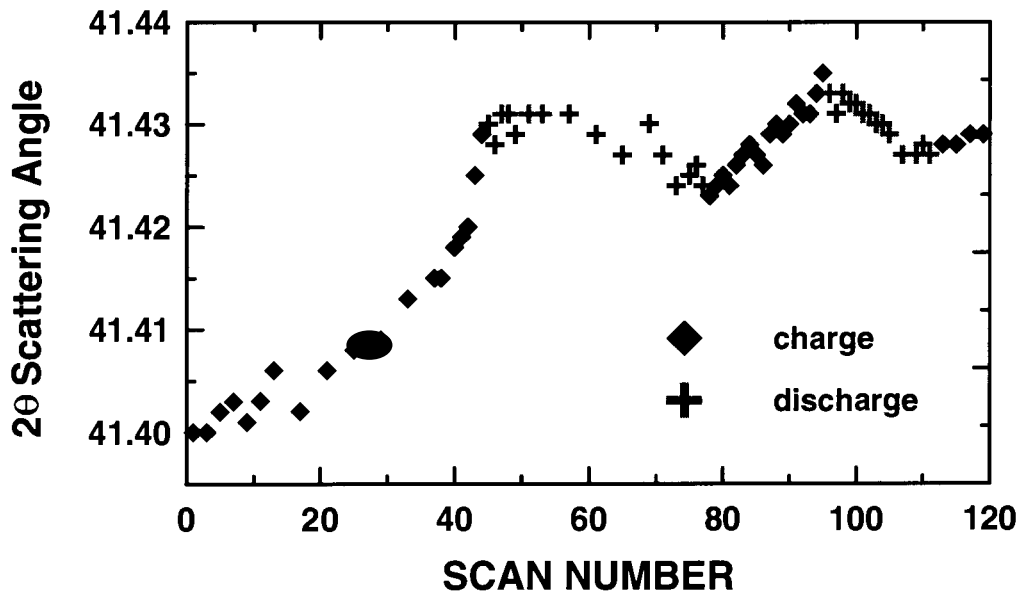

Figure 7.18: Shift of the 002 reflection of the bromellite phase (BeO).

density of lithium metal. For test 'Hero1' 0.76 $\times$ 10^{-4} g of lithium yield a layer thickness of 10 μm. If we assume that the plated lithium is only 50 % dense we

double the estimate. Additional thickness is necessary to include the formation of the SEI on initial charge, which is responsible for the dendritic growth of the lithium layer. We include an additional 20 μm for the SEI and predict a maximum increase of 40 μm.

Additional thickness will increase the stack pressure and lead to a stronger force on the beryllium foil disk. We expect the disk to bulge out, which translates into shifting of beryllium peaks to a *higher* angle. Consulting the cross sectional drawing of the *in situ* X-ray cell in Figure 5.3 will clarify this idea. The overall peak shift of 0.03 deg (2θ!) was measured by fitting the BeO002 reflection in the last scan (No.119) and comparing the position with the refinement for the first scan. According to Equation 4.13 this would correspond to an off axis movement for the foil disk of approximately 60 μm. This is rather large not only compared to our estimate of a maximum of 40 μm, but also compared to the thickness of the anode itself (lithium metal foil of 125 μm). Since the measured shift in the goniometer calibration runs before and after the experiment is an order of magnitude smaller we rule out mechanical runaway as an error source. We can only speculate that spring in the coin cell displayed non-linear behavior.[16]

Consistent with Figure 7.18 are the facts that the strongest shift appears with initial charge, that the shift reverses on discharge as we remove lithium and that the shift for the second charge is smaller, since we have already have porous lithium from the from the first charge on the lithium metal anode.

Multiplots for C440 Region

A third region where all the phase transitions are particularly visible is shown in Figure 7.19 for the angular range between 60 deg. and 67 degrees. In the beginning of the experiment we see the 122 and 131 reflections from the orthorhombic phase disappearing. At the same time a cubic phase[17] forms, evident by the 440 reflection. The 440 peak shifts to higher angles as lithium is removed from this new phase. In order to demonstrate the subtraction of the Lit211 reflection, Figure 7.19 is also split into two graphs (a) and (b). In the two phase region at 2.3 V we find again that the cubic 440 reflection disappears in the background noise and appreciable intensity is found at positions above and below the last measurable cubic position. These

[16]Sudden increase at scans 40 ?

[17]Not necessarily a single phase as we discussed it in section 7.1.

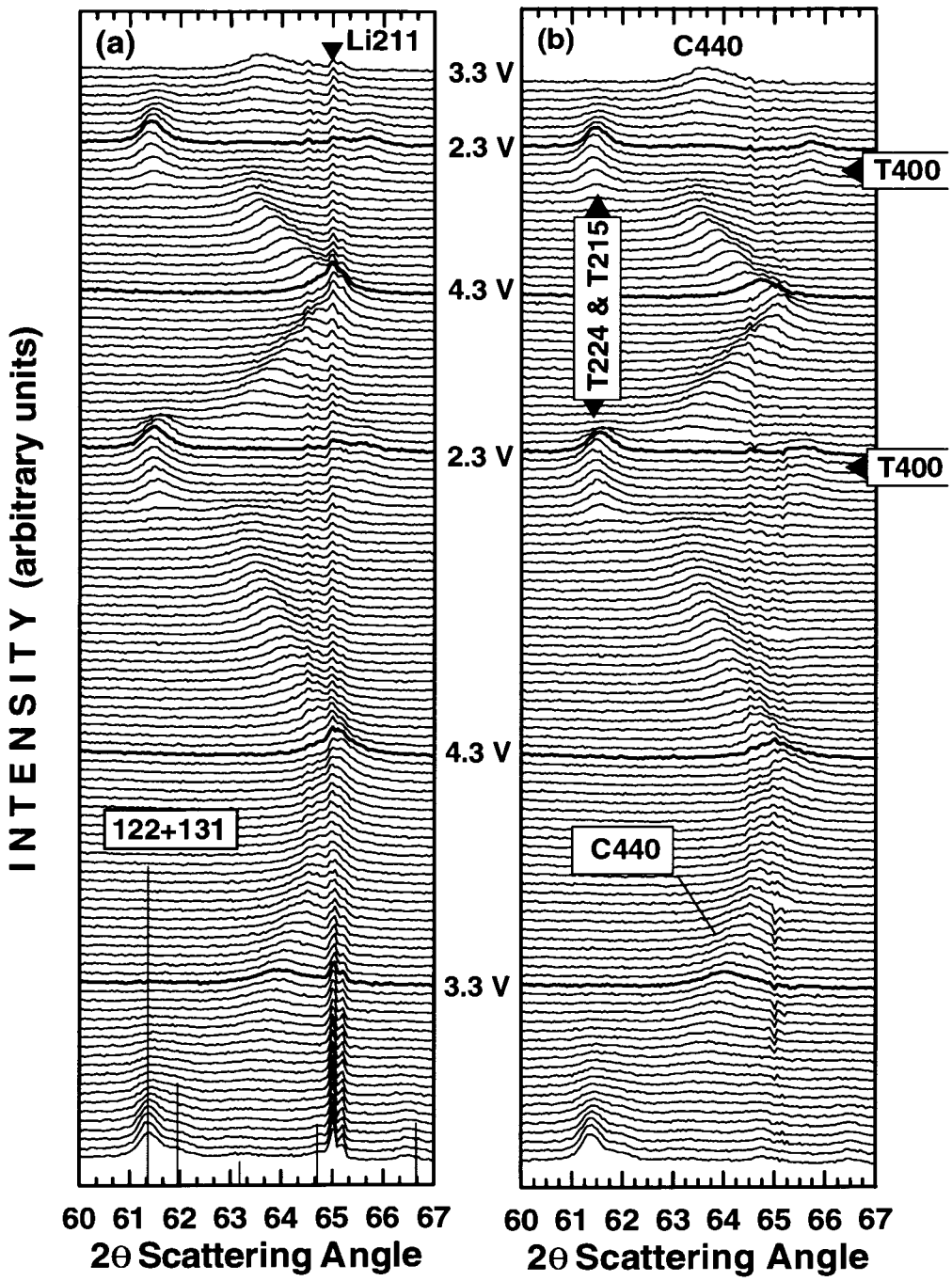

Figure 7.19: All 119 profiles for the region between 60 deg. and 67 deg. where the interplay of the three phases is particularly visible. (a) is before and (b) after subtraction of Lit211 at 65 deg.

reflections can again be identified as from the tetragonal phase. The strong peak at 61.4 deg. corresponds to the tetragonal 224 and 215 reflections and the weaker feature at 65.8 deg. to the 400 reflection. A quick examination allows one further to deduce that the half widths of both the C440 as well the T224 reflection become narrower if we compare cycle two with cycle one.

7.2.4 Intensity and Position Refinements

In order to show how complete the phase transition in the two phase region appears, we refined the intensities for the two strongest reflections of both phases (C400 and T220) for all 119 data sets. We kept the shape (gl-ratio) and halfwidth parameters constant and allowed only the variation of position and intensity, the result is shown in Figure 7.20. That meant necessarily that we did not refine for best G.O.F. as the

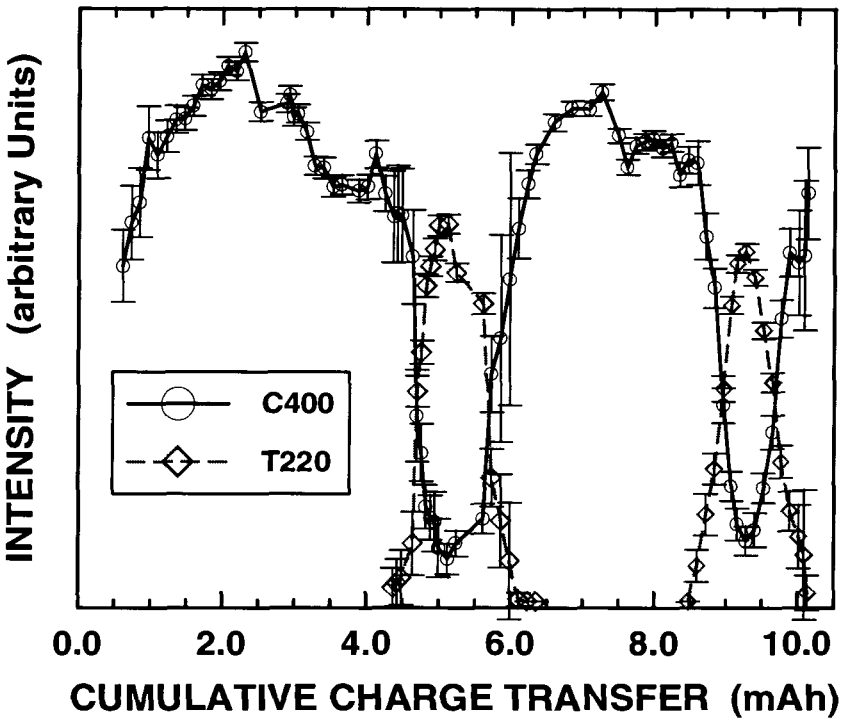

Figure 7.20: Intensity refinement of the 400 reflection belonging to the cubic phase. In the two phase region we see the intensity drop down dramatically and the intensity of the 220 peak of the tetragonal phase increases.

model for the peak became less appropriate with increasing scan number. However

the intensities are comparable and we find in both two phase regions (for cycle 1 and cycle 2) a dramatic drop of the C400 intensity along with a simultaneous increase of the intensity of the tetragonal 220 reflection. Instead of plotting these parameters against scan number we used parameter which we called *'cumulative charge transfer'*. It denotes the absolute value of all transferred charge in the experiment. Thus charge and discharge capacities are just summed by magnitude. We chose this parameter over time or scan number, since it reflects better the changes applied to the system. As we can see from Figure 7.13, there are times in the experiment where we transfer very little charge over a long period of time. For example beginning at 175 h where the battery is switched to potentiostatic mode in order to approach electrochemical equilibrium. The same parameter was chosen as a common abscissa for the plots shown in Figure 7.21. Here we plot in (a) voltage *vs.* cumulative charge transfer and compare to it the position refinements for the most prominent peaks of the cubic phase and the tetragonal phase (b) and (c). In the bottom panel (d) we show the refinements of the lattice parameter for the cubic phase as a function of cumulative charge transfer. We indicated for the position refinements the reported positions [54] of the tetragonal phase by thin dashed (dark) lines and the reported position of the cubic phase ($Li_{(1-x)}Mn_2O_4$ $x = 0$) by the thick dashed (grey) line. The simultaneous appearance of many reflections of the tetragonal phase are sufficient proof for the existence of this phase.

One peak deserves a further comment. The tetragonal 211 (and 202) reflection appears almost at the same postion where the cubic 222 peak dissapears. That we have in fact a two-phase phenomenon in that region is supported by two facts. The first is evident from Figure 7.16 at scans 77 and 111. The half width of the two close reflections of the tetragonal phase (T211 and T202) are smaller compared to the weaker C222 reflection. Not shown is the fact that an examination of the half widths of the peak in the intermediate two-phase region shows for scans 70 and 71 an unexpected increase of the halfwidth. This is typical if peaks of two different phases are too close in position in order to be resolved separately.

7.2.5 Lattice Parameters

The lattice parameter for the cubic phase was refined using the same method outlined in section 7.1.8 for test 'Safari'. It is a nice result to see that the lattice parameter for the cubic phase is strongly correlated to the cell potential as can be seen comparing

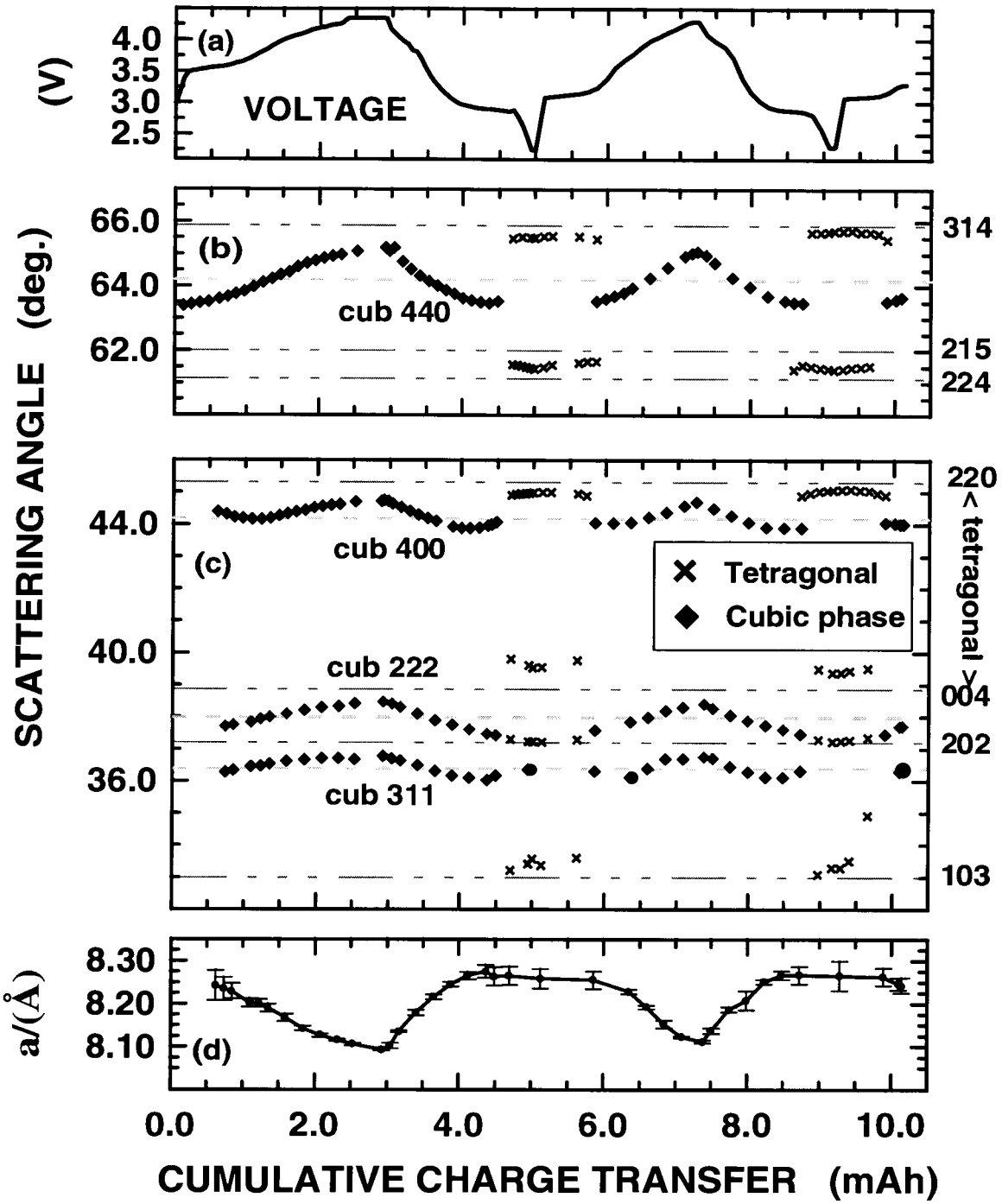

Figure 7.21: (b), (c) Position refinement of the strongest peaks belonging to the cubic phase and the tetragonal phase *vs.* cumulative charge transfer.

panel (a) with panel (d) in Figure 7.21. In Figure 7.22 we compare the lattice parameter refinements for the two *different* tests 'Hero1' and 'Safari' for the initial charge.

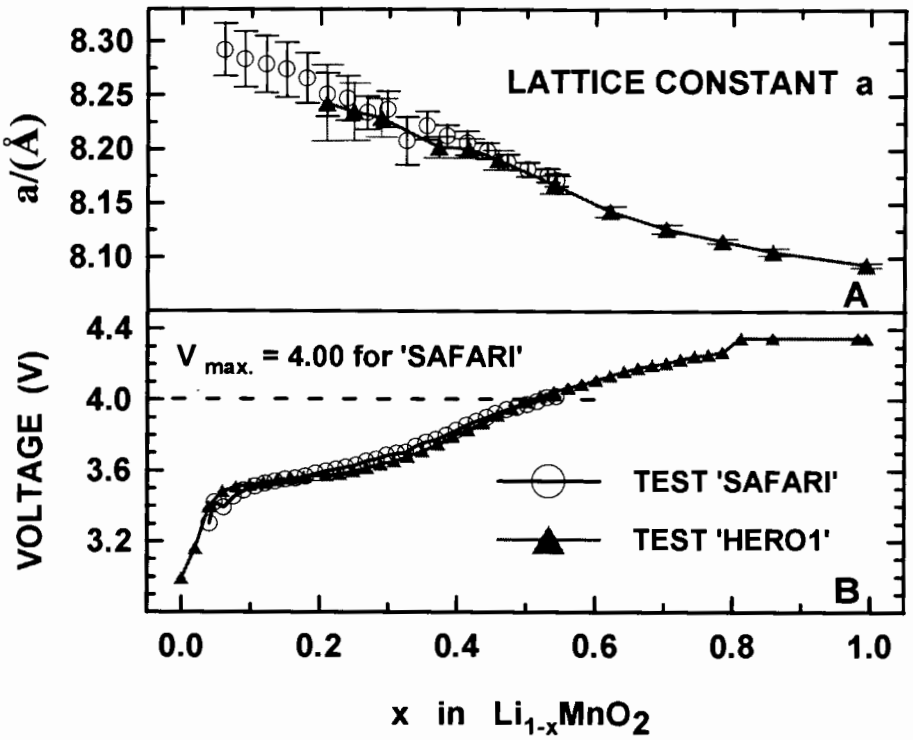

Figure 7.22: (A) Lattice constant for the cubic phase forming on initial charge for 'Hero1' and 'Safari' *vs.* x in $Li_{(1-x)\ 2}$and corresponding voltage (B). Although total capacities, the off-axis shift, and the charge rate greatly differ, we find good agreement for the lattice constants within the errors of the refinement.

In panel A we see that the parameters for the two tests agree well within the errors of the refinement. This is very encouraging.

It confirms that the expected impact on dissolving beryllium in test 'Safari' did not falsify the currents significantly. It also confirms that the values for the off axis in the two experiments must be close to the actual values. As pointed out in section 7.1.8, we used the off axis shift as a fixed parameter in the refinement of the lattice constant for the cubic phase. The third option, that the two error sources just cancel out, is rather unlikely.

7.3 Test 'Doberman'

7.3.1 Charge Protocol

The incentive for this experiment was the study of the crystallinity of the different phases as the cell is cycled. In order to obtain as many cycles as possible the cell was charged quickly at a 20 h rate and discharged even faster at a 10 h rate. The details of the charge protocol were already discussed in section 5.4. XRD spectra were only acquired at cell potentials of 4.3 V after charge, at 3.0 V (later 3.3 V) on discharge and at 2.3 V after full discharge. The battery was always given time to reach conditions close to equilibrium, which explains the more complicated nature of the charge protocol. Spectra taken at 3.0 V (later 3.3 V) extended over a larger angular range than spectra taken at the upper and lower trip-point. For comparison we report the specifications for this cell. The active mass of the cathode was 11.97 mg which corresponds to a total charge capacity of 3.411 mAh. The OCV after assembly was 3.242 V. The IVS-plot for the entire test is shown in Figure 5.9, and a magnification for one full cycle was given in Figure 5.8.

The faster discharge rate is justified by the fact that removal of lithium from the lithium metal anode is less problematic concerning the growth of dendrites. On charge however it is advisable to keep the rate rather slow, in order to allow for a uniform deposition process. To our satisfaction the test proceeded without any major interruptions until shunting occurred at the start of the 21st cycle.

In Figure 7.23 we plot the charge and discharge capacity *vs.* cycle number. Depending on the rate of discharge we distinguish two regions. For region 1 we notice, in particular, that the capacity is much lower for discharge, whereas for region 2 the charge transfer is balanced. Linear least squares fits emphasize the trends. As we approach cycle 20 the total capacity falls below the theoretical limit for the $LiMn_2O_4$ system (148 mAh/g). We also included the discharge capacities for the upper and lower plateau. Here we see for cycles 1 to 3 the discharge up to 3.0 V for the upper plateau and for cycles 4 to 20 we discharged the upper plateau to 3.3 V.

Initially we set the trip-point for discharge at 3.0 V but we decided to switch the trip-point to 3.3 V in order to obtain crystallographic information for $Li_{(1-x)}Mn_2O_4$ with approximately $x = 1$, which is the regular $LiMn_2O_4$ stiochiometry. The anticipated increase in internal resistance by incorporating three layers of separator was less profound than expected. This could only be assessed at run time after calculating

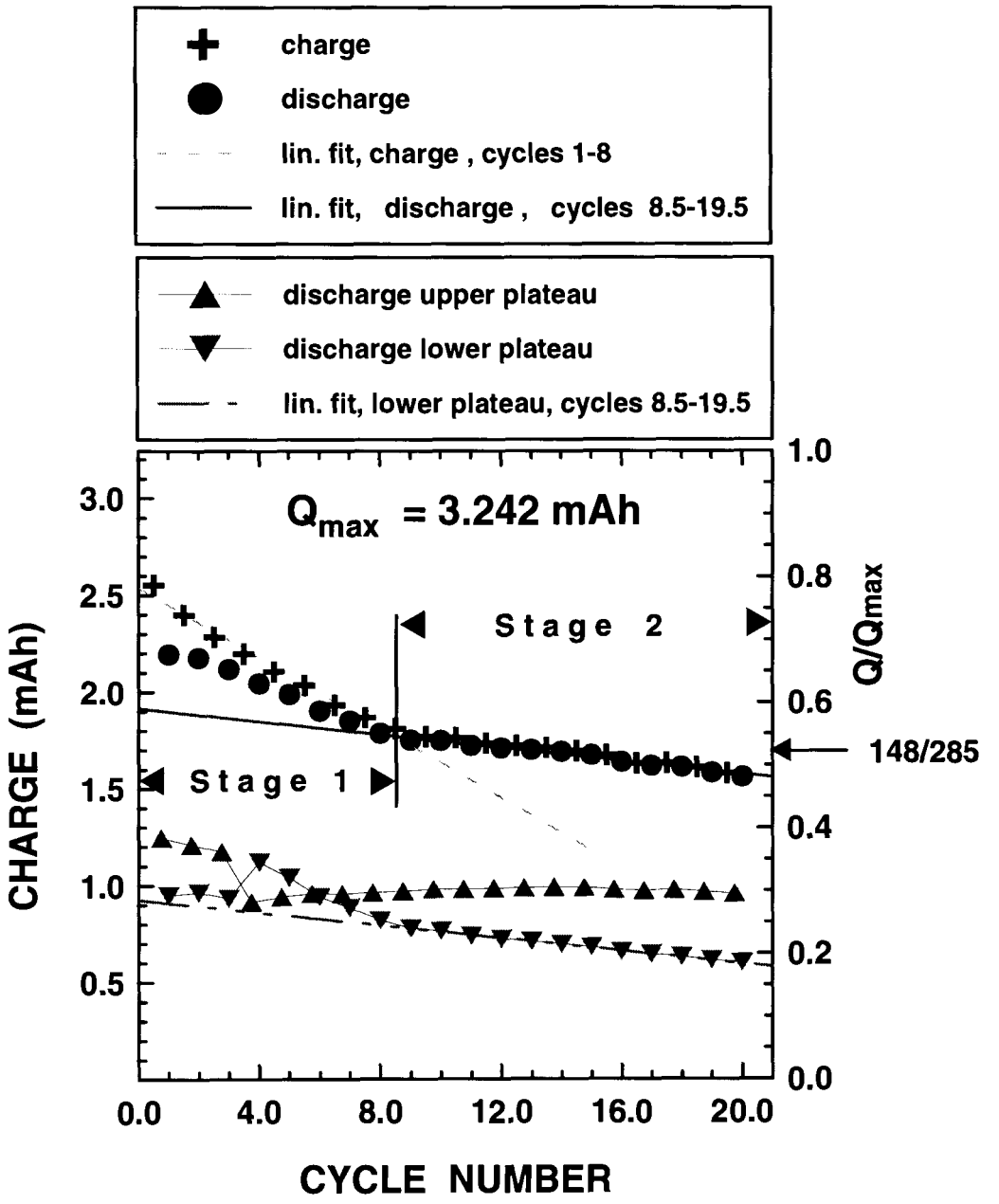

Figure 7.23: Charge and discharge capacity *vs.* cycle number. Up to cycle 8 there is strong capacity fade. In particular we notice the difference between charge and discharge capacity. After cycle 8 charge and discharge capacities are the same and the capacity fade is lower. For easier reference we call cycles 1 to 8 'stage 1'and cycles 9 to 19 'stage 2' of the experiment. The capacities for the upper and lower plateau are also indicated.

the transferred charge between the two plateaus.

7.3.2 XRD Raw Data

Figure 7.24 shows the all raw data for all XRD spectra for the angular range between 35 deg. to 47 deg., region 1, and Figure 7.25 shows all the profiles for region 2 which extends from 60 deg. to 67 degrees. The XRD patterns were sorted according to cell potential. For each scan we acquired three profiles, one at 4.3 V, the second at 3.3 V (3.0 V for the first three scans) on discharge and the the third at 2.3 V after full discharge. This provides us with direct comparison of the diffraction pattern as a function of cycle number for the three different electrochemical potentials. The ordinate is labeled 'Intensity (arbitrary units)', in order to spare space for the graph. The actual units are counts and in all multi-plots of this kind, the successive scans have an offset of 1000 counts each.

In particular we notice in Figure 7.24 that all the orthorhombic peaks are shifted to lower angles if we compare the positions of the initial scan to the calculated positions. The refined positions of the initial scan were used to refine the off-axis parameter as it was done for test 'Safari' and 'Hero1'. The center of the scattering plane is shifted 82 μm below the ideal plane. If we compare the initial scan with the subsequent scans taken at 3.0 V we find the orthorhombic phase is gone.

Aside from the peaks C222 and C400, we only see in Figure 7.24B at 3.0 V (3.3 V) constant and varying background peaks, of which the strongest are labeled on top in part A. The C400 peak strongly overlaps with the BeO101 reflection, which is indicated in Figure 7.24C. At 4.3 V we find the peaks of the cubic phase have shifted to higher angles about delithiation. No new phases are apparent at this potential.

At 2.3 V, we find in Figure 7.24A strong evidence for a phase transition from cubic to tetragonal or another intermediate phase. For the first two scans in the 2.3 V region the observed peaks[18], T211, T202, T004 and T220 are very broad and their positions are not where we expect them according to our calculated positions (see chapter 4 or Appendix B). In view of our knowledge of how the peaks in the tetragonal phase shift (see section 4.2.3) as they approach the cubic unit cell, we can still identify the observed peaks as belonging to a tetragonal phase with different lattice parameters (altered c/a ratio).

[18]which we labeled after the tetragonal phase since it seemed the most obvious choice.

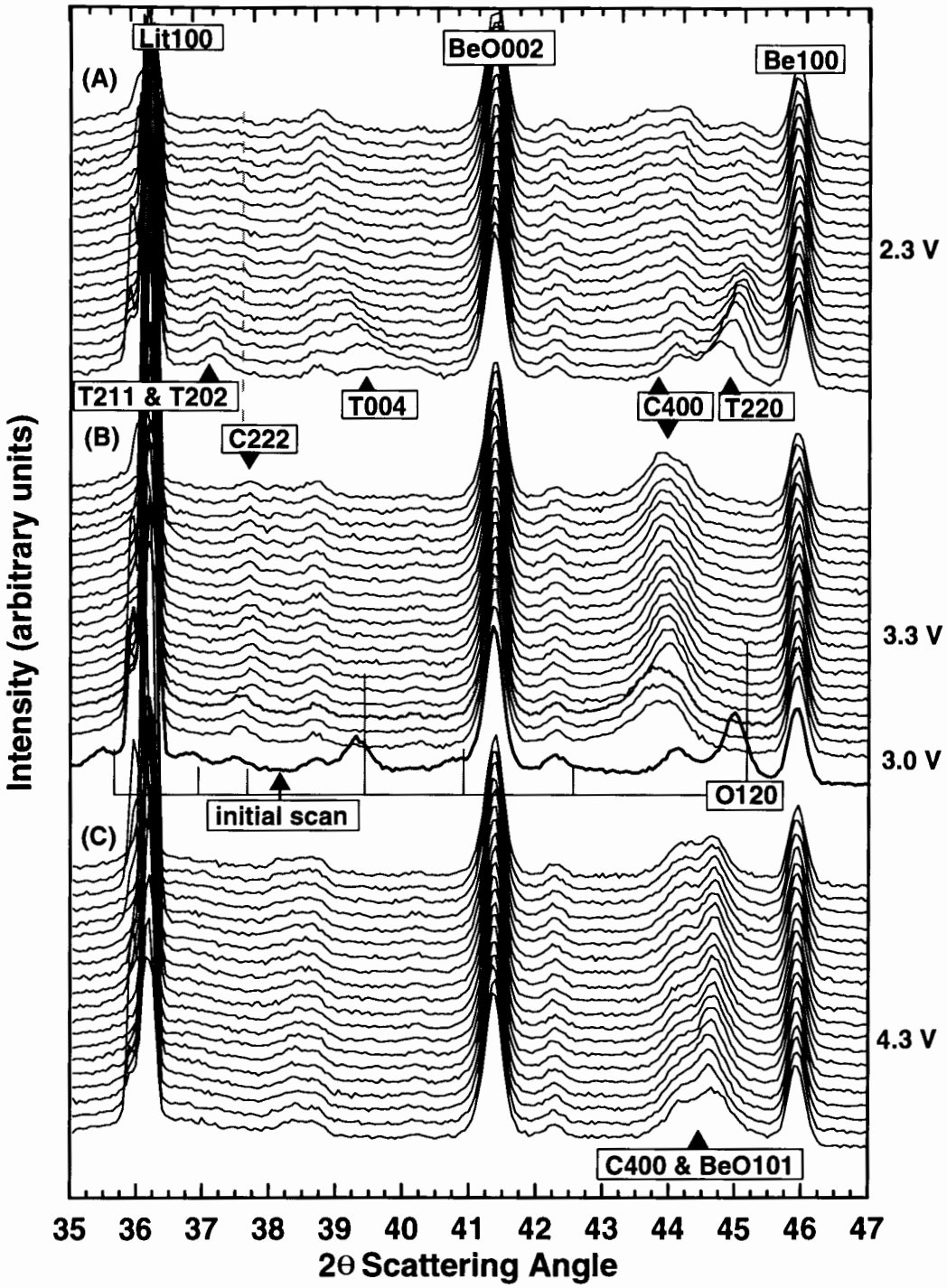

Figure 7.24: XRD raw data for region 1 (35 to 47 degrees). The consecutive scans were sorted according to cell potential: (A) 2.3 V, (B) 3.3 V (3.0 V for the first three scans), (C) 4.3 V. The scan plotted with a thick line is the initial pattern. The calculated positions for the orthorhombic phase are indicated.

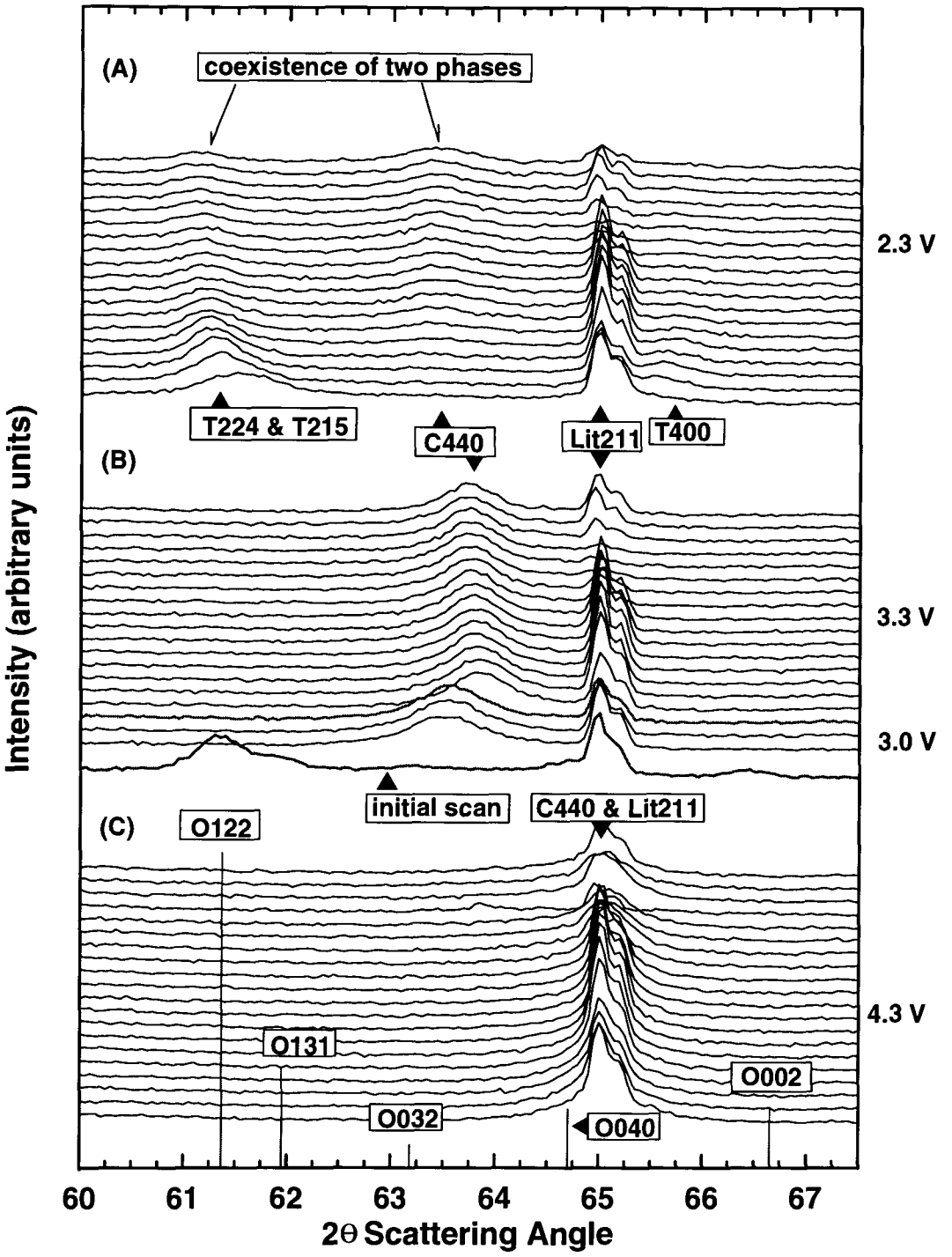

Figure 7.25: XRD raw data for region 2. Consecutive scans were sorted according to cell potential: (A) 2.3 V, (B) 3.3 V (3.0 V for the first three scans), (C) 4.3 V. The scan plotted with a thick line is the initial pattern. The calculated positions for the orthorhombic phase are indicated.

During the next three scans we observe that the intensity of the tetragonal peaks increases while their halfwidth is decreasing. We also notice the strong shift for the T004 and T220 reflection in opposite directions towards the calculated positions. After the intensity of the tetragonal peaks is at a maximum at scan 5 we find their intensity decreases while the intensity of the cubic phase increases steadily.

The same analysis applies to region 2, shown in Figure 7.25, except that there is less disturbance by background peaks at 2.3 V. In Figure 7.25C, however, we find the cubic 440 peak strongly overlaps with the 211 reflection from the lithium metal anode. In Figure 7.25A we find again evidence for the tetragonal phase with the two close 224 and 215 peaks at 61.5 deg. and the weaker 400 reflection at 65.75 degrees. The tetragonal and cubic phase clearly coexist for scans taken for cycles 5 to 19. Moreover we find that the intensity of the C440 peak increases as the intensity of the T224/T215 reflection decreases.

We want to point out explicitly that the peaks of the tetragonal phases cannot be attributed to the orthorhombic phase although the positions (and shape) of their peaks in the diffraction patterns do almost match. This is the case for O122/O131 and T224/T215 and apparent also in Figure 7.24A and B, if we compare O120 and T220, O002 with T004 and O021 with T211/T202. In order to give evidence for this we show in Figure 7.26 a similar graph for the region between 24.2 deg. to 26.6 degrees. Here we see a strong and broad peak belonging to the polyethylene separator. On the left tail of this peak we see clearly the 011 peak belonging to the orthorhombic phase. The calculated position is indicated by the single vertical line. Neither at 2.3 V in Figure 7.26A, 3.3 V (B), nor at 4.3 (V) (C) do we find any evidence that appreciable intensity is scattered in this direction for cycles 1 to 19. Another region between 75.5 deg. to 81 deg. is shown in Figure 7.27 and displays The 404 peak of the tetragonal phase and the 444 peak of the cubic phase at 2.3 V. The peaks were not included in the refinement due to time constraints. However we include the data since we want to refer to some qualitative properties of the T404 peak later on in the thesis. In summary we find a tetragonal distorted phase with different lattice constants.

7.3.3 Modified XRD Data

As described it in section 7.2.3 we removed interfering background peaks where it was possible by subtraction. The results are shown in Figure 7.28 for region 1 and in Figure 7.29 for region 2. In region 1 we marked two reflections as unknown.

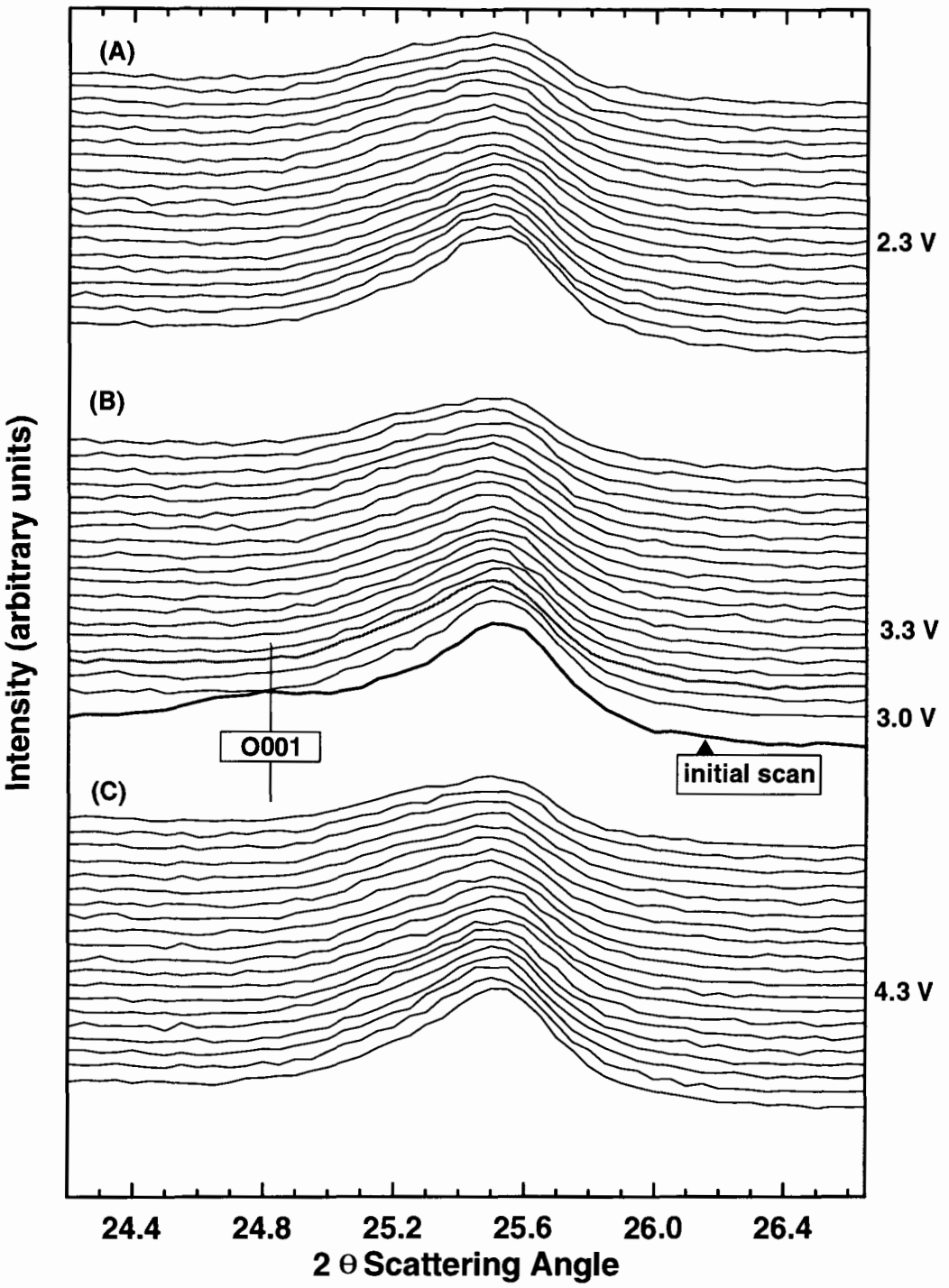

Figure 7.26: XRD raw data for region of the 011 peak of the orthorhombic phase. Consecutive scans were sorted according to cell potential, (A) 2.3 V,(B) 3.3 V (3.0 V for the first three scans) and (C) 4.3 V. The scan plotted with a thick line is the initial pattern. The calculated position for the O011 peak is indicated.

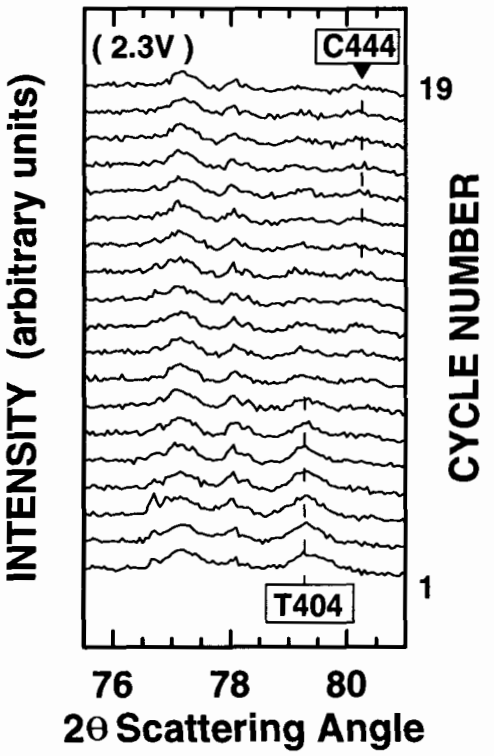

Figure 7.27: XRD raw data for region 3. T404 and C444 were not refined since their intensity is rather small. There is no shift in peak position apparent for the T404 peak. The position is unaffected by changes in the c/a ratio of a certain kind.

They appeared however consistently in all XRD raw spectra with the same strength, position and halfwidth. Most likely they are part of crystal phases belonging to the cell hard ware. Not shown are the modified data for region 1 and region 2 at cell potentials 3.3 and 4.3 V.

7.3.4 Individual Peak Refinements

The analysis so far is qualitative. In the following we display the results for peak parameter refinements as a function of cycle number. In order to obtain comparable results we refined the gl-ratio[19] in the beginning, but kept this parameter fixed for all subsequent refinements of the same peak.

The refinement tool

The task of refining the same peak for separate XRD spectra was greatly accelerated by an automated fitting program. Here one tests by trial and error the succession of refinement steps needed to arrive at a good fit for the first XRD dataset. The program allows one to repeat these steps automatically for the next XRD scans. For this purpose a scripting procedure allows the generation of refinement command scripts. The command script is executed automatically on XRD files which are listed in a separate file.

Typically one starts with the refinement of the constant background parameter, since the constant background level varies between different scans. Next one refines the intensities, positions and halfwidths separately. Combined refinements of intensity and halfwidth and halfwidth and position further improve the fit. The background is now refined a second time. If more than one peak is defined in the model function, than intensity and position and halfwidth are refined for each peak in succession. At the end all parameters are included in two or three final refinement steps.

Loading of XRD raw data, the refinement and the writing of appropriate output files for the results is all done automatically. During each refinement step the computer reports the χ^2-value and by this it is possible to monitor the consistency of the refinements across separate raw spectra. When the model becomes inappropriate or other problems occur, the χ^2 value will rapidly increase. If that happens it is possible to pause the whole refinement job and view the fitting function together with raw

[19]Shape parameter: ratio between Gaussian and Lorentzian

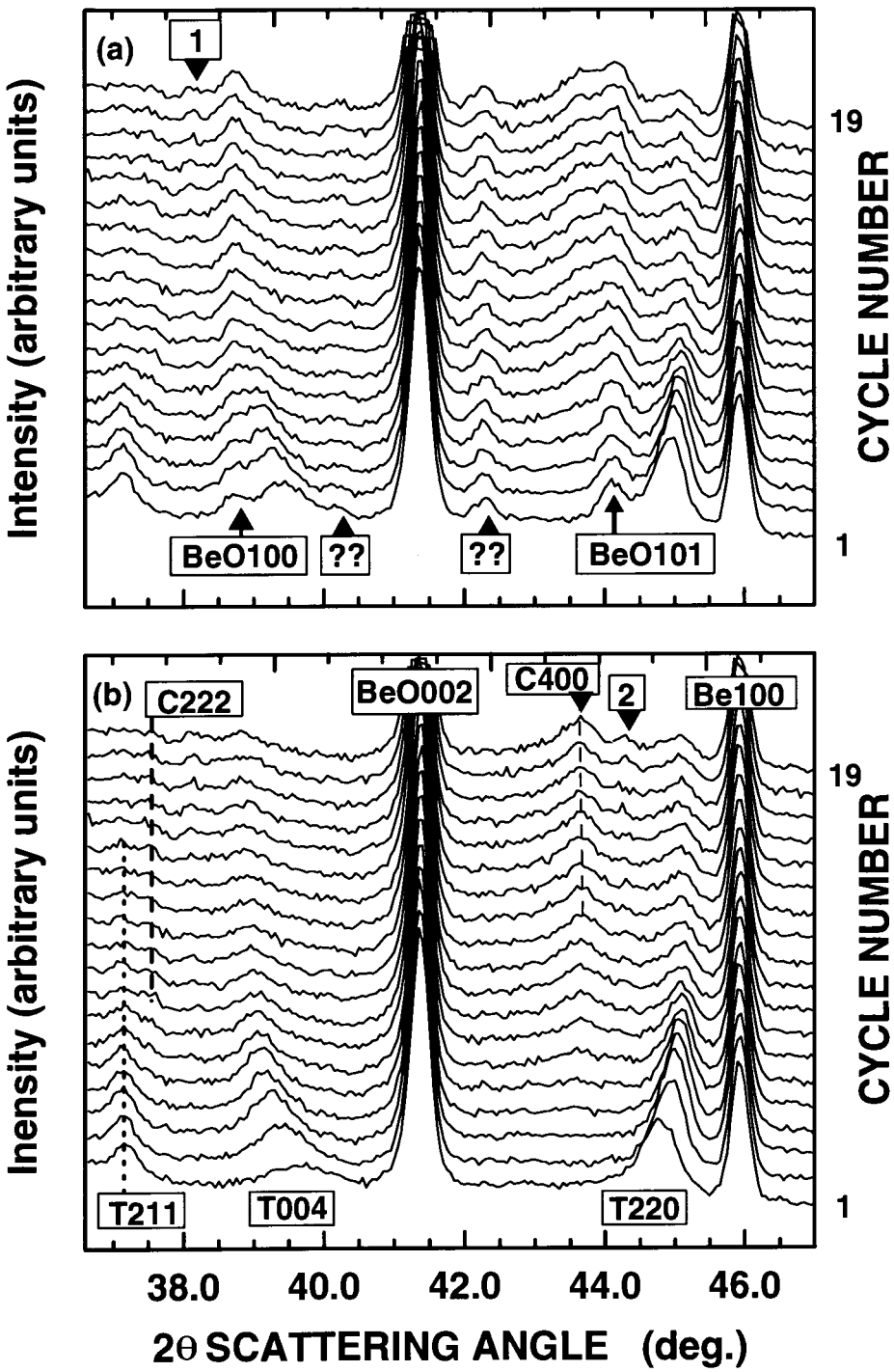

Figure 7.28: XRD data for region 1 where constant background peaks, labeled in (a) below the first scan, were removed by subtraction. The origin of the little peak labeled 1 in (a) and the larger peak labeled 2 in (b) are not yet understood. The questionmarks label constant background peaks.

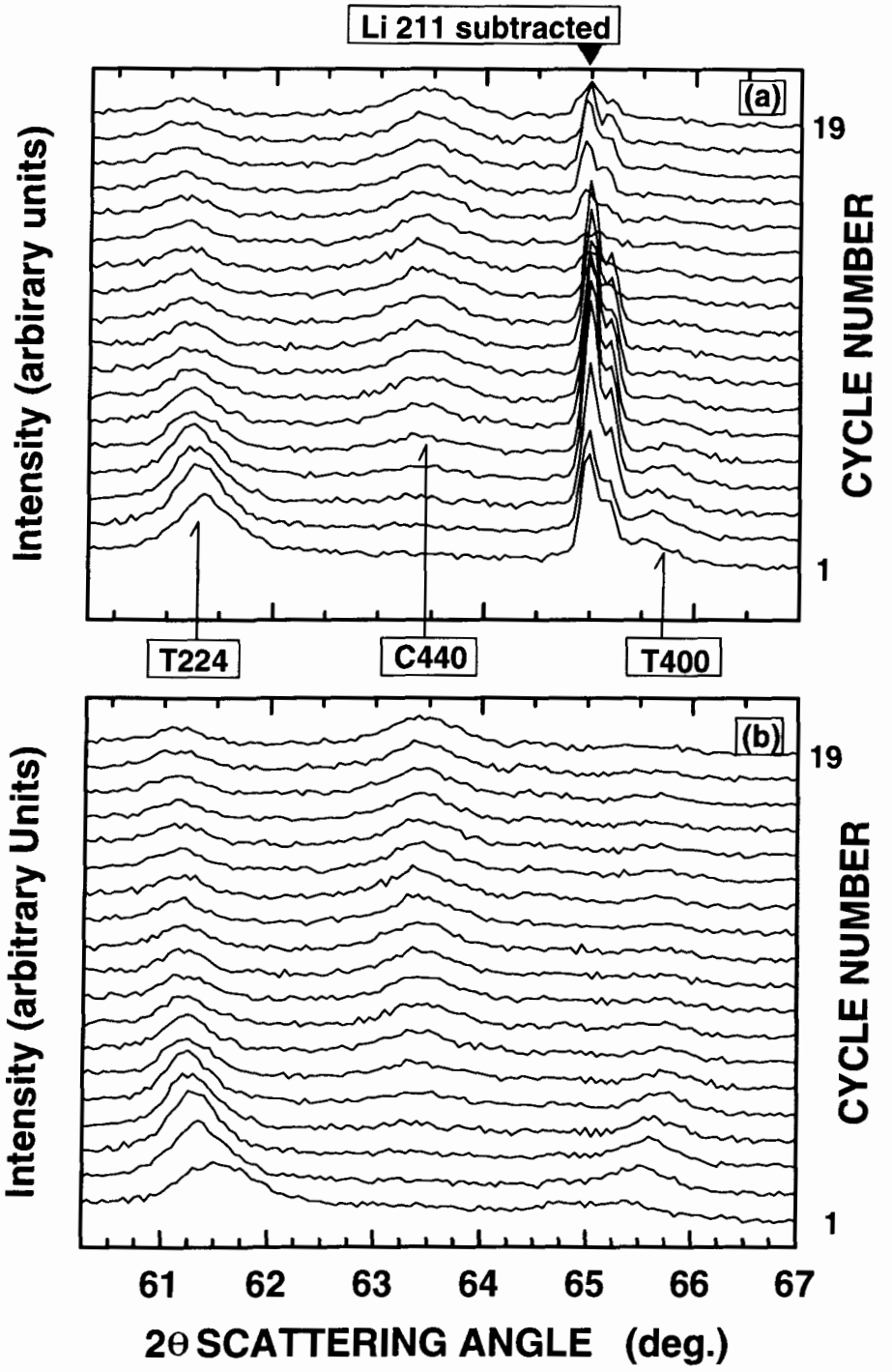

Figure 7.29: XRD data for region 2 where the variable background peak Li211 has been removed by a similar procedure as described for the 311 reflection in test 'Hero1'.

data in order to decide whether to proceed or to stop the entire refinement job. The automated fitting routine is part of the user interface for the refinement algorithm and was developed by the author.

Figure 7.30 shows the application of this method to a constant background peak, beryllium 100. Since the beryllium is chemically inert, no changes in shape or intensity of the peak are anticipated. The only possibility is that the peak may shift due to increasing stack pressure as discussed in section 7.2.3. Two refinement strategies were tested. In the first we kept the constant background parameter fixed[20] for each new XRD profile. The second strategy was to refine this parameter at the beginning for each new scan.

As we can see in Figure 7.30 the intensity does depend on the refinement strategy. The crosses mark the refinements where we kept the constant background parameter fixed and the round dots are the refinements where the constant background was refined. For reasons which we address later we find that the overall constant background increases as the *in situ* cell is cycled. Consequently we need to refine this parameter for each XRD profile in order to have comparable results. If we do this we find that halfwidth and intensity are constant within the error bounds of the refinement as can be seen in Figure 7.30. The systematic trend to higher intensities and halfwidths is gone. In Figure 7.30b we see that the position is almost unaffected by the fitting strategy. The shift for cycles 15 to 20 may be attributed to an assymetry in the peak (Cu-$K_{\alpha 2}$-contribution) and the slope of the linear background. The difference in halfwidth for the two strategies is not very profound. However, we have to keep in mind that the Be100 is a very strong peak and that the discrepancies between the two strategies are amplified for weaker peaks. The 5% error for the intensity and halfwidth may easily become as large 10 to 50% for weaker peaks.

As pointed out in chapter 6 refinement of any powder pattern needs always intelligent input. I suspect, that it will be very hard to formulate an algorithm which inverts a powder pattern from scratch and report the composition and structure of the powdered compound. However automation is possible and useful where we have to ensure consistence in the refinement of very similar datasets. As we have seen it is important to make the same refinement steps in succession for different raw data. Only then, we believe, is it reasonable to compare halfwidths, intensities and positions as a function of cycle number. In summary we find that the automated refinement

[20]at the value of the initial refinement

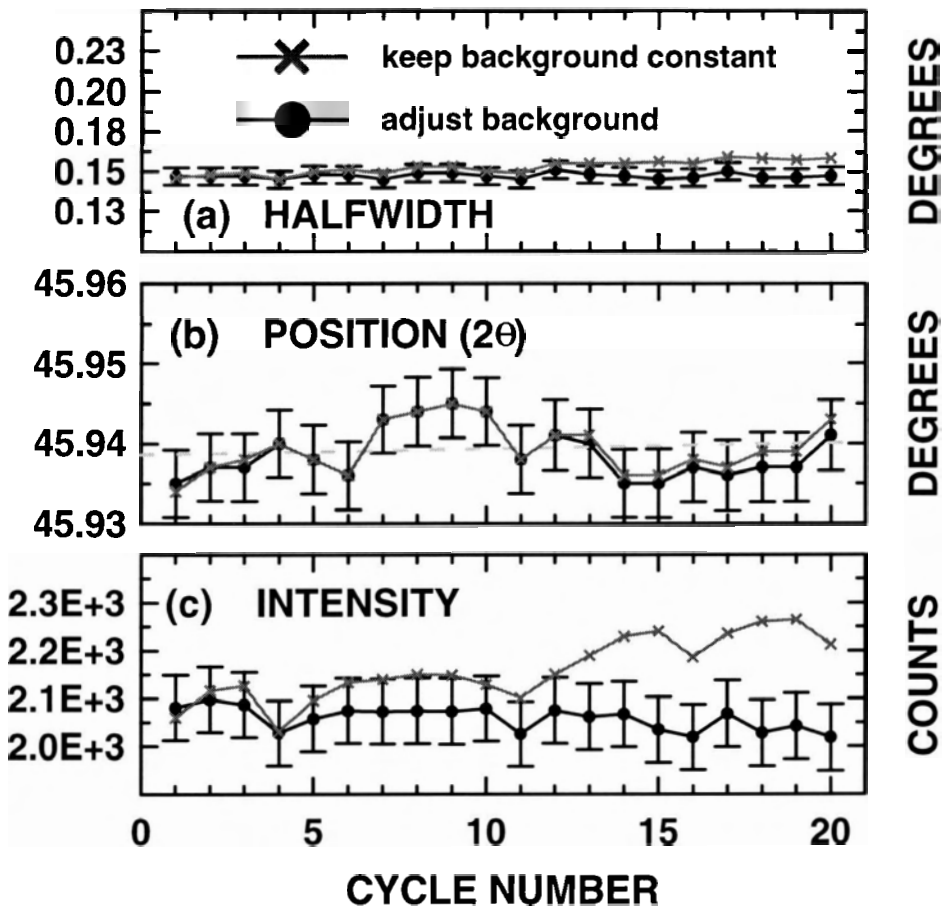

Figure 7.30: Halfwidth (a), position (b) and intensity (c) parameter *vs.* cycle number for the beryllium 100 peak. The extraction of the parameters from the 19 separate raw data files was done using an automated fitting routine. Refinement of the constant background parameter (round dots) has considerable impact on the consistency of the data.

tool works to our satisfaction. In the following we display the results. The massive task of fitting hundreds of similar data sets was greatly accelerated by the use of the automated fitting routine.

Halfwidths, Position and Intensity Results

Figure 7.31 shows the refined parameters for the two strongest peaks C400 and T220 at 2.3 V. The two stages indicated in Figure 7.23 are clearly observable in the trends for all three parameters. In Figure 7.32 and Figure 7.33 we see the refinements for the C400 peak at 3.3 V and 4.3 V respectively. The two stages are less pronounced.

The halfwidth in Figure 7.32 decreases rapidly over the first six cycles. Inverting the halfwidth of cycle 1 we obtain a correlation length of approximately 100 Å in the 400 direction. The correlation length for cycles 7 to 18 is constant at approximately 150 Å. For stage 1, the halfwidth of the C400 peak at 4.3 V (Figure 7.33) is also decreasing. The minimum is found for the 9th cycle and corresponds to a correlation length of almost 170 Å. This supports the idea that the cubic phase increases in crystallinity as we cycle the cell. The increase after cycle 10 is in contrast to the constant halfwidth for C400 at 3.3 V (Figure 7.32). We will address this later.

The position of the C400 peak decreases uniformly only for 2.3 V scans and for 3.3 V scans. At 4.3 V we find for the initial scans the opposite trend and for stage 2 there is only a slight decrease present at the end of the test.

The overall decrease in intensity in Figures 7.32 and 7.33 is not characteristic for the crystallographic transformations. We attribute this effect to stronger absorption. The idea is that as we cycle the cell, the lithium/separator interface becomes more disordered and electrolyte/lithium ion complexes can accumulate in the separator. Moreover we can assume that the lithium metal surface increases strongly from cycle to cycle as the dendrites form on each charge. The result is a stronger absorption and an increase in diffuse background scattering. Some evidence is given in Figure 7.34 where we plot the refinement parameters for the strong separator peak at 25.45 degrees. Clearly the increasing halfwidth indicates that the amount of order is reduced in the polypropylene layers and we also see that the intensity is decreasing. Interesting is the fact that the separator peak shifts also to lower angles. This supports the idea of a growing lithium/separator interface due to the formation of dendrites. The layers below that interface will be pushed down and, as the stack pressure increases on the top layer, the beryllium foil disk is pushed in opposite direction. In fact Figure 7.30b

displays a slight overall shift to higher angles (=scattering plane moves upward).

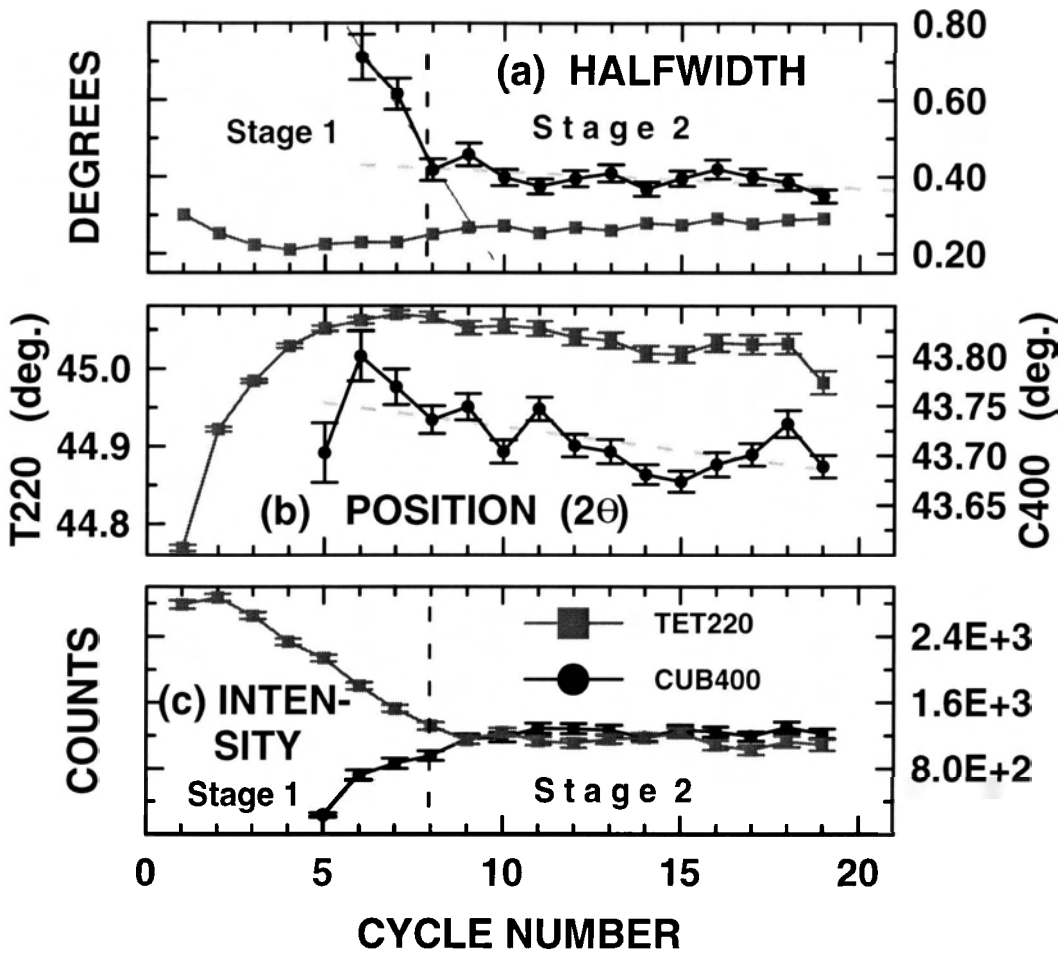

Figure 7.31: Peak parameters of C400 and T220 at 2.3 V. It is remarkable to see how the trends for the parameters follows the two stages indicated in the plot for capacity *vs.* cycle number. For stage 2 we notice how the position of *both* peaks shifts towards lower angles. The dramatic shift to higher angles of the T220 peak in stage 1 is apparent. As the intensity of the tetragonal peak decreases, the cubic peak picks up intensity. That is expected for two coexisting phases.

7.3.5 Lattice Constants of the Tetragonal Phase

The following three Figures 7.35, 7.36 and 7.37 display all the regions where we observed peaks belonging to the tetragonal phase. The top part is just an enlargement of the particular region in the XRD profiles for all 19 scans taken at 2.3 V. The

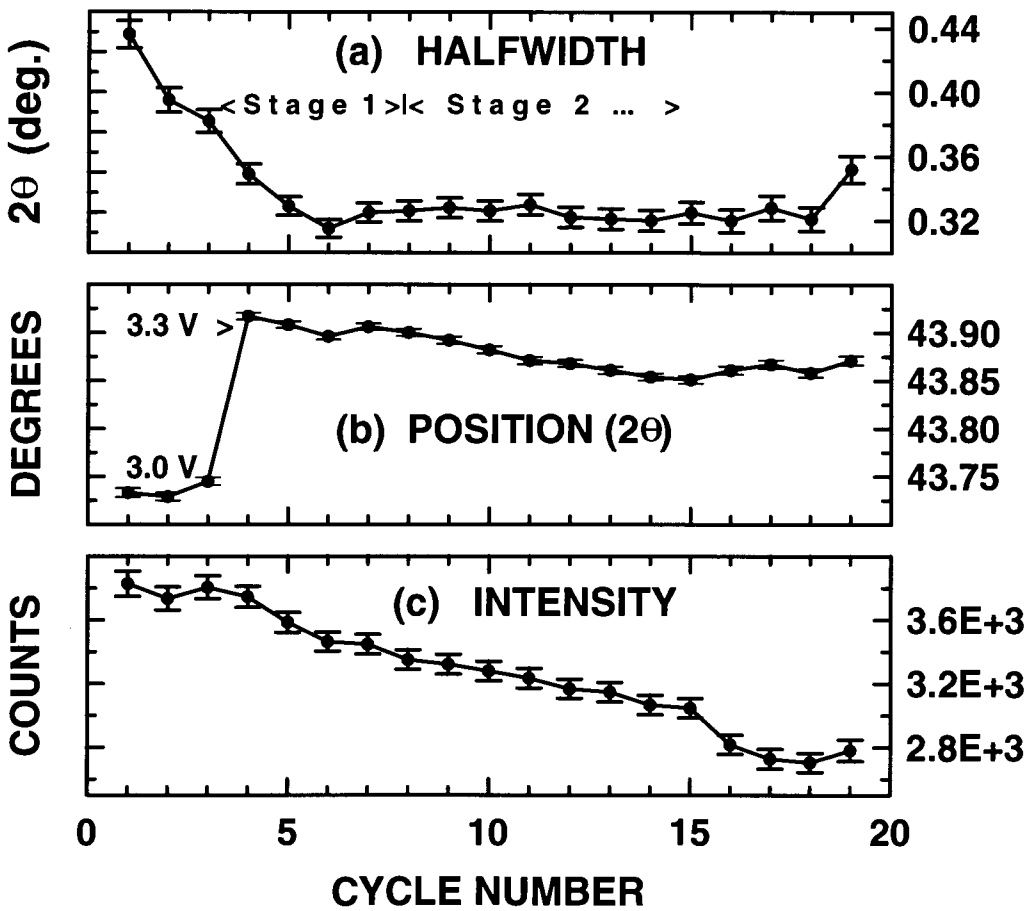

Figure 7.32: Peak parameters for C400 at 3.3 V. In (a) we indicate the two stages. The trend for the halfwidth changes two cycles before the end of stage 1. The shift of the peak to lower angles is apparent after the scanning potential was switched to 3.0 V. We assume that the halfwidth is not affected by the switch from 3.0 to 3.3 V. Here the halfwidth of 0.44 deg. corresponds to a correlation length of 100 Å and the halfwidth of 0.32 deg. corresponds to 150 Å, an indicator for increasing crystallinity of the cubic phase.

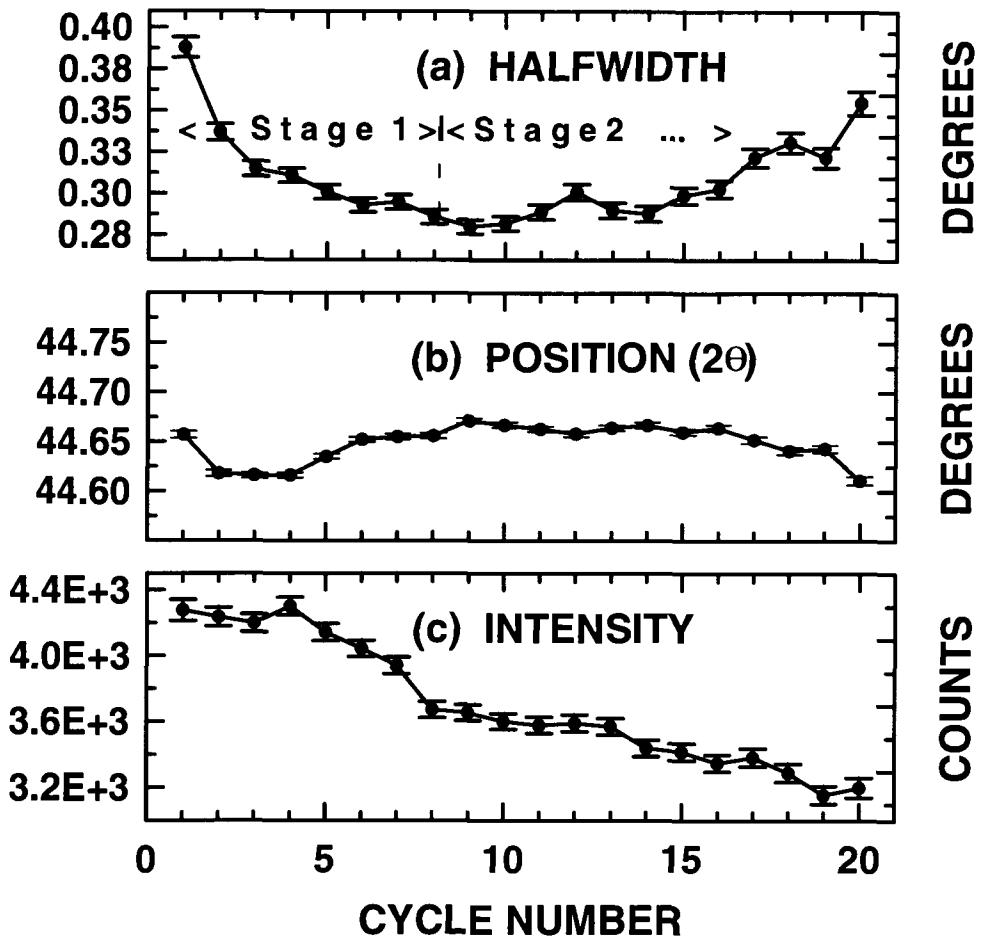

Figure 7.33: Peak parameters for C400 at 4.3 V. The two stages are less obvious compared to 2.3 V and 3.3 V. For stage 1 we find that the peak shifts to higher angles and for stage 2 there is a small shift towards lower angles. As in Figure 7.32 we observe an overall decreasing intensity. This may be attributed to a more disordered lithium/separator interface.

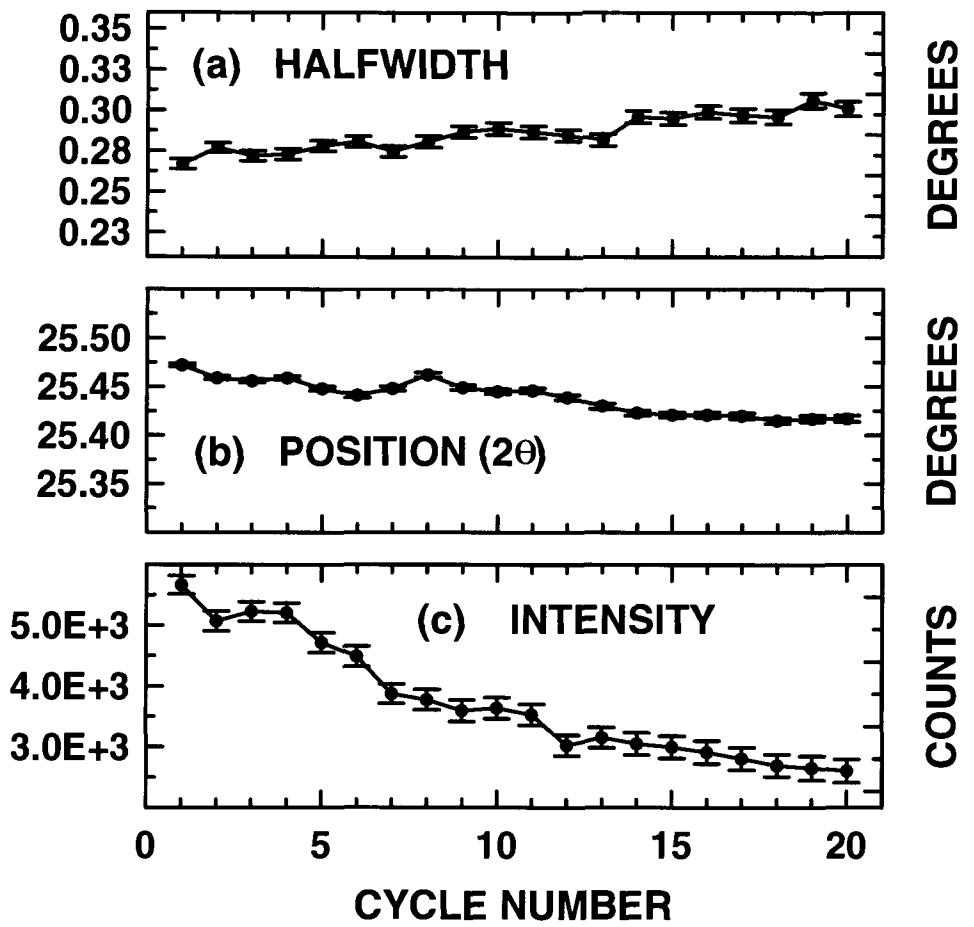

Figure 7.34: Peak parameters for a separator peak. The increasing halfwidth and the decreasing intensity indicate that the amount of disorder in the separator increases as lithium ions pass the layer on charge and discharge. The shift of the peak to lower angles is a consequence of the growth of dendrites.

second panel (b) plots the position *vs.* cycle number and the third panel (c) plots the intensity *vs.* cycle number. Some of the refinement data was displayed earlier (C400) in a different context. In all three intensity graphs cycle 8 indicates again a change in the slope for increase or decrease of the intensities. All of the tetragonal peaks consistently decrease in intensity whereas all of the cubic peaks consistently increase in intensity as we cycle the cell. This shows that the tetragonal phase forms less completely on each cycle.

The shift in position of the peaks is, however, not uniform. We can separate the tetragonal peaks into three groups. First there are peaks which shift to higher angles like T220 and T400. In the second group we have peaks which clearly shift to lower angles, such is the case for T004 and T224. The third group are the peaks which do not shift significantly like T211, T404. The peak positions allow the computation of the lattice constant and the tetragonal lattice is determined by two lattice constants. In Figure 2.10 in chapter 2 we labeled them a_t and c_t.[21] Then by convention (Miller indices) the positions of the T220 and T400 reflections are only determined by the lattice constant a. Likewise the position of T004 is only determined by the lattice constant c. The peaks in group three are determined by both lattice constants. If the peaks of the first group shift to lower angles we conclude that the lattice must contract in directions corresponding to the lattice parameter a. The shift for T004 to higher angles translates into an expansion of the lattice in c-direction. This is consistent with the discussion of peak shifts of the tetragonal phase in section 4.2.3.

Figure 7.38 shows the results of lattice parameter refinements as a function of cycle number. For each XRD-profile we used the refined position parameters of the tetragonal phase and refined those again using a fixed off-axis parameter of -82 μm for the lattice constants of a tetragonal unit cell. We confirm the proposed expansion of the the lattice constant c and the contraction of a. Although the errors are quite large, we find for both constants uniform behavior.

We have to add some qualifying remarks to this nice result. In section 7.3.4 we noticed that peaks shift towards lower angle with cycle number. The most likely cause for this phenomenon is a growth of the lithium/separator interface. A peak shift towards lower angles corresponds to an expansion in lattice constant. We did not correct the refined tetragonal peaks position for the lattice parameter refinements of all scans. Instead we extrapolated from Figures 7.31 and 7.32 an upper bound of 0.075 deg. for

[21] in the following we will drop the index t.

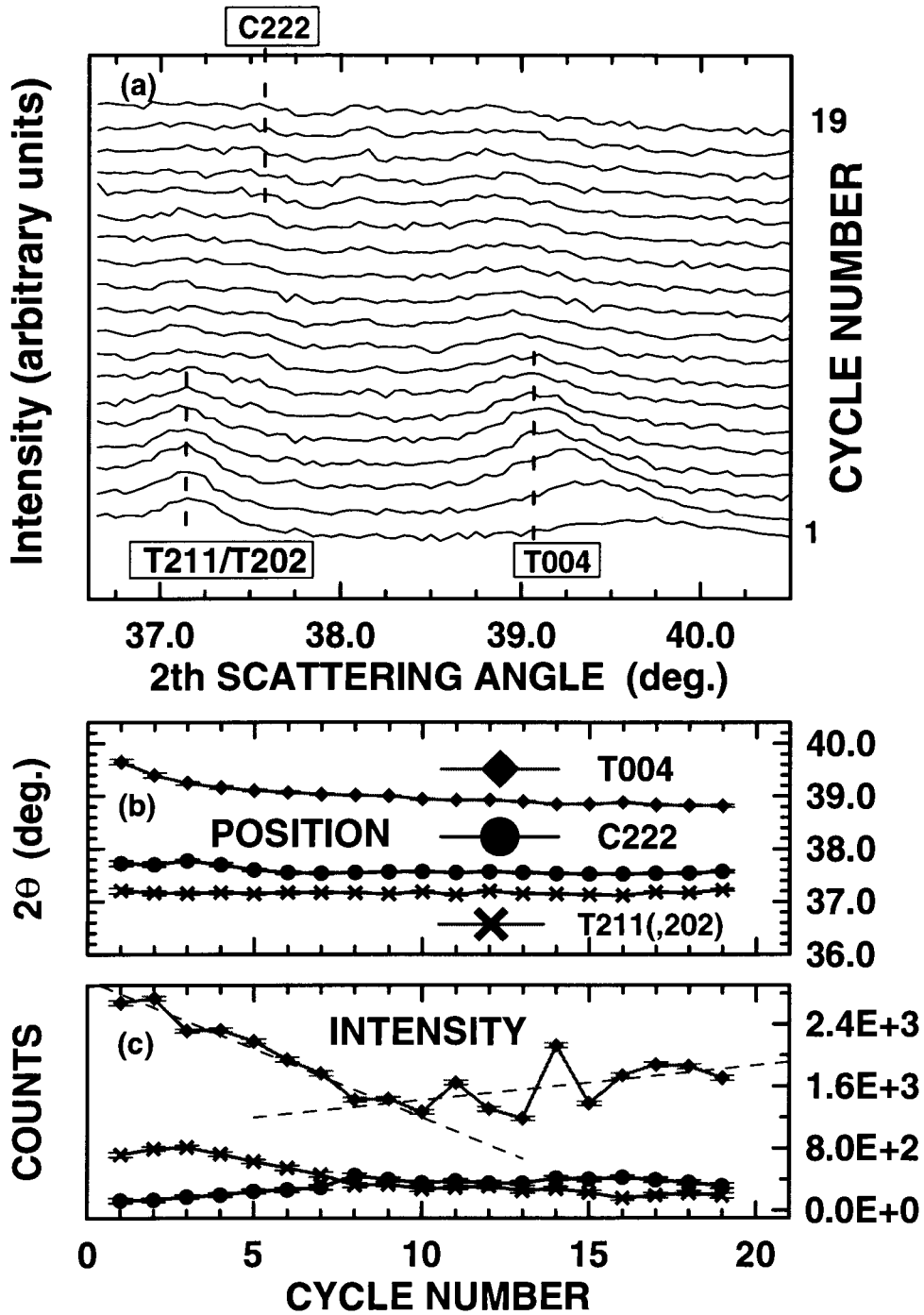

Figure 7.35: Modified XRD data for T211/202, T004 and C222. In (b) the positions refinements and in (c) intensity refinement are shown.

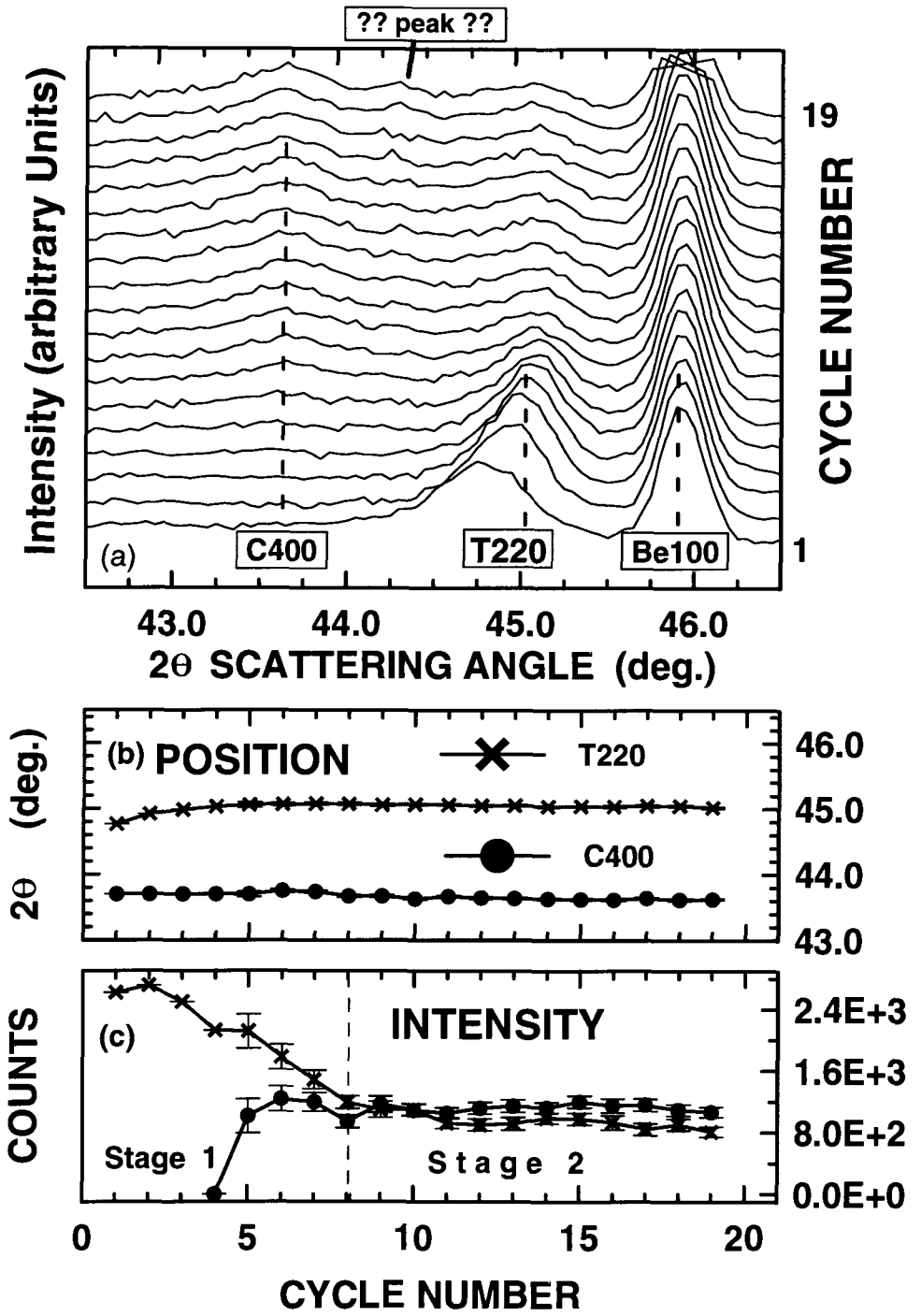

Figure 7.36: Position and halfwidth for C400 and T220. The peak with questionmarks could indicate the accumulation of inert cathode material upon subsequent cycling.

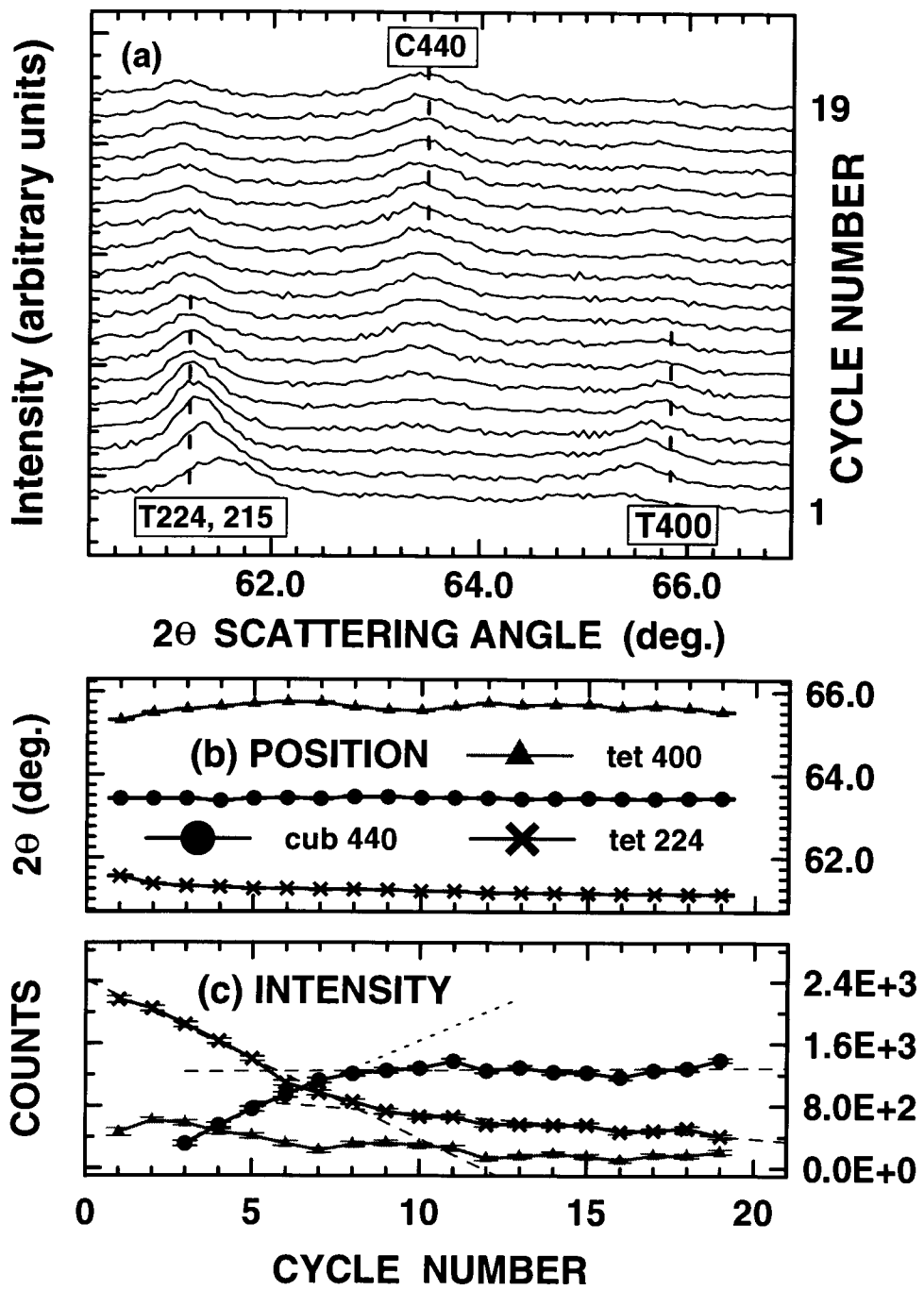

Figure 7.37: Position and halfwidth for C440 and T224/T215.

the shift of the C400 and T220 peaks due to the growth of the lithium/separator interface. The corresponding off-axis shift is approximately -100 μm . Using Equation 4.13 we corrected the peak positions and refined the lattice constants again for cycle 18. In Figure 7.38 we plotted the corrected lattice parameter for cycle 18 with black crosses. Both constants are smaller than the uncorrected values. However, the effect is rather small and this should suffice to convince ourselves that the overall trend is not affected by this correction.

7.3.6 Halfwidths and Crystallinity

Finally we analyzed the halfwidths as a function of cycle number for the cubic and tetragonal peaks at 2.3 V. Figure 7.40 shows the refinements for the two clearest peaks belonging to the cubic phase, 400 and 440. Figure 7.41 contains the results for the strongest tetragonal peaks. The rapid decrease of the halfwidth for C400 during stage 1 can be understood in terms of the proposed (slightly) tetragonal distorted cubic phase which formed broad peaks at the initial phase transition. As the crystallinity improves the cubic phase approaches the ideal parameters and the tetragonal distortion disappears. The true half with of the C400 peak is measures if T220 and T004 coincide for $c/a = \sqrt{2}$. A word of caution: the 400 peak is very weak for the first four scans, and this may overemphasize the trend. However the 440 reflection is also very weak in the beginning but displays a smaller halfwidth.

The halfwidths of the tetragonal peaks decrease uniformly over the first four cycles. The absolute magnitude is however not the same. This is understood if we consider that we average over a large ensemble of crystallites which underwent distortion from cubic to tetragonal symmetry. Some peaks depend more strongly on the c/a ratio than others, and will therefore shift more in position. This leads to a non uniform broadening of the peaks at intermediate stoichiometries[22]. For example the position of the T404 in Figure 7.27 is almost independent of the c/a ration whereas peaks like T400 and T004 are most sensitive to the c/a ratio. This hampers the analysis of sizes of crystallites as we shall see.

In Figure 7.42 we analyzed the halfwidths for Figures 7.40 and 7.41 and calculated the correlation lengths in the various directions. Taking the average correlation lengths we tried to extract the trends for the domain sizes of crystallites in the sample

[22]not all of the crystal is tetragonal.

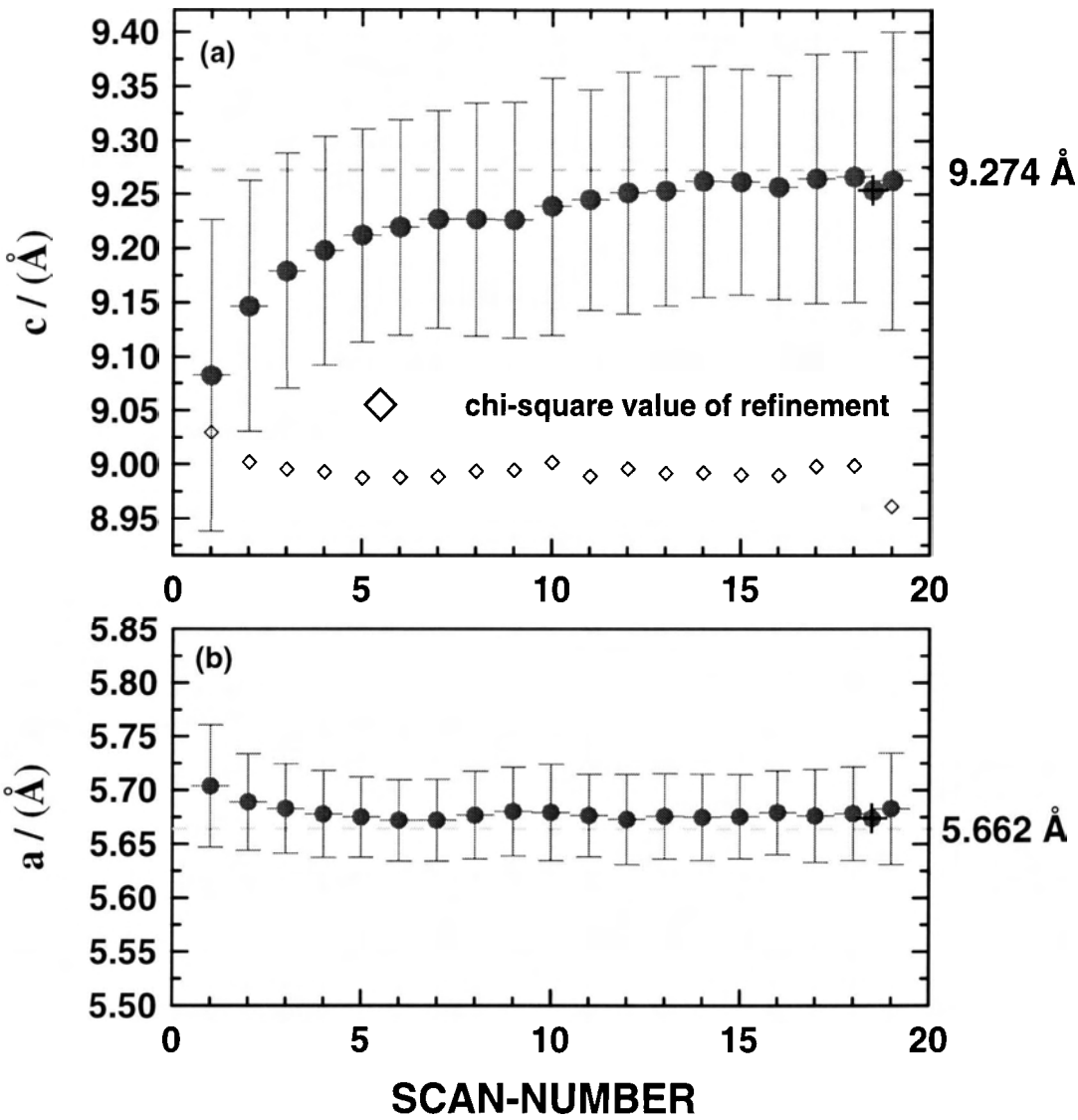

Figure 7.38: Lattice constants of the tetragonal phase. The unit cell expands along c and contracts in the perpendicular directions. As we cycle the cell we approach the reported literature values for the $Li_2Mn_2O_4$ phase indicated by dashed lines. The chi-square value for the lattice parameter refinement is also shown on arbitrary scale. Obviously the quality of this phase improves with increasing cycle number. However the amount which forms decreases with cycle number. The correction due to the shift of the scattering plane was not applied to all data sets. The cross in cycle 18.5 marks the corrected value of cycle 18.

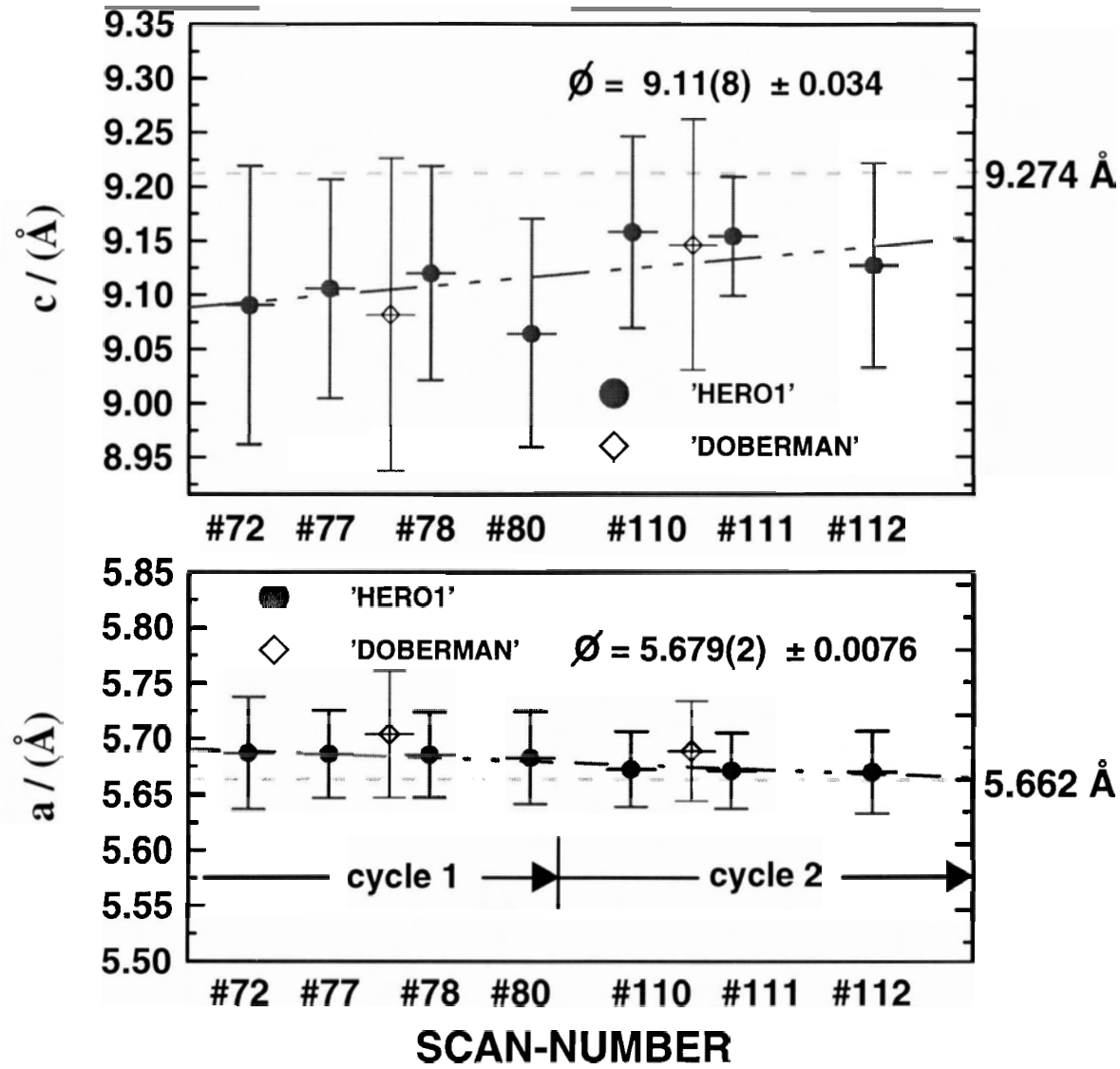

Figure 7.39: Comparison of the tetragonal lattice constants for experiment 'Hero1' and 'Doberman'. For 'Hero1' we plot the refinements of the lattice constants of a number of scans in the 2.3 V region for the two measured cycles. Linear least squares fits indicate that the formation of the tetragonal phase improves with increasing charge transfer. The calculated averages are the mean values and their standard deviation. For 'Doberman' we have only one XRD profile per cycle for refinement of tetragonal peaks at 2.3 V. The horizontal dashed lines correspond to the reported values in the literature.

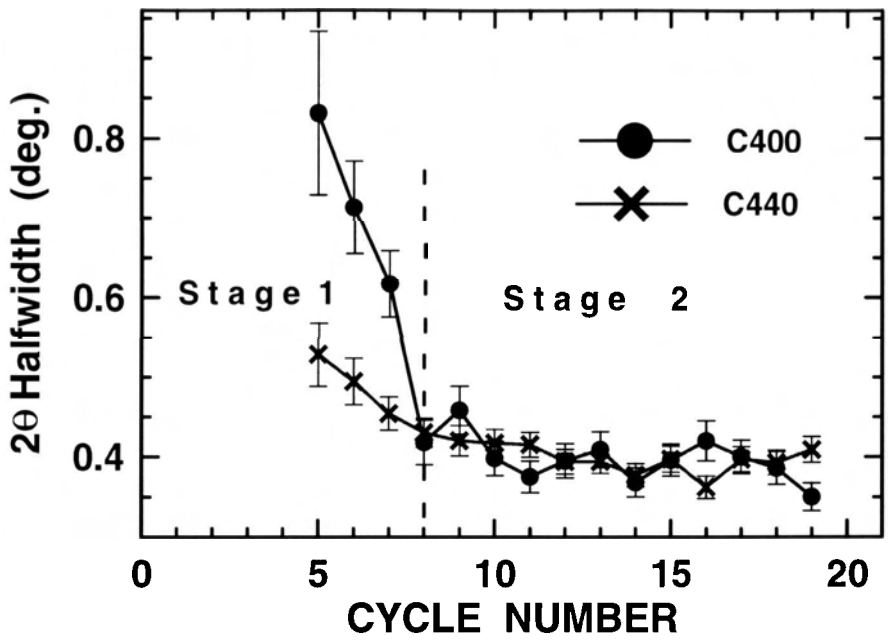

Figure 7.40: Halfwidths of C400 and C440 at 2.3 V. The strong decrease for C400 is not understood.

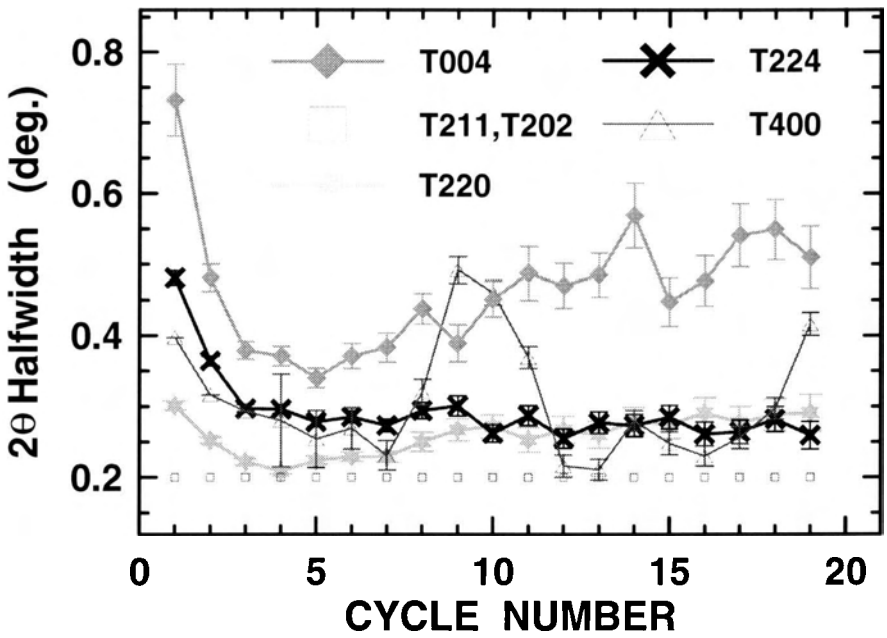

Figure 7.41: Halfwidths of the tetragonal peaks 2.3 V. The peaks most sensitive to the c/a ratio T004, T400 appear broadened.

as we did for 'Safari'.

During the first four cycles the average domain size of the tetragonal phase increases. The trend reverses for cycles 4 to 19, where we observe a net decrease for the average domain size as indicated by linear least squares fits to the average. The estimate of 150 Å for the domain size at cycle 19 is not accurate for the above mentioned reasons for nonuniform peak broadening. In some cases we could also not resolve two close peaks (T211/T202 and T224/215). However the value is a lower bound and is seen in contrast to the domain size of 100 Å for the first cycle. Obviously the crystallinity of the tetragonal phase improves over the first four cycles.

The competing cubic phase can only be refined with confidence for cycles 5 and above. The phase displays a strong growth in average domain size for cycles 5 to 8 and for the following cycles the growth rate is considerably less. Here we have more confidence in the validity of the estimate for the cubic domain sizes in the crystallites. Initially we have domains below 80 Å and for cycle 19 the domain size has almost doubled (155Å).

The tetragonal phase stops growing at cycle 4. This is strongly correlated with the increase in domain size of the cubic phase. The trends for stage 2 are also consistent with the model of a topotactic phase change. The cubic phase expands at the expense of the decreasing tetragonal phase. This is important since it indicates that we have truly a coexistence of two intimately connected phases in one and the same crystallite.

7.4 Discussion for Test 'Doberman'

In this last section we want to address particular results which were not fully addressed in section 7.3.

The first point is the position refinements of C400 at different potentials shown in Figure 7.31 and Figures 7.32 and 7.33. We found that for scans taken at 2.3 and 3.3 V the position of the C400 peak shifts to a lower angle as a function cycle number and attributed this trend to a shift in the position of the scattering plane. The trend for scans taken at 4.3 V was however not uniform. Here we found, after the position decreased from cycle 1 to 4, a shift towards higher angles. At the end of the experiment we found it again deceasing. The position of the C400 peak at 4.3 V volt measures directly the lattice constant at this particular charge state. A shift towards higher angles means that the lattice can contract more strongly. Since the

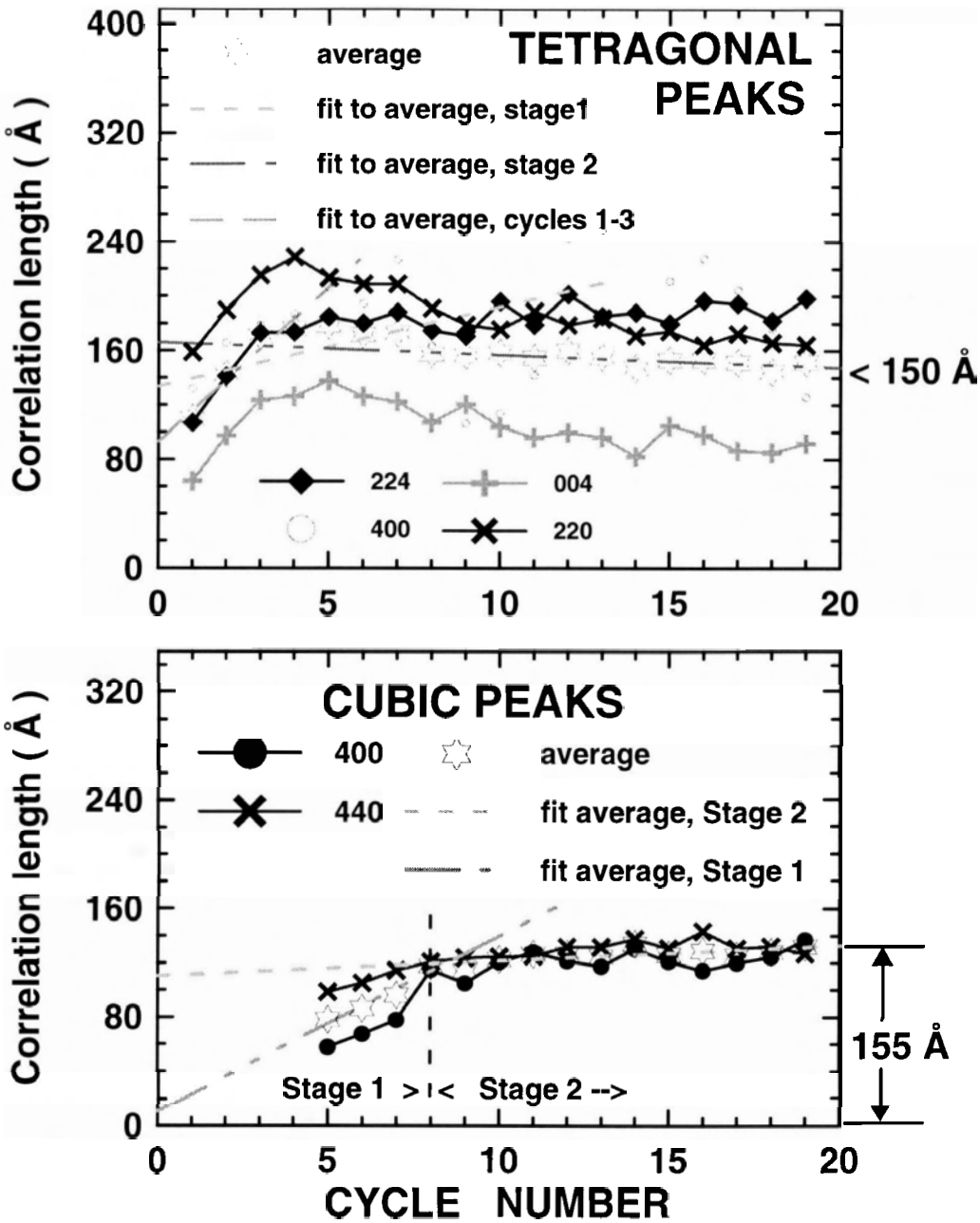

Figure 7.42: Correlation lengths in the tetragonal and cubic phase at 2.3 V. The linear least squares fit for the tetragonal phase is to the average of T224, T220 and T004. Due to broadening of peaks sensitive to the c/a ratio, the average correlation length is a lower bound. The cubic phase cannot be detected reliable for correlation lengths below 80 Å. During the experiment the correlation length of this phase almost doubled at this potential.

amount of lithium which can be removed from cycle to cycle always decreases, some Li atoms must be trapped in the structure which can not be removed at a potential of 4.3 V. This could be an indicator for a structural transformation process where cathode material is transformed into a electrochemically inert form like Li_2MnO_3.

The further explanation and interpretation of data involves the idea, that oxygen loss at high potentials $V \geq 4.1$ V plays a fundametal role in the structural transformations which occur on repetative cycling. As I discussed briefly in section 2.4.5, particular spinel phases are known to have their capacity plateaus distributed according to their oxygen deficiency [35].

Final Remarks

The discussion ends here although I could go on and present many (probably too many) interesting and exciting ideas. Due to the fact that I chose to finish my thesis here at SFU, rather than to follow our lab to Halifax, I lacked in the final stage of my research the necessary proximity to an environment where ideas could be discussed in a more fruitful manner. Being immersed in such an environment, it probably would have been possible to propose a concise and comprehensive model which fits all the data presented in this thesis. Such a model could then be tested and would stimulate future research. My attempt to propose a model on my own was in itself a very exciting and wonderful experience. The more I looked into all the questions the stronger was my desire to find a solution. However, in the end I had to realize that without proper guidance and the opportunity to discuss ideas 'on the spot' this became an endless task as I was running out of time. I also found it inherently difficult to discuss complex ideas over the phone, via e-mail and by fax machine. Jeff gave me the option to include some of my (already written) ideas in an appendix, with the note that the ideas presented there are questionable and rather speculative. I chose not to do so and removed the last month of work. This should explain why the end of the previous discussion is rather short and ends abruptly. There was no time left to carefully reformulate the discussion.

At this point I would like to thank Jeff Dahn again for his very critical and concise comments. I would also like to acknowledge that he replied very quickly to all of my questions. The experience I gained from this thesis project taught me a lot about honest and sucessful research and a multitude of other personal very valuable experiences. In the end I realize that the idea of presenting a *solution* to the many

cycle behaviour of $LiMnO_2$ needs a lot more work, much more than I possibly could include in this M.Sc. Thesis.

Chapter 8

Conclusions

The thesis reviews extensively the structures of three closely related lithium manganese oxide compounds: $LiMnO_2$, $LiMn_2O_4$ and $Li_2Mn_2O_4$. Their similarity can be understood by comparing their particular cation sublattices. The consequences of manganese being a typical Jahn Teller ion in these compounds are discussed in order to assess their stability under removal and insertion of lithium. The electrochemical behaviour of $Li/LiMnO_2$ cells and Li-ion cells has been studied in order to test the long-term cycling behavior. Capacity fade and a redistribution in the available capacity on the 3 V and 4 V plateau is documented.

A new design for *in situ* X-ray cells has been developed and tested which is particulary useful for long-term *in situ* X-ray studies.

The value and significance of *in situ* X-ray studies has been demonstrated. We have developed an interface which allows the accurate comparison of structural properties of powder electrodes at different potentials. The method has been applied to three experiments. Refinement techniques for the extraction of peak positions, halfwidths and intensities have been used extensively to accumulate large amounts of data. Test 'Safari' confirmed a phase transition from the orthorhombic phase to possibly a cubic phase. This cubic phase does not form exactly as one expects. The possible structural causes need further investigation.

Test 'Hero1' gave clear evidence for a two-phase region at 3 V. The new phase appears like a tetragonal distorted phase. At the end of discharge in the 3 V plateau, the transition from the cubic to this tetragonal phase is almost complete. The cubic phase at this stage is not directly apparent in the XRD profiles. With the analysis of multiplots in 'Hero1' we demonstrated that constant as well as varying background

peaks can be removed from the raw data in order to refine features belonging to the crystal phases in the cathode. The effects of varying thickness in the cathode stack, as the cell is charged and discharged, were also demonstrated.

Test 'Doberman' confirmed that the cubic phase transforms into a tetragonal phase in the two-phase regime which has initially different lattice parameters. We have shown that the crystallinity of the cathode material increases during subsequent cycles up to a certain point where the capacity fade changes to a lower rate.

Future Recommendations

A comprehensive model which includes the effects of volume reduction, Jahn-Teller distortions, the possibility of 'stacking faults' and other kinds of disorder must still be developed in order to explain the electrochemical data in conjunction with the observed X-ray data.

The effects and mechanisms of oxygen loss at battery potentials above 4.0 V seem crucial to finding an explanation of the capacity fade and the fact that the lower plateau in $LiMnO_2$ cells shrinks on the expense of the upper plateau.

It is also necessary to address the question of electronic conductivity in lithium manganese oxides. Intercalation is not possible if the cathode compound behaves like an insulator.

Finally there is the need of calculating the phase diagrams for the $Li_xMn_{1-x}O$ system. Of particular interest is the pressure dependence of $LiMnO_2$ and $LiMn_2O_4$at constant temperature.

Bibliography

[1] Alf M. Wilson, *Lithium Insertion in Carbonaceous Materials Containing Silicon*, Ph.D. thesis, Simon Fraser University (April 1997)

[2] Charles E. Mortimer, *Chemie*, Georg Thieme Verlag Stuttgart (1987)

[3] T. Ohzuku, A. Ueda and T. Hirai, "$LiMnO_2$ as a cathode for secondary lithium cell," *Chemistry Express* **7**, no. 3, 193–196 (1992)

[4] J.N. Reimers, E.W. Fuller, E. Rossen and J.R. Dahn, "Synthesis and electrochemical studies of $LiMnO_2$ prepared at low temperatures," *J. Electrochem. Soc.* **140**, no. 12, 3396–3401 (1993)

[5] R. J. Gummow, D. C. Liles and M. M. Thackeray, "Lithium extraction from orthorhombic lithium manganese oxide and the phase transformation to spinel," *Material Research Bulletin* **28**, 1249 (1993)

[6] L. Croguennec, P. Deniard, R. Brec, P. Biensan *et al.*, "Electrochemical behavior of orthorhombic $LiMnO_2$: influence of the grain size and cationic disorder," *Solid State Ionics* **89**, 127–137 (1995)

[7] Weiping Tang, Hirofumi Kanoh and Kenta Ooi, "Lithium ion extraction/insertion with orthorhombic $LiMnO_2$ in ammonium peroxodisulfate solutions," Submitted to *J. Electrochem. Soc.*

[8] W.D. Johnston and R.R. Heikes, "A study of the $Li_xMn_{1-x}O$ system," *Journal of the American Chemical Society* **78**, 3255 (1956)

[9] M. Tabuchi, K. Ado, C. Masquelier, I. Matsubara *et al.*, "Electrochemical and magnetic properties of lithium manganese oxide spinels prepared by oxidation at low temperature of hydrothermally obtained $LiMnO_2$," *Solid State Ionics* **89**, 53–63 (1996)

[10] R. Hoppe, G. Brachtel and M. Jansen, "Über $LiMnO_2$ und β-$NaMnO_2$," *Anorganische und Allgemeine Chemie* **417**, no. 1, 1–10 (1975)

[11] I.M. Kötschau, M.N. Richard, J.R. Dahn, J.B. Soupart *et al.*, "Orthorhombic $LiMnO_2$ as a High Capacity Cathode for Li-Ion Cells," *J. Electrochem. Soc.* **142**, no. 9, 2906–2910 (1995)

[12] R. R. Chianelli, J. C. Scanlon and B. M. L. Rao, "Dynamic X-ray diffraction," *J. Electrochem. Soc.* **125**, no. 10, 1563–1566 (1978)

[13] J.R. Dahn, *Thermodynamics and Structure of Li_xTiS_2: Theory and Experiment*, Ph.D. thesis, University of British Columbia (1982)

[14] Wu Li, *Lithium Transition Metal Oxides and Battery Applications*, Ph.D. thesis, Simon Fraser University (September 1994)

[15] Tao Zheng, *The Physics and Chemistry of High Capacity Carbonaceous Materials for Lithium-Ion Batteries*, Ph.D. thesis, Simon Fraser University (June 1996)

[16] Eric Dowty, "ATOMS for Windows 3.2," © (1995)

[17] Tsutomu Ohzuku, M. Kitagawa and T. Hirai, "Electrochemistry of manganese dioxide in lithium nonaqueous cell," *J. Electrochem. Soc.* **137**, no. 3, 769–775 (1990)

[18] T. Hahn, *International Tables for Crystallography*, Dordrecht, Holland and Boston, U.S.A (1984)

[19] Ralph W. G. Wyckoff, *Crystal Structures*, Interscience Publishers, Div. of John Wiley & Sons, New York, 2nd edn. (1965)

[20] A. Miller, *J. Appl. Phys. Suppl.* **30**, 24S (1959)

[21] J.B. Goodenough, M. M. Thackeray, W.I.F. David and P.G. Bruce, "Lithium insertion/extraction reactions with manganese oxides," *Revue de Chimie minérale* **21**, 435–450 (1984)

[22] R.D. Shannon and C.T. Prewitt, "Effective ionic radii in oxides and fluorides," *Acta Crystallographica B* **25**, 925–946 (1969)

[23] R.D. Shannon and C.T. Prewitt, "Revised values of effective ionic radii," *Acta Crystallographica B* **26**, 1046–1048 (1970)

[24] O. Muller and R. Roy, *The Major Ternary Structural Families*, Springer-Verlag, Berlin, 1st edn. (1974)

[25] R.J Gummow, A. de Kock and M.M. Thackeray, "Improved capacity retentions in rechargable 4 V lithium/lithium-manganese oxide (spinel) cells," *Solid State Ionics* **69**, 59–67 (1994)

[26] M. M. Thackeray, A. Gummow, R. J. de Kock, A.P. de la Harpe and D. C. and Liles, "Spinel electrodes for rechargable lithium batteries - a review," From 11th Int. Seminar on Primary and Secondary Batteries, Deerfield Beach, Florida (March 1994)

[27] J. Kanamori, "Crystal distortion in magnetic compounds," *J. Applied Physics* **31**, S14–23 (1960)

[28] M. M. Thackeray, W.I.F. David, P.G. Bruce and J.B. Goodenough, "Lithium insertion into manganese spinels," *Material Research Bulletin* **18**, 461–472 (1983)

[29] J.M. Tarascon, E. Wang, F.K. Shokoohi, W.R. McKinnon *et al.*, "The spinel phase of $LiMn_2O_4$ as a cathode in secondary lithium cells," *J. Electrochem. Soc.* **138**, no. 10, 2859–2864 (1991)

[30] A.F. Wells, *Models in Structural Inorganic Chemistry*, Oxford University Press (1970)

[31] C.N.R. Rao, *Solid State Chemistry*, Marcel Dekker, Inc. New York (1974)

[32] A. Mosbah, A. Verbaere and M. Tournoux, "Phases $Li_xMnO_2\lambda$ rattachees au type spinelle," *Material Research Bulletin* **18**, 1375–1381 (1983)

[33] K. Mizushima, M. Tanaka, A. Asai, S. Iida *et al.*, "Impurity levels of iron-group ions in TiO_2 (ii)," *J. Phys. Chem. Solids* pp. 1129–1140 (1979)

[34] H. Kanoh, Q. Feng, T. Hirotsu and K. Ooi, "AC Impedance analysis for Li^+ insertion of a Pt/λ-MnO_2 electrode in and aqueous phase," *J. Electrochem. Soc.* **143**, 2610–2615 (1996)

[35] M.N. Richard, E.W. Fuller and J.R. Dahn, "The effect of ammonia reduction on the spinel electrode materials, $LiMn_2O_4$ and $Li(Li_{1/3}Mn_{5/3})O_4$," *Solid State Ionics* **73**, 81–91 (1994)

[36] J.C. Rousche and J. Soupart, Sadachem S-A. - Tertre, Div. of Sedema; Research Laboratory; BP.9-7333 Tertre - Belgium

[37] Oliver Schilling, *Structural, Thermal, and Electrochemical Studies of Manganese Dioxides for Alkaline and Lithium-Ion Cells*, Ph.D. thesis, Simon Fraser University (April 1997)

[38] E. Peled, "The electrochemical behavior of alkali and alkaline earth metals in nonaqueous battery systems - the solid electrolyte interphase model," *J. Electrochem. Soc.* **126**, 2047–2051 (1979)

[39] Brian Way, *Lithium Intercalation in B_zC_{1-z} Solid Solutions*, Ph.D. thesis, Simon Fraser University (1995)

[40] Hang Shi, *Disordered Carbons and Battery Applications*, Ph.D. thesis, Simon Fraser University (1993)

[41] Y. Liu, J.S. Xue, T. Zheng and J.R. Dahn, *Carbon* **34**, 193 (1996)

[42] J.B. Bates, D. Lubben, N.J. Dudney and F.X. Hart, "5 volt plateau in $LiMn_2O_4$ thin films," *J. Electrochem. Soc.* **142**, no. 9, L149–151 (1995)

[43] N.F.M. Henry, H. Lipson and W.A. Wooster, *The Intepretation of X-Ray Diffraction Photographs*, MacMillan, London (1961)

[44] B.D. Cullity, *Elements of X-Ray Diffraction*, Addison-Wesley Publishing Company, Inc., 2nd edn. (1978)

[45] B.E. Warren, *X-Ray Diffraction*, Addison-Wesley Publishing Company, Reading Massachusetts (1990)

[46] A. Stokes and A.J.C. Wilson, *Proc. Camb. Phil. Soc.* **38**, no. 313 (1942)

[47] M.N. Richard, I.M. Kötschau and J.R. Dahn, "A cell for *In Situ* x-ray diffraction based on coin cell hardware and bellcore plastic electode technology," *J. Electrochem. Soc.* **144**, no. 2, 554–557 (1997)

[48] A.S. Gozdz, C.N. Schmutz, J.M. Taracscon and P.C. Warren, "Pat. coop. treaty appl." Tech. rep., PCT/US94/08772 (1994)

[49] Monique Richard, *The Behavior of Lithium and Sodium Iron Oxides as Cathode Materials for Lithium Batteries*, Master's thesis, Simon Fraser University (June 1996)

[50] Autodesk Inc., "Autocad, release 13 (Windows version 3.10)," © (1996)

[51] H.M. Rietveld, "A profile refinement method for nuclear and magentic structures," *J. Appl. Cryst.* **2**, 65–71 (1969)

[52] R. A. Young, *The Rietveld Method*, IUCr Monographs on Crystallography, Oxford University Press, New York (1995)

[53] C.J. Howard and R.J. Hill, "Report no. m112. technical report," Tech. rep., Australian Atomic Energy Commission (1986)

[54] "Powder diffraction file, 1993. pdf database sets 1-43." (1993), International Centre for Diffraction Data , 12 Campus Blvd., Newtown Square Pensylvania 19073-3273, U.S.A.

[55] W.H. Press, S.A. Teukolsky, Vetterling W.T. and Flannery B.P., *Numerical Recipies in Fortran. The Art of Scientific Computing.*, Cambridge University Press, Cambridge (1989)

[56] Henricks Sterling and Edward Teller, "X-Ray interference in partially ordered layer lattices," *The Journal of Chemical Physics* **10**, 147–151 (1942)